



The University of
Nottingham

UNITED KINGDOM • CHINA • MALAYSIA

Jaafar, Hasan Abdulhussein (2017) Detection and localisation of structural deformations using terrestrial laser scanning and generalised procrustes analysis. PhD thesis, University of Nottingham.

Access from the University of Nottingham repository:

http://eprints.nottingham.ac.uk/39376/1/Thesis%20_final_uploaded.pdf

Copyright and reuse:

The Nottingham ePrints service makes this work by researchers of the University of Nottingham available open access under the following conditions.

This article is made available under the University of Nottingham End User licence and may be reused according to the conditions of the licence. For more details see:
http://eprints.nottingham.ac.uk/end_user_agreement.pdf

For more information, please contact eprints@nottingham.ac.uk

**Detection and Localisation of Structural Deformations
Using Terrestrial Laser Scanning and
Generalised Procrustes Analysis**

by

HASAN ABDULHUSSEIN JAAFAR
B.Sc.(Hons), M.Sc.

Thesis submitted to the University of Nottingham for
the degree of Doctor of Philosophy

Nottingham Geospatial Institute

January 2017

This page intentionally blank


I certify that this thesis was prepared under my supervision at the University of Nottingham to satisfy the requirements for the degree of Doctor of Philosophy in Engineering Surveying and Space Geodesy.

Supervisor: *Dr Xiaolin Meng*

Signature: 

Date: 20/01/2017

Student: *Hasan Abdulhussein Jaafar*

Signature: 

Date: 20/01/2017

ABSTRACT

One of the most vital duties for engineers is to preserve life and nature by utilising safe designs that take into account environmental standards and monitoring the performance of structures against design criteria. Furthermore, monitoring can be used to determine any required maintenance of an important structure following a catastrophic event. Numerous different techniques and instruments can be employed for such a purpose with different requirements producing different results. For instance, some techniques need to embed sensors inside the building, such as Geotechnical Sensors. Others can offer high quality, but with a low point density and require fixed stations and targets, like Total Stations (TS). In such cases, the location of deformation tends to be known, such as in dams, bridges, and high-rise buildings. However, this is not always the case where it might be hard to expect deformation location as in the case of historic ruins where each part of the structure could be subject to deformation. The challenge in such case is to detect the deformation without any previous knowledge. Remote Sensing (RS) techniques, such as Digital Photogrammetry, Synthetic Aperture Radar (SAR), Interferometric Synthetic Aperture Radar (InSAR), and Terrestrial Laser Scanner (TLS) can be solutions for such an issue.

Interestingly, many researchers are focusing on using TLS for monitoring owing to the great spatial resolution system can offer. However, there are three challenges in using TLS in monitoring: the first one is a huge amount of data and the difficulty of handling it; the second one is the difficulty of comparing between two epochs because observations of TLS are not repeatable; and the third issue is the noise which is attached to the data. The first problem is solved by segmentation and point structure while the second and the third ones still need more investigation, although some interesting researches have been done in this area.

The aim of this research is to develop a new approach to detect and localise unpredictable deformation. It is based on TLS measurements and Generalised Procrustes Analysis (GPA) techniques to determine deformation vectors, while boxing structure and F-test are used to detect and localise deformation. In summary, after applying this approach, the whole concerned building is represented as parts, for each of which the displacement vector and the deformation probability are estimated. Ultimately, it is possible to monitor any part through different epochs. In addition, through this technique, it is possible to determine deformations - not just between two epochs, but for sequences of them. This can give more reliable results.

Four validation experiments have been conducted. The first test was designed to assess the performance of the developed software and to fix some variables. Therefore, it was based on simulated data with controlled white noise, distributed according to the normal distribution, and simulated deformations. The results of this test revealed the success of the proposed algorithm to detect and to localise deformations. In addition, it showed the success when no deformations exist. Furthermore, optimistically, it could observe deformations with magnitude less than the noise level; however, the probability was only 40%.

Correspondingly, real scan data with simulated deformations was used in the second test. The purpose of this test is to examine the performance of the proposed method in case of real errors budget. However, the short range of the test (about 10m), a featureless scanned area (wall only), and scanning from one position for all epochs (no need for registration) can reduce errors to a minimum. Results of this test showed the success of the proposed method to detect and localise deformations. Potentially, it can give indications for areas with deformations less than the noise level. Furthermore, results of the proposed method can be considered better than that of CloudCompare software.

The third test was conducted to examine the performance of the proposed technique regarding different materials and textures. For this purpose, the Nottingham Geospatial Building (NGB) was selected with more extensive ranges (between 20-25 m). Similar to the second test, all measurements were taken from the same scanner position. To some extent, the proposed technique succeeded to detect and to localise deformations. However, the researcher does not recommend it for monitoring modern and complicated buildings, instead it has been developed for monitoring historic ruins.

Finally, the proposed method was applied on the Bellmanpark Limekiln, Clitheroe, Lancashire monitoring project. This is a live project for Historic England and addresses a historic building that currently has some structural issues. The outcome of the proposed method revealed deformations in the faces South East (SE) and North East (NE). From examining these faces, three deformed areas were found: two in the face SE and one in the face NE, which might cause some cracks appeared in these faces. Alternatively, the CloudCompare software has been employed to detect deformation. Although results coincide with the proposed method for detected deformations, it cannot locate these deformations very well because it diffused over a wide area. In addition, it cannot determine actual directions of the deformations unlike the proposed method.

ACKNOWLEDGMENT

This research was carried at the Nottingham Geospatial Institute (NGI) within the Department of Civil Engineering at the University of Nottingham. The research was fully sponsored by the Iraqi Ministry of Higher Education and Scientific Research (MOHESR)

I would like to express my sincere thanks to my supervisors, Dr Xiaolin Meng and Dr Andrew Sowter, for their encouragement and invaluable advice.

The author would like to give special thanks to Dr Marcio Aquino for proofreading with invaluable advice.

Also, many thanks to who allowed me to attend their lectures Dr Richard Bingley, Dr Martin Smith, Dr Panagiotis Psimoulis, and all other lecturers for training courses I cannot remember their name.

Thanks also go to senior technician staff (Mr Sean Ince, Dr Nick Kokkas, and Dr Lukasz Bonenberg) for their real help in many aspects.

Finally, I would like to express my sincere thanks to my friend Mr Derrick Hartley for his suggestions on how to give the text a final “polish.”

DEDICATE

“In The Name of ALLAH Most Gracious Most Merciful”

In Memory of My Father (1941 – 2013)

&

To my wife “Nada”, my sons “Ali & Zaid”, and my daughter “Massara”.

TABLE OF CONTENTS

ABSTRACT	iv
ACKNOWLEDGMENT	vi
DEDICATE	vii
TABLE OF CONTENTS	viii
LIST OF FIGURES	xiii
LIST OF TABLES	xviii
LIST OF ABBREVIATIONS	xx
CHAPTER ONE: INTRODUCTION	1
1.1 Preface	1
1.2 Aims and Objectives	2
1.3 Methodology	3
1.4 Contribution to Knowledge.....	3
1.5 Thesis outline	4
CHAPTER TWO: BACKGROUND AND CONCEPTS	6
2.1 Introduction	6
2.2 Laser Light	6
2.3 Laser Scanner Classifications	7
2.4 TLS Measurements.....	9
2.4.1 Angle Measurement and Deflection System	10
2.4.2 Distance Measurements	11
2.5 Deformation Monitoring	16
2.5.1 Structural Deformation.....	17
2.5.2 Expected Deformation and Required Accuracy	18
2.6 Monitoring Techniques	19

2.7	Monitoring of Historic and Heritage Buildings	20
2.7.1	Conventional Surveying Technique	22
2.7.2	Geotechnical Sensors	23
2.7.3	Wireless Smart Sensors	24
2.7.4	Video Gauge Sensing	25
2.7.5	Interferometric Synthetic Aperture Radar	26
2.7.6	Photogrammetry and TLS	27
CHAPTER THREE: USING TERRESTRIAL LASER SCANNER FOR MONITORING.....		33
3.1	Introduction	33
3.2	TLS Monitoring Techniques	33
3.2.1	Using Targets.....	33
3.2.2	Cloud to Cloud Comparison	34
3.2.3	Interpolating Models	35
3.2.4	Surfaces Matching.....	37
3.2.5	Specific Solutions.....	38
3.3	Registration	39
3.3.1	Targets Based Registration.....	40
3.3.2	Geometrical Objects and Natural Features	40
3.3.3	Surface Matching	41
3.3.4	Coarse Initial Alignment.....	42
3.4	Georeferencing.....	44
3.4.1	Direct Georeferencing	44
3.4.2	Indirect Georeferencing	45
3.5	Chapter Summary	45
CHAPTER FOUR: ERROR SOURCES IN TLS		47

TABLES OF CONTENTS

4.1	Introduction.....	47
4.2	TLS Error Sources.....	47
4.2.1	Instrumental Errors.....	49
4.2.2	Object-related Errors.....	52
4.2.3	Environmental Effects.....	54
4.2.4	Methodological Impacts.....	55
4.3	Quantification of Errors.....	57
4.3.1	Scanstation P20.....	59
4.3.2	Scanstation P40.....	69
4.3.3	Comparison between P20 and P40.....	77
4.4	Noise Mitigation.....	78
4.5	Chapter Conclusion.....	86
CHAPTER FIVE: USING PROCRUSTES TECHNIQUE FOR STRUCTURAL HEALTH MONITORING.....		88
5.1	Introduction.....	88
5.2	Procrustes Analysis Developments.....	88
5.3	Procrustes Applications.....	89
5.4	Procrustes Application in Geomatics.....	90
5.5	GPA Mathematical Model.....	92
5.5.1	GPA Assumptions and Implications.....	94
5.5.2	WEOP Mathematical Model.....	95
5.6	Proposed Methodology.....	96
5.6.1	Registration of Point Clouds.....	97
5.6.2	Outlier Removal.....	97
5.6.3	Voxel Approach.....	98
5.6.4	Noise Mitigation.....	101

5.6.5	Determination Deformation Vectors	104
5.6.6	Localisation of Deformation	105
5.7	Algorithm Implementation.....	107
5.8	Chapter Conclusions.....	109
CHAPTER SIX: VALIDATION EXPERIMENTS WITH SIMULATED DATA AND SIMULATED DEFORMATIONS.....		110
6.1	Introduction.....	110
6.2	Create Simulated Data	110
6.3	Adding Noise.....	113
6.4	Validation for Non-deformed Data	114
6.5	Validation for Deformed Data	118
6.6	Time Cost.....	123
6.7	Wisely Downsampling.....	126
6.8	Chapter Conclusions.....	129
CHAPTER SEVEN: VALIDATION EXPERIMENTS WITH REAL DATA AND SIMULATED DEFORMATIONS.....		130
7.1	Introduction.....	130
7.2	Real Scan with Close Range.....	130
7.2.1	Non-deformed Epochs	132
7.2.2	Deformed Epochs	134
7.2.3	Comparison with Other Methods	137
7.3	Scanning Complicated Building.....	143
7.3.1	Post Processing	145
7.3.2	Improving Results.....	151
7.4	Chapter Conclusions.....	154

CHAPTER EIGHT: MONITORING OF BELLMANPARK LIMEKILN	155
8.1 Introduction	155
8.2 Location and Background	155
8.3 Received Data	157
8.4 Data Issues	158
8.5 Results	159
8.5.1 Unregistered Epochs	160
8.5.2 After ICP Registration	163
8.5.3 Deformation Results	172
8.6 Chapter Conclusions	176
CHAPTER NINE: CONCLUSIONS AND FUTURE PROSPECTS.....	177
9.1 Conclusions	177
9.2 Novelty	180
9.3 Shortcomings and Limitations.....	181
9.4 Future Prospects.....	181
REFERENCES	183
APPENDICES	194
A. Published Articles (extracted from thesis)	194
B. Cyclone Registration Report of Bellmanpark Limekilns Scans	195
C. The Output of the Proposed Method Applied on Bellmanprak Project Before ICP-Registration	201
D. The Output of the Proposed Method Applied on Bellmanprak Project After ICP-Registration	202
E. The Output of the Proposed Method Applied on Bellmanprak Project After ICP-Registration and Rotation	203

LIST OF FIGURES

Figure 2-1 Laser light properties (Laser Technologies, 2016). 7

Figure 2-2 Classification of laser scanners (Van Genechten et al., 2008). 8

Figure 2-3 The principle of TLS measurements (Reshetyuk, 2009). 9

Figure 2-4 Top: types of laser beam deflection units used in TLS with scanner types. Bottom: types of laser scanners according to FOV (Reshetyuk, 2009). 11

Figure 2-5 Time-of-flight laser scanner principle (Van Genechten et al., 2008)..... 12

Figure 2-6 Maximum Unambiguous Range versus pulse repetition frequency (Van Genechten et al., 2008). 13

Figure 2-7 Phase-difference distance measurement principle (Maar and Zogg, 2014). 14

Figure 2-8 Single shot signal (above) and 100 times accumulated signal (below) (Maar and Zogg, 2014).15

Figure 2-9 SmartBrick revision 2.0 (left), 2.1(center), and the IP68 SmartBrick enclosure (right) (Harms et al., 2009a). 24

Figure 2-10 Cracks monitoring technique in the Sala dei Battuti – Conegliano Cathedral (Lorenzoni et al., 2016). 26

Figure 2-11 The microwave interferometer (IDS, model IBIS-S)(Gentile, 2009). 27

Figure 4-1 Parameters are influencing the quality of the scans (Staiger, 2005). 48

Figure 4-2 Example of a mixed edge problem (updated from Van Genechten et al. (2008)). 50

Figure 4-3 Diffuse reflection of the laser beam (Van Genechten et al., 2008). 53

Figure 4-4 Refraction and reflection of the laser beam inside object materials (Van Genechten et al., 2008). 53

Figure 4-5 Reflection geometry is demonstrating incidence angle (Soudarissanane et al., 2011). 57

Figure 4-6 The location of error quantification test at photogrammetry lab in NGB. 59

Figure 4-7 The scanned object in error quantification test 59

Figure 4-8 The maximum errors of Scanstation P20. 62

Figure 4-9 Point errors of Scanstation P20 for different resolutions (50 mm, 25 mm, 12.5 mm, and 6.3 mm). 63

Figure 4-10 Point errors of Scanstation P20 for various resolutions (3.1 mm, 1.6 mm, and 0.8 mm). 64

Figure 4-11 The maximum errors of Scanstation P20 after outlier removal. 66

Figure 4-12 The mean errors of Scanstation P20 before and after removing outliers. 66

Figure 4-13 Point errors of Scanstation P20 for different resolutions (50 mm, 25 mm, 12.5 mm, and 6.3 mm) after outlier removal..... 67

Figure 4-14 Points errors of Scanstation P20 for different resolutions (3.1 mm, 1.6 mm, and 0.8 mm) after outlier removal..... 68

Figure 4-15 Characteristics of the WFD emitted signal, including the pulse width (T_{on}) and repetition rate (T_{Rep}) (Maar and Zogg, 2014)..... 71

Figure 4-16 The mean errors of Scanstation P40. 71

Figure 4-17 The maximum errors of Scanstation P40..... 71

Figure 4-18 Point errors of Scanstation P40 for different resolutions (50 mm, 25 mm, 12.5 mm, and 6.3 mm). 72

Figure 4-19 Point errors of Scanstation P40 for various resolutions (3.1 mm, 1.6 mm, and 0.8 mm). 73

Figure 4-20 Point errors of Scanstation P40 for various resolutions (50 mm, 25 mm, 12.5 mm, and 6.3 mm) after outlier removal..... 75

Figure 4-21 Point errors of Scanstation P40 for various resolutions (3.1mm, 1.6mm, and 0.8mm) after outlier removal..... 76

Figure 4-22 The maximum errors of Scanstation P40 after outlier removal. 76

Figure 4-23 The mean Errors for Scanstation P20 and P40. 77

Figure 4-24 The maximum errors for Scanstation P20 and P40. 77

Figure 4-25 The maximum errors estimation (based on points to planes distances) for different settings for Scanstation P20..... 80

Figure 4-26 The maximum errors estimation (based on points to planes distances) for various settings for Scanstation P40..... 80

Figure 4-27 Point errors of Scanstation P20 for various resolutions (50 mm, 25 mm, 12.5 mm, and 6.3 mm) based on point to plane distances..... 81

Figure 4-28 Point errors of Scanstation P20 for different resolutions (3.1 mm, 1.6 mm, and 0.8 mm) based on point to plane distances. 82

Figure 4-29 Point errors of Scanstation P40 for various resolutions (50 mm, 25 mm, 12.5 mm, and 6.3 mm) based on point to plane distances..... 83

Figure 4-30 Point errors of Scanstation P40 for different resolutions (3.1 mm, 1.6 mm, and 0.8 mm) based on point to plane distances. 84

Figure 4-31 The mean errors estimation (based on points to planes distances) for different settings for Scanstation P20.....	85
Figure 4-32 The mean errors estimation (based on points to planes distances) for various settings for Scanstation P40.....	85
Figure 5-1 GPA concept and the principle of the proposed method (updated from Crosilla and Beinart (2002)).....	95
Figure 5-2 TLS targets (Leica Geosystems, 2016b)	97
Figure 5-3 Box structure (Akca et al., 2005).	98
Figure 5-4 The proposed boxing structure.....	99
Figure 5-5 Top views for building (shown in Figure 5-4) structured in boxes before and after rotation.	100
Figure 5-6 Flow chart of the proposed algorithm.	108
Figure 6-1 3D model created by CloudCompare software.....	111
Figure 6-2 The point cloud created from the 3D model.....	112
Figure 6-3 Hidden point removal applied on point cloud.....	112
Figure 6-4 The noise in the point clouds.	113
Figure 6-5 Locations of the simulated deformations.	118
Figure 6-6 Total execution time for different fitting methods, different box sizes, and 2 mm resolution.	124
Figure 6-7 Total execution time for various fitting methods, different box sizes, and 3 mm resolution....	125
Figure 6-8 Total execution time for various fitting methods, different box sizes, and 5 mm resolution....	125
Figure 7-1 The location of the first test which was conducted on 10th of March 2015.	130
Figure 7-2 The scanned area of the first test with a 3D object which was used simulated deformation. ..	131
Figure 7-3 The results of the first six epochs without using the voxel filter.	132
Figure 7-4 The deformation probabilities for epoch six before applying the voxel filter.	132
Figure 7-5 The results of the first six epochs after applying the voxel filter.	133
Figure 7-6 The deformation probabilities for epoch six after applying the voxel filter.	133
Figure 7-7 The results of epoch seven.	134
Figure 7-8 The deformation probabilities for epoch seven.	134
Figure 7-9 The results of epoch eight.....	135
Figure 7-10 The deformation probabilities for epoch eight.	135
Figure 7-11 The results of epoch nine.	136

Figure 7-12 The deformation probabilities for epoch nine.....136

Figure 7-13 The comparison of epoch six displacements computed by CloudCompare and the proposed method.....137

Figure 7-14 The point displacements of epoch six with different methods, CloudCompare and the proposed.....138

Figure 7-15 The comparison of epoch seven displacements computed by the CloudCompare and the proposed method.....139

Figure 7-16 The point displacements of epoch seven with different methods, CloudCompare and the proposed.....140

Figure 7-17 The comparison of epoch eight displacements which computed by CloudCompare and the proposed method.....141

Figure 7-18 The point displacements of epoch eight with different methods, CloudCompare and the proposed.....141

Figure 7-19 The comparison of the epoch nine displacements which computed by CloudCompare and the proposed method.....142

Figure 7-20 The point displacements of the epoch nine with different methods, CloudCompare and the proposed.....142

Figure 7-21 Different textures and materials of NGB.....143

Figure 7-22 The location of the second test.....143

Figure 7-23 The 3D object which was used as a simulated deformation.....144

Figure 7-24 The results of epoch six with different resolutions, a- 3.1 mm, and b- 6 mm.....146

Figure 7-25 The results of epoch seven with different resolutions, a- 3.1 mm, and b- 6 mm.....147

Figure 7-26 The results of epoch eight with different resolutions, a- 3.1 mm, and b- 6 mm.....148

Figure 7-27 The results of epoch nine with different resolutions, a- 3.1 mm, and b- 6 mm.....149

Figure 7-28 The results of epoch ten with different resolutions, a- 3.1 mm, and b- 6 mm.....150

Figure 7-29 The results of epoch six after applying the voxel filter.....151

Figure 7-30 The results of epoch seven after applying the voxel filter.....152

Figure 7-31 The results of epoch eight after applying the voxel filter.....152

Figure 7-32 The results of epoch nine after applying the voxel filter.....153

Figure 7-33 The results of epoch ten after applying the voxel filter.....153

Figure 7-34 The deformation probabilities of the deformed area. 154

Figure 8-1 Bellmanpark Limekilns location (Historic, 2015a). 156

Figure 8-2 Bellmanpark Limekilns (source: GI-RST) 156

Figure 8-3 Bellmanpark Limekilns side names. 159

Figure 8-4 Deformation probabilities (%) for Limekilns faces before ICP-registration. 161

Figure 8-5 Absolute distances (m) by CloudCompare software for Limekilns before ICP-registration. 161

Figure 8-6 Deformation unit vectors for structure faces before ICP-registration. 162

Figure 8-7 Snapshot for results of ICP registration. 162

Figure 8-8 Deformation probabilities (%) for all faces after ICP-registration. 163

Figure 8-9 Deformation unit vectors after ICP-registration. 164

Figure 8-10 Deformation probabilities (%) for the SE face after ICP-registration. 165

Figure 8-11 Some fallen parts in the SE face. 165

Figure 8-12 Displacements (m) for the SE face after ICP-registration. 166

Figure 8-13 Deformation probabilities (%) for the SW face after ICP-registration. 167

Figure 8-14 Displacements (m) for the SW face after ICP-registration. 168

Figure 8-15 Deformation probabilities (%) for the NW face after ICP-registration. 169

Figure 8-16 Displacements (m) for NW face after ICP-registration. 169

Figure 8-17 Deformation probabilities (%) for the NE face after ICP-registration. 170

Figure 8-18 Displacements (m) for the NE face after ICP-registration. 171

Figure 8-19 Rotated point clouds for Bellmanpark Limekilns. 172

Figure 8-20 Cracks locations in faces SE and NE. 173

Figure 8-21 Actual locations and directions for deformation vectors. 174

Figure 8-22 Structure point clouds with deformations vectors representation. 175

Figure 8-23 Effect areas of DV2 and DV3 deformations vectors. 175

LIST OF TABLES

Table 2-1 Comparison among different distance measurements techniques (Maar and Zogg, 2014). 16

Table 2-2 Accuracy requirements for structure monitoring (USACE, 2002). 19

Table 2-3 Geodetic and non-geodetic methods and instruments (Kalkan et al., 2010). 20

Table 2-4 Classification of visible damage in masonry walls (Masciotta et al., 2016). 21

Table 2-5 Comparison between TLS and photogrammetric techniques. 30

Table 2-6 Suitability of monitoring techniques for heritage and historic buildings (good (+), average (o) or poor (-)). 31

Table 3-1 Advantages and disadvantages of the TLS techniques for monitoring surveying. 46

Table 4-1 Technical specifications for Scanstation P20 (Leica Geosystems, 2013) 60

Table 4-2 Number of measurements of different resolutions and quality levels (Geosystems, 2015). 61

Table 4-3 Error estimations for different settings for Scanstation P20. 61

Table 4-4 Error estimations for various settings for Scanstation P20 after removing outliers. 65

Table 4-5 Error estimations for different settings for Scanstation P40. 69

Table 4-6 Technical specifications for Scanstation P40 (Leica Geosystems, 2016a)..... 70

Table 4-7 Error estimations for different settings for Scanstation P40 after removing outliers. 74

Table 4-8 Error estimations (based on point to plane distances) for different settings for Scanstation P20. 78

Table 4-9 Error estimations (based on point to plane distances) for different settings for Scanstation P40. 79

Table 4-10 Summary for TLS errors with suggested dealings for monitoring surveying. 87

Table 6-1 The probability of deformation of non-deformed epochs for resolution 2 mm, for different box sizes and different surface fitting techniques. 115

Table 6-2 The probability of deformation of non-deformed epochs for resolution 3 mm, for different box sizes and different surface fitting techniques. 116

Table 6-3 The probability of deformation of non-deformed epochs for resolution 5 mm, for various box sizes and different surface fitting techniques. 117

Table 6-4 The simulated deformations for different parts. 118

Table 6-5 The probability of deformations of the deformed epochs for 2 mm resolution, different box sizes, and different surface fitting techniques. 120

Table 6-6 The probability of deformations of the deformed epochs for 3 mm resolution, various box sizes, and different surface fitting techniques.....	121
Table 6-7 The probability of deformation of the deformed epochs for 5 mm resolution, different box sizes, and different surface fitting techniques.....	122
Table 6-8 Total execution time (second) for the proposed algorithm for different cases.....	123
Table 6-9 Execution time cost (seconds) for different parts of the proposed algorithm for 2 mm resolution.....	123
Table 6-10 Execution time cost (seconds) for different parts of the proposed algorithm for 3 mm resolution.....	124
Table 6-11 Execution time cost (seconds) for different parts of the proposed algorithm for 5 mm resolution.....	124
Table 6-12 The probability of deformations of the deformed epochs for 5 mm resolution downsampled from 2 mm using voxel filter.....	127
Table 6-13 The probability of deformations of the deformed epochs for the 10 mm resolution downsampled from 2 mm using voxel filter.....	128
Table 7-1 The simulated deformations for different epochs.....	131
Table 7-2 The simulated deformations for different epochs.....	144
Table 8-1 Bellmanpark OS control points (source: GI-RST).....	157
Table 8-2 Targets of different scans (source: GI-RST data).....	158
Table 8-3 Deformation unit vectors before ICP-registration.....	161
Table 8-4 Deformation unit vectors after ICP-registration.....	163
Table 8-5 Deformation results unit vectors (re-rotated to the original coordinates system).....	174

LIST OF ABBREVIATIONS

4PCS	4-Points Congruent Sets
BIM	Building Information Modelling
DEM	Digital Elevation Model
DSM	Digital Surface Model
DTM	Digital Terrain Model
EOPA	Extended Orthogonal Procrustes Analysis
GIS	Geographical Information System
GNSS	Global Navigate Satellite System
GPA	Generalised Procrustes Analysis
GS	Geotechnical Sensors
HAR	Heritage At Risk
HDS	High Definition Survey
ICP	Iterative Closest Point
IMU	Inertial Measurement Unit
InSAR	Interferometric Synthetic Aperture Radar
K-4PCS	Key-point based 4-Points Congruent Sets
KNN	K-Nearest Neighbours
LASER	Light Amplification by Stimulated Emission of Radiation
LS3D	Least Square 3D
M3C2	Multiscale Model to Model Cloud Comparison
MAE	Mean Absolute Error
MSE	Mean Square Error
NGB	Nottingham Geospatial Building
NNA	Nearest Neighbour Averaging
NNS	Nearest Neighbour Search
NRTK	Network Real Time Kinematic
NURBS	Non-Uniform Rational B-Spline
OPA	Orthogonal Procrustes Analysis

TABLES OF CONTENTS

OS	Ordnance Survey
PCL	Point Cloud Library
Plane-OLS	Plane Ordinary Least Squares
Plane-TLS	Plane Total Least Squares
PPS	Post Processing Static
RANSAC	Random Sample Consensus
RBF	Radial Base Function
RMSE	Root Mean Square Error
RSE	Root Square Error
RTK	Real Time Kinematic
RTS	Robotic Total Station
SAR	Synthetic Aperture Radar
SfM	Structure-from-Motion
SLR	Satellite Laser Ranging
SNR	Signal to Noise Ratio
SVD	Singular Value Decomposition
TIN	Triangulated Irregular Network
TLS	Terrestrial Laser Scanner
TOF	Time of Flight
TS	Total Station
VRS	Virtual Reference Station
WEOP	Weighted Extended Orthogonal Procrustes Analysis
WFD	Wave Form Digitizer

CHAPTER One: **INTRODUCTION**

1.1 Preface

Many different instruments have been used in structural monitoring. Frequently, conventional surveying instruments are used in deformation monitoring, such as Theodolites, Total Stations (TS), precise levels, Global Navigate Satellite System (GNSS) and, recently, Robotic Total Station (RTS). This technique is based on measuring direct observations, such as distances, angles, and elevation differences, or indirect quantities, such as coordinates and elevations. Although it is considered a highly accurate method, it can only offer discrete monitoring points. Therefore, it needs to nominate key locations for these monitoring points based on structure design and expected deformation. Unfortunately, it is hard to select these points in case of historic ruins and heritage buildings because nobody can expect or they risk predicting deformations.

Furthermore, some monitoring sensors can be used, such as inclinometers, accelerometers, pendulums, dial gauges, extensometers, piezometers, pressure cells, and crack meters. These sensors are usually integrated with other sensors (Gonzalez-Aguilera et al., 2008, Meng, 2002). However, they can be used alone to give continuous data. The main drawback of these sensors is that they have the ability to acquire only one-dimensional measurements (Hill and Sippel, 2002, Park et al., 2007). Furthermore, the precision of their measurement decreases over time. Therefore, they need calibration for each period (Meng, 2002). In addition, regarding preservation, there are caveats in place in using the sensors in historic ruins and heritage buildings because they require contact or may need to be embedded in structures.

Moreover, there are a few remote sensing options that can be used in monitoring, such as Interferometric Synthetic Aperture Radar (InSAR) which can be used in architectural surveying as well as in multi-temporal observation in case of monitoring changes (Pesci et al., 2013). The drawback of this technique is that it only can measure one-dimension deformation which is in the line of sight direction and it cannot be used for structural condition monitoring.

Digital Photogrammetry and TLS may be considered as the best monitoring technique for historic ruins and heritage buildings due to their ability to offer high spatial resolution, and they do not require any prediction for deformations location.

1.2 Aims and Objectives

The aim of this research is to develop a new approach for heritage and historic buildings monitoring where deformations location are unpredictable. Therefore, the suggested method should have the ability to examine each part of the buildings and give the probability of its deformation. In addition, for more real results, it should exploit as many epochs as possible to estimate deformation vectors.

The proposed approach utilises TLS measurements and Generalised Procrustes Analysis (GPA) technique. To reach the aim mentioned above, the following objectives are fulfilled:

1) Investigate TLS based deformation monitoring techniques:

It helps to point out the shortcoming of previous methods.

2) Explore registration and georeferencing techniques:

Registration and georeferencing need to be investigated because there is a strong correlation between them and deformations monitoring using TLS. Furthermore, many monitoring techniques are based on registration methods. The decision about proper registration technique is taken.

3) Investigate TLS error sources:

To propose an approach with minimum error, we need to explore TLS error sources and their behaviour through measurement and post processing.

4) Investigate Procrustes Analysis techniques:

There are different applications for Procrustes Analysis, which is defined as a mathematical tool used to estimate similarity between data sets. Also, it has not been employed in TLS deformations monitoring. Therefore, it needs modification to satisfy this purpose.

5) Propose a new monitoring approach:

This approach is based on TLS measurements and the Procrustes Analysis technique.

6) Undertake validation experiments:

Simulated data and practical testing for the proposed method are conducted and compared with other known methods.

1.3 Methodology

The following methodology needs to be conducted to fulfil objectives:

- 1- Identify the shortcoming of known TLS based monitoring methods to fulfil the research aim.
- 2- Review registration and georeferencing methods and select the most suitable one for the proposed approach.
- 3- Review TLS error sources and propose a suitable procedure to reduce them to a minimum.
- 4- Review Procrustes Analysis and select proper version.
- 5- Develop software that can implement the developed technique.
- 6- Undertake simulation data testing to assess performance for the developed software and to determine some variables of the proposed approach.
- 7- Undertake practical testing for the proposed approach to detect simulated deformations with minimum error contribution. All measurements, all epochs, are taken from one position of TLS on the same day. This mitigates effects of atmospheric and geometric errors. In addition, the range is chosen to be about ten metres.
- 8- Undertake practical testing (as in point 7) with farther range, about 25 metres.
- 9- Undertake practical testing with real scanning and real deformations.

1.4 Contribution to Knowledge

Interestingly, the proposed method in this research has got attention from some interested. For instance, the published paper in “5th International Conference on Heritage and Sustainable Development” conference (Appendix A) has been considered as one of the top eight papers. In addition, Historic England (Historic, 2015b) has wondered the possibility of commercialising the proposed method because they keen on employing it in their monitoring projects. Essentially, the contribution of Knowledge for this research can be seen from different sides:

- 1) Proposing a new monitoring method which has the ability to detect and localise changes with unpredicted locations that may happen in heritage and historic buildings.
- 2) The proposed method is considered as a non-invasive method which can conduct monitoring remotely (without any contact). This is vital for monitoring of historic and heritage buildings.

- 3) The proposed technique can provide 3D visualisation of changes. This can help non-engineering clients to understand their building conditions. Also, it helps to present and discuss monitoring results with non-experts.
- 4) The proposed method has a good ability to localise changes by using voxel approach with estimating the probability of deformations.
- 5) The proposed method can provide more reliable outcomes because they result from multiple epochs.
- 6) Through noise mitigation, the proposed method can detect deformation below the noise level.
- 7) Utilising voxel approach, the proposed method has a better solution for obtaining displacements.
- 8) Due to dealing with data as matrices, the proposed method has the flexibility to add radiometric data (intensity) to detect deformations. Also, it can be used with point clouds created by digital photogrammetry after modifying the part of errors mitigation.

1.5 Thesis outline

This thesis is divided into nine chapters, and the contents of the next chapters are summarised here:

Chapter Two: the laser scanner technology will be described and overviewed in the first part of this chapter, while, the second part of this chapter will be assigned for addressing and defining concepts of the deformation monitoring and reviewing present monitoring techniques for heritage and historic buildings.

Chapter Three: the potentials of using TLS for monitoring purpose will be discussed in first part of this chapter. Commonly, five techniques can be employed to detect deformations from TLS data: using targets, direct cloud to cloud comparison, interpolation models, surfaces matching, and some specific solutions. The advantages and disadvantages of these methods will be clarified. The second part will be assigned for registration and georeferencing. Registration is the procedure of transforming reference system of scan scenes to a common reference system. There are three registration methods: targets base, natural and geometrical features, and surface matching. On the other hand, georeferencing is the procedure of transforming intrinsic reference system to ground reference system. Two methods are available for this procedure: direct and indirect methods.

Chapter Four: the TLS error sources will be discussed. Additionally, types and magnitudes of these errors will be figured out. Furthermore, some procedure of eliminating laser scanner outliers and reducing noise will be introduced.

Chapter Five: the Procrustes technique will be reviewed, which is the mathematical tool that is used to estimate least-squares matching between data sets up to their maximal agreement. In addition, the revisions and application of the Procrustes analysis will be discussed. In the second part of this chapter, the steps of the proposed technique and the background theories will be clarified, and mathematical models will be derived. It has six steps: registration, removing outliers, Voxel approach, noise mitigation, determination of deformation vectors, and localisation of deformation.

Chapter Six: the validation experiments for the proposed method in simulated data with simulated deformations will be summarised. The aims of using simulated data are checking the performance of the proposed algorithm, and fixing some variables in the proposed technique.

Chapter Seven: the second stage of the validation experiments will be discussed, which is testing the proposed technique in the real scan data with simulated deformations to examine its performance in the case of real errors budget.

Chapter Eight: the validation test in real scanning data with real deformations will be summarised, which will be included the results of applying the proposed method on the Bellmanpark limekilns monitoring project.

Chapter Nine: the general findings and conclusions of this research will be presented. In addition, recommendations and the prospects of future research will be listed.

CHAPTER Two: **BACKGROUND AND CONCEPTS**

2.1 Introduction

Since terrestrial laser scanner has been suggested in this research, this chapter will describe and overview the laser scanner technology. It begins with presenting the laser light properties that made it unique and different from light from other sources and ends with measurement techniques of the laser scanner. The second part of this chapter will be assigned for addressing and defining concepts of the deformation monitoring and reviewing present monitoring techniques for heritage and historic buildings.

2.2 Laser Light

Laser is an acronym for Light Amplification by Stimulated Emission of Radiation which was firstly demonstrated in May 1960 by Theodore Maiman at Hughes Research Laboratories. Hence, the laser is the device which is able to generate or amplify a wave of light employing only a narrow band of spectrum similar to transistors that generate and amplify electronic signals at audio, radio or microwave frequencies. In contrast to a light source such as the incandescent light bulb, which emits into a large solid angle and over a wide spectrum of wavelengths, a typical laser emits light in a narrow, low-divergence beam with a well-defined wavelength (Van Genechten et al., 2008).

Accordingly, the laser light, which generated by a laser device, has some very special properties (Figure 2-1), which distinguishes it from light from other sources (ibid):

- Due to coherence, laser beam propagates in a well-defined direction with minimum divergence. The term coherence means that the electric signal oscillates with a rigid phase relationship at different locations across the beam profile. Hence, the laser beam can propagate over long distances and can be focused to very small spots (footprint).
- Laser light has a high degree of temporal coherence which means long coherence lengths that imply a rigid phase relationship over relatively long time intervals, and therefore large propagation distances (often many kilometres).
- Visible laser beams have a certain pure colour, e.g. red, green or blue, but not white or magenta, as combining a large temporal coherence with a large coherence time or coherence length results in a narrow spectral bandwidth. For example, most laser measuring devices have a wavelength of

1064 nm (near infrared) or 532 nm (green laser). It should be noted that laser speckle phenomenon is resulting from a large coherence length which can be seen when a laser beam hits a metallic surface.

- Due to linear polarisation of laser light, the electric field oscillates in a particular spatial direction.
- Waves of laser light travel with a finite and constant velocity in a certain medium, and therefore it is highly suited to the measurement.

For all above remarkable properties, lasers are employed in everyday life such as optical storage devices (compact disc and DVD players), bar code readers, laser pointers, etc. Also, the laser is employed in the industry for cutting materials such as steel and marble. Furthermore, it has different applications in military and medical (ibid).

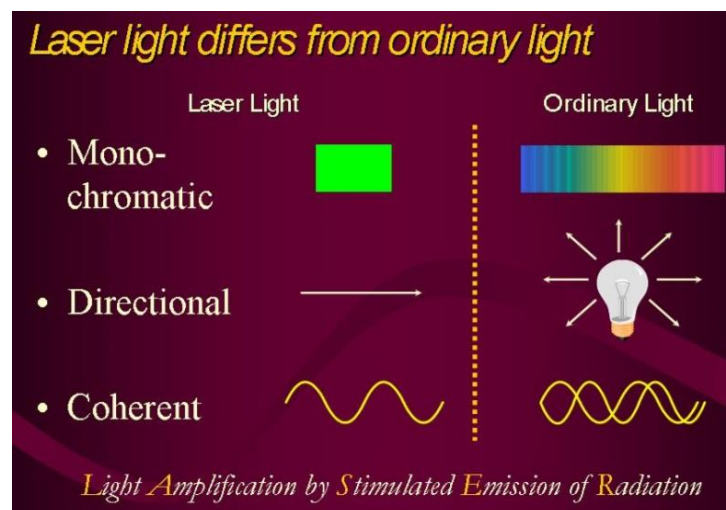


Figure 2-1 Laser light properties (Laser Technologies, 2016).

2.3 Laser Scanner Classifications

Laser scanning describes a method where object surface is sampled or scanned using laser devices. Consequently, object shape and its appearance (colour) are collected during this process which can be used to construct digital, two-dimensional drawings or three-dimensional models useful for a wide variety of applications. The most obvious advantage of the laser scanner is that it can collect enormous numbers of points in a relatively short period (Van Genechten et al., 2008). However, the huge amount of data has been shifted difficulties from data collection stage at the field to the office stage where data is processed (Belton and Lichti, 2006).

In general, laser scanners are divided into two types: static and kinematic (dynamic or mobile) each of them has its own applications (Figure 2-2). Static laser scanners normally remain stationary during the

data acquisition. Relatively, it is considered as a higher precision and point density compared with the kinematic laser scanner (Van Genechten et al., 2008). On the other hand, kinematic laser scanners are mounted on a mobile platform such as cars, trolleys, helicopters, aircrafts, from an unmanned aerial vehicle (UAV). Usually, mobile scanners are integrated with other positioning systems such as Inertial Navigation Systems (INS) or Global Navigate Satellite System (GNSS) which makes the system more complex and expensive (Ingensand, 2006). In this research, static laser scanners are concerned and wherever Terrestrial Laser Scanners (TLS) are mentioned we mean static laser scanner.

Additionally, laser scanners can be classified according to working range: close, mid, and long. At the beginning, close-range scanners were mainly employed in the automotive and industrial design process to facilitate the Computer Aided Design (CAD) process which helped in the mass production of consumer products. On the other hand, developing of mid-range scanning is credited to the petrochemical industry where laser scanning led to the full 3D management of the complex plants which were only documented as 2D drawings. Recently, the obvious advantages of laser scanning like: contactless measurement, high accuracy, long range, fast data acquisition, etc., many other disciplines are starting to steadily adopt this technology such as cultural heritage, architecture, urban development, forensics, and the entertainment (Figure 2-2) (Van Genechten et al., 2008). In this research, we are focusing in mid-range scanning.

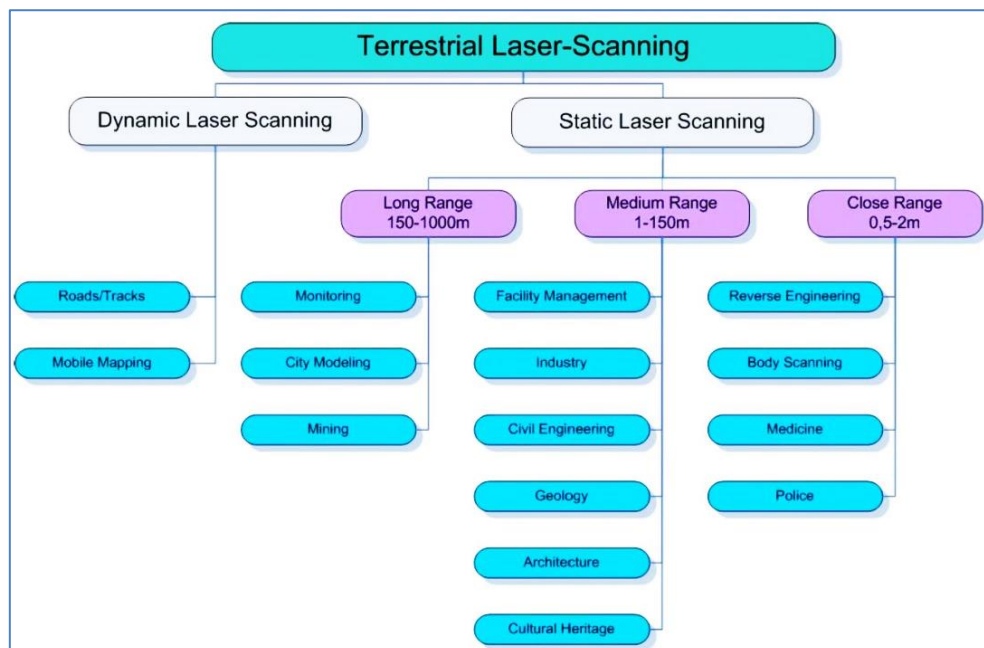


Figure 2-2 Classification of laser scanners (Van Genechten et al., 2008).

2.4 TLS Measurements

The principle of TLS operation is based on the transmission of a laser beam from TLS instrument with visual wavelength or near Infrared which is reflected by objects and return to the instrument, and the distance is estimated by the time of flight (TOF) or by the phase difference. The direction of the laser beam is determined as vertical Φ and horizontal θ angle by encoders and combined with distance. Then Cartesian coordinates (x, y, z) of objects is obtained from distance R and angle θ and Φ (Armesto et al., 2010). In addition, the intensity I of the reflected laser beam is often recorded which represents a fourth dimension (x, y, z, I) . The result of a scan is millions of 4D points which are called point cloud.

Although the raw measurements are R , θ , and Φ , most scanner software packages provide x , y , and z at the output, which are treated as measurements. The relationship between these measurements (Figure 2-3) can be expressed as follows (Reshetyuk, 2009):

$$P_i = \begin{bmatrix} x_i \\ y_i \\ z_i \end{bmatrix} = \begin{bmatrix} R_i \cos\phi_i \cos\theta_i \\ R_i \sin\phi_i \cos\theta_i \\ R_i \sin\theta_i \end{bmatrix} \quad (2.1)$$

Where R_i , ϕ_i and θ_i are the measured range, horizontal and vertical angle, respectively, to the i -th point in the point cloud, and (x_i, y_i, z_i) are its rectangular (Cartesian) coordinates in the scanner coordinate system.

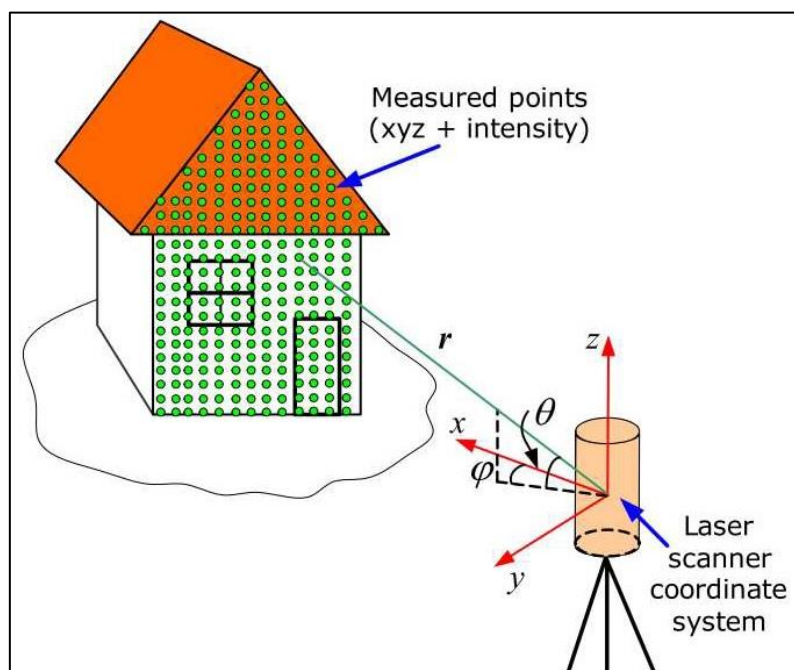


Figure 2-3 The principle of TLS measurements (Reshetyuk, 2009).

2.4.1 Angle Measurement and Deflection System

The angle measurement system in TLS consists of deflection system, which directs the laser beam to different directions, and attached high-resolution angular encoders, which measure the horizontal and vertical angle of the laser beam (Ingensand, 2006). There are different types of beam deflection units used in TLS, yet they rely on oscillating mirrors or rotating polygonal mirrors (Figure 2-4). Normally, the field-of-view (FOV) of the TLS is determined by the technique of deflecting laser beam, hence, three different types of scanners exist (Figure 2-4) (Reshetyuk, 2009):

- 1) **Camera-scanner:** in this type, the scanner head remains stationary during the data acquisition so it is called “fixed-head”. The laser beam is deflected by only mirrors oscillating about the horizontal and vertical axes. Consequently, it has a limited FOV, e.g. the laser scanner Leica HDS 2500 has only 40°x 40° FOV.
- 2) **Hybrid- scanners:** in this scanner, the laser beam is deflected in two steps. First, a vertical deflection is made with the oscillating mirror or rotating polygonal mirror to obtain a vertical profile. And then, with the help of the servomotor, the scanner head rotates horizontally in small steps around the vertical axis, and the next vertical scan is made. In this way, the scanner has 360° horizontal FOV, but a limited vertical FOV, e.g. Trimble GX has 60° vertical FOV.
- 3) **Panoramic-scanners:** it is similar to Hybrid-scanner which deflects the laser beam horizontally in small steps with the help of servomotor, but the only difference is that its vertical deflection is made by a flat rotating mirror with a single reflecting facet centred on the rotational axis. This type of scanners have 360° horizontal FOV and nearly the same vertical FOV, the space under scanner only cannot be captured. Usually, this type is useful in indoors scanning where the whole space around the scanner can be captured, e.g. Imager 5003 from Z+F has 360° horizontal FOV and 310° vertical FOV.

As aforementioned, oscillating or rotating mirrors, and rotating polygonal mirrors are used to deflect the laser beam. Comparatively, the oscillating mirrors are slow and provide a limited vertical FOV (90° maximum). They are usually used in pulsed laser scanner such as Leica HDS 3000. The instantaneous scanning angle of an oscillating mirror can be described by the following equation (Reshetyuk, 2009):

$$\theta(t) = \frac{\theta_{max}}{2} \sin(\omega t) \quad (2.2)$$

Where, where θ_{max} is the maximum scan angle, ω is the oscillating frequency of the mirror and t is time.

On the other hand, the rotating polygonal mirrors are very fast with constant velocity and can provide vertical FOV as large as 180°, e.g. Riegl LMS-Z series. The maximum vertical scanning angle, which can be achieved with this scanner, can be computed as follows (Reshetyuk, 2009):

$$\theta = \frac{720^\circ \cdot C}{n_{facets}} \quad (2.3)$$

Where, n_{facets} is the number of facets in the polygon and C is the duty cycle, i.e. the ratio of the active scan time to the total time. Also, the number of the scan lines per second can be computed as follows (Reshetyuk, 2009):

$$f_{sc} = n_{facets} \cdot v \quad (2.4)$$

Where, f_{sc} is the line per second, and v is the rotation speed.

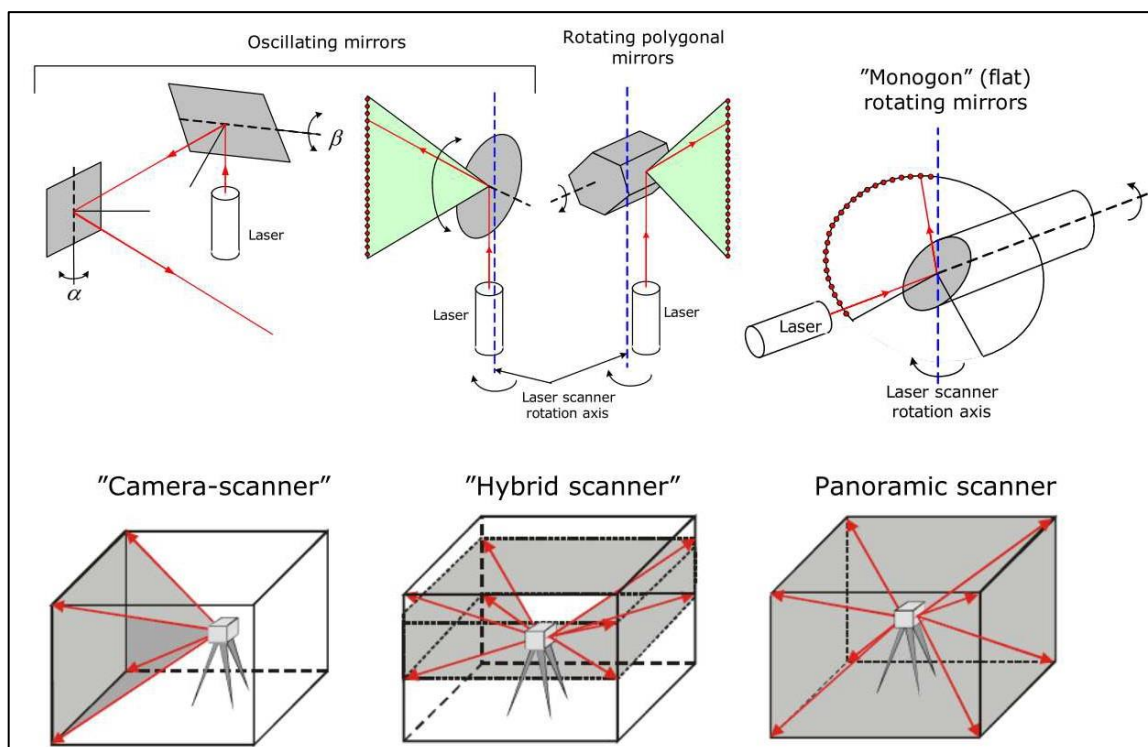


Figure 2-4 Top: types of laser beam deflection units used in TLS with scanner types. Bottom: types of laser scanners according to FOV (Reshetyuk, 2009).

2.4.2 Distance Measurements

The distances in TLS are measured in two well-known methods: time of flight (TOF), and phase difference. However, recently, a new technique has emerged, combines these methods, which is called Wave Form Digitizer (WFD).

2.4.2.1 Time of Flight

The distance is calculated by measuring time delay created by light travelling from the instrument to the object and back to the instrument (Figure 2-5), according to the following formula (Van Genechten et al., 2008):

$$D = \frac{c \cdot t}{2} \quad (2.5)$$

Where, c is the speed of light in air, and t is the time between sending and receiving the signal.

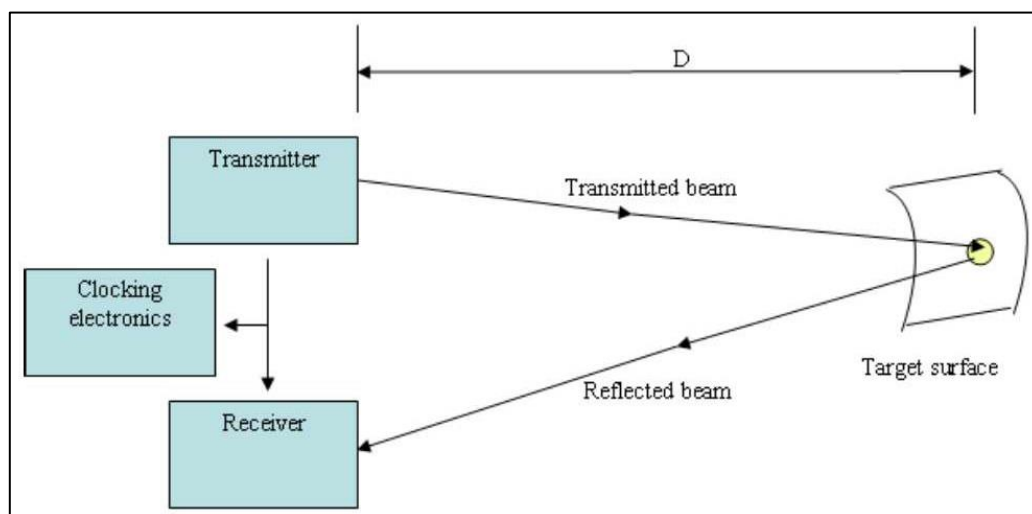


Figure 2-5 Time-of-flight laser scanner principle (Van Genechten et al., 2008).

TOF scanners are also called pulse based because they scan their entire field of view by laser pulses, i.e. measuring range for one point at a time. It should be noted that for a non-ambiguous measurement, the time measured (t) should be greater than the pulse width, T_{pulse} , hence (ibid):

$$t > T_{pulse} \quad (2.6)$$

Or

$$d > \frac{1}{2} c \cdot T_{pulse} \quad (2.7)$$

Evidently, this technique requires very accurate clocking mechanism, e.g. for 1 mm distance accuracy it needs to be able to measure a time delay of about 3.33 picoseconds (10^{-12} second), taking into account the speed of light in a vacuum is $c = 299,792,458$ m/s. In addition, it should be noted that measuring the time of return pulse depends on the desired time resolution, the counting rate and the required dynamic range of the pulse (Van Genechten et al., 2008).

In addition, the maximum pulse repetition frequency is restricted by the fact that the transmitter cannot send another pulse until receiving the echo from the previous one, in order to avoid confusion in the pulses arriving at the time interval counter. This is called the maximum unambiguous range and it depends on the pulse duration and its frequency (Figure 2-6) (ibid).

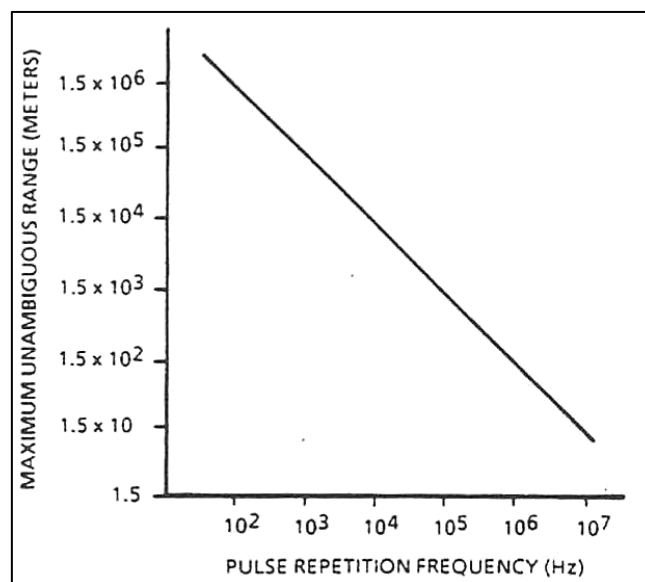


Figure 2-6 Maximum Unambiguous Range versus pulse repetition frequency (Van Genechten et al., 2008).

The advantage of TOF scanners is that its capability to measure accurate long ranges (few hundred metres) owing to the high concentration of transmitted laser power which makes it possible to achieve the required SNR (signal to noise ratio) needed. In addition, the error of this scanner is almost independent of the distance itself (except for the laser footprint, will discuss later). On the other hand, due to the changeable nature of the optical threshold and atmospheric attenuation, the drawback is the problem of detecting the exact arrival time of the returned laser pulse.

2.4.2.2 Phase Difference

To avoid using high precision clocks, another distance measuring technique is existed which is based on the phase-shift between the emitted and reflected signal and the number of full wavelengths (Figure 2-7). This can be done by modulating the power of the laser beam with different methods (Van Genechten et al., 2008): sinusoidal, amplitude based (AM), frequency based (FM), pseudo-noise, or polarization modulation.

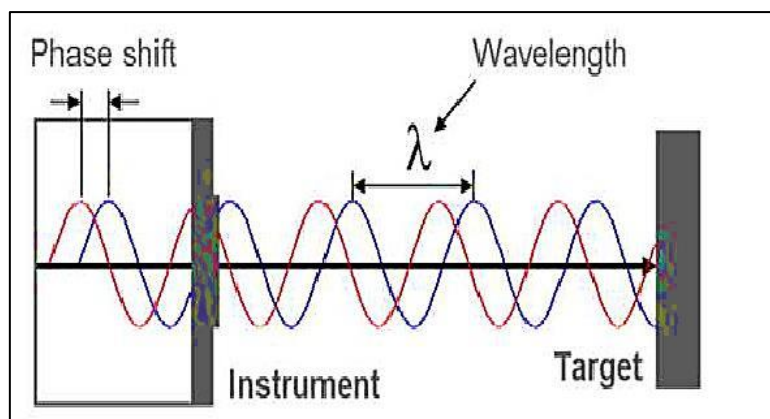


Figure 2-7 Phase-difference distance measurement principle (Maar and Zogg, 2014).

Similar to TOF, the phase-difference scanners can be related to a time delay. This can be clarified in the relationship between phase difference ($\Delta\Phi$), modulation frequency ($f_{modulated}$), and time delay (t), is (Van Genechten et al., 2008):

$$t = \frac{\Delta\Phi}{2\pi \cdot f_{modulated}} \quad (2.8)$$

Then distance is calculated according to the distance measuring equation of TOF scanners (ibid):

$$D = \frac{c \cdot t}{2} = \frac{c \cdot \Delta\Phi}{4\pi \cdot f_{modulated}} \quad (2.9)$$

This type of scanners also has a maximum unambiguous range which is limited to that one causes a phase delay in the sine wave of one complete cycle. Hence, the maximum unambiguous (Z_{amb}) can be expressed by the following equation (ibid):

$$Z_{amb} = \frac{c}{2 \cdot f_{modulated}} \quad (2.10)$$

It is worth to mention that phase-difference scanners have higher speeds and better resolution, but less precision than TOF scanners which is limited by (Van Genechten et al., 2008):

- The modulated frequency.
- Stability of the modulation oscillator.
- Atmospheric conditions.
- The accuracy of the phase-measurement loop which in turn depends on SNR.

2.4.2.3 Wave Form Digitizer

The WFD is a kind of TOF method, yet combines advantages of phase-difference and TOF techniques into one system. In this technique, the distance is calculated based on the time delay between a start and stop pulse which is digitized out of the received signal. Hence, to precisely recognize and extract the start and stop pulses, the waveform of all reflected signals is constantly evaluated, digitized and accumulated (Maar and Zogg, 2014).

Accordingly, the distance is not calculated from a single shot, but from multiple pulses. For each pulse, a small portion (fragment) is directed through an internal channel inside the instrument which is called start pulse. On the other hand, the major portion of the pulse leaves instruments and reflects back from the object. The backscattered signal is detected by the photosensor inside the instrument which is known as the stop pulse. Both start and stop pulses are digitised as a full waveform and accumulated from multiple signals. Then, the time delay between accumulated start and stop pulse is estimated, and therefore the distance is calculated similar to TOF technique (ibid).

Hence, the more pulses the better the signal-to-noise ratio (SNR). Consequently, the better estimation of the time delay and more accurate distances can be determined (Figure 2-8). According to Maar and Zogg (2014), the SNR increases with the square root of the measurement time, e.g. 9 seconds leads to a SNR about three times better than for a measurement time of 1 second.

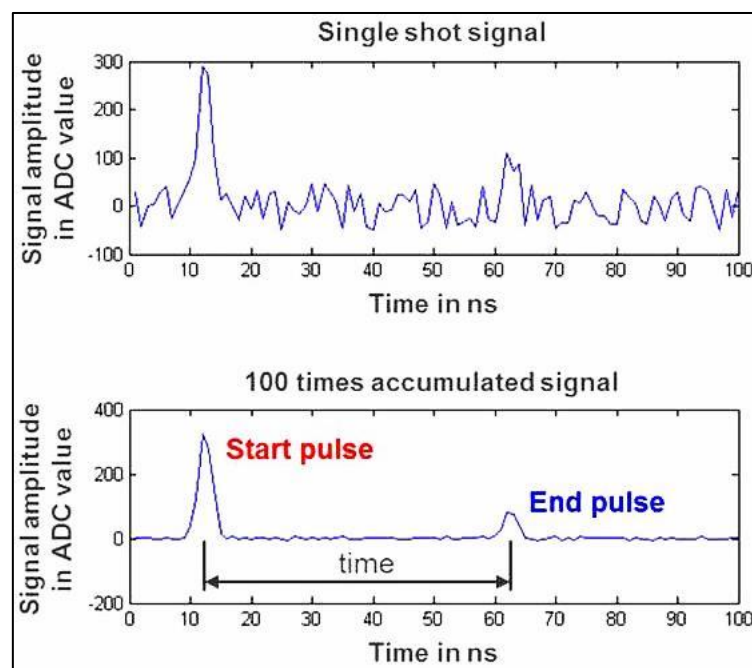


Figure 2-8 Single shot signal (above) and 100 times accumulated signal (below) (Maar and Zogg, 2014).

Consequently, the WFD can be considered a better overall measurement performance Compared to a pure time-of-flight measurement method. Table 2-1 reveals the comparison among three different techniques: TOF, Phase-Shift (Phase-Difference), and WFD.

Table 2-1 Comparison among different distance measurements techniques (Maar and Zogg, 2014).

Technology	Description
Time-Of-Flight	<ul style="list-style-type: none"> ▪ fast measurement time ▪ larger laser spot size ▪ lower measurement accuracy ▪ no (single shot) measurements if signal to noise ratio is too low
Phase-Shift	<ul style="list-style-type: none"> ▪ longer measurement time ▪ small laser spot ▪ highest measurement accuracy of all technologies
WFD	<ul style="list-style-type: none"> ▪ fast measurement time ▪ small laser spot size similar to phase-shift ▪ high measurement accuracy ▪ long ranges ▪ configurable

2.5 Deformation Monitoring

According to the dictionary, monitoring is defined: ‘observe and check the progress or quality of (something) over a period of time; keep under systematic review’. In surveying, deformation monitoring (also called deformation survey or monitoring survey) is defined as the systematic measurements which are tracking the change in the shape or dimensions of an object due to changes in circumstances (Moore, 1992). Hence, the monitoring surveying is conducted at regular time intervals rather than by continuous measurements that are more typical of geotechnical instrumentation. The interval between deformation surveys is normally correlated to conditions of the structure and it varies according to the purpose for monitoring. Also, it is essential allowing sufficient time to permit at least two sets of observations to establish datum measurements before possible deformation takes place (ibid).

Due to direct concern with the human life and safety, deformation monitoring has an important status among various engineering surveying (Kalkan et al., 2010). In general, the main purpose of the deformation monitoring is (USACE, 2002):

- In order to detect unpredicted deformations at an early stage, checking the behaviour of the investigated object and its environment whether they follow predicted pattern.
- In the case of abnormality, estimating as accurately as possible the actual deformation which can be employed for the determination of causative factors that trigger the deformation.

In general, coordinate differencing and observation differencing are the two principal methods used to estimate deformations from surveying data. Coordinate differencing methods are suggested for most applications that require long-term periodic monitoring. Whereas observation differencing is mainly used for short-term monitoring projects or as a quick field check on the raw data meanwhile it is collected (USACE, 2002).

2.5.1 Structural Deformation

Deformation is defined as the alteration in the shape and the form of an object. The shape is the geometrical information which remains after filtering out location, scale, and rotational effects. On the other hand, the form is the geometrical representation of an object which can be represented by a set of landmarks. In addition, the form of an object is the characteristic which remains invariant under rigid body transformation (Anwary, 2012).

In terms of structural deformation, any indication of an abnormal behaviour may threaten the safety of the structure which causes by external loads is known as deformation (USACE, 2002). Normally, structures are affected by daily factors (solar effects, heavy rainfalls), long period factors (dead load), and dynamic factors (resonance, wind, and loads) that might cause deformations (Abdullahi and Yelwa, 2016). This deformation can be in two forms according to construction materials and influencing factors (Callister and Rethwisch, 2007, USACE, 2002):

- **Elastic deformation:** or as so-called reversible deformation because structures are returns to its original shape after the influencing factors are no longer applied. For instance, deformation of concrete dams due to reservoir water pressure and temperature variations. Monitoring of this type of deformation is based on the design criteria of the structure.
- **Plastic deformation:** or well-known as a permanent deformation because the deformation in this case is irreversible which remains even if the influencing factors are no longer existed. For example, cracks and settlement in any type of structures which usually happen due to buildings

aging and fatigue. It should be noted that such type of deformation is not considered unsafe if it does not go beyond a predetermined critical value.

In this research, the permanent deformation is concerned.

2.5.2 Expected Deformation and Required Accuracy

The expected deformation in structure deformation depends on the size and type of the structure, and the cause of deformation. For instance, the effects deforming foundation of superstructure under load or incipient instability may be of quite different magnitudes and form (Moore, 1992). Normally, the magnitude of expected deformation is estimated using either deterministic modelling (by finite or boundary element methods), or empirical (statistical) prediction models. For example, the displacement trends may be predicted from geotechnical instruments or documented in design memorandums prepared for construction (USACE, 2002). However, the expected deformation likely to be millimetres, up to 10 or 20, but cracks will often require extending over months or even years before a valid assessment of performance can be made (Moore, 1992).

On the other hand, the required accuracy is directly related to the expected deformation occurring under normal operating conditions. According to Moore (1992), the required accuracy (at the 95% probability level) should be equal to one-fourth (0.25 times) the expected deformation for the given span of time between the epochs. Yet, in the case of any abnormal deformations are noticed, maximum possible accuracy is required to determine the mechanism of any unpredicted deformations. Hence, deformation monitoring may need to update the initial measurement accuracy over the duration of the monitoring project (ibid).

For guidance, the following table (Table 2-2) suggests the required accuracy for performing dam deformation surveys. These figures represent either absolute or relative target point accuracies which are observed from external reference points. Evidently, the accuracy of the external reference network should exceed these accuracies (USACE, 2002).

Table 2-2 Accuracy requirements for structure monitoring (USACE, 2002).

Case	Required accuracy
concrete structure dams, outlet works, locks, intake structures:	
long-term movement	± 5-10 mm
relative short-term deflections	± 0.2 mm
crack/joint movements	
monolith alignment	
vertical stability/settlement	±2 mm
embankment structures earth-rock-fill dams, levees:	
slope/crest stability	±20-30 mm
crest alignment	± 20-30 mm
settlement measurements	± 10 mm
control structures spillways, stilling basins, approach/outlet channels, reservoirs	
scour/erosion/silting	±0.2 to 0.5 foot

In this research, from all above discussion, the expected deformation is about centimetres and the required accuracy is sub centimetre.

2.6 Monitoring Techniques

Different monitoring techniques are employing different instruments. Many researchers have classified these instruments according to their criteria consequently, there are different classifications. For instance, Moore (1992) identified the principal of monitoring approaches according to the type of measurements such as vertical movements, inclination (out of plumb), horizontal movements, and cracks. For instance, he suggested precise levelling and electrical transducers for vertical movements, laser system and precise optical plummets for inclination, theodolite and EDM for horizontal movements, and a calliper gauge for cracks.

Hill and Sippel (2002) have categorised instruments that are used in deformation monitoring into three groups: surveying, geotechnical, and meteorological. According to Hill and Sippel (2002), one-dimension measurements can be provided by geotechnical and meteorological instruments, while, three-dimensional displacement can be determined by using surveying sensors. They did not mention to Photogrammetry and Remote Sensing and just focused on Total Station and Global Navigate Satellite System (GNSS) for surveying method. Geotechnical Sensors such as extensometers, inclinometers, piezometers, strain gauges, pressure cells, tilt sensors, and crack meters are widely used for monitoring. Whereas, meteorological instruments collect data about temperature, relative humidity, barometric pressure, wind speed, wind direction, global radiation (solar energy) and precipitation are usually used to calibrate other sensors (ibid).

Park et al. (2007) grouped sensors that are employed in monitoring functionally: sensors used to check safety and sensors used to check serviceability, e.g. safety sensor such as strain gauges and serviceability sensors like accelerometers and GNSS. However, there are vision-based sensors used for safety and serviceability such as photogrammetry techniques.

Other researchers (Kalkan et al., 2010, USACE, 2002) divided monitoring sensors into two groups: geodetic sensors, and non-geodetic (geotechnical) sensors (Table 2-3).

Table 2-3 Geodetic and non-geodetic methods and instruments (Kalkan et al., 2010).

	Methods	Instruments and Equipment
Geodetic	Alignment Survey	Theodolite, Laser Optic, Invar Wire...etc.
	Conventional Survey	Theodolites and Electronic Distance Measurement Instruments (EDM)
	Satellite Base Survey	GPS, GLONASS and GALILEO Receivers
	Precise Trigonometric Levelling	Precise Theodolite and EDM
	Precise Geometric Levelling	Precision Levelling Equipment
	Laser Scanner Technique	Laser Scanner
	Interferometry SAR Image	Processing of SAR Images
Non-geodetic	Slope Measurement	Inclinometer
	Displacement Measurement	Settlement Column
	Length Change Measurement	Extensometer
	Pore Water Measurement	Piezometer
	Vertical Displacement Measurement	Reversed Pendulum
	Grouting Measurement	Joint meter
	Crack Measurement	Crack meter

2.7 Monitoring of Historic and Heritage Buildings

Broadly, historic and heritage buildings can be monitored by any technique that listed in the previous section. However, not all available techniques are equally suitable for monitoring of such buildings due to the size, complexity of the shape, and the level of detail of the building. Also, the costs of the technique, the time required for operating, and the required skill level of the user are important when choosing a suitable measurement system (van Dijk et al., 2016). Furthermore, there are some critical constraints which particularly restrict the used method in this type of buildings:

- **Unpredicted deformations**

Normally, the largest parts of historic and heritage buildings are made of ancient masonry constructions characterized by a wide range of uncertainties such as the lack of knowledge about the construction techniques, the structural changes over time and the effects of the decay and local damages (De Stefano et al., 2016). Hence, even when based on accurate field survey, the structural model of a historic building always involves simplified hypothesis and different

uncertainties in the material properties and their distribution, in the geometric layout and in the boundary conditions (Saisi et al., 2016a, Yardim and Mustafaraj, 2015). Therefore, it is difficult to predicate type and location of deformations of this type of buildings that made some researchers recommend, for an effective structural health monitoring, distributing redundant sensors (De Stefano, 2007). Other researchers have proposed a numerical modal analysis using finite elements (FE) to choose the appropriate locations for monitoring sensors (Bilello et al., 2016, Elyamani et al., 2016), or employing digital photogrammetry and terrestrial laser scanning to obtain the finite element model (FEM)(Yardim and Mustafaraj, 2015). Consequently, the required technique should have the ability to detect unpredictable deformations.

- **Required accuracy**

Because cracks are the most frequent cause of masonry performance failure, heritage and historic masonry buildings are likely to experience cracking (Masciotta et al., 2016). According to Masciotta et al. (2016), no limiting values of crack width are provided in the actual codes and regulations for unreinforced stone masonry structures. However, he adapted, from original reference Burland et al. (1978), five levels of damage based on observed crack widths and ease of repair of masonry (Table 2-4). The target of this research is to detect moderate cracks. Hence, the required technique should have sub-centimetre accuracy.

Table 2-4 Classification of visible damage in masonry walls (Masciotta et al., 2016).

Degree of damage	Description of damage	Approximate crack width
Negligible	Hairline cracks	< 0.10 mm to 0.15 mm
Very slight	Fine cracks which can easily be treated during normal conservation	~ 1 mm
	Cracks which can be easily filled and probably require re-decoration. Possible need of repointing to ensure weather-tightness.	< 5 mm
Moderate	Moderate cracks which can be easily patched or masked by suitable linings.	5 mm to 15 mm
Severe	Large cracks which require extensive repair work. Impair of functionality.	15 mm to 25 mm
Very severe	Very large cracks which require major repair job. Danger of instability.	> 25 mm

- **Non-invasive**

Preservation of heritage and historic building needs a balance between the requirement of the structural safety and the respect for their architectural and cultural value (De Stefano et al.,

2016). In this context, the required technique should be a minimal invasiveness with the minimum number of sensors that conforming the international criteria and protocols on cultural heritage preservation (Ubertini et al., 2016). Currently, a large number of contactless (remote sensing) monitoring systems are available as a more convenient method (van Dijk et al., 2016).

- **Static monitoring**

Dynamic monitoring is usually employed to monitor elastic deformation which provides information about the whole-body response and the overall structural integrity. For this purpose, for flexible structures, vibration tests with modal parameters are used. On the other hand, the static monitoring is fundamental for assessing the structural performance and identifying changes (plastic deformation) (De Stefano et al., 2016, Masciotta et al., 2016).

Regarding heritage and historic building, due to aging and fatigue, the plastic deformation is dominant, and therefore the static monitoring technique is required (Tang et al., 2016).

In the following sections, the implications of the above criteria on the monitoring techniques that are presently being used in heritage and historic building are discussed.

2.7.1 Conventional Surveying Technique

This technique is based on measuring direct observations, like distances, angles, and elevation differences, or indirect quantities, such coordinates and elevations. Usually, conventional surveying instruments are used in this method, such as theodolites, Total Stations (TS), precise level, and recently Robotic Total Station (RTS).

Although this technique usually attains required accuracy and supplies a sufficient redundancy of observations for the statistical evaluation of their quality and for a detection of errors, it is labour intensive and requires skilful surveyors (USACE, 2002). In addition, it requires reference points which should be located in a stable area and target points are positioned in a predicted deformed area.

For instance, Margottini et al. (2016) have used a robotic total station (LEICA TM 30) for monitoring the Siq of Petra, Jordan. Another example, Castagnetti et al. (2016) have implemented a strategy to compute differential vertical displacements starting from results obtained by repeated high-precision levelling network adjustments. This approach is applied to the Ghirlandina Tower, Modena (Italy).

Regarding criteria for heritage and historic building, evidently, this method can satisfy required accuracy and static monitoring, yet it needs pre-knowledge for deformation location and may require contacting monitored objects.

2.7.2 Geotechnical Sensors

According to Gattulli et al. (2016), the most employed sensors in the field of structural monitoring are the accelerometers in dynamic monitoring and the displacement transducers (strain gauges) in static monitoring. Also, other geotechnical sensors, such as an inclinometer, a pendulum, dial gauges, extensometers, piezometers, pressure cells, and crack meters, have been used for relative deformation measurements within the deformable object and its surroundings. They are simple to operate, require only infrequent checks on their performance once installed, and easy to adapt for automatic and continuous monitoring than conventional surveying instruments (USACE, 2002).

These sensors give very localised and, frequently, locally disturbed information without any check unless compared with other sensors (USACE, 2002). Hence, they are usually integrated with another instrument (Gonzalez-Aguilera et al., 2008, Meng, 2002). The main drawback of these sensors is that it acquires just one-dimensional measurement (Park et al., 2007, Hill, 2002). Furthermore, the precision of their measurement is decreasing after time, and therefore they need periodical calibration (Meng, 2002). In addition, it requires embedding sensors in specific deformation locations, in the other words, invasive and predicated deformations.

For instance, linear variable differential transformers (LVDT) and strain gauges have been used in monitoring Diocletian's Palace in Split, Croatia (Duvnjak et al., 2016). In the Roman Arena in Verona, Italy the vibration properties of the monument have been acquired by means of acceleration transducers, and the control of the surveyed crack pattern through the implementation of displacement transducers installed on the main cracks (De Stefano et al., 2016, Lorenzoni et al., 2016). The monitoring system of the church of Saint Torcato North of Portugal, consisting of crack and tilt meters as well as temperature and humidity sensors (Masciotta et al., 2016). The monitoring of the bell-tower of the Benedictine Abbey of San Pietro in Perugia has been carried out using six high-sensitivity piezoelectric uni-axial accelerometers (Ubertini et al., 2016). The monitoring system of the Gabbia tower in Mantua, Italy is composed by three piezoelectric accelerometers (Gentile et al., 2016, Saisi et al., 2016b). Furthermore, there are many other

heritage building in Italy are employing these type of sensors such as the Sanctuary of Vicoforte, the Ghirlandina Tower in Modena, the medieval Bell Tower of S. Giorgio in Trignano, the Cochlid Columns in Rome, etc. for more details refer to De Stefano et al. (2016).

2.7.3 Wireless Smart Sensors

Although several wired monitoring systems have been prospered, they suffer from high cost, and difficult installation and maintenance. Alternatively, the wireless smart sensors can be considered as a promising technique for structural health monitoring due to sensing capability, on-board computation, wireless communication, self-powered, plug-in functionalities, and low cost; with facilitating autonomous and remote monitoring. In addition, the cost effectiveness of these sensors can enable dense arrays of them to be implemented on a huge structure (Harms et al., 2010, Kim et al., 2016).

A mote can be considered as the most famous commercialised prototype, developed firstly at the University of California-Berkeley and then produced by Crossbow Inc. such as the Tmote Sky by Moteiv, and Mica and MicaZ (Kim et al., 2016). For instance, Tmote Sky motes incorporate an accelerometer, strain transducer, temperature sensor and analog-to-digital converter, along with signal conditioning circuitry (Harms et al., 2010). Another example, Harms et al. (2009b) have been developed the SmartBrick (Figure 2-9) base station which offers monitoring capabilities, including on-board and external sensors for measurement of environmental and structural phenomena such as temperature, strain, tilt, and vibration.



Figure 2-9 SmartBrick revision 2.0 (left), 2.1 (center), and the IP68 SmartBrick enclosure (right) (Harms et al., 2009a).

Another example, an Imote2 has been interfaced with a sensor board, either an SHM-A (structural health monitoring-acceleration) board to measure multi-metric data or an SHM-W (structural health

monitoring-wind) sensor board to measure wind speed and direction by interfacing with a 3-axis anemometer (Cho et al., 2010).

Due to self-powered nodes relying on radio communication reduce the invasiveness of the system and allowing the deployment of more devices, these sensors have been used in monitoring heritage buildings (Ceriotti et al., 2009). For example, the main monitoring platform of the Basilica of S. Maria di Collemaggio, Italy is based on a wireless communication. Mainly, the wireless sensors type Imote2 SHM-A have been installed in the church. Another example, wireless sensors have been used in the Mosque-Cathedral of Córdoba for monitoring parameters involved in the deterioration process (Mesas-Carrascosa et al., 2016).

However, problems arise in the time synchronization and the communication reliability due to unique characteristics comes from design, construction, and materials used in heritage buildings. This has created interests for some researchers for assessing the quality of wireless communications and validating the network used (Aparicio et al., 2016, Martínez-Garrido and Fort, 2016). Also, similar to geotechnical sensors, these sensors require pre-knowledge for deformation locations.

2.7.4 Video Gauge Sensing

This system is based on a Digital Image Correlation (DIC) technique which can resolve two- or even three-dimensional points movements depending on the number of cameras used and their geometry setup. The principal of DIC relies on digital image correlation to analysis the flow of camera images observing an illuminated scenario. For purpose of monitoring, feature-based (e.g. point features realized by edges, corners or structural discontinuities) or intensity variation are tracked from frame to frame in an image sequence. The drawback of this method is that their measured displacements need to be converted to the actual displacements on the structure which is not always a straightforward procedure. In addition, for longer ranges, the atmospheric effects (e. g. cloudy versus a clear sky background) would affect the measurement stability. Finally, high precision topographic measurements are required for establishing the setup geometry between the cameras and the monitored structure (Piniotis et al., 2016).

In terms of heritage buildings, for instance, this technique has been used to detect the relative displacement of four small optical targets placed on the two sides of a crack in the Sala dei Battuti –

Conegliano Cathedral, Italy (Figure 2-10)(Lorenzoni et al., 2016). Obviously, it also requires known deformation locations.



Figure 2-10 Cracks monitoring technique in the Sala dei Battuti – Conegliano Cathedral (Lorenzoni et al., 2016).

2.7.5 Interferometric Synthetic Aperture Radar

Interferometric Synthetic Aperture Radar (InSAR) is a non-invasive imaging technique which used to detect and monitor surface displacement based on comparing sequential satellite radar images covering the same scenario (Tapete et al., 2013, Urrego et al., 2016). This technique is gaining importance due to unique characteristics such as its cost-effectiveness, high accuracy, covering of broad areas, and no need of equipment installation in-situ (Urrego et al., 2016).

In general, InSAR is employed to monitor ground deformations of cultural heritage sites. For instance, Urrego et al. (2016) have investigated the damage that occurred at the Saint Vincent's church during the coal mining activity in Zolder, Belgium by InSAR. Tang et al. (2016) have monitored the site deformation of the Summer Palace in Beijing, China by jointly analysing Persistent Scatterers (PSs) and Distributed Scatterers (DSs) using high-resolution SAR images. Finally, Le et al. (2016) have estimated subsidence patterns detected in the Historical Centre of Hanoi, Vietnam by InSAR.

On the other hand, ground-based synthetic aperture radar interferometry (GBInSAR) is a radar-based technique which was developed by the Italian company IDS (Ingegneria Dei Sistemi, Pisa, Italy) (Figure 2-11) (Gentile, 2009). It utilises the phase information obtained by a microwave radar sensor from repeated electromagnetic pulse transmissions to compute scattering object displacements which are employed to estimate the kinematic characteristics of a deforming structure for use in dynamic and modal analysis studies (Piniotis et al., 2016). The advantage of this technique is that it is a higher accuracy, a longer range, a possibility of work in bad weather (e.g. fog or rain), and a high recording rate (Gentile, 2009, Piniotis et al., 2016, Pratesi et al., 2015). However, the main drawback of this technique is that it measures only one-dimensional displacement in the line of sight direction (Piniotis et al., 2016).

Recently, this technique has been used to monitor heritage buildings. For example, Tapete et al. (2013) have integrated GBInSAR with TLS to monitor displacements of the Domus Tiberiana sited along the northern side of the Palatino Hill in the central archaeological area of Rome, Italy. Another example, Saisi et al. (2016a) have assessed the structural condition of the bell-tower of the Church Santa Maria del Carrobiolo in Monza, Italy by dynamic tests were carried out by GBInSAR.

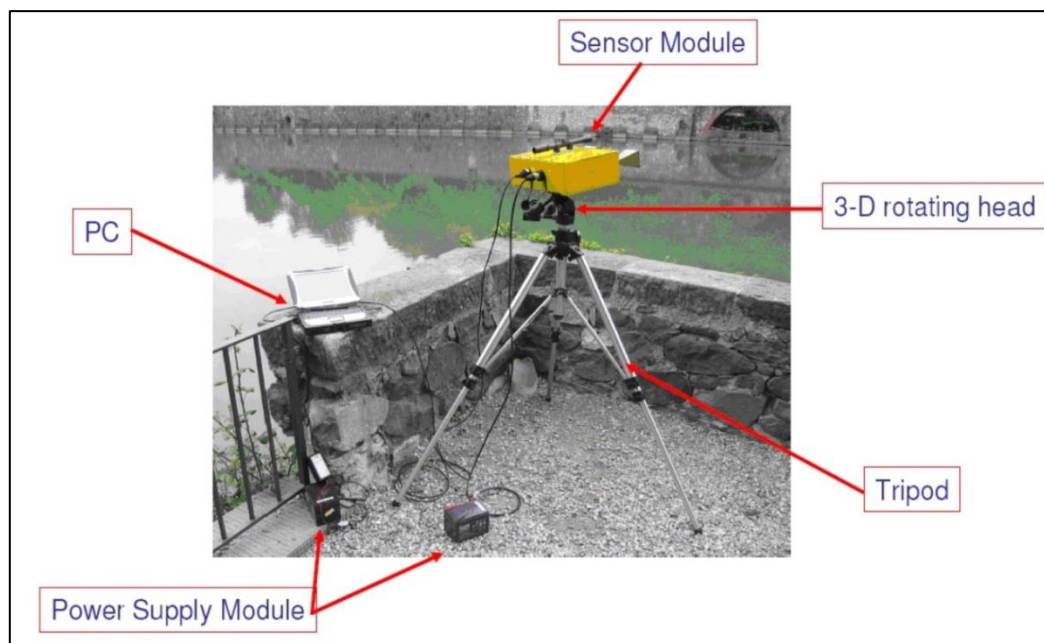


Figure 2-11 The microwave interferometer (IDS, model IBIS-S)(Gentile, 2009).

2.7.6 Photogrammetry and TLS

It has been expected that the developments in the TLS over last decade may lead to a loss of the interest in the photogrammetry. Nevertheless, developments in image analysis and computer vision have resulted in the appearance of a novel photogrammetric approach called Structure-from-Motion (SfM) (Javernick et

al., 2014, Nadal-Romero et al., 2015, Ouédraogo et al., 2014). Many researchers have carried out comparison between these methods, due to the fact that they have common characteristics; especially in the world of documentation and monitoring of cultural heritage and historic ruins, such as:

- Can perform measurements contactless.
- Can handle unpredicted deformations, no need to determine locations of deformation.
- Non-invasive.
- Can create dense point clouds.
- Can provide 3D visualisation.
- Can perform any 3D measurements.
- Can extract different types of typical 2D drawings such as profile and cross-section.

For instance, Lichti et al. (2002) have conducted comparative testing between digital photogrammetry and TLS measurements on wooden bridge undergoing a series of structure load test. Interestingly, they have used digital photogrammetry as a base to quantify scanner sensitivity. They concluded that differences between the photogrammetric and the top surfaces scanner measurements were nearly constant.

Böhler and Marbs (2004) have compared these techniques in five projects: a stone wall with archaeological findings, façade of a classical castle, renaissance relief plate, archaeological artefacts, and antique statue. They have advised using close range photogrammetry if objects can be described predominantly by point- or line-based structures, especially for distinct textures. In addition, the short time needed for photogrammetry in heritage recording is considered an advantage. On the other hand, they believe that TLS can capture very accurately and in full detail complex and irregular objects such as sculptures, reliefs or archaeological findings.

Kolecka (2011) has compared modelling of steep mountain wall by using TLS and terrestrial digital photogrammetry. They proved that both methods have similar precision and level of detail. Furthermore, Fassi et al. (2013) have compared using TLS and image-based automated 3D modelling for the purpose of reconstructing complex and extensive cultural heritage areas. They believed that image-based modelling could be comparable with 3D scanner clouds in terms of point density and precision.

Ouédraogo et al. (2014) evaluated the ability of TLS and unmanned aerial system (UAS) for producing accurate, high-resolution digital elevation models (DEMs) in a small watershed area. Their assessment revealed that DEM derived from TLS data was more accurate than the DEM derived from UAS. Retamozo et al. (2015) have compared the accuracy of three 3D modelling techniques: Total Station (TS), TLS, and Unmanned Aerial Vehicles (UAV). Their comparison revealed that TLS is the most accurate method.

Nadal-Romero et al. (2015) compared the performance of TLS and the SfM photogrammetry techniques in geomorphological erosion studies. They concluded that TLS provided the highest accuracy models, compared to SfM photogrammetry at short distances. Finally, Teza et al. (2016) compared the performance of TLS and SfM in a morphological analysis of the façades of a masonry building. Their results showed that the quality of both methods is the same under the condition of optimal viewpoint positions for SfM, and the relative differences are lower than 10%-20%. Table 2-5 summarises the comparison between these techniques according to the literature.

Another group of researchers stated that limitations of both technologies are complementing one another; hence, they have suggested a combination of scanning and photogrammetric techniques. For instance, Guidi et al. (2008) have suggested combining images and active sensors (TLS) to model complex archaeological sites. For this purpose, aerial images, TLS, and terrestrial images were employed. This approach allows exploiting the intrinsic advantages of each technique, hence, they can each be used where best suited. González-Aguilera et al. (2009) integrated a terrestrial laser scanner, a high-resolution digital camera and a total station to model cave geometry, to overcome drawbacks of each method. Lerma et al. (2010) have combined TLS and close-range photogrammetry to document archaeological cave. They demonstrated the effectiveness of the combination to ensure a solution to complex archaeological sites. Assali et al. (2014) combined terrestrial laser scanning and dense image matching data for 3D mapping and characterising rock faces. Their study revealed that both laser scanning and image matching could give similar quality results.

Table 2-5 Comparison between TLS and photogrammetric techniques.

	Photogrammetry	TLS
working fields	<ul style="list-style-type: none"> • For objects which can be delineated fundamentally by point- or line-based structures (Böhler and Marbs, 2004). • Objects have distinct textures (Böhler and Marbs, 2004). • For objects ranging from a few decimetres up to 200m (Lerma et al., 2010). 	<ul style="list-style-type: none"> • Very complex and irregular objects like sculptures (Böhler and Marbs, 2004). • Can apply to range up to 1500 m.
Advantages	<ul style="list-style-type: none"> • Short time needed for the recording on site (Böhler and Marbs, 2004). • Low-cost (González-Aguilera et al., 2009, Kolečka, 2011, Lerma et al., 2010, Nadal-Romero et al., 2015). • Easy to set up (Lerma et al., 2010) • A higher geometric accuracy (Kolečka, 2011) • SfM photogrammetry can be considered a precise and faster methodology at short distances (Nadal-Romero et al., 2015). • The relative differences of qualities of SfM-based and TLS are lower than 10%–20% under the condition that the viewpoint positions are optimal (Teza et al., 2016). • The overall geometries provided by TLS and SfM were very similar (Teza et al., 2016) 	<ul style="list-style-type: none"> • More precise (Fassi et al., 2013, Nadal-Romero et al., 2015, Ouédraogo et al., 2014, Retamozo et al., 2015) • It can provide full resolution scans in real time (Fassi et al., 2013). • TLS superbly fulfils the demand for a high level of detail (Kolečka, 2011). • Unlike photogrammetry, only one location for TLS can collect 3D data (Kolečka, 2011). • For TLS, point clouds are created instantly in the field, while in the digital photogrammetry, they are generated in post-processing and can be time-consuming (Fassi et al., 2013, Kolečka, 2011).

Disadvantages		
	<ul style="list-style-type: none"> • It is infrequent to extract quantitative data from photographs (González-Aguilera et al., 2009) • Deficiency of fully automatic techniques which can produce satisfactory results especially when dealing with textureless imagery (Kolecka, 2011, Lerma et al., 2010). • Stereoscopic plotting requires expert operators (Kolecka, 2011, Lerma et al., 2010). • The post-processing time (even if completely autonomous) can become extremely long (Fassi et al., 2013). • A scale-independent measurement technique (Assali et al., 2014). • Traditional photogrammetric DEMs were typically less accurate and precise than airborne LiDAR (Javernick et al., 2014). 	<ul style="list-style-type: none"> • Costly (Assali et al., 2014, González-Aguilera et al., 2009, Guidi et al., 2008) • Usually massive size (Guidi et al., 2008) • Limited flexibility (affected by surface properties) (Guidi et al., 2008) • It is poor colour resolution (González-Aguilera et al., 2009) • The complexity of the related data management (Fassi et al., 2013, Lerma et al., 2010). • Can only give results of very similar quality of photogrammetry (Assali et al., 2014).

In general, it is not logical to give an answer for which is the better method, yet it should be whichever is the suitable one because each method has got its advantages at different working fields (Böhler and Marbs, 2004). Therefore, the choice of technique should mainly be based on the project requirements, observational constraints, human and technical resources (Kolecka, 2011, Teza et al., 2016).

In this research, according to the aforementioned constraints for heritage and historic buildings, possibly, the best technique is the TLS. This is clarified in Table 2-6 which is identical to De Stefano (2007) prediction *“The general trend of structural monitoring technologies, anyway, is going towards a really distributed sensing, no more by means of many small low cost sensors but by means of smart sensing surface or volume extended devices”*.

Table 2-6 Suitability of monitoring techniques for heritage and historic buildings (good (+), average (o) or poor (-)).

Techniques	Unpredicted deformations	Required accuracy	Non-invasive	Static monitoring
Conventional Surveying	-	+	0	+
Geotechnical sensors	-	+	-	+
Wireless sensors	-	+	0	+
Video gauge	-	+	0	+

InSAR (GB InSAR)	+	+	+	0
Photogrammetry	+	-	+	+
TLS	+	+	+	+

CHAPTER Three: **USING TERRESTRIAL LASER SCANNER FOR MONITORING**

3.1 Introduction

The objective of this chapter is to investigate TLS based deformation monitoring techniques. At end of this chapter, advantages and disadvantages of existing methods will be pointed out. Consequently, the proposed method will be designed to cope with cons and utilise all pros. Furthermore, registration and georeferencing need to be reviewed because both or one is a mandatory step for any TLS based monitoring survey. Additionally, there is a strong correlation between them and monitoring techniques. Hence, the second part of this chapter will be assigned to discuss registration and georeferencing techniques.

3.2 TLS Monitoring Techniques

Interestingly, many researchers are focusing on this new approach due to the great advantages it can offer. According to Zogg (2008), the first research discussed using TLS in monitoring was done by Gordon et al. (2001), after that many researchers have dealt with the same topic. There are however three distinct challenges to using TLS in structure monitoring: first, the enormous amount of data and the difficulty in handling it; second, it is impossible to scan the same point in different epochs even if the scans are well registered, due to the deficient set-up of TLS on the same point and laser beam footprint; third, data is contaminated by noise. The first problem is solved by segmentation and point structure while the second and the third still need more investigation, although many interesting studies have been carried out in this area. In general, solutions can be classified into five categories: using targets, cloud to cloud comparison, interpolation models, surfaces matching, and some specific solutions that apply only to particular cases.

3.2.1 Using Targets

Some groups of researchers have suggested using targets where TLS can act as the same as a total station. The first research which discussed this technique was done by Gordon et al. (2001) then further by a few other researchers (Dal Piaz et al., 2007, Hejbudzka and Dumalski, 2011, Roberts and Baddley, 2007, Valanis and Tsakiri, 2004).

Fundamentally, it is based on the target acquisition which can be acquired automatically at a scanning session or possibly be determined later at post-processing and defined as the technique of estimating target centre by comparing the intensity of different parts of the target (Pejić, 2013). Consequently, several researchers are focusing on improving the accuracy of the target identification. For instance, Valanis and Tsakiri (2004) developed automatic targets identification based on fuzzy classification, gridding and averaging techniques. Through their algorithms, they reduced errors coming from automatic targeting. Another example, Hejbudzka and Dumalski (2011) analysed the precision of the position of High Definition Survey (HDS) target centre. They compared Cyclone software results with their program.

The advantage of this method is that it can determine three-dimensional deformations and detect deformations of less than 0.45mm (Tsakiri et al., 2006). However, the single point precision of targets is much higher when conventional surveying, such as Total Station, is implemented (Tsakiri et al., 2006). Therefore, it is illogical to use a high-cost technique to get less accurate results.

3.2.2 Cloud to Cloud Comparison

Another group of researchers applied direct cloud-to-cloud comparison. In this case, point clouds can be used directly to detect changes between two clouds collected at different times. Several researchers discussed this method and introduced some procedure to improve accuracy. For instance, Girardeau-Montaut et al. (2005) used Octree point structure to detect changes on building sites. This method can offer quick detection where the speed of the data analysis plays a critical role (Monserrat and Crosetto, 2008). Limited accuracy and the high noise level prevent detection of small deformations (Monserrat and Crosetto, 2008, Tsakiri et al., 2006). Lindenbergh and Pfeifer (2005), and Lindenbergh et al. (2005) used the direct comparison of observed points to detect deformation between two scans. The assumption of this method is that the scanner positions are same. The drawbacks of this method are that only one-dimensional deformation can be detected, which is in the direction of the range. In addition, a huge number of points are required to judge the deformations and the same point cannot be identifiable on multiple epochs for the same surface (Tsakiri et al., 2006). Finally, Abellán et al. (2009) could detect 2.3 mm deformation at 50 m compared with 15 mm if using raw data by the Nearest Neighbour Averaging (NNA) method. The drawback of this method is that it is a two-dimensional deformation.

3.2.3 Interpolating Models

Another technique developed for structural monitoring is based on model interpolation. According to Pesci et al. (2013), the difference between point cloud and an interpolated primitive models is much more sensitive to deformations compared to the difference between two point clouds in different epochs. There are many researchers interested in this technique, and different models have been developed. Despite some advantages, all of these models can only detect a one-dimensional deformation (Monserrat and Crosetto, 2008).

In general, triangular mesh model is widely used in computer field among different 3D models. Possibly because it may be considered that constructing and manipulating triangle mesh is a simple operation. Furthermore, the ability to change the resolution of the model through merging triangles, deleting nodes, and swapping edges. Nevertheless, this operation needs more post-processing procedure like mesh optimisation. Additionally, visual limitation of triangular mesh restricted it, and therefore other methods have received more attention (Park et al., 1999).

For landslide monitoring, Digital Terrain Model (DTM), Digital Elevation Model (DEM), and Triangulated Irregular Network (TIN) have been used (Barbarella and Fiani, 2013, Bitelli et al., 2004, Corsini et al., 2013, Mill and Ellmann, 2014, Pesci et al., 2007, Schäfer et al., 2004, Wang et al., 2011). These models are evolved very fast and now include explicit calculation of uncertainties (Lague et al., 2013). In addition, they can reduce possible data storage and provide a good digital representation for surface study, volume estimation and other interesting applications (Pesci et al., 2007). Finally, GIS software can be used to represent and analyse such models. On the other hand, they are a one-dimension deformation and limited sensitivity to small deformation (Monserrat and Crosetto, 2008). Furthermore, they cannot be applied properly in the 3D environments as they cannot describe vertical surfaces such as cliffs (Lague et al., 2013).

Lindenbergh and Pfeifer (2005) estimated the parameters of the common plane from the parameters of planes in different epochs; statistical tests were then used to check if there was any deformation between planes. The advantage of this method is its capability to detect deformations with magnitudes with less than single point precision. However, it cannot be applied in different applications (Monserrat and Crosetto, 2008).

Pesci et al. (2011a) used planes to detect deformation. The first plane was vertical to examine building inclination, while the second was the best fitting for point clouds. According to Pesci et al. (2011a), and Pesci et al. (2013) this technique allows an accurate definition of the deformation patterns. However, it is a particular case and cannot apply for all structures and can detect a one-dimensional deformation.

For dam monitoring, Alba et al. (2006) used a triangular mesh computed from resampled point clouds then they interpolated a regular polynomial 3D surface from this mesh. They could overcome the point's unrepeatability problem and achieved accuracy better than using point clouds. However, it is also a one-dimensional deformation (Monserrat and Crosetto, 2008).

Gonzalez-Aguilera et al. (2008) have used a Radial Base Function (RBF), which is developed by Carr et al. (1997), Carr et al. (2001) to interpolate surface from the 3D coordinates, for dam monitoring. They proposed multiple orthogonal cross sections to overcome one-dimensional deformation; however, it is only valid for structures with predictable deformation.

Zhou et al. (2011) used Non-Uniform Rational B-Spline (NURBS) surface modelling to monitor concrete continuous beam bridges. One benefit of NURBS method is that its interpolated surface will be more precise descriptions of the object than the un-modelled observations. Another advantage is that it is robust to the noise present in the data because the outliers affect just part of the area of the whole surface. Finally, it is known as a semi-automated or automated method (Park et al., 1999).

The drawback of monitoring using surface modelling based on NURBS, in addition to one-dimensional deformation monitoring, is that its data should be organised and arranged on a grid, which is not always possible in a real situation, such as TLS data (Park et al., 1999). Another disadvantage is that a large computer memory is required, and instability may occur if both the number of measured points and the number of control points are increased (Ma and Kruth, 1998).

Some researchers have used nonparametric estimation based on local bivariate kernel smoothers to interpolate surface (Armesto et al., 2010, de Asís López et al., 2014, Roca-Pardiñas et al., 2008). In this technique, there is no need to specify parameters between data and the response variable (Roca-Pardiñas et al., 2008). In addition, nonparametric regression can be used to filter noise as well as to reduce data volume if it is huge, consequently reduce time cost (Roca-Pardiñas et al., 2008). Despite the usefulness of nonparametric technique, its fitness depends on the selecting bandwidths which are regarded an open

problem (Roca-Pardiñas et al., 2008). Furthermore, it can be considered a high-cost computation (Armesto et al., 2010).

Some researchers interpolate not only surfaces, but three-dimensional shapes such as cylinders to determine deformation in a tunnel (Van Gosliga et al., 2006). This method allowed determining deformations of the completed tunnel with respect to the design. However, it only works with a specific type of structure, such as tunnels, and one-dimensional deformation.

Finally, it is worth mentioning another model interpolation approach, which is based on Multiscale Model to Model Cloud Comparison (M3C2) proposed by Lague et al. (2013). According to Barnhart and Crosby (2013), it is the most robust analysis for point clouds because it includes confidence interval for each distance measurement which is estimated based on point cloud roughness and registration error. Furthermore, it can offer accurate surface monitoring that is independent of point density (Lague et al., 2013). Nevertheless, it is a one-dimensional deformation, which is in surface normal direction. In addition, if there is a deflection between normals of two clouds (reference and compare), the average normal is considered. In this case, the deformation direction will be wrong.

3.2.4 Surfaces Matching

Some researchers employed a technique which is based on determining transformation parameters required to match two surfaces. When two or more georeferenced models obtained by multi-temporal scans are available, two methods are used for this purpose: Iterative Closest Point (ICP), and Least Square 3D (LS3D).

For instance, Teza et al. (2007) used ICP to monitor landslide due to its robustness against noise and small morphological modifications and its ability to determine three-dimensional deformation. However, this technique has drawbacks. To begin with, the clouds' roughness or highly deformed objects may reduce surface matching and consequently yield incorrect results (Lague et al., 2013). In addition, the presence of holes or other defects may prevent correct surface matching, particularly with the presence of high noise and sometimes the convergence does not happen at all (Teza et al., 2007). Furthermore, it considers all unknowns with the same scale, and it cannot handle multi-scale data. Finally, due to linearization, it needs approximate values for the corresponding points (Guarnieri et al., 2005).

Another example is that Monserrat and Crosetto (2008) used LS3D for deformation monitoring. This method has the flexible procedure and is sensitive to small deformations with values below the noise of the single TLS points. In addition, it can determine three-dimensional deformations. Furthermore, it has suitable tools for accuracy and reliability checks through using the LS standard (Guarnieri et al., 2005, Monserrat and Crosetto, 2008). Finally, it is considered as an automatic or at least semi-automatic procedure for deformation analysis (Monserrat and Crosetto, 2008). Despite all of these advantages, it undoubtedly has drawbacks. Firstly, as long as it is a non-linear functional model, convergence may not happen unless good approximations of the unknowns existed (Guarnieri et al., 2005, Monserrat and Crosetto, 2008). In addition, in the case of significant deformations or structural changes of the objects, it is not possible to match the point clouds which represent partly or wholly different objects (Monserrat and Crosetto, 2008).

3.2.5 Specific Solutions

Some researchers have used specific techniques for particular structures or a certain type of deformation with an observed trend. For instance, Gordon et al. (2004a), Gordon et al. (2004b), and Gordon and Lichti (2007) developed a physical model that represents the deflection of a loaded beam. With this technique, they could reach to sub-millimetre accuracy, tenfold more accurate than the advertised single-point precision (Gordon et al., 2004b, Tsakiri et al., 2006). However, the generation of this model needs prior knowledge of the dimensions of the beam, spatial position of the load point(s) and support points. This means they are particular deformation analysis cases (Gordon et al., 2004a, Monserrat and Crosetto, 2008). Furthermore, it is one-dimensional deformation.

Schneider (2006) tested bending the line of a television tower by cutting the tower into layers. He could obtain to more accurate than original TLS data, but it works in specific buildings only (Monserrat and Crosetto, 2008).

Park et al. (2007) presented a displacement measurement model for the purpose of health monitoring of structures. They could estimate deflections less than 1 mm by this model. However, it is a manual technique that can work on structure member level only, not whole structure, and one-dimensional deformation again. Olsen et al. (2010) used intuitive slicing analysis technique for damage detection and

volumetric change analysis for a full-scale structural test specimen. This method can be automated for a rapid generation of results, but it is a particular case of deformation.

For deriving a surface deformation, Aryal et al. (2012) implemented cross-correlation-based particle image velocimetry. Through this method, it can derive continuous displacement fields from active, slow-moving landslides. However, it has limited accuracy at the decimetres level. In addition, it may produce spurious results if parts of ground features remain stationary. Furthermore, the correlation may degrade if the ground surface is highly deformed, this may occur during rapid movement or transition to a debris flow (Aryal et al., 2012). Finally, only two-dimensional deformations can be determined.

Kim et al. (2014) employed TLS to localise and quantify spalling defects on concrete surfaces using angle deviation and distance deviation. The advantage of this method is that it can detect and localise the spalling defect autonomously and simultaneously. However, it only works for the particular case when the concrete is a flat surface, and for two types of defects, concave-shape and flat-top flaws. Hence, slight spalling defects less than 3 mm deep can hardly be detected (Kim et al., 2014). In addition, it is vulnerable to scan parameters; i.e. the incident angle recommended is less than 15°.

3.3 Registration

Since the TLS is a line of sight sensor, multiple scans from different positions need to be conducted, if the object being surveyed is quite large. Consequently, all scans need to be aligned to a common coordinate system for any further analysis; this procedure is called registration (Gruen and Akca, 2005, Theiler et al., 2014).

Broadly, registration should resolve four ambiguities: (1) the registration primitives for corresponding features which can be points, lines, surfaces; (2) the transformation formula from reference systems of the involved datasets to a common reference system; (3) the similarity measure which can describes the coincidence of corresponding features after the registration; and (4) the matching strategy which is a guide for the automatic registration process (Habib and Alruzouq, 2004).

There are three main registration methods, targets based, natural point features, and surfaces matching. According to Alba and Scaioni (2007), there are two factors affect selecting suitable registration method: required accuracy and configuration of scan view.

3.3.1 Targets Based Registration

It is a common method where targets are located in positions can be seen from different scans. The target points in such a way are called tie points (Reshetyuk, 2009). To transform reference system from one scan to another, six parameters (three translations and three rotations of reference system) should be estimated. The scale factor is considered unity and irrelevant in the transformation since TLS provides real scale (Al-Durgham et al., 2014, Gordon and Lichti, 2004, Reshetyuk, 2009). These parameters are known as rigid-body or three-dimensional Helmert transformation parameters (Reshetyuk, 2009).

Minimum of two target points, known in both reference systems, are required to determine six degrees of freedom. Usually, increasing of these points improves the registration quality. However, Gordon and Lichti (2004) showed no considerable improvement after the fourth target. Furthermore, the location of tie points with respect to the scanned area may affect directly on the quality of registration. Therefore, they need to be well-distributed geometrically (ibid).

The acquiring of the centre of targets is a vital for this method, usually, is done automatically by scanners' software e.g. Cyclone. In addition, type and shape of targets play a fundamental role in data quality. For instance, the sphere targets may produce more accurate data than flat targets because the sphere is better spatial distribution and it needs no orientation over different scans.

Registration using targets marks affords high accuracy and robustness because the errors come from setting up, and levelling of TLS does not contribute to the total errors budget. However, levelling of TLS can reduce the degree of freedom to four since in this case rotation angle around X and Y will be zero.

On the other hand, the drawback of this technique is that it is labour-intensive and time-consuming. In addition, targets might occlude some scene part and usually have to be removed from point clouds (Liang et al., 2014, Theiler et al., 2014, Yang et al., 2013, Yang and Zang, 2014).

3.3.2 Geometrical Objects and Natural Features

Alternatively, sharp features and geometrical objects, such as lines, planes, and spheres, can act as tie points instead of targets. Probably most scanners' software can detect sharp features with different ways. For instance, it is possible to detect sharp features from point cloud by finding points with normal vector different entirely from neighbours (Walsh et al., 2013).

According to Al-Durgham et al. (2014), the most comprehensive work for features registration was introduced by Yao et al. (2010). They proposed a Random Sample Consensus (RANSAC) algorithm to register laser scans in pairs. Their technique is based on extracting groups of linear and planar features and then using these features as tie points. However, it is reported that their technique is sensitive to the presence of repetitive patterns, and failed in outdoor scans registration (Al-Durgham et al., 2014).

In general, this registration method is not recommended because features may be not well-distributed geometrically, hence, less quality. Furthermore, the effect of the incident angle can reduce the quality of registration owing that features are scanned from different locations (Liang et al., 2014). For these reasons, English Heritage recommends avoiding using natural point features for the point clouds registration (Reshetyuk, 2009).

3.3.3 Surface Matching

This approach is based on matching the whole overlapped area instead of district tie points. Evidently, one of the main disadvantages of the surfaces matching registration is that it requires of overlapping vast area between scans, at least 30% (Reshetyuk, 2009). In addition, to get better results, this overlapped area should have a good spatial distribution where different features exist (e.g. plant). While flat surfaces, such as walls and roadways, with a reduced spatial distribution, may give bad registration quality.

Furthermore, due to the nonlinear algorithm (i.e. iteratively estimate parameters), applying this method directly to scans with arbitrary relative orientation will in most cases fail (Theiler et al., 2014). Therefore, it requires accurate initial approximations for the transformation parameters to estimate the correspondence and thus registration (Al-Durgham et al., 2014, dos Santos et al., 2013, Guarnieri et al., 2005, Monserrat and Crosetto, 2008, Reshetyuk, 2009, Theiler et al., 2014, Yang et al., 2013). For all these reasons, it is not suggested to be used in monitoring survey.

There are two known methods in surfaces matching, Iterative Closest Point (ICP), and Least Square 3D (LS3D).

3.3.3.1 Iterative Closest Point

Iterative Closest Point (ICP) is the most common registration technique, firstly developed by Besl and McKay (1992). To determine transformation parameters, the ICP starts with two meshes and the initial

approximations for their relative rigid-body transform, then minimises distances between corresponding points, in the overlapping area, in different scans. Furthermore, it iteratively revises these parameters until convergence. Variant derivatives of the ICP have been proposed to improve either the speed or the robustness of this method. Rusinkiewicz and Levoy (2001) classified many of these variants and evaluate their effects on the speed. In general, there are six stages of the ICP algorithm (ibid):

1. Selecting a set of points in one or both meshes which are created for both clouds.
2. Matching between these points and samples in the other mesh.
3. Suitable weighting the corresponding pairs.
4. Filtering out certain pairs based on individual or whole constraints.
5. Based on the point pairs, estimating errors.
6. Minimising the errors.

According to Akca et al. (2005), the central computationally expensive part of the ICP is the search for the correspondence, and typically, it will converge after 30-50 iterations even more in some cases.

3.3.3.2 Least Square 3D

Gruen and Akca (2005) have developed a new approach for registration which is called Least Squares 3D (LS3D). It is a generalisation of the least squares image matching which was introduced by Chen and Medioni (1991). The transformation parameters are estimated in this method by minimising the sum of squares Euclidean distances between two or more surfaces, instead of distances between correspondence points in the ICP method. It starts with search surface estimation, then, Euclidean distances between the reference point cloud and the search surface are minimised to determine transformation parameters which are applied on the search surface, and the whole process is repeated until convergence. Alternatively, the numerical derivatives can also be calculated on the template surface, if there are insufficient initial approximations (Akca, 2007).

3.3.4 Coarse Initial Alignment

As has been mentioned early, the surfaces matching registration technique requires initial alignment, i.e. coarse registration, before it can be applied. This alignment can be done manually if there are a few numbers of scans. However, it could be complicated, if the number of scans increased, i.e. multiple registrations, with more than pairs overlapped. In such a case, automation is needed to fulfil the coarse registration; and thus, the fine registration can be applied.

There are different techniques existed for fully automated coarse registration without targets. Most of them have a common framework: first, extracting a set of features or key points; second, forming subsets and match overlapping area; finally, estimating transformation parameters from the best match (Theiler et al., 2014). Following are some examples of these techniques.

To begin with, Aiger et al. (2008) have introduced 4-Points Congruent Sets (4PCS) as a fast registration technique without any need for assumptions about starting alignment. This technique is based on extracting all 4-points coplanar sets from a point clouds which are almost congruent, under rigid transformation, to a given set of coplanar 4-points (Aiger et al., 2008). The main drawbacks of this technique are: (i) it does not well cope with high different point densities, such as that usually happen in TLS; and (ii) the huge TLS point clouds need to down-sample in order to use this technique efficiently, thus probably point-to-point correspondence may no longer be guaranteed (Theiler et al., 2013).

To cope with this limitation, Theiler et al. (2013) proposed a new technique termed Key-point based 4-Points Congruent Sets (K-4PCS). They suggested using key-points to represent point cloud instead of applying original point cloud. Although this method is faster than original 4-PCS, it is too slow for regular use in practice. In addition, it failed in some circumstances when more key-points were found close to the scanner due to more detail was observed (Theiler et al., 2014). For these reasons, Theiler et al. (2014) applied some extensions to improve their technique. In general, they improved time-cost and reduced the failure rate, yet failures still occur in the presence of symmetries or repeated structures and new solutions are needed (Theiler et al., 2014).

Al-Durgham et al. (2014) introduced a new automatic registration technique which is based on linear features that are extracted from the scans by a region-growing segmentation approach. The spatial separation and angular deviation between all the existing line pairs in each scan are used to identify linear pairs' correspondence. After that, the transformation parameters are determined for each pair. The clusters of transformation parameters that are numerically close to each other represent the final transformation parameters (Al-Durgham et al., 2014). This technique is a time expensive and impractical particularly when a lot of linear features exist.

Another interesting research for the coarse registration which is based on extracting spatial curves as matching primitives (Yang and Zang, 2014). The proposed technique involves three key parts: extracting

spatial curves which are representing crest line of prominent features, estimating deformation energy model from the crest lines which has been proposed here to determine the shape similarity between extracted crest lines, and matching conjugate curves to determine transformation parameters (ibid).

It is worth to mention some automated techniques that have been developed to solve coarse and fine registration in one step. For instance, Toldo et al. (2010) proposed embedding Generalized Procrustes Analysis (GPA) (chapter five) in ICP and called it ICP-GPA. Another example, Yang et al. (2013) proposed a global optimal solution for ICP and called it GO-ICP. They combined ICP with a branch-and-bound scheme to avoid local minima which frequently happen if ICP starts with arbitrary initialisation. However, this method has been evaluated on limited point cloud, yet does not scale up to massive data sets (Theiler et al., 2014).

3.4 Georeferencing

If there is a requirement to integrate TLS data with other geospatial data, e.g. ground control points, the registered point cloud of the whole object should be transformed to selected external coordinate system, which is either local or national. This procedure is called georeferencing (Reshetyuk, 2009). Hence, the georeferencing is defined as the procedure of transforming the intrinsic coordinate system, TLS coordinate system, to a national or local coordinate system. There are two methods for georeferencing: direct, and indirect. Broadly, two factors can affect the selection of adopted method: the scene characteristics and the required accuracy (Alba and Scaioni, 2007).

3.4.1 Direct Georeferencing

In this method, TLS acts as same as Total Station (TS), and it sets up over a known point and orients to another known point. In other words, the six degrees of freedom are determined practically, when TLS optically centred over a known point, three translation parameters are set, and the other rotation angles around X and Y axes are set through levelling, finally, rotation angle around Z-axis is fixed from orienting instrument to a known point (Alba and Scaioni, 2007).

Recently, TLS is integrated with other sensors, such as Global Navigation Satellite System (GNSS) and an Inertial Measurement Unit (IMU), to adopt direct georeferencing. Therefore, the integrated sensors can provide the platform position and altitude at each moment of data acquisition, and thus establishing coarse registration among multiple scans. However, the integrated sensor is preferable for mobile laser

scanner not for static because it imposes additional expenses to the scanning system (Al-Durgham et al., 2014, dos Santos et al., 2013).

Eventually, the quality of the data acquired by direct georeferencing technique depends on (Reshetyuk, 2009):

- The accuracy of the TLS setup procedure, such as centring, levelling, measuring the instrument height and orienting toward a known point.
- The accuracy of the control points been used or integrated system.

3.4.2 Indirect Georeferencing

This technique is the same as targets based registration (Sec. 3.3.1), the only difference that targets in indirect georeferencing are placed on points with known coordinates in the external reference system which are called in this case, control points rather than tie points (Reshetyuk, 2009). Conventionally, with the absence of control points, surveying before scanning is required to distribute points relate to a local reference system, or to the national reference system if GNSS is used (dos Santos et al., 2013).

It is worth to mention to interesting research which has proposed using control line instead of targets for indirect georeferencing (dos Santos et al., 2013). In this research, the corresponding lines are derived by segmenting and intersecting two adjacent planes which are not parallel, and then the transformation parameters are estimated by minimising the distance between the control lines and their corresponding (ibid).

According to Reshetyuk (2009), the indirect georeferencing is the most accurate technique because the quality of results only depends on the accuracy of control points. However, it is time-consuming and labour intensive (dos Santos et al., 2013).

3.5 Chapter Summary

In this chapter, the potentials of using TLS for monitoring purpose have been discussed. Commonly, five techniques can be employed to detect deformations from TLS data: using targets, direct cloud to cloud comparison, interpolation models, surfaces matching, and some specific solutions. Each of these methods has pros and cons and Table 3-1 summarises the advantages and disadvantages of these techniques.

Table 3-1 Advantages and disadvantages of the TLS techniques for monitoring surveying.

No.	Technique	Advantage	Disadvantage
1	Using targets	<ul style="list-style-type: none"> ▪ 3D deformation. ▪ High accurate. 	<ul style="list-style-type: none"> ▪ The single point accuracy of targets is much greater when conventional surveying is implemented. ▪ Expensive compared to conventional methods. ▪ Needs pre-knowledge for the location of the deformed area.
2	Cloud-to-cloud comparison	<ul style="list-style-type: none"> ▪ Quick where the speed of the data analysis plays a critical role. ▪ Easy to implement. 	<ul style="list-style-type: none"> ▪ Limited accuracy due to noise.
3	Interpolation models	<ul style="list-style-type: none"> ▪ Can detect deformations with magnitudes less than the nominal single point precision 	<ul style="list-style-type: none"> ▪ One dimension.
4	Surfaces matching	<ul style="list-style-type: none"> ▪ 3D deformation. ▪ Sensitivity to small deformations with magnitudes below the noise of the single TLS points. 	<ul style="list-style-type: none"> ▪ Non-linear functional model, care should be taken for approximate. ▪ Convergence might not happen if there is significant deformation. ▪ Cannot detect the shift. ▪ Deformation for whole object (rigid transformation).
5	Specific solutions	<ul style="list-style-type: none"> ▪ More accurate than original data. 	<ul style="list-style-type: none"> ▪ Apply in particular cases.

In terms of registration and georeferencing, because monitoring survey is a comparative procedure, it rarely needs georeferencing if there is no integration with other sensors. Therefore, it just requires that data for all epochs be related to the one coordinate system. In other words, only registration is required. However, in a massive structure monitoring, georeferencing can be used; hence, a control network needs to be established.

Regarding buildings monitoring, targets-based registration can work perfectly after fixing tie points in stable areas, which can be part of the concerned building or on surrounding objects. Care should be taken to assess these points each period to be sure that they have not moved between epochs. This method is adopted in this research.

CHAPTER Four: **ERROR SOURCES IN TLS**

4.1 Introduction

One of the most difficult tasks in surveying monitoring is to distinguish between deformations and existing errors which result from the uncertainty of measurements. Conventionally, statistical significance tests are employed to cope with this, assuming that all gross and systematic errors are eliminated from measurements. Initially, we need to figure out magnitudes and types of expected errors in used technique, and then, remove all outliers and systematic errors.

In terms of laser scanners, this is a complicated task due to different error sources with many variables in each of these. For instance, unlike conventional surveying methods, objects shape and reflection play a key role in errors of TLS measurements. In addition, there are some unobvious error sources such as that known as the mixed edge problem.

Normally, laser scanner manufacturers state precisions of their instruments up to millimetre level. However, does this mean that all scanned points have this accuracy? Definitely, the answer is no. According to Lichti and Gordon (2004), the precision of all points was poorer than the announced precision. Therefore, creating observation conditions which can reach such accuracies is vital for TLS monitoring surveying.

In this chapter, TLS error sources will be discussed, and types and magnitudes of these errors will be assessed. Furthermore, a procedure for eliminating laser scanner outliers and reducing noise will be introduced.

4.2 TLS Error Sources

Attention towards the problem of TLS calibration and validation has increased recently, due to the significant growth in TLS use, particularly by 'non-experts' from non-surveying and photogrammetric fields (Lichti, 2007). Commonly, physical models of a total station are used for this purpose due to mutual properties with TLS (ibid), although there are some different error sources for it.

In general, there are different classifications for TLS error sources. For instance, Lichti and Gordon (2004) divided errors between internal and external sources, and outlined the contributed error sources in the directly georeferenced point clouds: (i) control points used for scanner orientation; (ii) instrument

setting-up; (iii) targeting; (iv) scanner noise; and (v) laser beam width. Another example, Staiger (2005) stated that there are five sources for TLS errors (Figure 4-1).

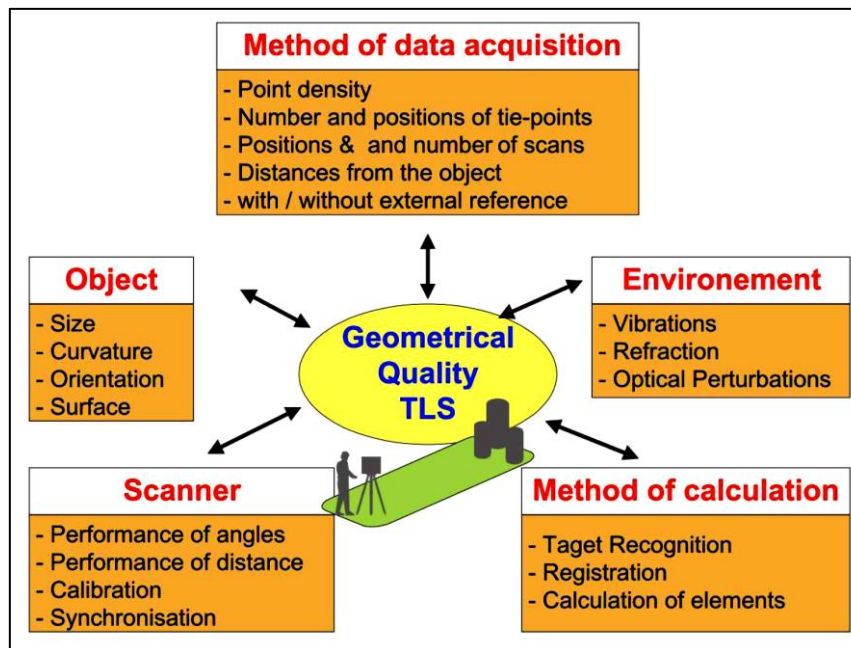


Figure 4-1 Parameters are influencing the quality of the scans (Staiger, 2005).

Another group of researchers (Holst and Kuhlmann, 2016, Kaasalainen et al., 2011, Soudarissanane et al., 2008, Soudarissanane et al., 2009, Soudarissanane et al., 2011) have indicated four main sources for TLS errors:

- Hardware mechanism precision (instrumental errors), e.g. angular uncertainty, axes errors.
- Object properties, e.g. roughness, reflectivity, colour.
- Atmospheric conditions, e.g. ambient light, humidity, temperature.
- Scanning geometry, e.g. incidence angle, range differences.

Some researchers (Hodge et al., 2009, Hodge, 2010) have added data processing (e.g. registration), and data resolution to these sources.

In this research, we are adopting Van Genechten et al. (2008) classification for TLS error sources due to the comprehensive listing. He spilled error sources to four parts: instrumental, object-related, environmental, and methodological.

4.2.1 Instrumental Errors

Instrumental errors come from imperfect manufacturing of the TLS, which can be in two forms: geometrically and electronically. Due to the topic of this research, electronic errors will not be discussed here (refer to Kilpelä (2004) for more details).

For a calibrated instrument, the geometrical errors commonly are classified as random errors. For instance, the range and angular measurements of TLS may include random errors and act as an uncertainty of measurements.

4.2.1.1 Beam Divergence

Beam divergence is the widening of the laser beam due to the distance travelled. It can be considered as the most significant random error (Laefer et al., 2009). Generally, it has a high influence on the point cloud resolution, mixed edge problem, range and angular precisions. Virtually, the recorded range and angular measurements are along the centre line of the emitted beam while the actual point location lies somewhere in the projected footprint. This case may yield a position uncertainty which is approximately equal to one-quarter of the laser beam diameter (Lichti and Gordon, 2004, Van Genechten et al., 2008).

The beam divergence can be computed by the following equation (Lichti and Gordon, 2004, Van Genechten et al., 2008):

$$w(\rho_w) = w_o \sqrt{1 + \left(\frac{\lambda \cdot \rho_w}{\pi \cdot w_o^2}\right)^2} \quad (4.1)$$

Where:

ρ_w : the range relative to the beam waist location.

w : radius of the beam.

w_o : beam waist (the minimum beam radius).

λ : wavelength.

However, for long range, it can be considered linear, so it is usually specified in terms of linear divergence, which may be stated in milliradian (mrad), plus an initial diameter (Lichti and Gordon, 2004, Lichti and Jamtsho, 2006).

4.2.1.2 Mixed Edge

Mixed edge (mixed pixel) happens when the emitting beam hits an edge of the object, and due to the footprint, reflects back from different surfaces (Figure 4-2), if they are separated by less than half the

pulse length (Lichti et al., 2005). Consequently, the recorded point position is calculated based on different returned signals, hence, a wrong position. As aforementioned, the influence of the mixed edge is increased due to the beam divergence and the latter increases over distance. In addition, increasing the scan resolution will increase the chances of the beam hitting an edge and therefore resulting in more mixed edges (Van Genechten et al., 2008).

In general, the mixed edge can be classified as a gross error and might be removed through manual deletion, or by outlier removal based on a median filter (Lichti et al., 2005).

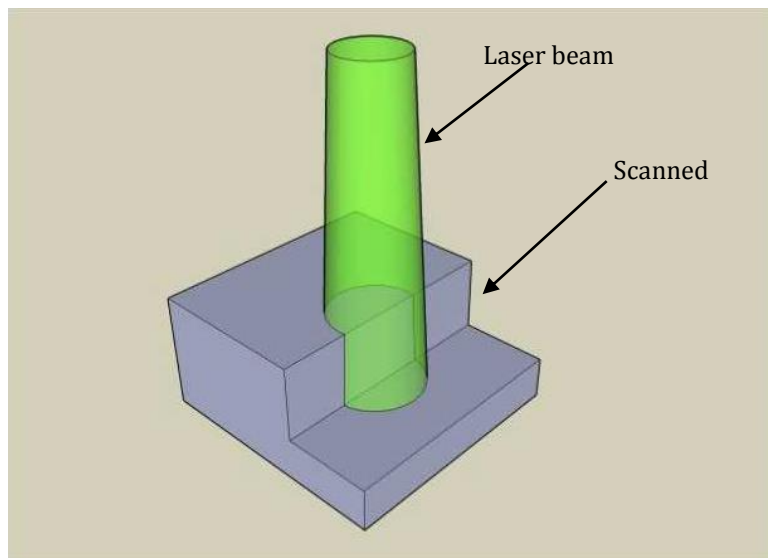


Figure 4-2 Example of a mixed edge problem (updated from Van Genechten et al. (2008)).

4.2.1.3 Range Uncertainty

The precision of the range is based on the scanner types and their working principle. Mainly, the precision of ranges of time of flight scanner depends on the timing clock and can be expressed as follows (Beraldin et al., 2005, Van Genechten et al., 2008):

$$\delta_r \approx \frac{c \cdot T_{Rep}}{2 \cdot \sqrt{SNR}} \quad (4.2)$$

Where:

T_{Rep} : pulse rise time.

SNR: signal to noise ratio.

c: speed of light in vacuum.

On the other hand, there is no need for a high-speed timing clock in continuous wave based scanners.

Hence, for such type of scanners, the range uncertainty depends on the modulated wavelength (λ_m) and

the signal to noise ratio (SNR), in case of amplitude modulation (Beraldin et al., 2005, Van Genechten et al., 2008):

$$\delta_r \approx \frac{\lambda_m}{4\pi \cdot \sqrt{SNR}} \quad (4.3)$$

Whereas for the continuous wave scanners which are based on frequency modulated, the range uncertainty is estimated as (Beraldin et al., 2005):

$$\delta_r \approx \frac{c}{4\Delta f_t} \quad (4.4)$$

Where Δf_t = tuning range or frequency excursion.

As can be seen, in both scanner types, the range precision depends on the SNR, defined as the ratio of the power of the signal to the power of the noise, which is, in turn, depends on different factors (refer to Reshetyuk (2009) for more details). To get reliable range measurements, the required SNR should be ten at a minimum, while no range can be measured when the SNR equals five (Reshetyuk, 2009).

4.2.1.4 Angular Uncertainty

In all TLS instruments, there is a mechanism (mirror or prism) to deflect the beam in certain directions (Boehler et al., 2003). The imperfection of this mechanism along with the angle measuring system (angular encoding) introduces another source of instrumental errors (Reshetyuk, 2009). For calibrated instruments, these are random errors.

4.2.1.5 Axes Errors

Similar to most surveying instruments, TLS has three axes as following (Reshetyuk, 2009, Van Genechten et al., 2008):

- **Vertical axis:** this axis allows the rangefinder to move emitting beam horizontally. Normally, it is the rotation axis of the TLS head.
- **Horizontal axis:** it is the rotation axis of TLS mirror.
- **Collimation axis:** it is the direction of the laser beam.

These axes are assumed to be orthogonal to each other similar to a total station (Holst and Kuhlmann, 2016). Due to imperfect manufacturing, or misuse, these axes may not be perfectly aligned and therefore

introduce errors. Fortunately, the systematic part of these errors can be removed in a calibration procedure leaving only the random errors.

4.2.2 Object-related Errors

Unlike most of the surveying techniques, the object shape, materials, and colour have a strong influence on the quality of the TLS outcomes. Mainly, the reflectance of the object surface plays the key role for the object-related error source. It is defined as the ratio between the reflected and incident laser beams, and is a function of the following factors (Reshetyuk, 2009):

- Object materials properties: such as conductivity, electric permittivity, and magnetic permeability.
- Object colour.
- The wavelength of the laser beam.
- Incidence angle.
- Surface roughness which is related to the wavelength and incidence angle of the laser beam.
- Object temperature.
- Object moisture.

Normally, the incident laser beam is reflected from the object surface in many directions (Figure 4-3). This type of diffused reflection is commonly described by Lambert's cosine law (Van Genechten et al., 2008):

$$I_{reflected}(\lambda) = I_i(\lambda) \cdot K_d(\lambda) \cdot \cos \alpha \quad (4.5)$$

Where:

$I_i(\lambda)$: the intensity of the incident light which is a function of wavelength.

$K_d(\lambda)$: the coefficient of reflection diffusion which is also a function of wavelength.

α : incidence angle which is defined as the angle between the incident light and the surface normal vector.

Normally, dark objects (black) absorb most of the incident laser beam and reflect a weak signal (low SNR), and therefore point precision will be corrupted by noise; bright objects with high reflectance can give more precise range measurements and hence more reliable outcomes. However, too high reflectance might cause noise called speckle noise, which is same as the multipath errors in GNSS technique, where the laser beam is fully reflected in the mirroring direction and then reflects toward TLS (Van Genechten et al., 2008). In this case, the measured range will not be for the desired point, but the point in the second

reflection. This type of error can be of any magnitude up to the maximum unambiguous range and can be removed by manual editing (Lichti et al., 2005).

Another error occurs in a highly reflective surface which is called “Detector Saturation”, where objects look nearer due to a range bias which is caused by the received energy exceeding the dynamic range of the detector. It is hard to quantify the magnitude of this error, but for extreme cases, it might easily be identified manually through point cloud editing (ibid).

Similarly, “Blooming” phenomenon is closely related to the saturation problem and takes place when returns are received from an object, such as a retroreflector target, making it appear bigger in size. Different factors can affect the amount of blooming such as laser power, material reflectivity, detection electronics (i.e. detection threshold), beam diameter, and the sampling interval (ibid).

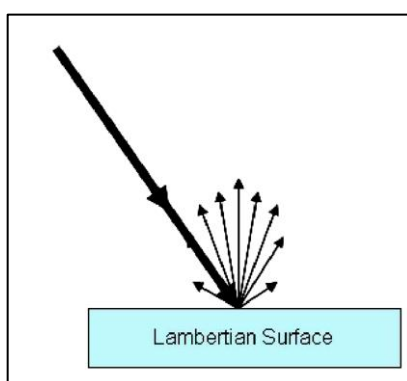


Figure 4-3 Diffuse reflection of the laser beam (Van Genechten et al., 2008).

In addition to reflectance effects, the objects could have a semi-transparent coating which allows the laser beam to refract and reflect inside the material itself (Figure 4-4). Consequently, it can add a systematic error to the measured range (Van Genechten et al., 2008). In terms of monitoring, this error has no effect because it will subtract during epoch differencing assuming that the same instrument is used, with the same laser wavelength.

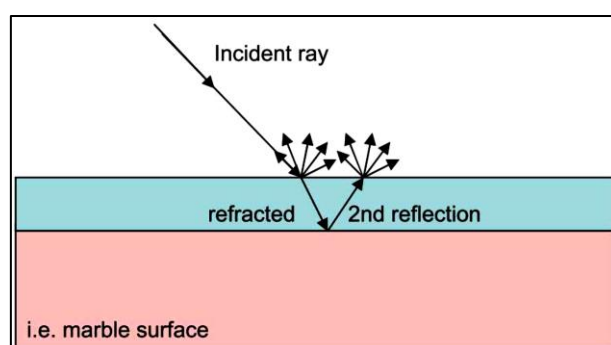


Figure 4-4 Refraction and reflection of the laser beam inside object materials (Van Genechten et al., 2008).

Finally, it is worth mentioning research, conducted by Voegtle et al. (2008), which assessed the influence of different materials and object colours on recorded TLS measurements. The results of this research showed the increase of measurement precision at night-time and on luminescent materials. In addition, the effect of different wood species and wetness seem to be insignificant, while transparency and metal plates induce MSE values much higher than the general range precision of the laser scanner (Voegtle et al., 2008).

4.2.3 Environmental Effects

4.2.3.1 Temperature

It can be noted that the temperature inside the TLS may be far hotter than the surrounding atmosphere due to internal heating or an external source (e.g. the sun) (Boehler et al., 2003). In addition, in an industrial environment, scanning hot objects may reduce SNR and in turn the precision of range measurements (Van Genechten et al., 2008).

4.2.3.2 Atmosphere

As in all instruments based on electromagnetic energy, the laser beam suffers from refraction when travelling through air. Consequently, it introduces a systematic error in the range measurements due to a change in laser light velocity. The refraction index is affected mainly by temperature, pressure and humidity. Hence, the most scanning acquisition software provides a correction for this refraction based on certain parameters. Therefore, the difference between actual atmospheric conditions and these parameters need to be adapted. For short and medium ranges, such as in monitoring surveys, this error can be easily corrected by inputting temperature, pressure and humidity before data collection, and any changes meanwhile surveying will introduce negligible errors. For instance, a difference in temperature of 10° C or air pressure of 35 hPa leads to range error of about 1mm/100m (Van Genechten et al., 2008).

4.2.3.3 Interfering Radiation

The precision of the range measurements may be affected by external radiation, such as illumination sources. Particular optical interference filters can be applied to the instrument to prevent incorrect frequencies from reaching the receiver (Boehler et al., 2003, Van Genechten et al., 2008).

4.2.3.4 Motion

Although the TLS can collect data at rates of up to 1000,000 points per second (Leica Geosystems, 2013, Leica Geosystems, 2016a), scanning still takes 10-30 minutes depends on resolution and scanner type. During this time, any motion obstacles could prevent laser light reaching the scanned object, and therefore recording incorrect ranges (positions) for these points. In addition, any movement or vibration of the scanner meanwhile scanning will cause an error in all points. Therefore, the scanner needs to be mounted on a stable platform preventing any motion obstacles during monitoring survey.

4.2.4 Methodological Impacts

Methodological errors are errors that come from a wrong choice of survey methods, instruments or position, and configurations to handle scanning. Evidently, the position of the TLS has an influence on the incidence angle, the range and the point density, and therefore the quality of the point cloud (Soudarissanane et al., 2009). For instance, the quality of the point clouds can be improved by 25 % through moving a TLS by two metres (Soudarissanane et al., 2008).

Mainly, methodological errors can be divided into three sources: resolution, registration, and incidence angle.

4.2.4.1 Resolution

Resolution is defined as the smallest object or object feature that can be detected in the point cloud (Boehler et al., 2003), or the ability to detect two objects on adjacent lines-of-sight (Lichti and Jamtsho, 2006, Pesci et al., 2011b). It is important when recording fine details such as cultural heritage features (Lichti and Jamtsho, 2006). Technically, two different specifications contribute to it: laser footprint (the size of the laser spot), and the point density (or sampling interval which is the average distance between points in a point cloud). Commonly, the point density demonstrated in two styles (Andrews et al., 2015, Heritage, 2011):

- Spatial: the average distance at a specific range (e.g. 5 mm at 10 m).
- Angular: angular increments for vertical and horizontal angle (e.g. 0.3°x0.3°).

In general, scanning with higher resolution (smaller average distance between points) can offer more detailed point clouds and better precision. Emphasis is often placed on the finest possible sampling

interval, which might be smaller than the laser footprint. In this case, the data resolution is determined by the laser footprint rather than the sampling interval (Hodge et al., 2009, Lichti and Jamtsho, 2006). Furthermore, an extra noise will create and the processing time will increase dramatically (Van Genechten et al., 2008). Hence, setting the sampling interval equal to the laser footprint might appear the optimal solution, although Lichti and Jamtsho (2006) approved that the best sampling interval equal to 86% of the footprint.

4.2.4.2 Registration

Errors can also be introduced in the post-processing of raw data. One obvious significant source is the registration and georeferencing technique (Hodge et al., 2009). As has been mentioned in chapter three, there are different techniques for registration and georeferencing, and each has its pros and cons. In terms of monitoring, the most accurate method, target based, is advised which in turn introduces other possible errors from target design and spatial distribution.

4.2.4.3 Incidence Angle

The Incidence angle (α), is defined as the angle between incoming laser beam (P) and surface normal (N), on the position of a scan point (Soudarissanane et al., 2009):

$$\alpha = \cos^{-1}\left(\frac{\vec{P} \cdot \vec{N}}{\|\vec{P}\| \|\vec{N}\|}\right) \quad (4.6)$$

According to Soudarissanane et al. (2011), 20% of the measurement noise comes from signal deterioration, caused by the incidence angle. The radar range equation can be used to estimate such deterioration with the assumption that reflection is according to Lambert's cosine law (4.5) (Soudarissanane et al., 2009):

$$P_r = K P_t \cos \alpha \quad (4.7)$$

Where:

P_r : Power of received signal.

P_t : Power of transmitted signal.

K: Constant (depended on different factors such as the target reflectance, the range, the receiver aperture diameter, and some systematic and atmospheric transmission).

α : Incidence angle.

Hence, the received signal power decreases with increasing incidence angle and therefore decreases the point cloud quality. Furthermore, the object surface reflectivity should be included to estimate the correction for incidence angle effects (Kaasalainen et al., 2011).

Additionally, an elongated footprint occurs due to increasing the incidence angle (Figure 4-5) and both of them (footprint and incidence angle) give rise to a range bias which can be parameterised (Lichti et al., 2005):

$$\Delta_\rho = \frac{\rho \delta}{2 \tan \alpha} \tag{4.8}$$

Where:

Δ_ρ : the range error, ρ : the range, δ : the beam divergence (footprint), α : the incidence angle.

For instance, a 3 mrad beam divergence could produce a range error of 0.15 m at a range of 100 m and 45° incidence angle (Lichti et al., 2005). To avoid such error, Lichti (2007) has suggested a threshold of a maximum incidence angle of 65° for removing non-reliable measurements. Similarly, Laefer et al. (2009) have recommended the maximum incidence angle of 45° for ranges of about 12-15 m to minimise this error.

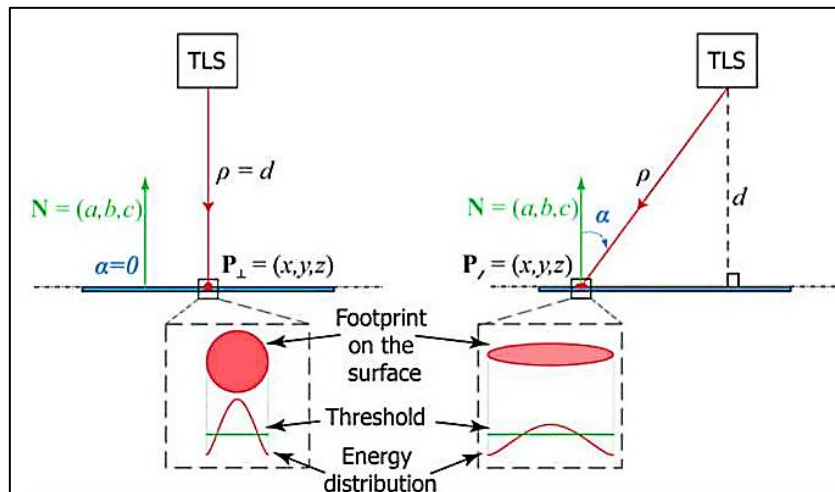


Figure 4-5 Reflection geometry is demonstrating incidence angle (Soudarissanane et al., 2011).

4.3 Quantification of Errors

Although many manufacturers supply technical information about the operating efficiency of their laser scanners, it is recommended to conduct experiments to inspect data quality (Pesci et al., 2007), for different reasons:

- It may help to identify the error sources and may, therefore, suggest strategies for the removal of erroneous points and the technique for improving data quality (Hodge et al., 2009).
- According to Laefer et al. (2009), the error figures published by equipment manufacturers are often misleading.
- Normally, equipment manufacturers supply error figures in terms of standard deviation or MSE, while for some projects, such as monitoring, the maximum of errors is vital for final consequences. For instance, Hodge et al. (2009) conducted a test to estimate the errors of a Leica HDS300 laser scanner through considering residuals, by fitting a least-squares plane to the total station measurements and scanner point cloud, as range errors. Although they estimated standard deviation (2mm) better than the manufacturer guidance (4mm), the maximum error was up to 15 mm.
- To set and fulfil realistic project specifications (Lichti and Gordon, 2004).

For all above reasons, a test to quantify errors of a laser scanner has been conducted. For this purpose, two models of laser scanner were examined: Leica Scanstation P20 and P40, which are employed in validation. The potential is to quantify random errors only, hence, it has been designed in such a way that systematic and gross errors are minimum, as follows:

- 1) Controlled atmospheric conditions were suggested. Hence, it was taken place at the indoors location. The photogrammetry lab in the Nottingham Geospatial Building (NGB) was used for this purpose (Figure 4-6).
- 2) To reduce object related errors, a plane white surface was advised. Accordingly, a projector screen (Figure 4-7) was used as a scanning object.
- 3) The distance between scanner and object was about 10m (exactly 10.028 m in P20 test and 9.991 m in P40 test). The beam footprint is minimal at this close range. Additionally, the maximum incidence angle is less than six degrees (two metres length object), hence, negligible effects.
- 4) The seven preset (default) point spaces were tested (50 mm, 25 mm, 12.5 mm, 6.3 mm, 3.1 mm, 1.6 mm, and 0.8 mm).
- 5) To estimate errors, the projector screen was scanned twice, and the distances between the corresponding points in point clouds were considered as noise. For this purpose, CloudCompare software was used to compute cloud to cloud distances.

- 6) To remove mixed edge errors, the scanned area was trimmed out before computing cloud-to-cloud distances.

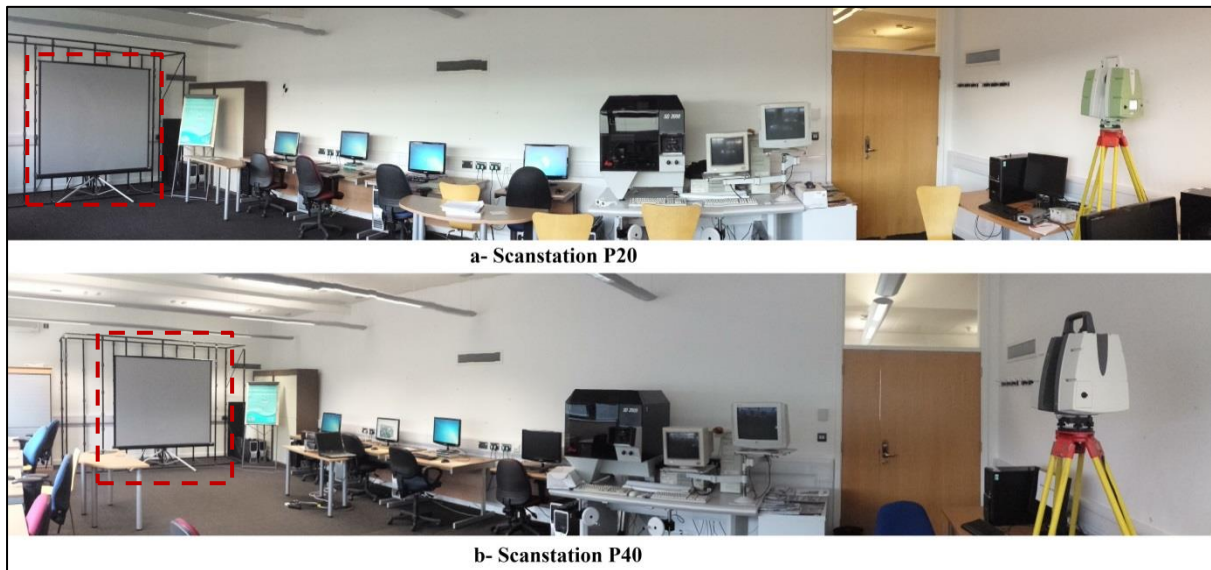


Figure 4-6 The location of error quantification test at photogrammetry lab in NGB.



Figure 4-7 The scanned object in error quantification test.

4.3.1 Scanstation P20

As mentioned before, seven different point spaces were tested. In addition, for each point space, there are different quality levels (Table 4-1). The higher the selected quality, the more range measurements for the same collected point (Geosystems, 2015), hence, the recorded range is the average of multiple measurements (see

Table 4-2 for the number of measurements in each case). Consequently, errors were quantified for 24 different settings. For each, the mean errors (the mean distances between corresponding points in two

scans) and the maximum errors (the maximum distances between corresponding points in two scans) were estimated (Table 4-3 and Figure 4-8).

Table 4-1 Technical specifications for Scanstation P20 (Leica Geosystems, 2013)

General		Environmental																																												
Instrument type	Compact, ultra-high speed pulsed laser scanner with survey grade accuracy, range and field-of-view; integrated camera and laser plummet	Operating temperature	-20° C to +50° C / -4° F to 122° F																																											
User interface	Onboard control, notebook or tablet PC, PDA	Storage temperature	-40° C to +70° C / -40° F to 158° F																																											
Data storage	Integrated solid-state drive (SSD) or external USB flash drive	Lighting	Fully operational between bright sunlight and complete darkness																																											
Camera	Auto-adjusting, integrated high-resolution digital camera with zoom video	Humidity	Non-condensing																																											
		Dust/Humidity	IP54 (IEC 60529)																																											
System Performance		Physical																																												
Accuracy of single measurement		Scanner																																												
3D Position Accuracy	3 mm at 50 m; 6 mm at 100 m	Dimensions (D x W x H)	238 mm x 358 mm x 395 mm / 9.4" x 14.1" x 15.6"																																											
Linearity error	≤ 1 mm	Weight	11.9 kg / 26.2 lbs, nominal (w/o batteries)																																											
Angular accuracy	8" horizontal; 8" vertical	Battery (internal)																																												
Target acquisition*	2 mm standard deviation up to 50 m	Dimensions (D x W x H)	40 mm x 72 mm x 77 mm / 1.6" x 2.8" x 3.0"																																											
Dual-axis compensator	Selectable on/off, resolution 1", dynamic range +/- 5', accuracy 1.5"	Weight	0.4 kg / 0.9 lbs																																											
		Battery (external)																																												
		Dimensions (D x W x H)	95 mm x 248 mm x 60 mm / 3.7" x 9.8" x 2.4"																																											
		Weight	1.9 kg / 4.2 lbs																																											
		AC Power Supply																																												
		Dimensions (D x W x H)	170 mm x 85 mm x 42.5 mm / 6.6" x 3.3" x 1.6"																																											
		Weight	0.86 kg / 1.9 lbs																																											
		Mounting	Upright or upside down																																											
Laser Scanning and Imaging System		Standard Accessories Included																																												
Type	Ultra-high speed time-of-flight enhanced by Waveform Digitising (WFD) technology	Scanner transport case																																												
Wavelength	808 nm (invisible) / 658 (visible)	Tribrach (Leica Geosystems Professional Series)																																												
Laser class	1 (in accordance with IEC60825:2014)	4 x Internal batteries																																												
Beam divergence	0.2mrad	Battery charger / AC power cable, car adapter, daisy chain cable																																												
Beam diameter at front window	≤ 2.8 mm	Data cable																																												
Range	Up to 120 m; 18% reflectivity (minimum range 0.4 m)	Height metre and distance holder for height metre																																												
Scan rate	Up to 1'000'000 points/s	1 year CCP Basic support contract																																												
Range noise**	<table border="1"> <thead> <tr> <th>Range</th> <th>Black (10%)</th> <th>Gray (28%)</th> <th>White (100%)</th> </tr> </thead> <tbody> <tr> <td>10 m</td> <td>0.8 mm rms</td> <td>0.5 mm rms</td> <td>0.4 mm rms</td> </tr> <tr> <td>25 m</td> <td>1.0 mm rms</td> <td>0.6 mm rms</td> <td>0.5 mm rms</td> </tr> <tr> <td>50 m</td> <td>2.8 mm rms</td> <td>1.1 mm rms</td> <td>0.7 mm rms</td> </tr> <tr> <td>100 m</td> <td>9.0 mm rms</td> <td>4.3 mm rms</td> <td>1.5 mm rms</td> </tr> </tbody> </table>	Range	Black (10%)	Gray (28%)	White (100%)	10 m	0.8 mm rms	0.5 mm rms	0.4 mm rms	25 m	1.0 mm rms	0.6 mm rms	0.5 mm rms	50 m	2.8 mm rms	1.1 mm rms	0.7 mm rms	100 m	9.0 mm rms	4.3 mm rms	1.5 mm rms																									
Range	Black (10%)	Gray (28%)	White (100%)																																											
10 m	0.8 mm rms	0.5 mm rms	0.4 mm rms																																											
25 m	1.0 mm rms	0.6 mm rms	0.5 mm rms																																											
50 m	2.8 mm rms	1.1 mm rms	0.7 mm rms																																											
100 m	9.0 mm rms	4.3 mm rms	1.5 mm rms																																											
Scan time and resolution (hh:mm:ss)	<table border="1"> <thead> <tr> <th rowspan="2">Spacing mm</th> <th colspan="4">Quality level</th> </tr> <tr> <th>1</th> <th>2</th> <th>3</th> <th>4</th> </tr> </thead> <tbody> <tr> <td>50</td> <td>00:20</td> <td>00:20</td> <td>00:28</td> <td>----</td> </tr> <tr> <td>25</td> <td>00:33</td> <td>00:33</td> <td>00:53</td> <td>01:43</td> </tr> <tr> <td>12.5</td> <td>00:58</td> <td>01:44</td> <td>03:24</td> <td>06:46</td> </tr> <tr> <td>6.3</td> <td>01:49</td> <td>03:25</td> <td>06:46</td> <td>13:30</td> </tr> <tr> <td>3.1</td> <td>03:30</td> <td>06:47</td> <td>13:30</td> <td>26:59</td> </tr> <tr> <td>1.6</td> <td>13:33</td> <td>27:04</td> <td>54:07</td> <td>----</td> </tr> <tr> <td>0.8</td> <td>54:07</td> <td>1:48:13</td> <td>----</td> <td>----</td> </tr> </tbody> </table>	Spacing mm	Quality level				1	2	3	4	50	00:20	00:20	00:28	----	25	00:33	00:33	00:53	01:43	12.5	00:58	01:44	03:24	06:46	6.3	01:49	03:25	06:46	13:30	3.1	03:30	06:47	13:30	26:59	1.6	13:33	27:04	54:07	----	0.8	54:07	1:48:13	----	----	
Spacing mm	Quality level																																													
	1	2	3	4																																										
50	00:20	00:20	00:28	----																																										
25	00:33	00:33	00:53	01:43																																										
12.5	00:58	01:44	03:24	06:46																																										
6.3	01:49	03:25	06:46	13:30																																										
3.1	03:30	06:47	13:30	26:59																																										
1.6	13:33	27:04	54:07	----																																										
0.8	54:07	1:48:13	----	----																																										
Field-of-View		Additional Accessories & Services																																												
Horizontal	360°	B&W scan targets and target accessories																																												
Vertical	270°	Range of Customer Care Products (CCPs) that include Support, Hardware & Software maintenance and Extended warranty.																																												
Aiming/Sighting	Parallax-free, integrated zoom video	External battery with charging station, AC power supply and power cable																																												
Scanning optics	Vertically rotating mirror on horizontally rotating base	Professional charger for internal batteries																																												
	Up to 50 Hz with internal battery	AC power supply for scanner																																												
	Up to 100 Hz with external power supply	Tripod and tripod star																																												
Data storage capacity	256 GB onboard solid-state drive (SSD) or external USB device	Upside down mounting adapter																																												
Communications	Gigabit Ethernet or integrated Wireless LAN	Control Options																																												
Imaging	5 megapixels per each 17° x 17° colour image; streaming video with zoom; auto-adjusts to ambient lighting	Full colour touchscreen for onboard scan control.																																												
Onboard display	Touchscreen control with stylus, full colour VGA graphic display (640 x 480 pixels)	Remote control: Leica CS10/CS15 controller or any other remote desktop capable device, including iPad, iPhone and other Smartphones.																																												
Level indicator	External bubble, electronic bubble in onboard software	Ordering Information																																												
Data transfer	Ethernet, WLAN or USB 2.0 device	Contact your local Leica Geosystems representative or an authorised Leica Geosystems dealer.																																												
Laser plummet	Laser class 1 (IEC60825:2014) Centering accuracy: 1.5 mm at 1.5 m Laser dot diameter: 2.5 mm at 1.5 m Selectable ON/OFF	<p>All specifications are subject to change without notice. All accuracy specifications are one sigma unless otherwise noted. * Algorithmic fit to planar B&W targets ** Detailed explanation on request</p> <p>Scanner: Laser class 1 in accordance with IEC60825:2014 Laser plummet: Laser class 1 in accordance with IEC60825:2014</p> <p>iPhone and iPad are trademarks of Apple Inc.</p> <p>Illustrations, descriptions and technical data are not binding. All rights reserved. Printed in Switzerland – Copyright Leica Geosystems AG, Heerbrugg, Switzerland, 2013. 795781en - 07.14 - galledia</p>																																												
Electrical																																														
Power supply	24 V DC, 100 – 240 V AC																																													
Power consumption	40 W typical																																													
Battery type	Internal: Li-Ion; External: Li-Ion																																													
Power ports	Internal: 2, External: 1 (simultaneous use, hot swappable)																																													
Duration	Internal > 7 h (2 batteries), External > 8.5 h (room temp.)																																													

Table 4-2 Number of measurements of different resolutions and quality levels (Geosystems, 2015).

Quality	Resolution at 10 m (mm)						
	50	25	12.5	6.3	3.1	1.6	0.8
1	8	4	4	2	1	1	1
2	16	8	8	4	2	2	2
3	32	16	16	8	4	4	-----
4	-----	32	32	16	8	-----	-----

Table 4-3 Error estimations for different settings for Scanstation P20.

No	Name	Resolution (mm)	Quality	Time (seconds)	No. of points	Mean errors (m)	Max. errors (m)
1	50mm_Q1	50	1	4	983	0.0016	0.0057
2	50mm_Q2	50	2	4	984	0.0012	0.0495
3	50mm_Q3	50	3	4	990	0.0011	0.0035
4	25mm_Q1	25	1	6	3905	0.0020	0.0110
5	25mm_Q2	25	2	6	3899	0.0013	0.0258
6	25mm_Q3	25	3	6	3947	0.0011	0.0049
7	25mm_Q4	25	4	8	3934	0.0007	0.0037
8	12.5mm_Q1	12.5	1	8	15888	0.0020	0.0128
9	12.5mm_Q2	12.5	2	9	15851	0.0013	0.0128
10	12.5mm_Q3	12.5	3	14	15855	0.0010	0.0126
11	12.5mm_Q4	12.5	4	23	15852	0.0009	0.0125
12	6.3mm_Q1	6.3	1	12	63635	0.0028	0.0109
13	6.3mm_Q2	6.3	2	15	63675	0.0019	0.0094
14	6.3mm_Q3	6.3	3	26	63662	0.0014	0.0077
15	6.3mm_Q4	6.3	4	49	63660	0.0010	0.0069
16	3.1mm_Q1	3.1	1	19	254256	0.0015	0.0067
17	3.1mm_Q2	3.1	2	26	254385	0.0022	0.0107
18	3.1mm_Q3	3.1	3	49	254395	0.0018	0.0079
19	3.1mm_Q4	3.1	4	96	254397	0.0015	0.0066
20	1.6mm_Q1	1.6	1	49	1021567	0.0012	0.0081
21	1.6mm_Q2	1.6	2	96	1022042	0.0015	0.0092
22	1.6mm_Q3	1.6	3	191	1022041	0.0014	0.0093
23	0.8mm_Q1	0.8	1	190	4064717	0.0009	0.0079
24	0.8mm_Q2	0.8	2	380	4084268	0.0010	0.0090

Evidently, the mean error is better than that published point position precision (3mm at 50m (Table 4-1)), taking into account it is based on the difference between two points, it needs to be divided by square root of 2. On the other hand, the maximum error is much more than that expected, as high as 5 cm. This is possible because outliers occur which result from differencing between incorrect corresponding points. Figure 4-9 supports this assumption, especially in resolutions 50 mm, 25 mm, and 12.5 mm (a, b, and c) where few points show a clear difference compared to others. However, it is less clear for higher resolutions (Figure 4-10). This might be because, due to tiny distances in case of high resolutions, there are many points have all or most of the corresponding point properties and converging to any of them gives nearly the same results. Incorrect corresponding is the obvious disadvantage of using cloud differencing based on point-to-point distances to determine deformations because there is a chance to interpret outliers as deformations. In this case, it is advised to use higher resolutions or use another method to determine distances between two clouds; this will be discussed later in this chapter.

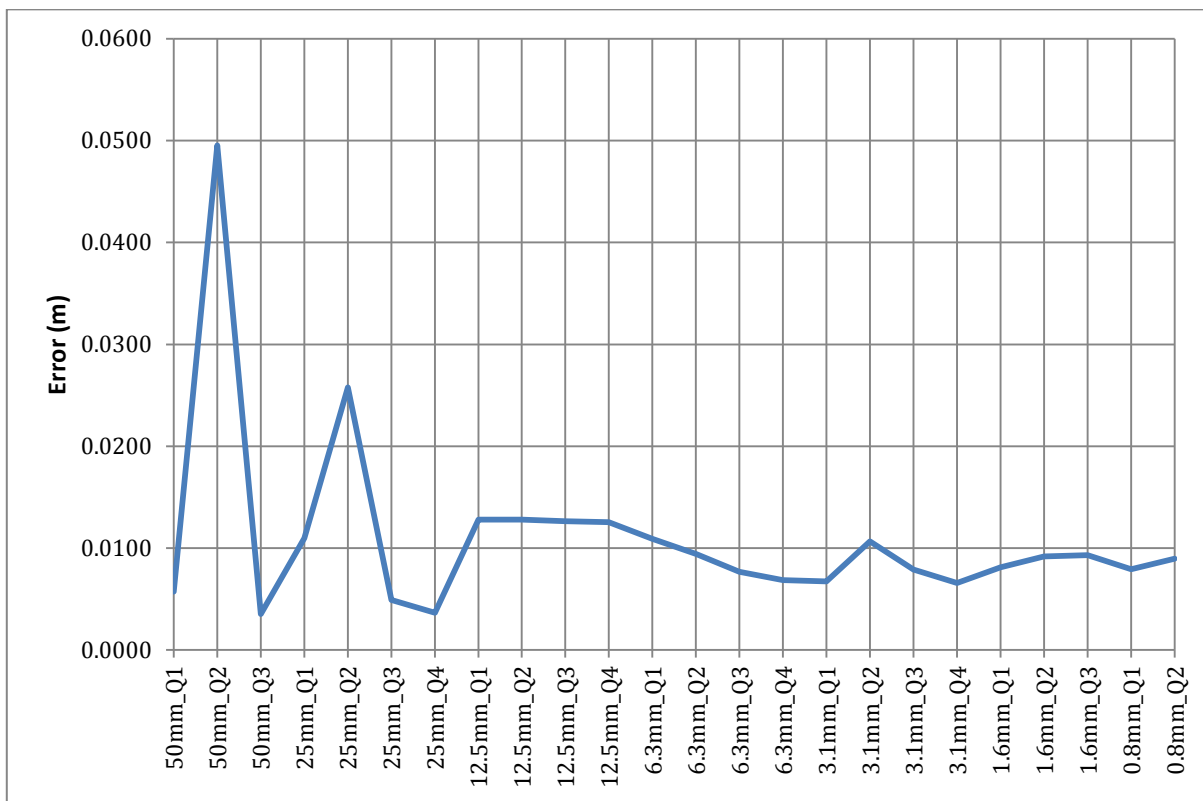


Figure 4-8 The maximum errors of Scanstation P20.

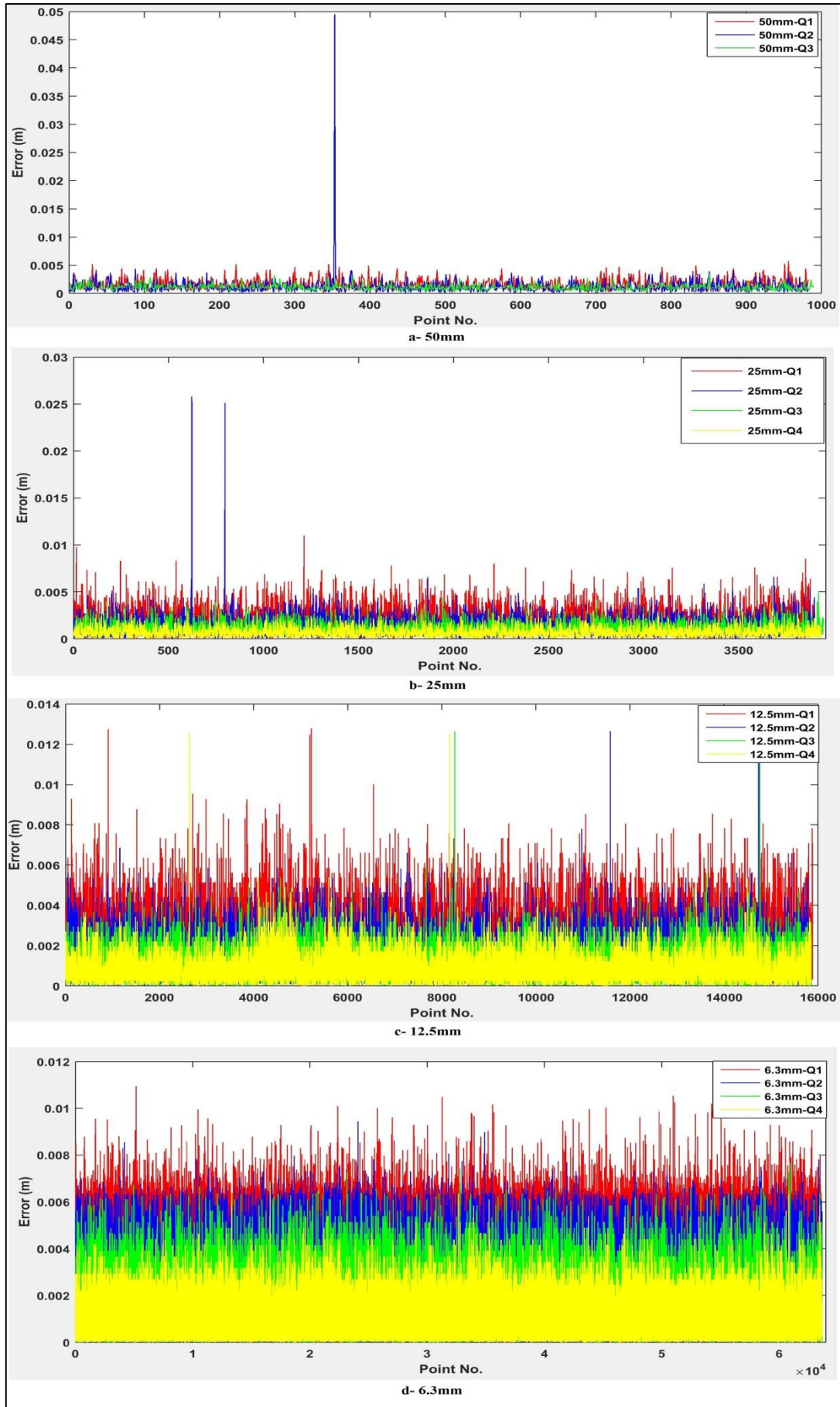


Figure 4-9 Point errors of Scanstation P20 for different resolutions (50 mm, 25 mm, 12.5 mm, and 6.3 mm).

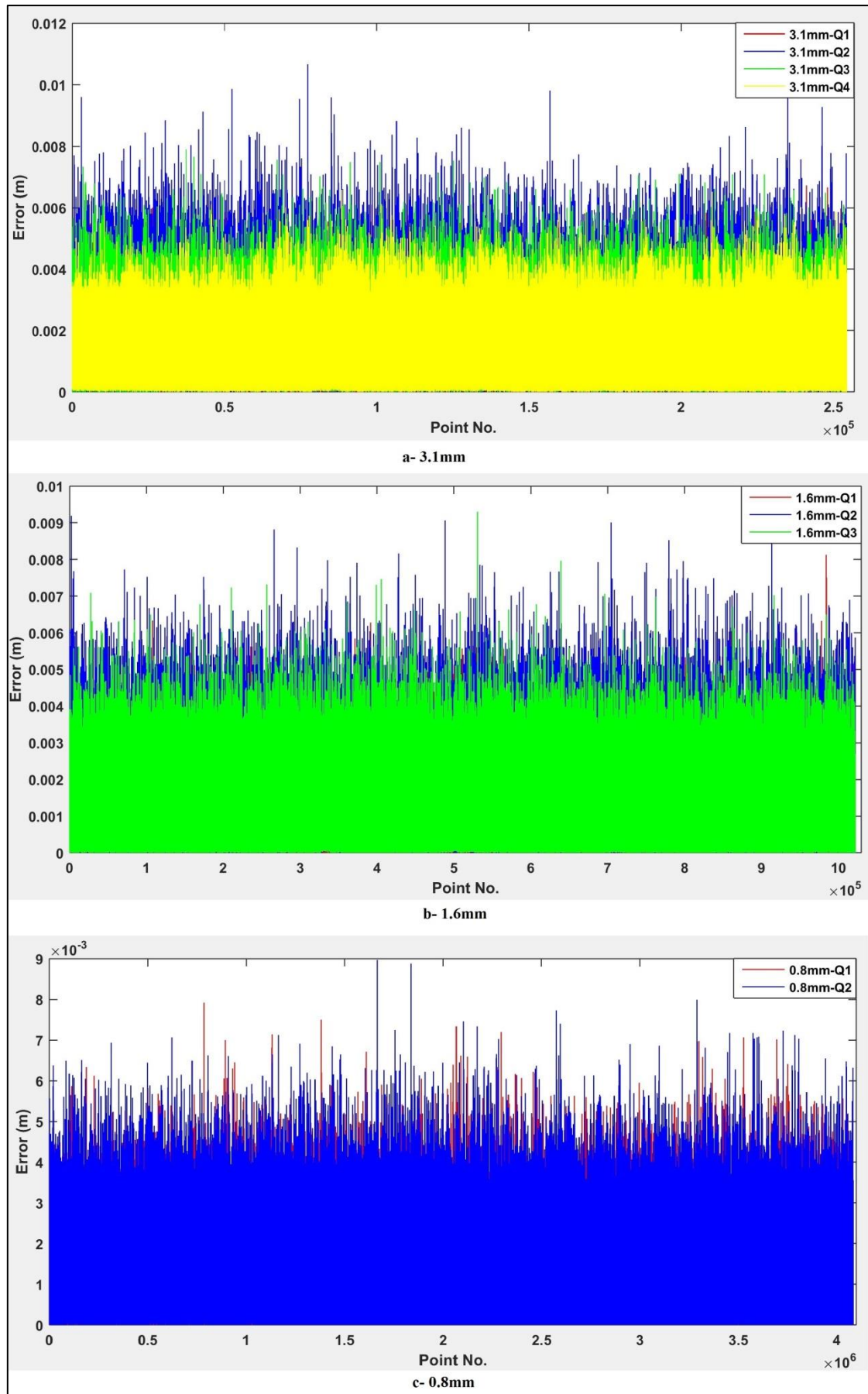


Figure 4-10 Point errors of Scanstation P20 for various resolutions (3.1 mm, 1.6 mm, and 0.8 mm).

Assuming errors are normally distributed; all errors that exceed three times standard deviation were excluded as outliers (Table 4-4). Obviously, there is an improvement in the maximum of errors, which decreased to less than 9 mm (Figure 4-11). In addition, Figure 4-13 and Figure 4-14 show no outliers for all cases.

However, the mean errors remained the same values (Figure 4-12) which mean the noise level remains without any mitigation after applying this technique. Furthermore, it reduced the point density by about one percent; in other words, losing some details.

In terms of monitoring, it is risky to cut out any points after cloud differencing because it could exclude deformed points from the data. In this case, removing outliers can be applied before differencing or by applying a different technique for estimating distances between two point clouds.

Table 4-4 Error estimations for various settings for Scanstation P20 after removing outliers.

No.	Name	Resolution (mm)	Quality	No. of Point	Remained (%)	Mean errors (m)	Max. errors (m)
1	50mm_Q1	50	1	971	98.8%	0.0016	0.0044
2	50mm_Q2	50	2	983	99.9%	0.0012	0.0044
3	50mm_Q3	50	3	977	98.7%	0.0011	0.0025
4	25mm_Q1	25	1	3876	99.3%	0.0019	0.0064
5	25mm_Q2	25	2	3886	99.7%	0.0013	0.0047
6	25mm_Q3	25	3	3905	98.9%	0.0011	0.0030
7	25mm_Q4	25	4	3897	99.1%	0.0007	0.0022
8	12.5mm_Q1	12.5	1	15730	99.0%	0.0019	0.0064
9	12.5mm_Q2	12.5	2	15710	99.1%	0.0013	0.0044
10	12.5mm_Q3	12.5	3	15680	98.9%	0.0010	0.0034
11	12.5mm_Q4	12.5	4	15630	98.6%	0.0008	0.0027
12	6.3mm_Q1	6.3	1	63550	99.9%	0.0028	0.0087
13	6.3mm_Q2	6.3	2	63080	99.1%	0.0019	0.0062
14	6.3mm_Q3	6.3	3	63070	99.1%	0.0014	0.0047
15	6.3mm_Q4	6.3	4	63020	99.0%	0.0010	0.0032
16	3.1mm_Q1	3.1	1	253800	99.8%	0.0015	0.0045
17	3.1mm_Q2	3.1	2	253700	99.7%	0.0022	0.0059
18	3.1mm_Q3	3.1	3	254000	99.8%	0.0018	0.0052
19	3.1mm_Q4	3.1	4	254000	99.8%	0.0015	0.0045
20	1.6mm_Q1	1.6	1	1016000	99.5%	0.0012	0.0033
21	1.6mm_Q2	1.6	2	1013000	99.1%	0.0015	0.0033
22	1.6mm_Q3	1.6	3	1015000	99.3%	0.0013	0.0034
23	0.8mm_Q1	0.8	1	4010000	98.7%	0.0009	0.0023
24	0.8mm_Q2	0.8	2	4027000	98.6%	0.0010	0.0024

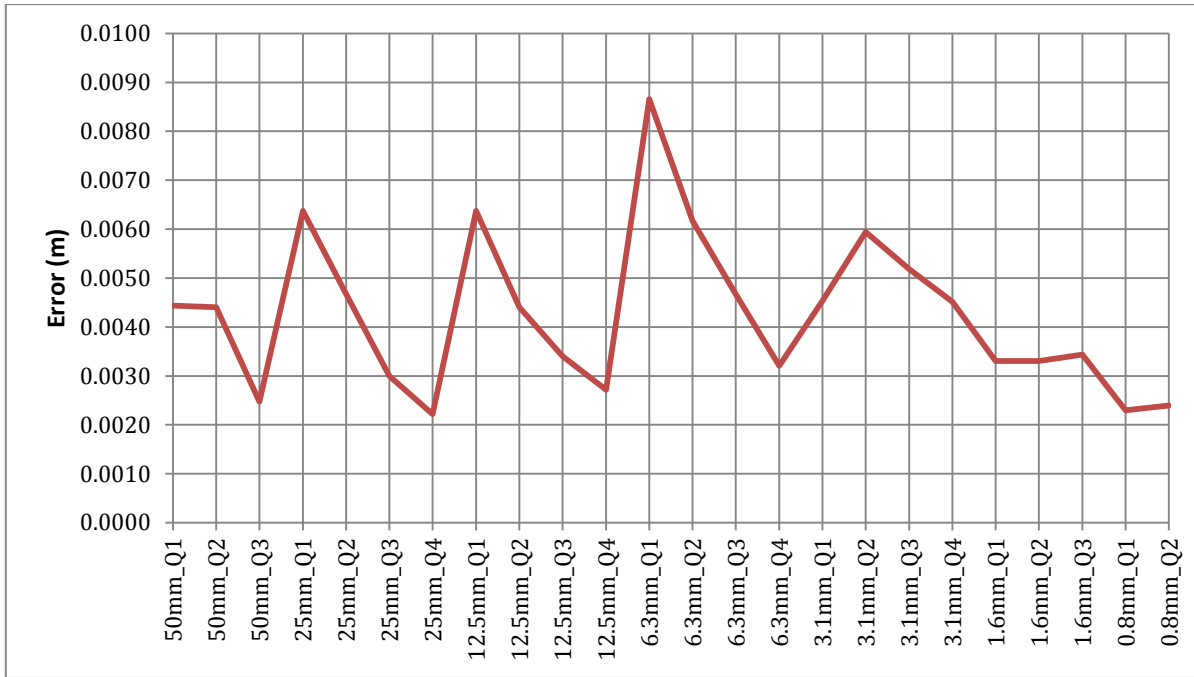


Figure 4-11 The maximum errors of Scanstation P20 after outlier removal.

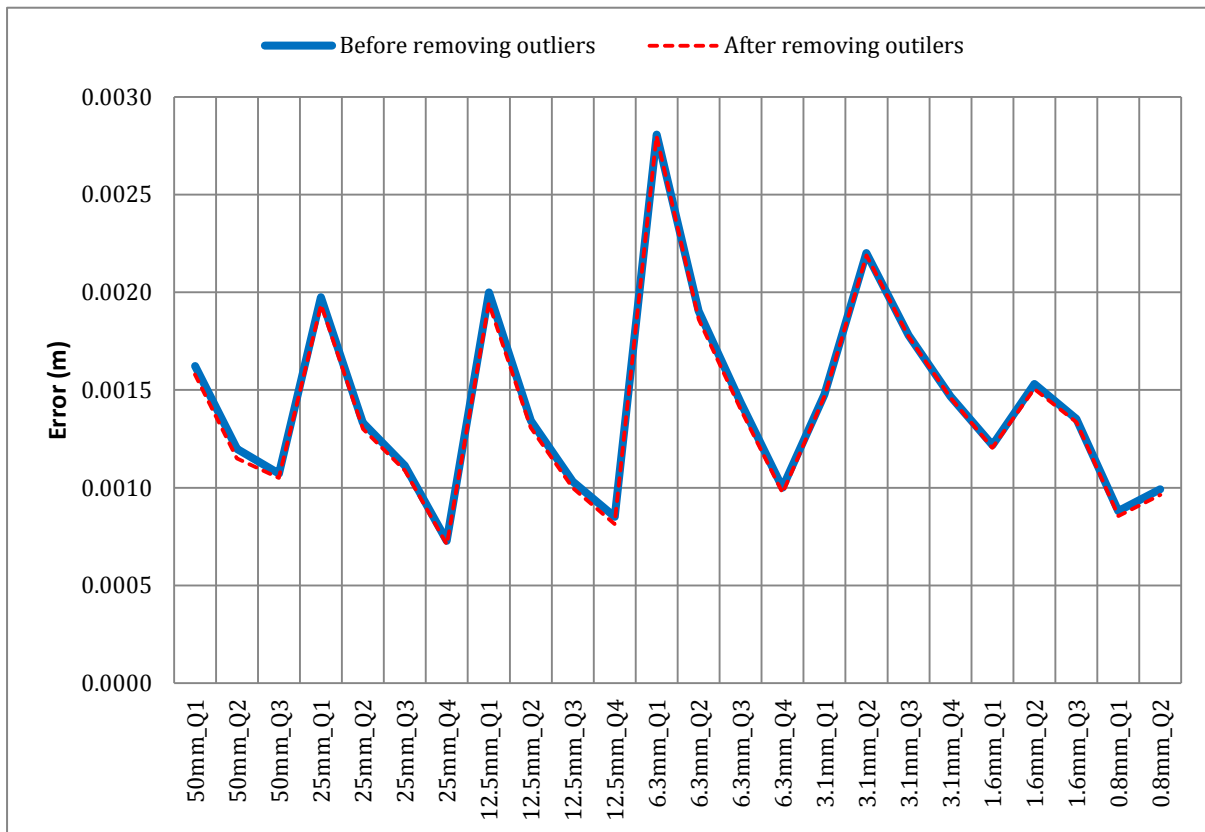


Figure 4-12 The mean errors of Scanstation P20 before and after removing outliers.

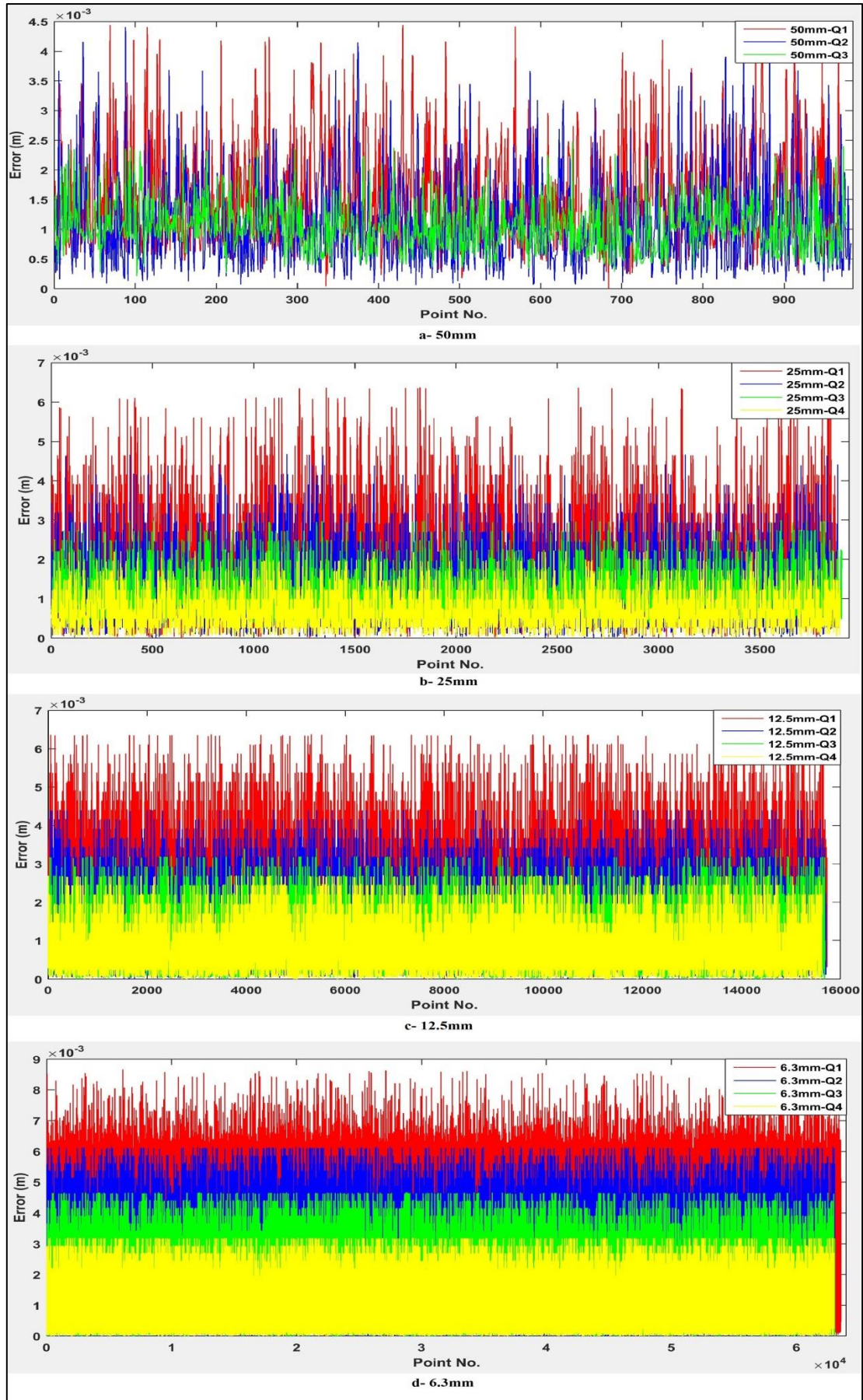


Figure 4-13 Point errors of Scanstation P20 for different resolutions (50 mm, 25 mm, 12.5 mm, and 6.3 mm) after outlier removal.

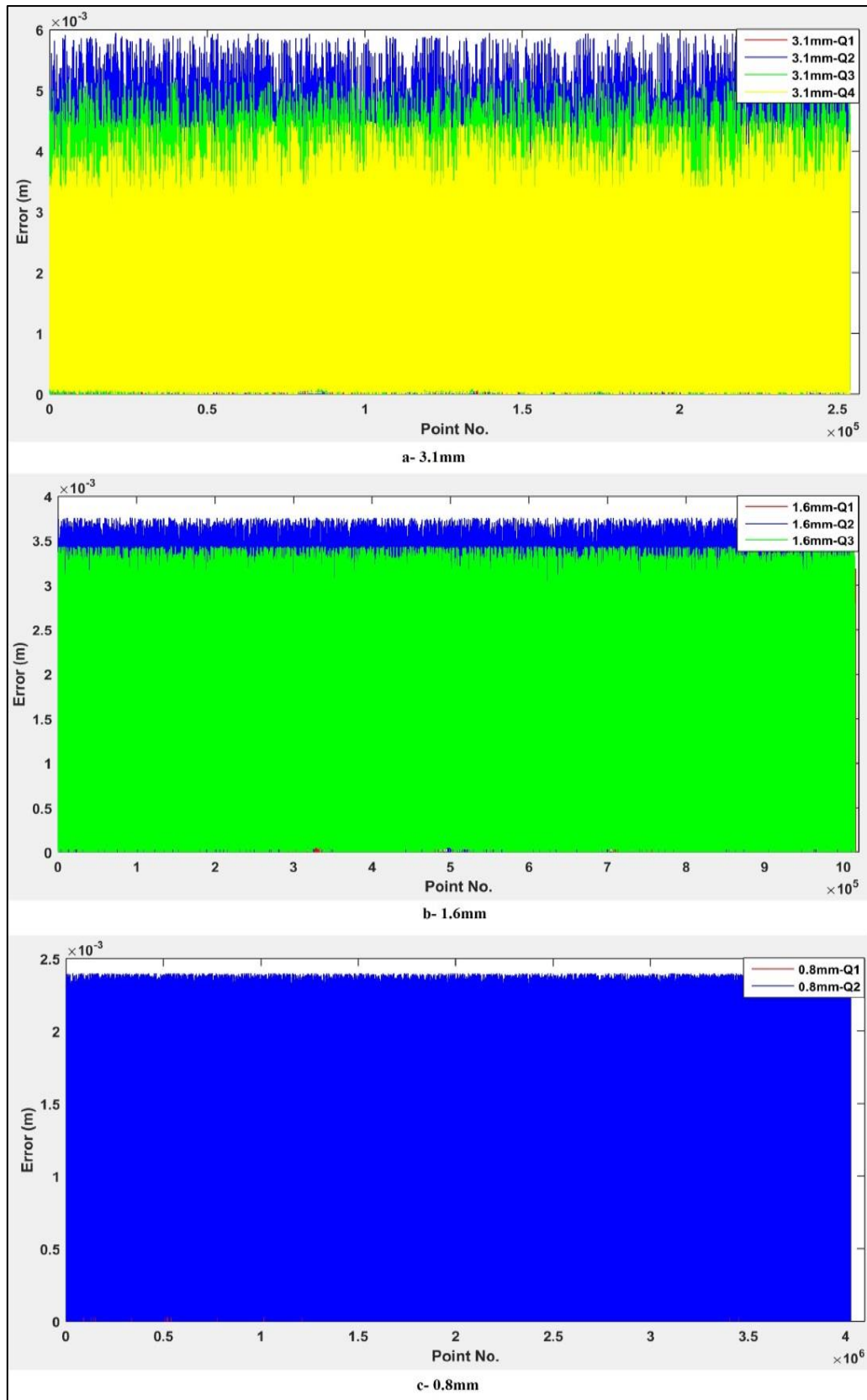


Figure 4-14 Points errors of Scanstation P20 for different resolutions (3.1 mm, 1.6 mm, and 0.8 mm) after outlier removal.

4.3.2 Scanstation P40

Due to using Wave Form Digitizer (WFD) technology, Scanstation P40 (Table 4-6) has the flexible reconfigurability of both the duty cycle (the ratio between pulse width and repetition (Figure 4-15)) and the number of accumulations which affect the measurement time and range (Maar and Zogg, 2014). For instance, a lower repetition rate can lead to a better sensitivity, while a more precise determination of the pulse's barycenter can be achieved by a smaller pulse width and therefore a higher measuring precision. Furthermore, the more signal shot accumulations, the better the SNR and therefore the more accurate distances can be determined (ibid).

Accordingly, there are four setting options in P40: two for different EDM modes (SPEED and RANGE) and two for different sensitivities (HIGH and NORMAL). Each of them has been tested with various resolutions (50 mm, 25 mm, 12.5 mm, 6.3 mm, 3.1 mm, 1.6 mm, and 0.8 mm) and resulted in 28 cases (Table 4-5). The mean errors (Figure 4-16) decreased to the quarter of that of P20, 0.7 mm compared with 2.8 mm for P40 and P20 respectively. Similarly, maximum errors are improved as well (Figure 4-17). However, there are some cases revealed as high as 12 mm. This possibly due to outliers and this assumption can be accepted based on Figure 4-18 (c and d) and Figure 4-19 (a).

Table 4-5 Error estimations for different settings for Scanstation P40.

No	Resolution (mm)	Name	Sensitivity	EDM mode	Time (seconds)	No. of Points	Mean Errors (m)	Max. Errors (m)
1	50	50mm_N_R	Normal	Range	4	990	0.0007	0.0012
2	50	50mm_N_S	Normal	Speed	4	990	0.0004	0.0010
3	50	50mm_H_R	High	Range	4	990	0.0004	0.0012
4	50	50mm_H_S	High	Speed	4	990	0.0003	0.0010
5	25	25mm_N_R	Normal	Range	6	3960	0.0004	0.0020
6	25	25mm_N_S	Normal	Speed	6	4020	0.0003	0.0012
7	25	25mm_H_R	High	Range	6	4047	0.0002	0.0010
8	25	25mm_H_S	High	Speed	6	4020	0.0004	0.0010
9	12.5	12.5mm_N_R	Normal	Range	8	16066	0.0004	0.0126
10	12.5	12.5mm_N_S	Normal	Speed	8	16158	0.0004	0.0124
11	12.5	12.5mm_H_R	High	Range	9	16089	0.0003	0.0124
12	12.5	12.5mm_H_S	High	Speed	9	16054	0.0003	0.0013
13	6.3	6.3mm_N_R	Normal	Range	14	64582	0.0006	0.0062
14	6.3	6.3mm_N_S	Normal	Speed	14	64554	0.0003	0.0063
15	6.3	6.3mm_H_R	High	Range	26	64576	0.0002	0.0062
16	6.3	6.3mm_H_S	High	Speed	15	64542	0.0002	0.0062
17	3.1	3.1mm_N_R	Normal	Range	26	257836	0.0003	0.0032
18	3.1	3.1mm_N_S	Normal	Speed	20	257734	0.0004	0.0032
19	3.1	3.1mm_H_R	High	Range	96	257777	0.0003	0.0032
20	3.1	3.1mm_H_S	High	Speed	49	257811	0.0003	0.0032
21	1.6	1.6mm_N_R	Normal	Range	97	1034831	0.0005	0.0017
22	1.6	1.6mm_N_S	Normal	Speed	50	1034782	0.0005	0.0017
23	1.6	1.6mm_H_R	High	Range	383	1034762	0.0002	0.0016
24	1.6	1.6mm_H_S	High	Speed	192	1034708	0.0002	0.0016
25	0.8	0.8mm_N_R	Normal	Range	382	4039386	0.0004	0.0015
26	0.8	0.8mm_N_S	Normal	Speed	192	4039459	0.0003	0.0014
27	0.8	0.8mm_H_R	High	Range	764	4039708	0.0004	0.0011
28	0.8	0.8mm_H_S	High	Speed	764	3949006	0.0004	0.0013

Table 4-6 Technical specifications for Scanstation P40 (Leica Geosystems, 2016a).

System Accuracy		Power	
Accuracy of single measurement *		Power supply	24 V DC, 100 - 240 V AC
Range accuracy	1.2 mm + 10 ppm over full range	Battery type	2× Internal: Li-Ion; External: Li-Ion (connect via external port, simultaneous use, hot swappable)
Angular accuracy	8" horizontal; 8" vertical	Duration	Internal > 5.5 h (2 batteries) External > 7.5 h (room temp.)
3D position accuracy	3 mm at 50 m; 6 mm at 100 m		
Target acquisition **	2 mm standard deviation at 50 m	Environmental	
Dual-axis compensator	Liquid sensor with real-time onboard compensation, selectable on/off, resolution 1", dynamic range ±5', accuracy 1.5"	Operating temperature	-20°C to +50°C / -4°F to 122°F
		Storage temperature	-40°C to +70°C / -40°F to 158°F
Distance Measurement System		Humidity	95%, non-condensing
Type	Ultra-high speed time-of-flight enhanced by Waveform Digitising (WFD) technology	Dust/Humidity	Solid particle/liquid ingress protection IP54 (IEC 60529)
Wavelength	1550 nm (invisible) / 658 nm (visible)	Physical	
Laser class	1 (in accordance with IEC 60825:2014)	Scanner	
Beam divergence	< 0.23 mrad (FWHM, full angle)	Dimensions (D×W×H)	238 mm × 358 mm × 395 mm / 9.4" × 14.1" × 15.6"
Beam diameter at front window	≤ 3.5 mm (FWHM)	Weight	12.25 kg / 27.0 lbs, nominal (w/o batteries)
Range and reflectivity	Minimum range 0.4 m Maximum range at reflectivity	Battery (internal)	
	120 m 180 m 270 m	Dimensions (D×W×H)	40 mm × 72 mm × 77 mm / 1.6" × 2.8" × 3.0"
	P30 18% - -	Weight	0.4 kg / 0.9 lbs
	P40 8% 18% 34%	Mounting	Upright or inverted
Scan rate	Up to 1'000'000 points per second	Control Options	
Range noise *	0.4 mm rms at 10 m 0.5 mm rms at 50 m	Full colour touchscreen for onboard scan control. Remote control: Leica CS10/CS15 controller or any other remote desktop capable device, including iPad, iPhone and other Smartphones; external simulator.	
Field-of-View		Functionality	
Horizontal	360°	Survey workflows and onboard registration	Quick Orientation, Set Azimuth, Known Backsight, Resection (4 and 6 parameters)
Vertical	270°	Check & Adjust	Field procedure for checking of angular parameters, tilt compensator and range offset
Data storage capacity	256 GB internal solid-state drive (SSD) or external USB device	Onboard target acquisition	Target selection from video or scan
Communications/Data transfer	Gigabit Ethernet, integrated Wireless LAN or USB 2.0 device	Onboard user interface	Switchable from standard to advanced
Onboard display	Touchscreen control with stylus, full colour VGA graphic display (640×480 pixels)	One button scan control	Scanner operation with one button concept
Laser plummet	Laser class 1 (IEC 60825:2014) Centring accuracy: 1.5 mm at 1.5 m Laser dot diameter: 2.5 mm at 1.5 m Selectable ON/OFF	Scan area definition	Scan area selection from video or scan; batch job scanning
Imaging System		Ordering Information	
Internal camera		Contact your local Leica Geosystems representative or an authorised Leica Geosystems dealer.	
Resolution	4 megapixels per each 17°×17° colour image; 700 megapixels for panoramic image	All specifications are subject to change without notice. All accuracy specifications are one sigma unless otherwise noted.	
Pixel size	2.2 µm	* At 78% albedo ** Algorithmic fit to planar HDS 4,5" B&W targets	
Video	Streaming video with zoom; auto-adjusts to ambient lighting	Scanner: Laser class 1 in accordance with IEC 60825:2014 Laser plummet: Laser class 1 in accordance with IEC 60825:2014	
White balancing	Sunny, cloudy, warm light, cold light, custom	iPhone and iPad are trademarks of Apple Inc.	
HDR	Tonemapped / full range	Illustrations, descriptions and technical specifications are not binding. All rights reserved. Printed in Switzerland - Copyright Leica Geosystems AG, Heerbrugg, Switzerland 2015. 832266en - 03.15 - INT	
External camera	Canon EOS 60D and 70D supported		

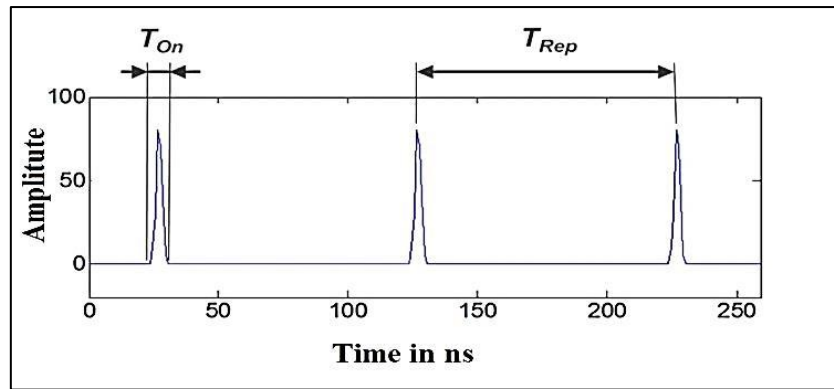


Figure 4-15 Characteristics of the WFD emitted signal, including the pulse width (T_{On}) and repetition rate (T_{Rep}) (Maar and Zogg, 2014).

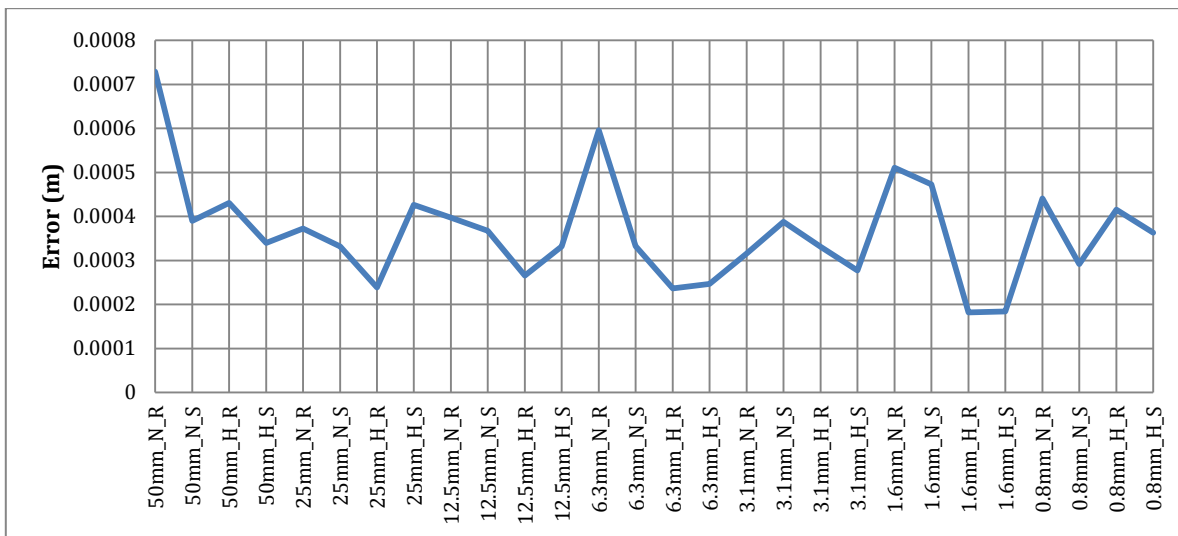


Figure 4-16 The mean errors of Scanstation P40.

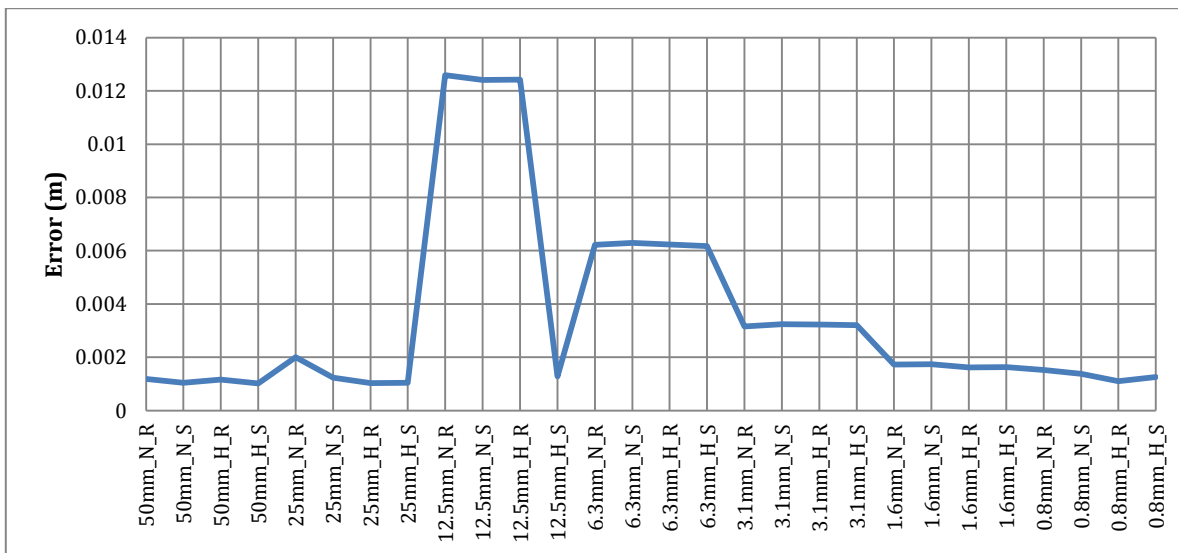


Figure 4-17 The maximum errors of Scanstation P40.

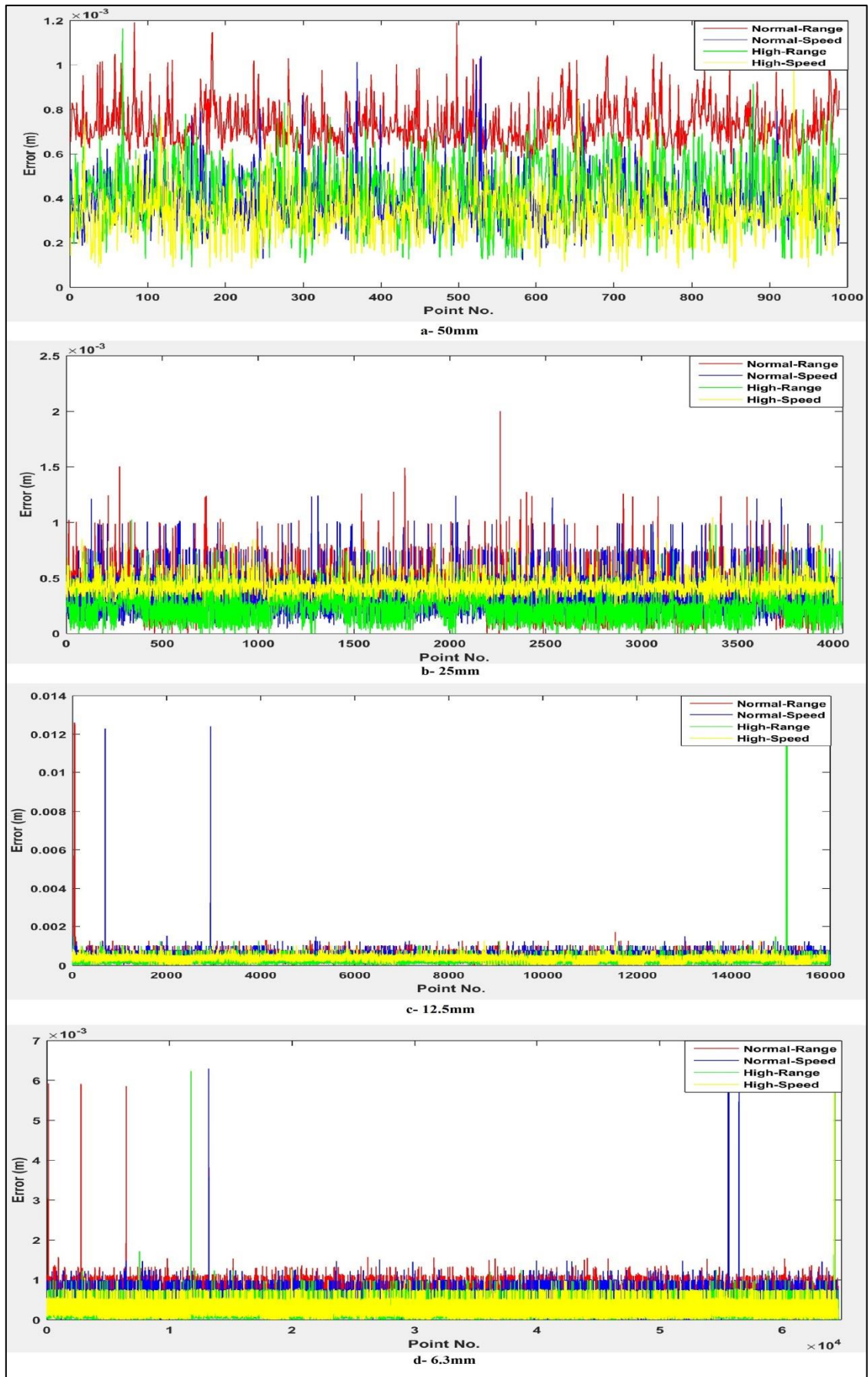


Figure 4-18 Point errors of Scanstation P40 for different resolutions (50 mm, 25 mm, 12.5 mm, and 6.3 mm).

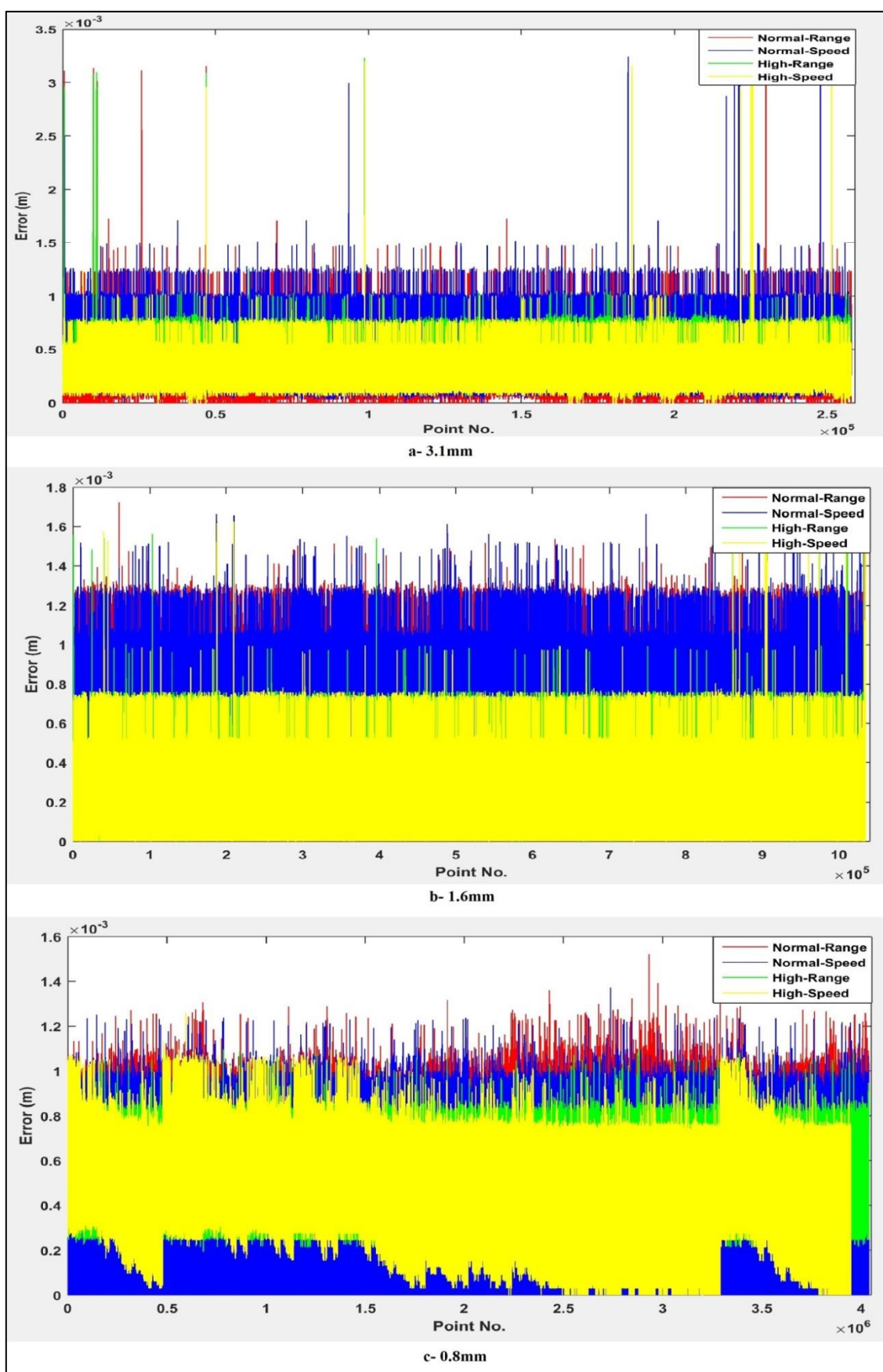


Figure 4-19 Point errors of Scanstation P40 for various resolutions (3.1 mm, 1.6 mm, and 0.8 mm).

Similarly, removing outliers, based on excluding errors that have a value equal or more than three times the standard deviation, was applied (Table 4-7). Evidently, all outliers were cut out, and the resulting maximum error is around 1 mm (Figure 4-20, Figure 4-21, and Figure 4-22).

Table 4-7 Error estimations for different settings for Scanstation P40 after removing outliers.

No	Resolution (mm)	Name	Sensitivity	EDM mode	No. of Points	Remained (%)	Mean Errors (m)	Max. Errors (m)
1	50	50mm_N_R	Normal	Range	978	98.8%	0.0007	0.0010
2	50	50mm_N_S	Normal	Speed	975	98.5%	0.0004	0.0007
3	50	50mm_H_R	High	Range	988	99.8%	0.0004	0.0008
4	50	50mm_H_S	High	Speed	979	98.9%	0.0003	0.0006
5	25	25mm_N_R	Normal	Range	3884	98.1%	0.0004	0.0008
6	25	25mm_N_S	Normal	Speed	3963	98.6%	0.0003	0.0008
7	25	25mm_H_R	High	Range	3999	98.8%	0.0002	0.0006
8	25	25mm_H_S	High	Speed	3991	99.3%	0.0004	0.0007
9	12.5	12.5mm_N_R	Normal	Range	16030	99.8%	0.0004	0.0011
10	12.5	12.5mm_N_S	Normal	Speed	16120	99.8%	0.0004	0.0010
11	12.5	12.5mm_H_R	High	Range	16080	99.9%	0.0003	0.0010
12	12.5	12.5mm_H_S	High	Speed	15840	98.7%	0.0003	0.0008
13	6.3	6.3mm_N_R	Normal	Range	64240	99.5%	0.0006	0.0011
14	6.3	6.3mm_N_S	Normal	Speed	63580	98.5%	0.0003	0.0010
15	6.3	6.3mm_H_R	High	Range	63450	98.3%	0.0002	0.0007
16	6.3	6.3mm_H_S	High	Speed	63650	98.6%	0.0002	0.0006
17	3.1	3.1mm_N_R	Normal	Range	253800	98.4%	0.0003	0.0008
18	3.1	3.1mm_N_S	Normal	Speed	253800	98.5%	0.0004	0.0009
19	3.1	3.1mm_H_R	High	Range	255800	99.2%	0.0003	0.0007
20	3.1	3.1mm_H_S	High	Speed	255700	99.2%	0.0003	0.0006
21	1.6	1.6mm_N_R	Normal	Range	1022000	98.8%	0.0005	0.0009
22	1.6	1.6mm_N_S	Normal	Speed	1018000	98.4%	0.0005	0.0009
23	1.6	1.6mm_H_R	High	Range	1032000	99.7%	0.0002	0.0006
24	1.6	1.6mm_H_S	High	Speed	1032000	99.7%	0.0002	0.0006
25	0.8	0.8mm_N_R	Normal	Range	3984000	98.6%	0.0004	0.0008
26	0.8	0.8mm_N_S	Normal	Speed	4030000	99.8%	0.0003	0.0009
27	0.8	0.8mm_H_R	High	Range	3975000	98.4%	0.0004	0.0006
28	0.8	0.8mm_H_S	High	Speed	3938000	99.7%	0.0004	0.0008

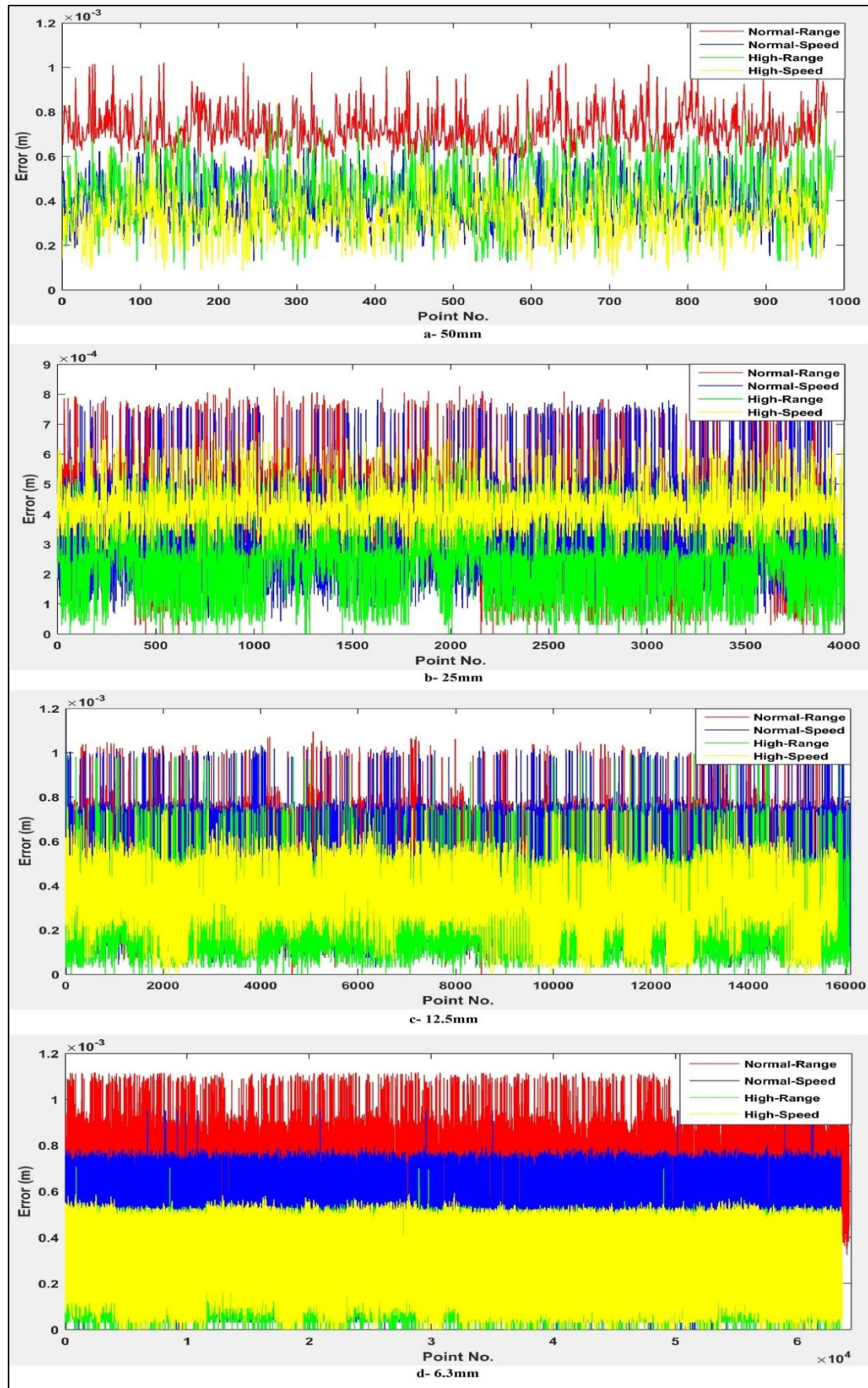


Figure 4-20 Point errors of Scanstation P40 for various resolutions (50 mm, 25 mm, 12.5 mm, and 6.3 mm) after outlier removal.

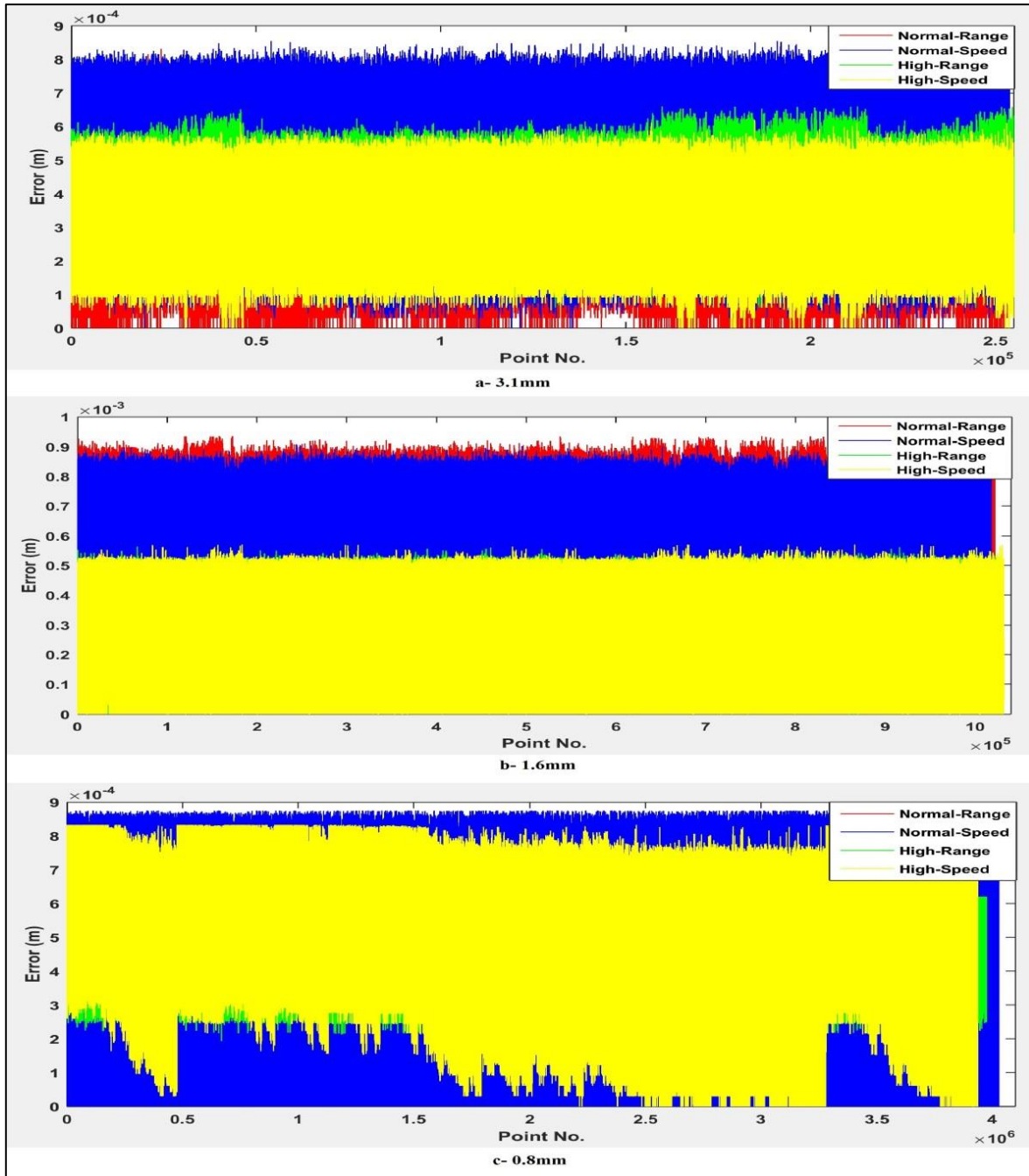


Figure 4-21 Point errors of Scanstation P40 for various resolutions (3.1mm, 1.6mm, and 0.8mm) after outlier removal.

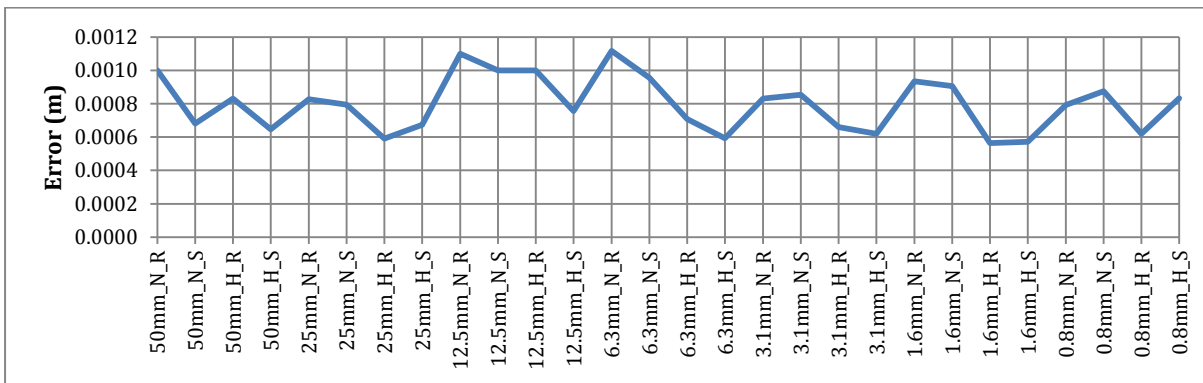


Figure 4-22 The maximum errors of Scanstation P40 after outlier removal.

4.3.3 Comparison between P20 and P40

Although this research is not concerned with a comparison between instruments, it is beneficial to have an idea about how to compare instruments regarding precision. For this purpose, the average of each resolution is estimated. Obviously, P40 reveals better results in both cases of mean error (Figure 4-23) and maximum error (Figure 4-24).

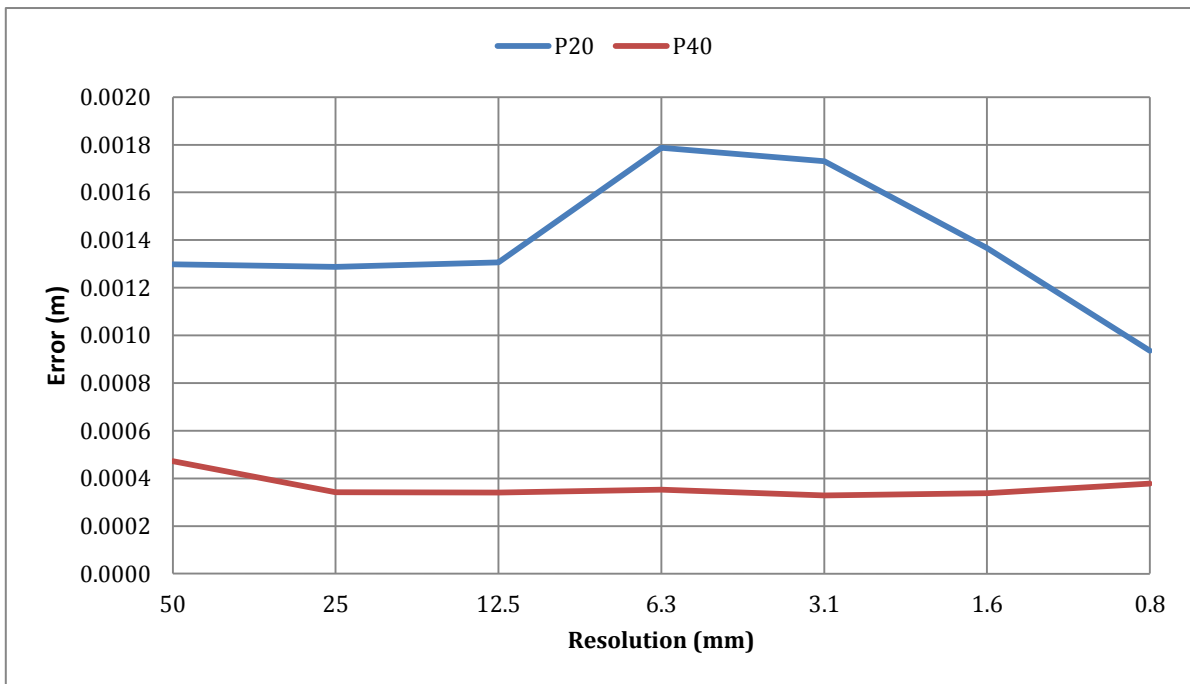


Figure 4-23 The mean Errors for Scanstation P20 and P40.

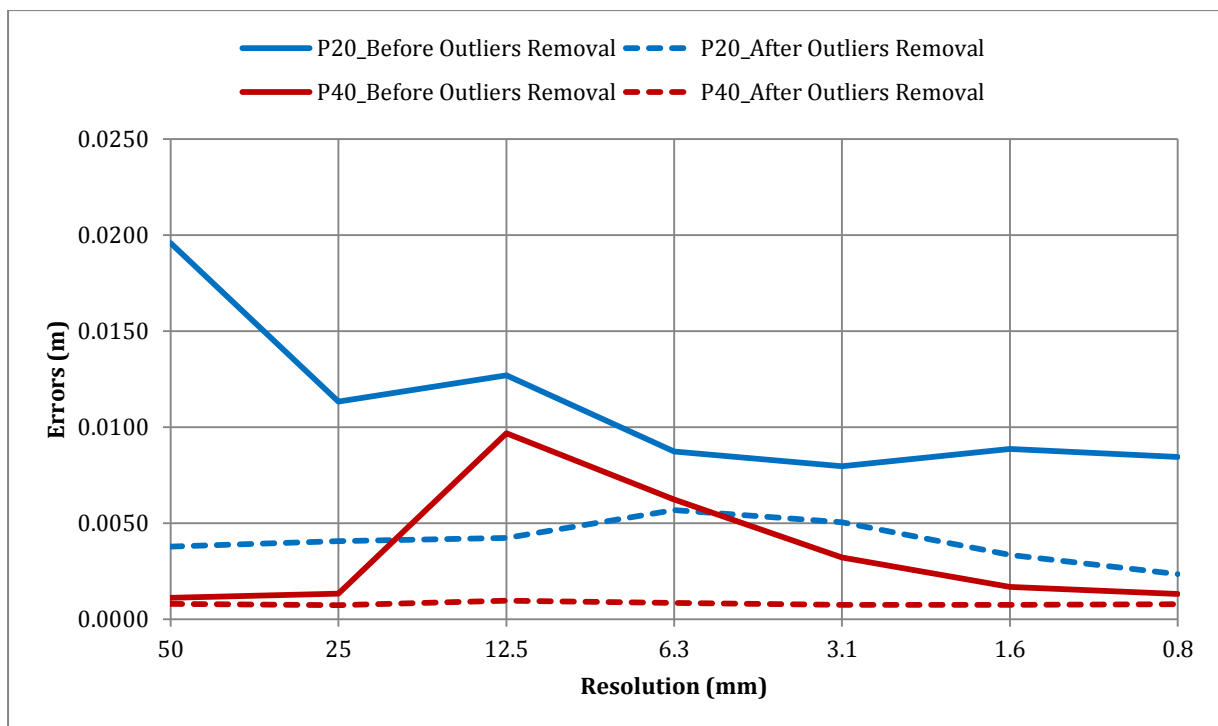


Figure 4-24 The maximum errors for Scanstation P20 and P40.

4.4 Noise Mitigation

As aforementioned, error estimating based on distances between nearest points might introduce outliers due to incorrect convergence. Therefore, it has been advised to compute distances between points in one cloud and the surface model, which is created by a group of nearest points, in the second cloud. For this purpose, distances between points and least-square planes were fitted from a group of nearest points (10 points was suggested), have been computed for all cases for P20 and P20 instruments (Table 4-8 and Table 4-9). As can be seen in Figure 4-25 and Figure 4-26, the maximum errors decreased from 50 mm to 10 mm and from 12 mm to about 1 mm for P20 and P40 respectively. Additionally, there are no obvious outliers (values far from mean) can be observed in Figure 4-27, Figure 4-28, Figure 4-29, and Figure 4-30.

Interestingly, even the mean errors decreased (Figure 4-31 and Figure 4-32), from which we might conclude that this technique can mitigate noise without any reduction in point density. It is possibly the reason why many researchers are interested in the model interpolation method (Sec 3.2.3) for monitoring by TLS.

Table 4-8 Error estimations (based on point to plane distances) for different settings for Scanstation P20.

No.	Name	No. of Points	Mean Errors (m)	Max. Errors (m)
1	50mm_Q1	983	0.0010	0.0042
2	50mm_Q2	984	0.0007	0.0037
3	50mm_Q3	990	0.0006	0.0026
4	25mm_Q1	3905	0.0012	0.0063
5	25mm_Q2	3899	0.0008	0.0059
6	25mm_Q3	3947	0.0007	0.0032
7	25mm_Q4	3934	0.0005	0.0027
8	12.5mm_Q1	15888	0.0012	0.0076
9	12.5mm_Q2	15851	0.0008	0.0054
10	12.5mm_Q3	15855	0.0006	0.0054
11	12.5mm_Q4	15852	0.0006	0.0037
12	6.3mm_Q1	63635	0.0017	0.0106
13	6.3mm_Q2	63675	0.0012	0.0090
14	6.3mm_Q3	63662	0.0009	0.0059
15	6.3mm_Q4	63660	0.0007	0.0054
16	3.1mm_Q1	254256	0.0010	0.0067
17	3.1mm_Q2	254385	0.0014	0.0107
18	3.1mm_Q3	254395	0.0012	0.0079
19	3.1mm_Q4	254397	0.0009	0.0066
20	1.6mm_Q1	1021567	0.0009	0.0081
21	1.6mm_Q2	1022042	0.0010	0.0092
22	1.6mm_Q3	1022041	0.0009	0.0080
23	0.8mm_Q1	4064717	0.0006	0.0073
24	0.8mm_Q2	4084268	0.0007	0.0090

Table 4-9 Error estimations (based on point to plane distances) for different settings for Scanstation P40.

No	Name	No.pf Points	Mean Errors (m)	Max. Errors (m)
1	R50mm_N_R	990	0.0002	0.0009
2	R50mm_N_S	990	0.0002	0.0009
3	R50mm_H_R	990	0.0002	0.0007
4	R50mm_H_S	990	0.0002	0.0008
5	R25mm_N_R	3960	0.0002	0.0011
6	R25mm_N_S	4020	0.0002	0.0010
7	R25mm_H_R	4047	0.0001	0.0008
8	R25mm_H_S	4020	0.0002	0.0008
9	R12_5mm_N_R	16066	0.0002	0.0010
10	R12_5mm_N_S	16158	0.0002	0.0015
11	R12_5mm_H_R	16089	0.0001	0.0010
12	R12_5mm_H_S	16054	0.0002	0.0010
13	R6_3mm_N_R	64582	0.0002	0.0013
14	R6_3mm_N_S	64554	0.0002	0.0011
15	R6_3mm_H_R	64576	0.0001	0.0010
16	R6_3mm_H_S	64542	0.0001	0.0010
17	R3_1mm_N_R	257836	0.0002	0.0012
18	R3_1mm_N_S	257734	0.0002	0.0012
19	R3_1mm_H_R	257777	0.0001	0.0009
20	R3_1mm_H_S	257811	0.0001	0.0010
21	R1_6mm_N_R	1034831	0.0002	0.0013
22	R1_6mm_N_S	1034782	0.0002	0.0013
23	R1_6mm_H_R	1034762	0.0001	0.0008
24	R1_6mm_H_S	1034708	0.0001	0.0008
25	R0_8mm_N_R	4039386	0.0002	0.0014
26	R0_8mm_N_S	4039459	0.0002	0.0013
27	R0_8mm_H_R	4039708	0.0002	0.0010
28	R0_8mm_H_S	3949006	0.0002	0.0011

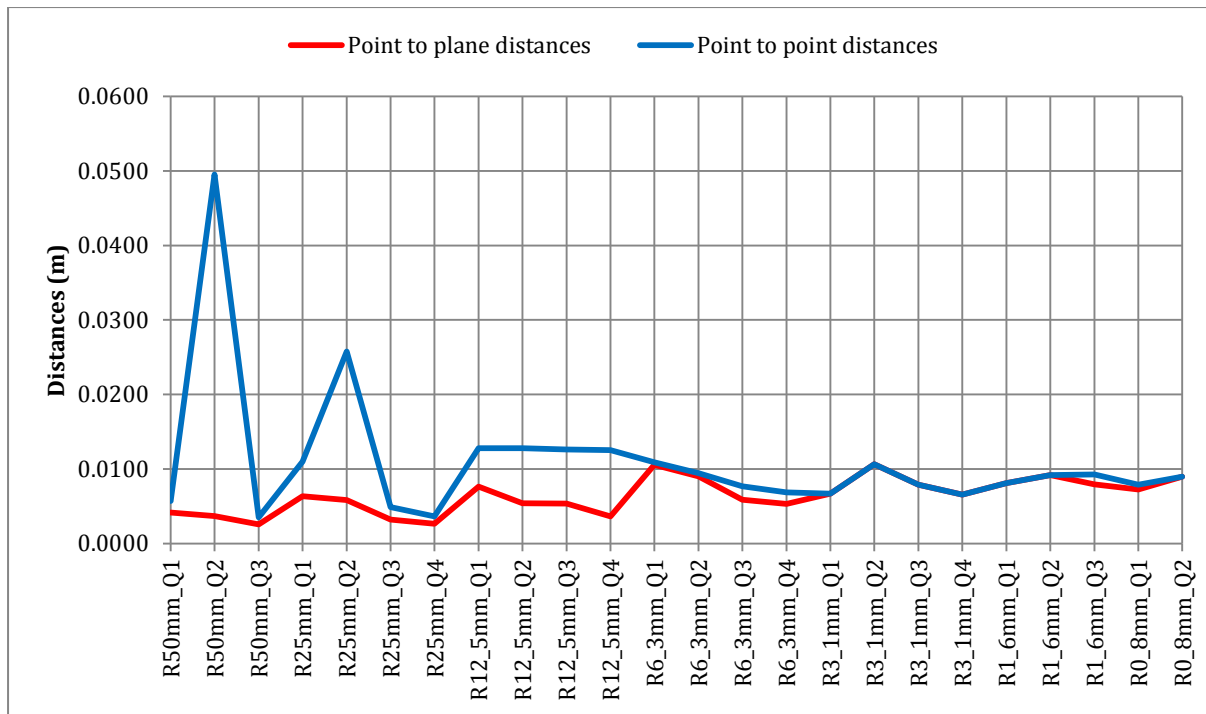


Figure 4-25 The maximum errors estimation (based on points to planes distances) for different settings for Scanstation P20.

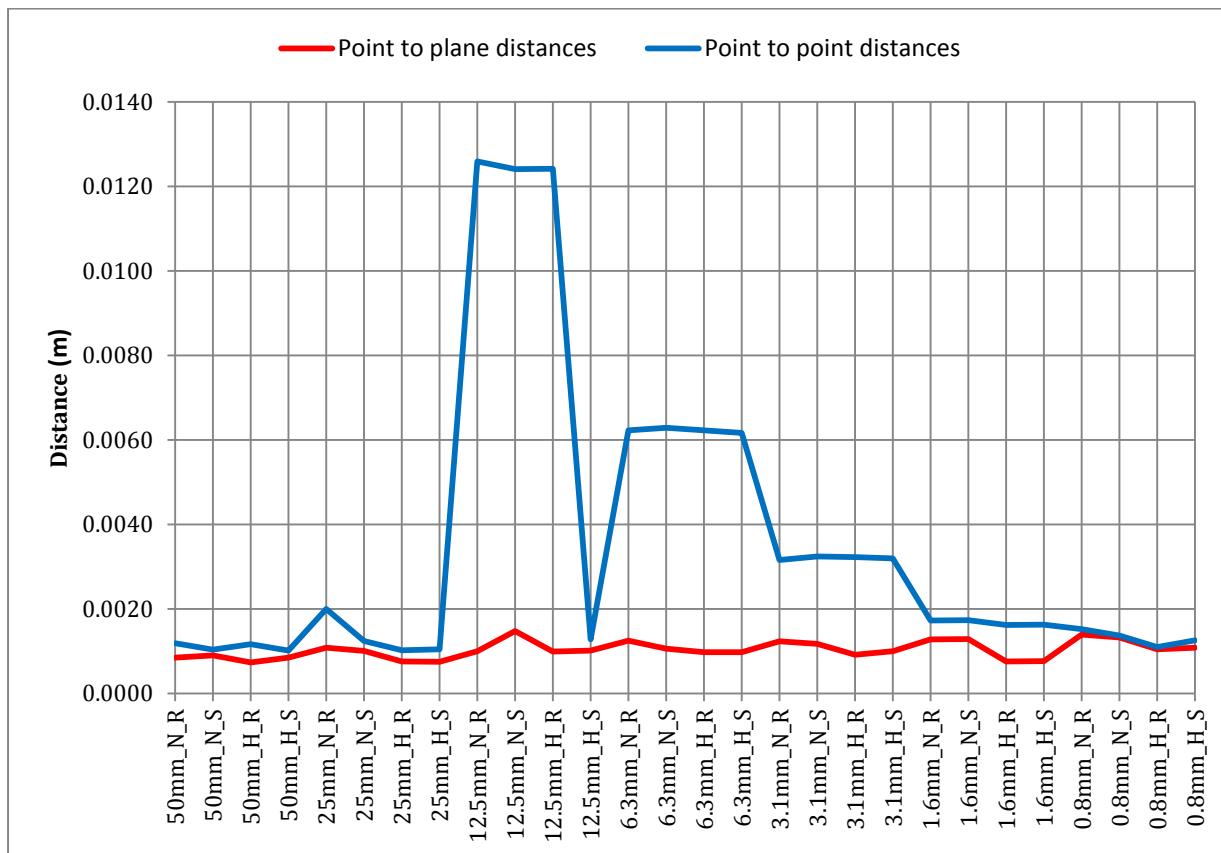


Figure 4-26 The maximum errors estimation (based on points to planes distances) for various settings for Scanstation P40.

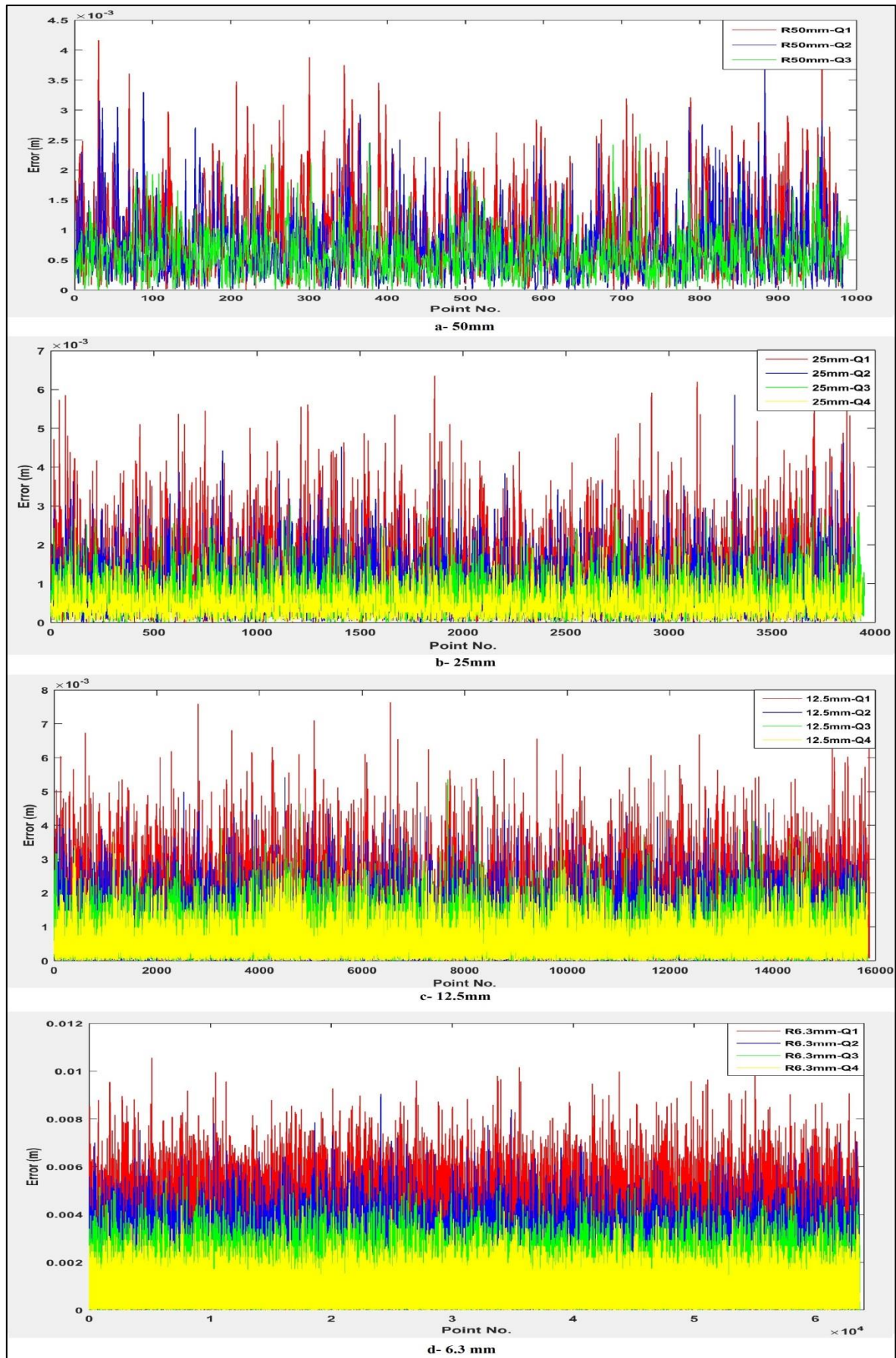


Figure 4-27 Point errors of Scanstation P20 for various resolutions (50 mm, 25 mm, 12.5 mm, and 6.3 mm) based on point to plane distances.

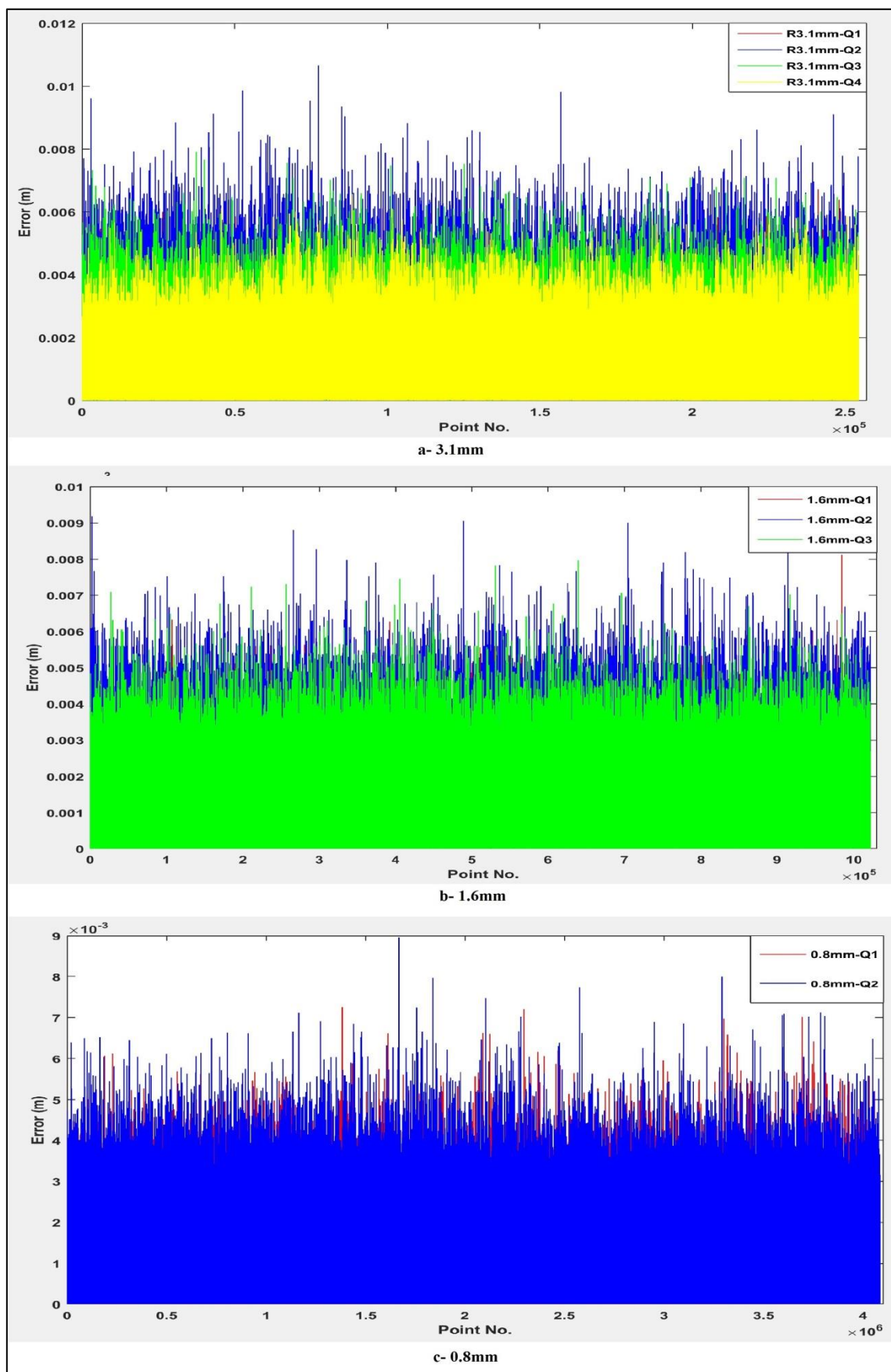


Figure 4-28 Point errors of Scanstation P20 for different resolutions (3.1 mm, 1.6 mm, and 0.8 mm) based on point to plane distances.

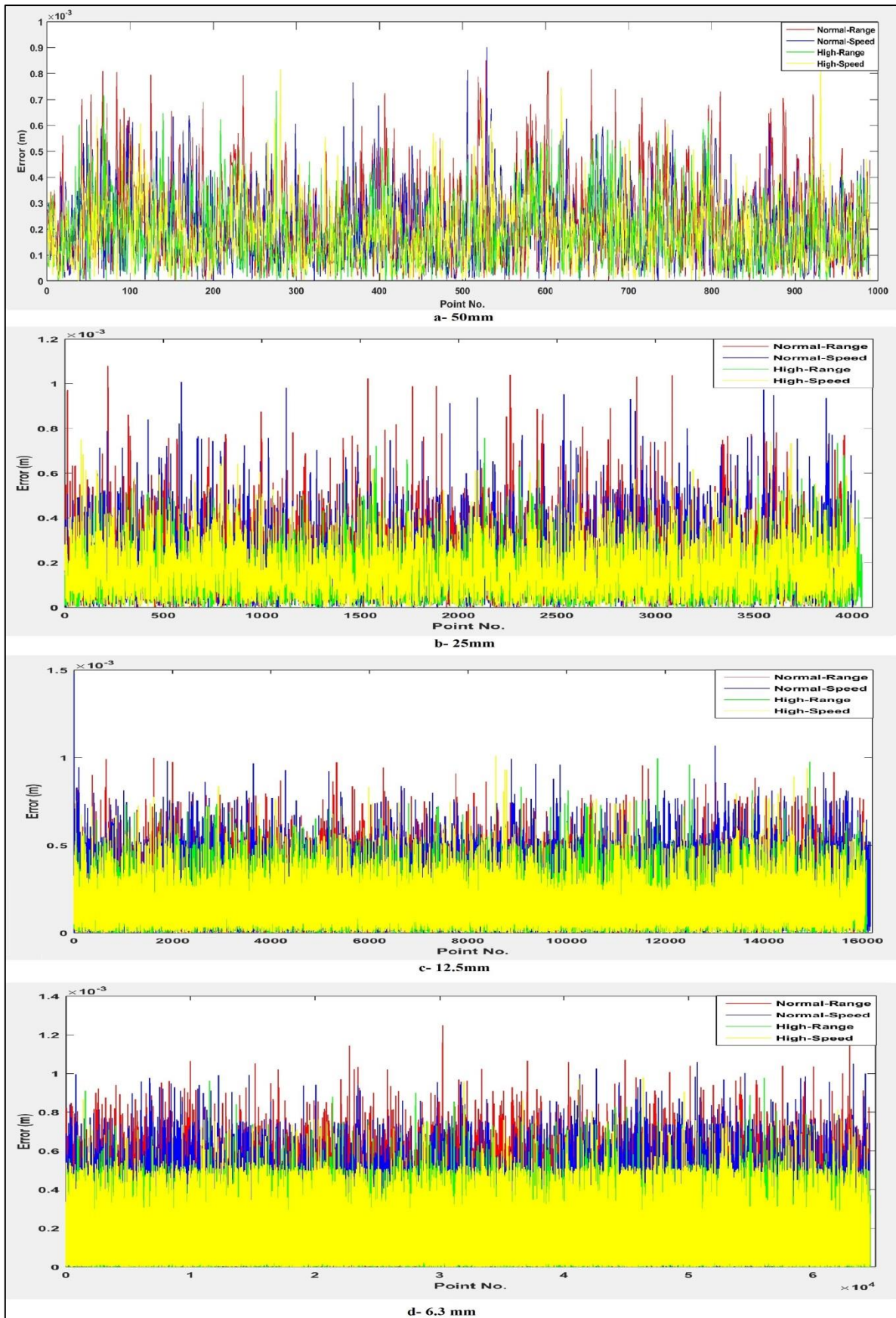


Figure 4-29 Point errors of Scanstation P40 for various resolutions (50 mm, 25 mm, 12.5 mm, and 6.3 mm) based on point to plane distances.

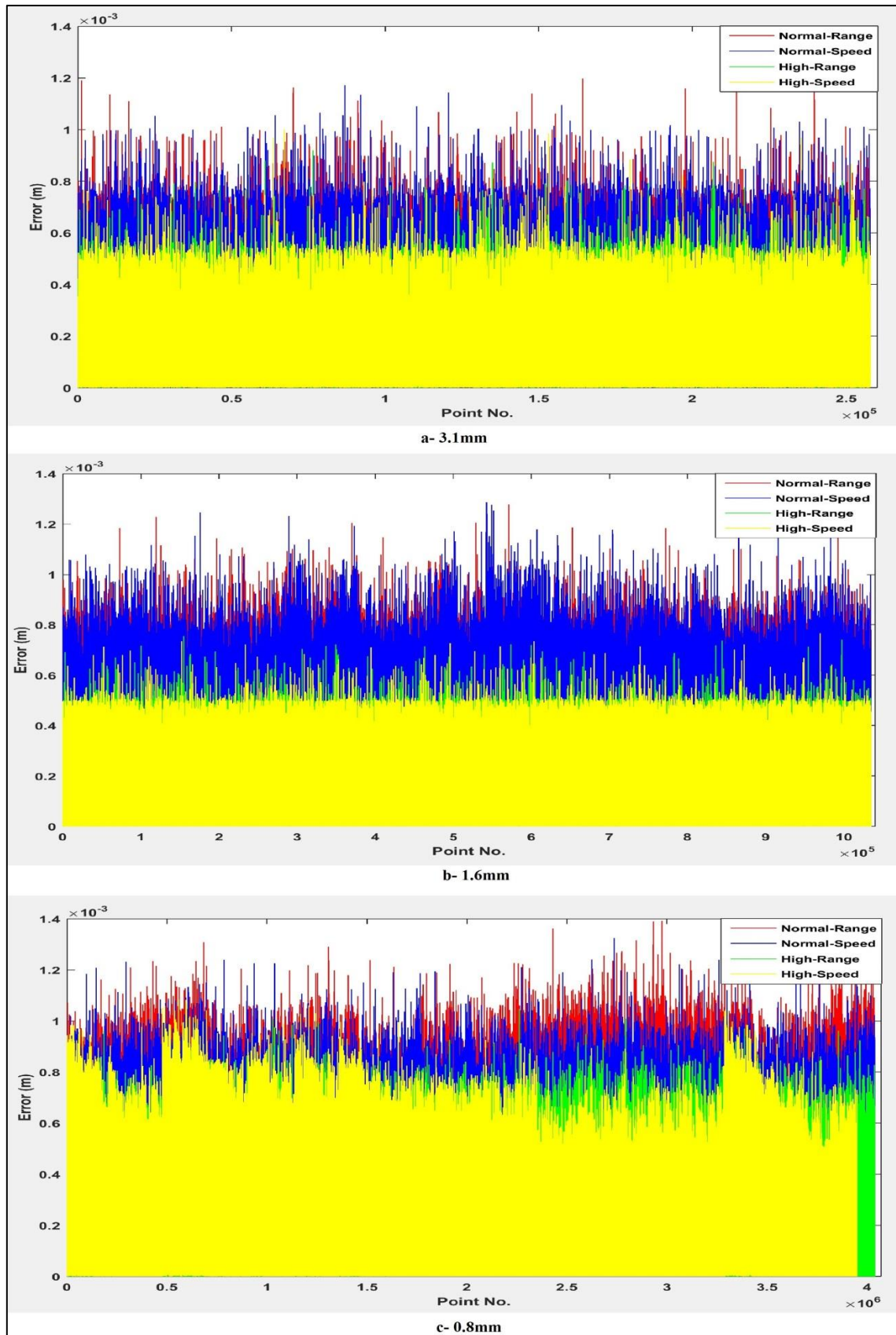


Figure 4-30 Point errors of Scanstation P40 for different resolutions (3.1 mm, 1.6 mm, and 0.8 mm) based on point to plane distances.

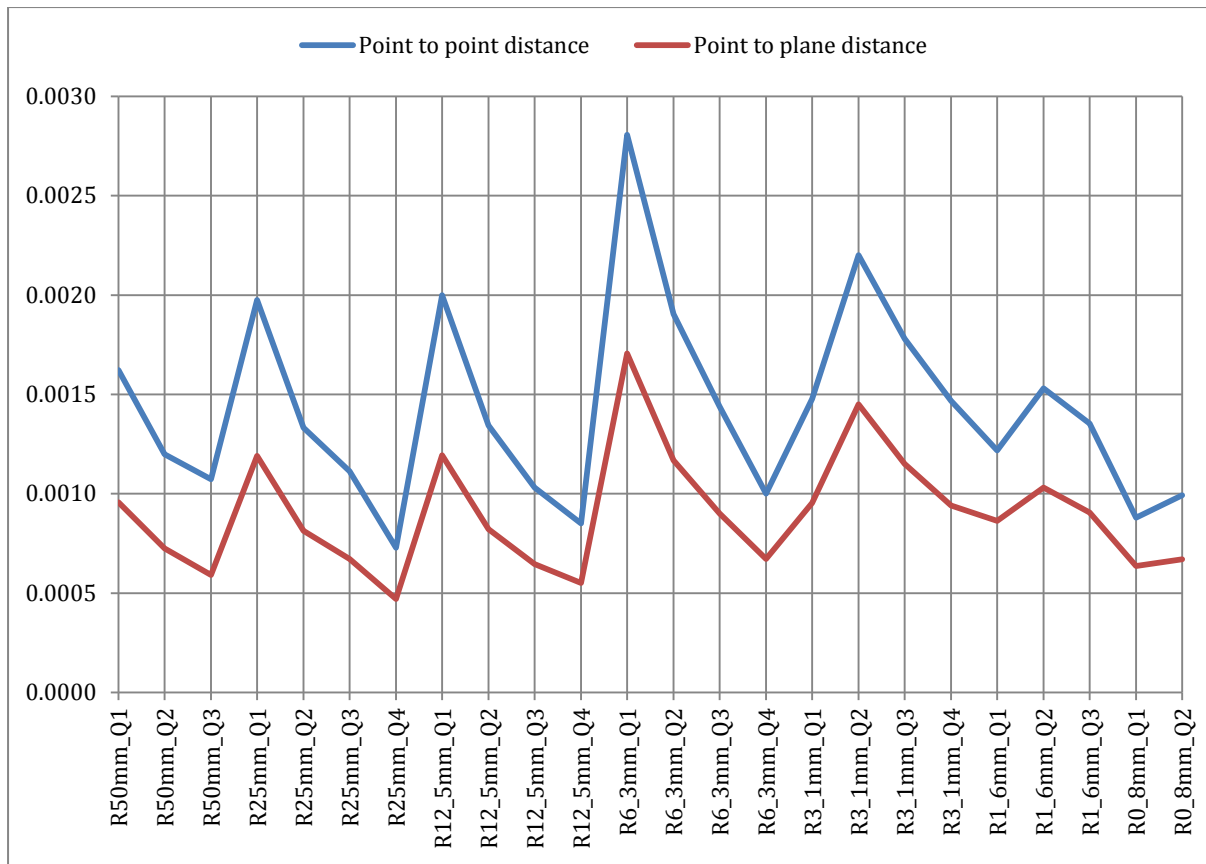


Figure 4-31 The mean errors estimation (based on points to planes distances) for different settings for Scanstation P20.

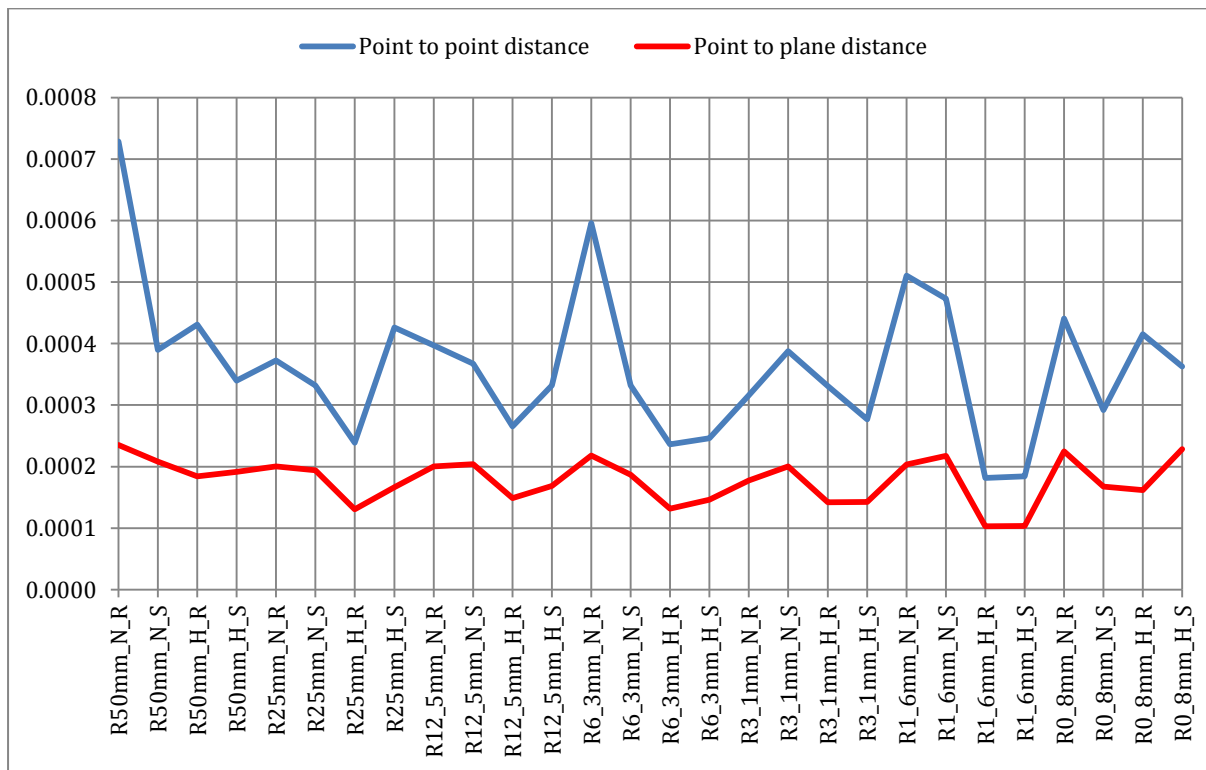


Figure 4-32 The mean errors estimation (based on points to planes distances) for various settings for Scanstation P40.

4.5 Chapter Conclusion

The objective of this chapter is to review the TLS error sources and to assess types and magnitudes of these errors. Furthermore, another objective is to introduce some procedures for eliminating laser scanner outliers and reducing noise. The conclusions of this chapter can be summarised as follows:

- There are several suggestions to deal with TLS errors that can be summarised in Table 4-10 with the assumption that the instruments are calibrated.
- The error quantification tests reveal the average noise level (mean errors) between two scans can be improved by using surface model rather than direct point to point differencing, hence, it decreased from 2.8 mm to 1.7 mm and from 0.7 mm to 0.2 mm for P20 and P40 respectively.
- The surface model technique can remove outliers without reducing point density. Hence, the maximum errors decreased from 50 mm (due to outliers) to 11 mm and from 13mm (due to outliers) to 1 mm for P20 and P40 respectively.

Table 4-10 Summary for TLS errors with suggested dealings for monitoring surveying.

No.	Source	Error	Type	Suggested dealing
1	Instrumental	beam divergence	random	Using instrument with small beam divergence - set up instrument as near to objects as possible
		mixed edge	gross	Using instrument with a small footprint - Using instrument with a shorter pulse length - Removing by manual editing - outliers' removal based on median filter
		range uncertainty	random	Set up instrument as near to objects as possible - Repeat scanning
		angular uncertainty	random	Using instrument with higher angular precision - Repeat scanning
		axes errors	random	Using instrument axis compensator - Multiple scans with different faces (for some brand of scanner)
2	Object-related	speckle noise	gross	Avoid mirror objects - Avoid scanning with high incidence angle - Using instrument with shorter wavelength - Removing by manual editing
		detector saturation	gross	Avoid high reflective objects - Using instrument with shorter wavelength - Removing by manual editing
		penetrative beam	systematic	Theoretically, this will not affect the result for monitoring purpose if the same instrument is used for all epochs.
3	Environmental	temperature	systematic	Avoid to scan hot objects - Avoid increasing scanner temperature (from external sources such as the sun or long working hours)
		atmosphere	systematic	Configure instrument for correct ambient temperature, atmospheric pressure, and humidity
		interfering radiation	gross	Using instruments with optical interference filters - Removing by manual editing
		dynamic objects	gross	Mount instrument on a stable platform - Preventing any motion obstacles during monitoring survey (e.g. scanning overnight) - Removing by manual editing
4	Methodological	resolution	random	Using sampling interval equal to 86% of footprint
		registration	random	Using the target based registration - Direct georeferencing if accurate control points exist
		incidence angle	Systematic	Threshold of a maximum incidence angle of 65° - Set up instrument in suitable location

CHAPTER Five: USING PROCRUSTES TECHNIQUE FOR STRUCTURAL HEALTH MONITORING

5.1 Introduction

According to Greek mythology, the origin of the name “Procrustes” refers to a bandit from Attica in Greece, who made his victims fit his magic bed (as he claimed) either by stretching their limbs or cutting them off (Awange and Grafarend, 2005). In statistics, the Procrustes analysis is a mathematical tool which is used to estimate matching between data sets up to their maximal agreement by least-squares fitting. One of the most significant advantages is that it is a linear least-squares solution for estimating the similarity transformation parameters. Therefore, it does not require initial approximations for the unknown parameters (Gruen and Akca, 2003).

In general, there are different revisions of the Procrustes analysis and each can solve a specific case, such as Orthogonal Procrustes Analysis (OPA), Extended Orthogonal Procrustes Analysis (EOPA), Weighted Extended Orthogonal Procrustes Analysis (WEOPA), and Generalized Procrustes analysis (GPA) (Anwary, 2012).

The Procrustes technique has not been used in monitoring surveying; hence, this research is investigating the ability to employ it to detect and localise deformations using TLS measurements. The proposed method is based on GPA to determine the deformation model, assuming that TLS datasets for various epochs act as matrix configurations. The resulting deformations are interpolated from multiple epochs so they can be more reliable.

The objective of this chapter is to review the Procrustes analysis in the first part, while the second part will be assigned to introduce the proposed method.

5.2 Procrustes Analysis Developments

Firstly, this technique was proposed by Schönemann (1966), a scientist in Quantitative Psychology, who named it as Orthogonal Procrustes Analysis (OPA). In this technique, he used direct least-squares solution for fitting a given matrix (A) to another given matrix (B) under choice of an unknown orthogonal rotation matrix (T), through minimizing the sum of squares of the residual matrix ($E = AT - B$) (Crosilla and Beinat, 2002, Crosilla, 2003, Gruen and Akca, 2003, Toldo et al., 2010).

The first revision for the OPA technique was introduced by Schönemann and Carroll (1970) when an unknown translation and an unknown central dilation were added to the solution of fitting (A) and (B). The revised technique is known in statistics and psychometry as Extended Orthogonal Procrustes Analysis (EOPA) (Crosilla, 2003, Gruen and Akca, 2003, Guarnieri et al., 2005, Toldo et al., 2010).

A further extension for the EOPA, which allows different weighting of matrix elements, across rows or across columns, which is called Weighted Extended Orthogonal Procrustes Analysis (WEOP) (Crosilla, 2003, Gruen and Akca, 2003, Guarnieri et al., 2005, Toldo et al., 2010).

Furthermore, the classical Procrustes analysis was generalised by Gower (1975) and Ten Berge (1977) to deal with the problem of matching more than two matrices; it is well-known Generalised Procrustes Analysis (GPA). Instead of considering the best fitting of all possible pair's matrices, the GPA works in such way that multiple matrices are subjected simultaneously to similarity transformation until a proper match is reached (Bennani Dosse et al., 2011, Crosilla, 2003).

Recently, Awange et al. (2008) have proposed an extension of the conventional 7-parameter Procrustean algorithm named ABC (Awange, Bae and Claessens)-Procrustes algorithm. The ABC-Procrustes gives solution for the 3D affine transformation with anisotropic scale. It is proved to be successful only in cases of very mild anisotropy in scaling (Paláncz et al., 2010). Consequently, Paláncz et al. (2010) extended the ABC-Procrustes algorithm for strong anisotropy in scaling, to give a more generally valid solution of the problem, and named it PZ- Procrustes algorithm.

5.3 Procrustes Applications

This technique has been used in different fields. For instance, it has been used in medicine for gene recognition analysis. Additionally, it is used to identify of Malaria parasites by comparing the electrophoretic gel images (Awange and Grafarend, 2005). Furthermore, Anwary (2012) applied the Procrustes analysis to distinguish deformed backs from normal backs. Recently, there are some researchers have investigated the applicability of the Procrustes analysis in the same field (Ikeda et al., 2016, Meaike et al., 2016).

Another example, the Procrustes analysis was popularised for the analysis of sensory profiling data, when different assessors judge properties of different products. It is impossible to average the assessor data

directly because it makes no sense to combine different properties. Hence, the Procrustes analysis was used (Bennani Dosse et al., 2011, Lorenzo et al., 2016, Mauricio et al., 2016, Tomic et al., 2015).

In Chemistry (i.e. Chemometrics), Wentzell et al. (2015) have used Procrustes analysis as a diagnostic tool to assess the results of projection pursuit in case of variable compression or regularisation. Hence, it has been used to evaluate the similarity of projections generated under different conditions.

In Human Genetics, Wang et al. (2015) have applied Procrustes analysis to estimate individual ancestry in a principal component ancestry map created by a reference set of individuals.

In Geology, Vermeesch and Garzanti (2015) have used GPA to draw out geological insights from 'Big Data' in a provenance context. Hence, it has been applied to extract a 'consensus view' from five different 'configuration' for all the data which is considered together.

In Zoology, Druml et al. (2015) have applied GPA to analyse variation of horse shapes for the purpose of validation of equine conformation scoring.

Finally, it has been employed in the virtual trial assembly to verify the correspondence between two data sets (design and as-built), both extracted from the Building Information Modelling (BIM) structure, which allowed finding out the optimal analytical least squares assembling of the various built elements. In this case, the GPA techniques was applied to verify the correspondences between the data sets due to more than two point configurations relative to the various structure elements are available, (Case et al., 2014).

5.4 Procrustes Application in Geomatics

In Geomatics, in many cases, it requires coordinate system transformation which involves scaling, rotation and translation operations of different matrix configurations. For instance, in photogrammetry, it is necessary to determine the orientation of the camera during the aerial photogrammetry and transform photo coordinates into the ground coordinates. This process can be done by the reference system transformation. Similarly, this technique is applicable to the remote sensing and the Geographical Information System (GIS) where maps have to be transformed to different reference systems (Awange and Grafarend, 2005).

Seemingly, the Procrustes technique can be a promising method in Geomatics applications when coordinates systems often need to be solved. Compared to classical least squares, the Procrustes analysis takes advantage of the fitting properties of two matrices without any approximate value of the unknown parameters and with less computational time (Awange and Grafarend, 2005, Crosilla, 2003).

The traditional system transformation approach requires linearising the nonlinear equations and then applying the least squares method iteratively. On the other hand, the Procrustes method can give a direct solution, without linearization, if inserting coordinates of one system in one matrix and the second system in another matrix (Awange and Grafarend, 2005).

The first effort of using the Procrustes technique in Geomatics can be attributed to the research of F. Crosilla (1983a), Crosilla (1983b) (Awange, 2003, Awange and Grafarend, 2005). After that, Beinat and Crosilla (2001) implemented the simultaneous global registration of 3D range images by the Procrustes technique. Then, they proposed a generalisation for the analytical model to solve the problem of the global registration of low-resolution aerial laser scan images. In addition, they formulate an anisotropic method to estimate the global registration in a more accurate and flexible way through assigning different weighting factors to the tie points coordinates (Beinat and Crosilla, 2002).

According to Crosilla and Beinat (2002), the GPA is proved to be an invaluable technique to co-register datasets, i.e. block adjustment, of different coordinate systems. Particularly, it is proper for laser scanning and photogrammetric applications, when additional attributes associated with the tie points, such as intensity, can be employed in conjunction with the corresponding coordinate values.

Awange (2003) examined the applicability of the partial Procrustes procedure in providing a direct solution to the three-dimensional orientation problems. The author proved that it is adequate to solve such problem and to determine the three-dimensional orientation parameters leading to the determination of the deflection of the vertical component.

Gonzalez-Aguilera et al. (2008) developed a modification to the WEOP technique to overcome its limitation to detect and localise gross errors and then they used it in the georeferencing terrestrial laser scanner for the purpose of dam deformations.

Toldo et al. (2010) have proposed a new technique, ICP-GPA, for registering multi-scenes point clouds through integrating of ICP (Sec.3.3.3.1) and the GPA. Through experiments, authors proved the effectiveness of this technique compared with the classical sequential ICP method regarding the accuracy and the convergence.

Garro et al. (2012) formulated the problem of estimating the position and orientation of a perspective camera in terms of an instance of the anisotropic orthogonal Procrustes problem and derive its solution. Through experiments with synthetic and real data they reached the best trade-off between speed and accuracy. Recently, they have used the same approach to solve the classical photogrammetric bundle block adjustment (Fusiello and Crosilla, 2015).

Finally, Zou et al. (2016) have proposed a robust indoor positioning system through standardising Wi-Fi fingerprints based on Procrustes Analysis.

Despite the fact of the ability of the GPA to solve many problems and widely applicable in Geomatics, care should be taken when using it. The most important drawback of the Procrustes technique is a lack of reliability criterion to detect and localise the outliers, which might be included in measurements. Consequently, the results that produced by the Procrustes technique may be wrong in the case of the existence of outliers in the data set. Therefore, filtering of outliers is vital for using this technique properly (Crosilla, 2003, Gruen and Akca, 2003, Guarnieri et al., 2005).

5.5 GPA Mathematical Model

For the purpose of monitoring, a matrix is formed for each epoch, and each row of this matrix contains three-dimensional coordinates of one point of the point cloud. To determine deformation, GPA is used to find the best fit for these matrices (epochs). The result of the GPA solution leads to six parameters (three rotations and three translations, the scale factor is considered unified) of deformation.

Let us consider m data epochs of the same object, produced by TLS. Let us consider that each epoch has P landmarks, representing the shape of that object. Therefore, we can form m matrices $A_1, A_2 \dots A_m$ of size $P \times 3$ as follows:

$$A_1 = \begin{bmatrix} X_{11} & Y_{11} & Z_{11} \\ X_{21} & Y_{21} & Z_{21} \\ \dots & \dots & \dots \\ X_{p1} & Y_{p1} & Z_{p1} \end{bmatrix}, A_2 = \begin{bmatrix} X_{12} & Y_{12} & Z_{12} \\ X_{22} & Y_{22} & Z_{22} \\ \dots & \dots & \dots \\ X_{p2} & Y_{p2} & Z_{p2} \end{bmatrix} \dots \dots A_m = \begin{bmatrix} X_{1m} & Y_{1m} & Z_{1m} \\ X_{2m} & Y_{2m} & Z_{2m} \\ \dots & \dots & \dots \\ X_{pm} & Y_{pm} & Z_{pm} \end{bmatrix} \quad (5.1)$$

According to the GPA concept, each matrix A_i can be estimated by a similarity transformation applied to a matrix that contains the true coordinates of the P points called here Z (consensus), to which a random error matrix (E_i) is added (Crosilla and Beinat, 2002, Goodall, 1991).

$$Z + E_i = \hat{A}_i = SA_i R_i + J_3 t_i^T \quad (5.2)$$

Where:

$R_i=3 \times 3$ rotation matrix.

$t_i=3 \times 1$ translation vector.

$S=$ the scale factor.

$J_3=3 \times 1$ unit vector.

The least squares estimation of the unknown transformation parameters (R_i , t_i , and S) can be computed as follows (Crosilla and Beinat, 2002):

$$\sum_{i=1}^m \sum_{j=i+1}^m \|\hat{A}_i - \hat{A}_j\|^2 = \min \quad (5.3)$$

Let us consider C as the geometrical centroid of the transformation matrices.

$$C = \frac{1}{m} \sum_{i=1}^m \hat{A}_i \quad (5.4)$$

Therefore equation (5.3) may be written as (Crosilla and Beinat, 2002):

$$m \sum_{i=1}^m \|\hat{A}_i - C\|^2 = \min \quad (5.5)$$

GPA can be conducted by any method explained by Crosilla and Beinat (2002). In this research, it is solved based on iterative estimation of centroid (C), as follows (ibid):

- 1- Initial approximation of C_0 is computed from matrices data:

$$C_0 = \frac{1}{m} \sum_{i=1}^m A_i \quad (5.6)$$

- 2- Similarity transformation between each matrix of A_i and C_0 , using WEOP technique (Sec. 5.5.2), result the first estimation of \hat{A}_i .
- 3- Update value of C based on \hat{A}_i .
- 4- Repeat steps (2) and (3) until global convergence, which can be examined by:

$$m \sum_{i=1}^m \text{tr}((\hat{A}_i - C)^T (\hat{A}_i - C)) = \min \quad (5.7)$$

5.5.1 GPA Assumptions and Implications

Statistically, with the assumption of data free from systematic and gross errors, each adjusted epoch (\hat{A}_i) should differ from other epochs by only random errors, so the sum of the square differences between any two epochs must equal to minimum (stated in equation (5.3)). In addition, the centroid is the most probable value for repeatable measurements (epochs) (stated in equation (5.4)). It is worth to mention that the centroid here is not a point, but as a matrix of points which is representing a centroid fit to all epochs after similarity transformation, called Z (consensus). According to Crosilla and Beinat (2002), “*the sum of the square distances between the m points is always equal to m times the sum of the square distances between the m points and their centroid*”. Consequently, the equation (5.5) is equivalent to equation (5.3).

In our proposal, in the case of no changes exist, insignificant differences exist between Z and any epoch (\hat{A}_i). On the other hand, in the case of deformation, Z will represent the final fitting for the deformation (after last epoch) and \hat{A}_i is the deformation at each epoch.

Due to the above assumptions, it is worth to mention limitations of this technique to detect fluctuated deformations. In this case, the final results will converge to a false value.

Figure 5-1 demonstrates the concept of GPA and the principle of the proposed method.

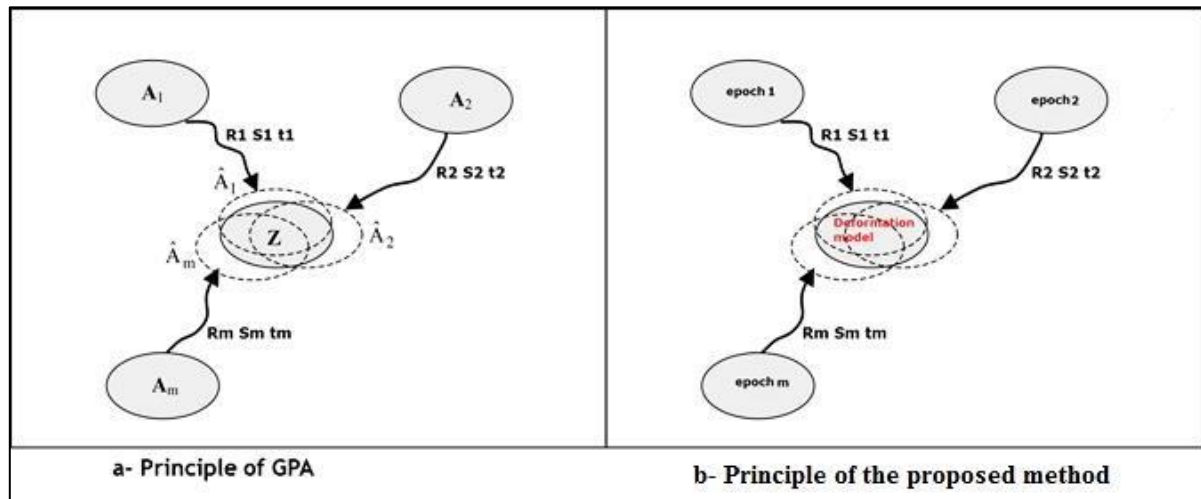


Figure 5-1 GPA concept and the principle of the proposed method (updated from Crosilla and Beinai (2002)).

5.5.2 WEOP Mathematical Model

As aforementioned, the GPA solution is based on the mathematical model of WEOP, which is a similarity transformation of two matrices, and it is optionally weighted by rows and columns.

Let A and B be two matrices containing P points in the domain R^3 , source and target respectively, with dimension $(P \times 3)$. Let $W_p(P \times P)$ and $W_3(3 \times 3)$ be optional weights for rows and columns respectively. WEOP is a technique of obtaining transformation parameters (orthogonal rotation matrix (R), and translation vector (t), i.e. scale factor is considered unity according to section 3.3.1 thus all equations are adapted accordingly), by which A is transformed to best fit B . This can be done through minimising the following equation (Goodall, 1991):

$$tr((AR + jt^T - B)^T W_p (AR + jt^T - B) W_3) = min \quad (5.8)$$

Where: $J = (P \times 1)$ unit vector, and $R^T R = I$ (orthogonal condition). If all columns have the same weight then $W_3 = I_3$.

Using Cholesky decomposition:

$$W_p = Q^T Q \quad (5.9)$$

By applying weight:

$$A_W = Q A \quad (5.10)$$

$$B_W = Q B \quad (5.11)$$

$$j_W = Q j \quad (5.12)$$

Adapting the Singular Value Decomposition of the matrix product:

$$svd \left\{ A_W^T \left(I - \frac{j_W j_W^T}{j_W^T j_W} \right) B_W \right\} = V D_S W^T \quad (5.13)$$

Where V and W are orthonormal eigenvector matrices and D_S is the diagonal eigenvalue matrix, then transformation parameters are obtained (Schönemann and Carroll, 1970):

$$R = V W^T \quad (5.14)$$

$$t = (B_W - A_W R)^T \frac{j_W}{j_W^T j_W} \quad (5.15)$$

It is worth to mention that this method exists in MATLAB software as a built-in function named “*Procrustes*”, but without weights.

5.6 Proposed Methodology

By applying the GPA technique, transformation parameters can be determined, yet it does not achieve the research aim to localise deformation. In addition, it needs to suggest solutions for the lack of GPA to detect outliers. Therefore, a methodology has been devised for the proposed technique, which contains the following main steps:

- 1) Registration of point clouds.
- 2) Outlier removal.
- 3) Voxel approach.
- 4) Noise mitigation.
- 5) Determination of the deformation vectors.
- 6) Localisation of the deformations.

Following is a detailed discussion of each step:

5.6.1 Registration of Point Clouds

To make the comparison, all epochs should be related to one reference system which can be local or national. In addition, the quality of data is the most important issue in the monitoring procedure. Therefore, targets-based registration (Sec.3.3.1) is suggested in the proposed technique. Hence, four stable locations are nominated for TLS targets in such a way that they are geometrically well distributed. These can be within monitored building or in surrounding areas. Furthermore, they need to be observed periodically to verify their stability. The best way to monitor these points is by establishing a control network with farther and more stable points which have been used as a reference for targets points. In this case, indirect georeferencing is applied, instead of registration, to relate epochs to the same reference system.

On the other hand, different targets type and shape can be used for this purpose (Figure 5-2). Spherical targets can offer best spatial representation because it is 3D shape, and it can be scanned from different positions. However, black & white can act as total station targets as well; hence data fusion can be done directly.

In this research, spherical targets are suggested for registration (i.e. tie points), while black/white targets are suggested for georeferencing (i.e. control points act as targets for TLS and TS).

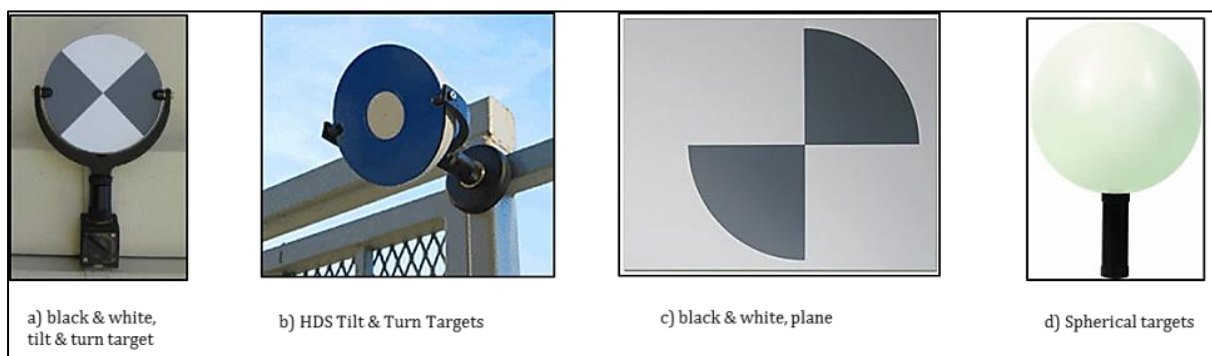


Figure 5-2 TLS targets (Leica Geosystems, 2016b)

5.6.2 Outlier Removal

As has been mentioned, GPA does not have a reliability criterion to detect and localise the outliers, which might be included in measurements. Consequently, it might tend to give wrong outputs, if outliers exist in the data set. Therefore, the proposed technique should have the ability to filter out outliers before applying GPA. For this purpose, using statistical approach has been proposed. The proposed method in this research is based on removing points which are sparse relative to their mean. Hence, for each point,

mean of distances is computed to k Nearest Neighbours (KNN). All points whose mean distances are bigger than n times of global standard deviation will then be considered as outliers and filtered out from point clouds, according to the assumption of Gaussian distribution (Rusu, 2011).

Two variables need to be chosen in this technique, the number of neighbour points used to compute mean distances (k), and the standard deviation multiplier (n). These variables are fixed in the practical test.

This technique of outlier removal can be computed by the open source software CloudCompare (Girardeau-Montaut et al., 2006) which is stated as a plugin from the original source Point Cloud Library (PCL) (Rusu, 2011).

5.6.3 Voxel Approach

If GPA technique is applied for whole point clouds, it may lead to false results even if there are deformations in just a few points. Furthermore, it cannot localise deformations. Instead, it gives deformation vectors for whole objects. Therefore, the proposed technique divides the data into subsets, and then the GPA is applied for each of them.

Inspired by Akca et al. (2005), the point cloud is reformed to boxes structure. In this method, the point cloud is divided spatially where each set of points is separated if they are located in the same box (Figure 5-3).

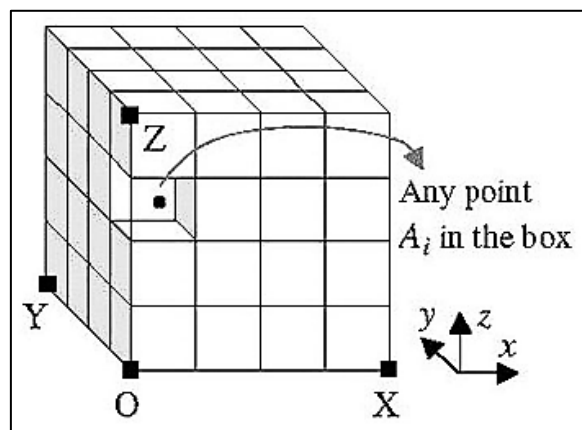


Figure 5-3 Box structure (Akca et al., 2005).

Hence, in the proposed technique, the boxes are monitored over different epochs, instead of a single point of the point clouds. The assumption behind this suggestion is that it is frequently each a group of points has the same deformation behaviour due to tiny distances between these points (only a few millimetres based on sampling interval).

Consequently, concerned buildings are divided into boxes and each of them contains a group of points which are examined each epoch (Figure 5-4). These groups are formed as matrices (as in equation (5.1)) which represent inputs for equation (5.5).

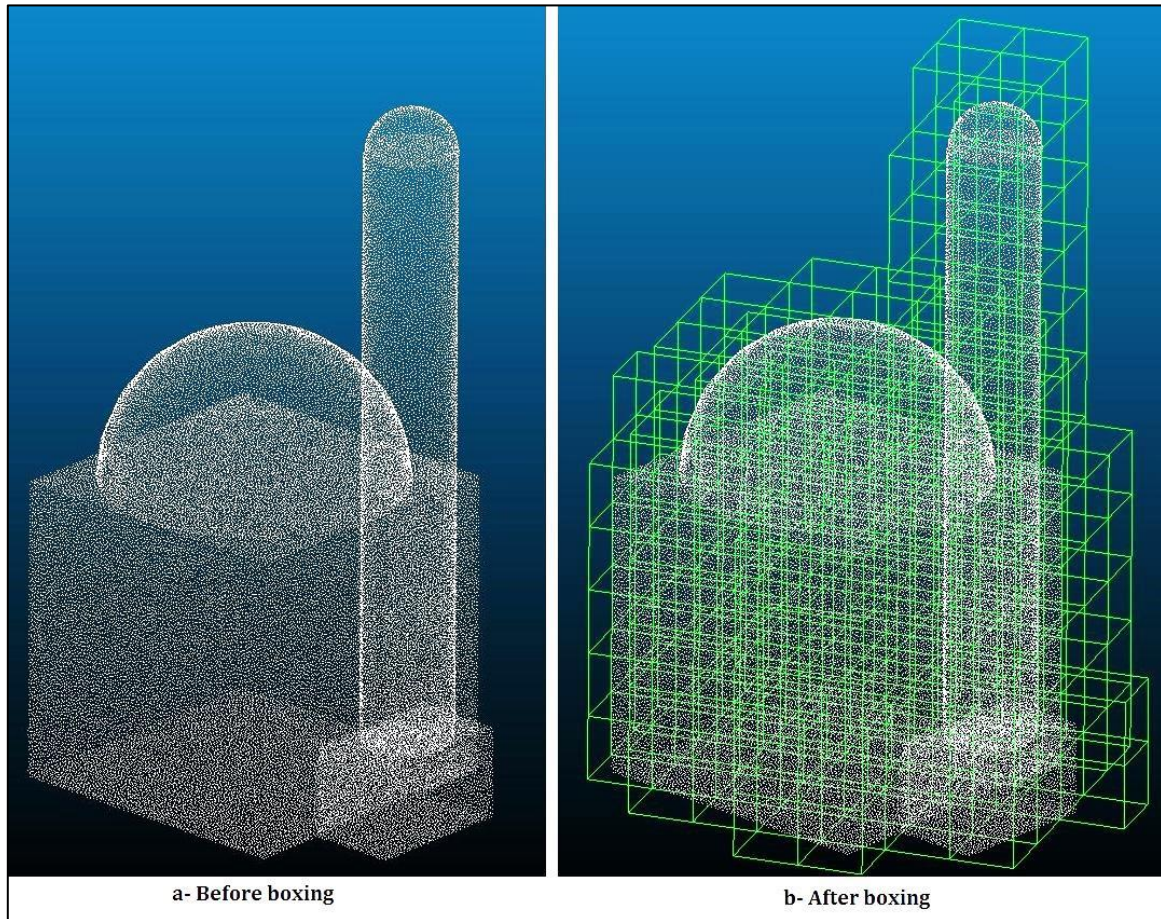


Figure 5-4 The proposed boxing structure.

5.6.3.1 Voxel Advantages and Disadvantages

Ultimately, applying voxel approach can offer the following advantages:

- 1- Cope with unrepeatable measurement of TLS as the boxes are monitored instead of points.
- 2- Data can be easily handling and processing due to dealing with it separately for each box.
- 3- The deformations can be localised by voxel approach.
- 4- Can offer better accuracy as the deformation vectors are estimated based on all points within the box (a large number of redundant).

However, using this approach might introduce some disadvantages:

- 1- Boxes contain few points might appear based on resolution and box size as in Figure 5-5 (a) which are drawn in red line. Consequently, these boxes may show wrong indication for deformations. The proposed algorithm is prepared with different procedures to solve this problem. For instance, change box size, change origin, or rotating the concerned building as shown in Figure 5-5 (b) where rotation solves such problem. Eventually, if such boxes remain after all procedures, they proposed algorithm is designed to filter them out as will be seen in validation. Fortunately, this issue needs to be solved only one time and all followed epochs can use the same configurations.
- 2- As aforementioned, due to dealing with data as groups, it is difficult to detect displacement of a single point in boxes.
- 3- Missing parts cannot be detected because a null matrix is created in this case and the proposed algorithm is designed to remove such boxes.

It is worth to mention that dimensions of the boxes can play a key role in the proposed method because bigger boxes can estimation deformations better due to a lot number of redundant. However, smaller size boxes can localise deformation more accurately. In this research, three different dimensions (10, 20, and 30 cm) have been tested.

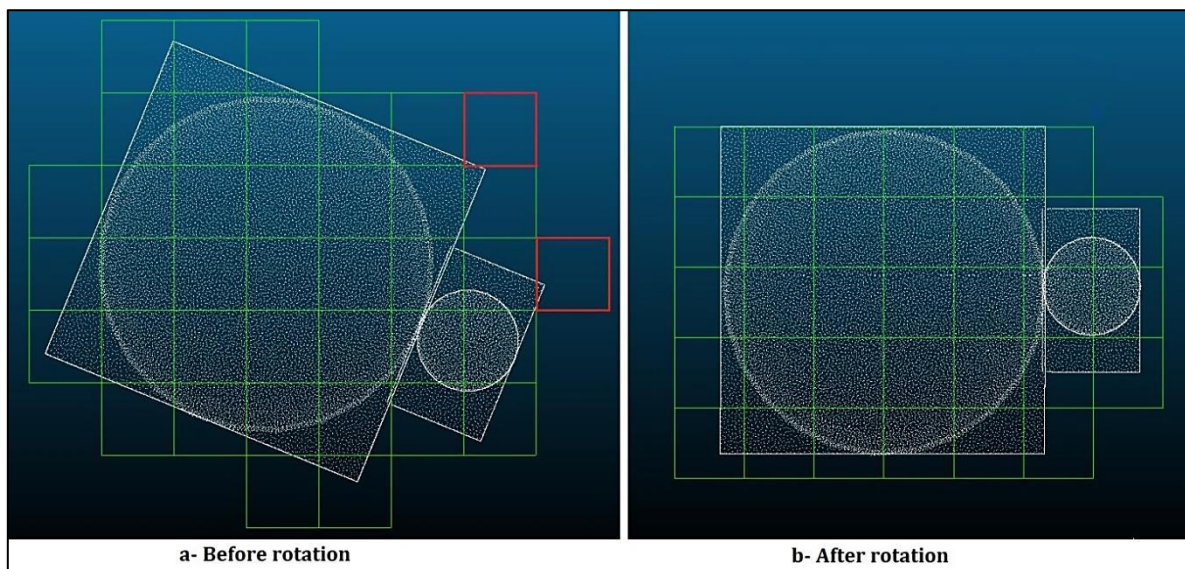


Figure 5-5 Top views for building (shown in Figure 5-4) structured in boxes before and after rotation.

5.6.4 Noise Mitigation

As has been seen in chapter four, point clouds are contaminated with noise. Fortunately, part of this is white noise which is distributed according to the normal distribution. Therefore, it can be mitigated by statistical analysis. In the proposed technique, two methods have been used to reduce noise, namely Voxel filter, and surface interpolation.

Voxel filter is a downsampling technique; i.e. it reduces the number of points, which creates tiny 3D boxes in space over the point cloud data. And then, in each box, all points are represented with their centroid (Rusu, 2011). Voxel size is the only variable that needs to be determined. It is worth mentioning that this filter existed as a class in PCL named "VoxelGrid" (ibid).

On the other hand, three methods of surface interpolation are suggested in the proposed technique: Plane best fitting by Ordinary Least Squares (Plane-OLS), Plane best fitting by Total Least Squares (Plane-TLS), and Locally Weighted Scatter Plot Smooth (LOWSS). Two of these are based on plane interpolation because it is frequently the key part of many buildings.

5.6.4.1 Plane Best Fitting by Ordinary Least Square

It is a well-known method of fitting a plane through least squares approach with the polynomial observation equation. It is named in this research Plane-Ordinary Least Square (Plane-OLS). Let x , y , and z be coordinates of a set of points in R^3 , in such a way:

$$Z = f(x, y) \quad (5.16)$$

By using polynomial:

$$Z = Ax + By + C \quad (5.17)$$

Where A , B , and C are plane coefficients to be computed. We can create following system equations from n data points:

$$\begin{aligned}
 Z_1 &= Ax_1 + By_1 + C \\
 Z_2 &= Ax_2 + By_2 + C \\
 &\dots\dots\dots \\
 Z_n &= Ax_n + By_n + C
 \end{aligned}
 \tag{5.18}$$

In matrix form:

$$\begin{bmatrix} x_1 & y_1 & 1 \\ x_2 & y_2 & 1 \\ \dots & \dots & \dots \\ x_n & y_n & 1 \end{bmatrix} \begin{bmatrix} A \\ B \\ C \end{bmatrix} = \begin{bmatrix} Z_1 \\ Z_2 \\ \dots \\ Z_n \end{bmatrix}
 \tag{5.19}$$

In the least square form:

$$Ax = l
 \tag{5.20}$$

Where:

$$A = \begin{bmatrix} x_1 & y_1 & 1 \\ x_2 & y_2 & 1 \\ \dots & \dots & \dots \\ x_n & y_n & 1 \end{bmatrix}, x = \begin{bmatrix} A \\ B \\ C \end{bmatrix}, \text{ and } l = \begin{bmatrix} Z_1 \\ Z_2 \\ \dots \\ Z_n \end{bmatrix}$$

Then, it can be solved by the least square method to compute A, B, and C.

Fortunately, MATLAB software can directly compute these coefficients from data points using a function named “fit” with selection method “poly11”.

There is still an issue in the proposed method that needs to be addressed if the polynomial is applied for plane fitting: that is determining which axis (X, Y, or Z) is going to be minimised. In other words, it needs to determine the direction of interpolated plane, e.g. horizontal or vertical. To solve this issue, the spatial distribution of the data set is examined; hence, minimising is applied on axis direction with minimum range.

5.6.4.2 Plane Best Fitting by Total Least Squares

One of the most obvious drawbacks of ordinary least squares for the plane fitting is that it is minimised along a particular axis direction. On the other hand, the total least square which is based on linear

Where x is the data point, x_i are the neighbour points within the span, and $d(x)$ is the longest distance within the span from data points to neighbours. Hence, points with nearest distances are given bigger weight and therefore make a greater contribution in the interpolation. Also, points outside the span have zero weight, consequently, they will not influence on the fit (ibid). After that, a first-degree polynomial is fitted by performing a weighted linear least-squares regression. Thus, a new value for each data point is obtained. This process is repeated for all data points and the fitted surface will pass through the new set of points. Fortunately, MATLAB software can implement this technique through a built-in function named “fit” by applying “lowess” for fitting method (ibid).

Obviously, the span is the only variable that needs to be addressed in this method, which is determined in the practical test.

5.6.5 Determination Deformation Vectors

Clearly, the outcomes of the GPA (Sec.5.5) do not satisfy the aims of this research. Instead, deformation vectors are required, which are computed from transformation parameters. According to Monserrat and Crosetto (2008), for monitoring purpose, it is sufficient to compute three translation parameters, which represent components of the deformation vector.

Hence, the deformation vectors can be computed based on the transformation parameters, which are estimated through GPA as follows:

From equation (5.2) (considering $S=1$):

$$\hat{A}_i = A_i R_i + j t^T \quad (5.25)$$

Where:

A_i (Px3): data matrix at epoch i (known).

\hat{A}_i (Px3): matrix A_i after solving GPA (known).

R_i (3x3): rotation matrix for epoch i (to be estimated).

t_i (3x1): translation vector for epoch i (to be estimated).

j (Px1): unit vector.

Consider $R_i=I$, then:

$$\hat{A}_i = A_i + jt^T \quad (5.26)$$

$$\hat{A}_i - A_i = jt^T \quad (5.27)$$

By multiplying both sides by j^T :

$$j^T \times (\hat{A}_i - A_i) = j^T \times jt^T \quad (5.28)$$

Hence:

$$t^T = \frac{j^T \times (\hat{A}_i - A_i)}{j^T \times j} \quad (5.29)$$

Ultimately, the deformation vector (t) is computed for all boxes.

5.6.6 Localisation of Deformation

Until this stage of the proposed technique, translation vectors have been obtained for all boxes at all epochs. However, these vectors may be resulting from observation errors. Therefore, deformation detection is a delicate problem because the deformations to be detected are of the same order of magnitude as the precision of observations (Gründig et al., 1985).

To solve such an issue, statistical tests are employed to examine if there is significant displacement in the observations. The assumption of all tests is that the data has only white noise. Therefore, if colour noise or outliers exist, an incorrect result could occur (Betti et al., 2011).

Inspired by Gründig et al. (1985), the proposed technique uses an F-test to detect significant displacements in all translation vectors. The null hypothesis (H_0) which states that there are no deformations between the epochs will either be accepted or rejected. The corresponding condition is the translation vectors resulting from equation (5.29):

$$t = 0 \quad (5.30)$$

Hence, the quantity Ω^2 can be computed:

$$\Omega^2 = \frac{t^T \times t}{3} \quad (5.31)$$

If the null hypothesis that there is no deformation between the epochs is accepted, Ω^2 will exceed the variance of the observations (σ^2) by the effect of random errors. Otherwise, the null hypothesis has to be rejected. This can be tested as follows:

$$F^* = \frac{\Omega^2}{\sigma^2} \quad (5.32)$$

The null hypothesis is to be accepted if F^* fits the Fisher distribution, i.e. if the probability equation:

$$p(F^* < F_{1-\alpha, f_1, f_2} | H_0) = 1 - \alpha \quad (5.33)$$

Where:

1- α : level of significance.

f_1 : degree of freedom for numerator (equal 3).

f_2 : degree of freedom for denominator (redundancy).

$$f_2 = (3 * \text{No. of points} - 6) * \text{No. of Epochs} \quad (5.34)$$

The variance (σ^2) is computed according to GPA concept, where the covariance matrix can be computed as follows (Crosilla and Beinat, 2002):

$$(\text{covariance})_j = \frac{1}{m} \sum_{i=1}^m (\hat{A}_i^T - Z^T)_j (\hat{A}_i - Z)_j \quad (5.35)$$

$$V^2 = \sum_{j=1}^p \text{tr}(\text{covariance})_j \quad (5.36)$$

$$\sigma^2 = \frac{\sum_{i=1}^m V_i^2}{(3 * p - 6) * m} \quad (5.37)$$

Where:

\hat{A}_i : Best fit for data matrix at epoch i (Sec.5.5).

Z : consensus matrix (Sec.5.5).

m : No. of epochs.

P : No. of points.

Finally, to localise deformation, deformation probabilities for each box at all epochs are estimating:

$$\text{Probability (\%)} = p(F^*, f_1, f_2) \times 100 \quad (5.38)$$

Eventually, the probability of deformations is computed for each box at each epoch.

5.7 Algorithm Implementation

Apart from the software used for data retrieving from TLS, the proposed method is performed by written or open source software. In general, it is implemented with three sources: MATLAB script has been written by the researcher; PCL open source C++ library; and CloudCompare open source software.

The PCL is employed to apply Voxel filter, and removing outliers (Sec. 5.6.4). For this purpose, inspired by Rusu (2011), a function is created to call PCL classes. The function has been written in C++ programming language. Both input and output are arranged in text files which can be read by different programmes.

On the other hand, CloudCompare is utilised for representation and visualisation. Thus, the proposed technique begins, if point clouds need any edit, and finishes with it, where deformation probabilities are represented. Similarly, input and output of this software are text files.

Almost all computations are executed by MATLAB script which has been written by the researcher. Figure 5-6 shows the flow chart for the proposed algorithm.

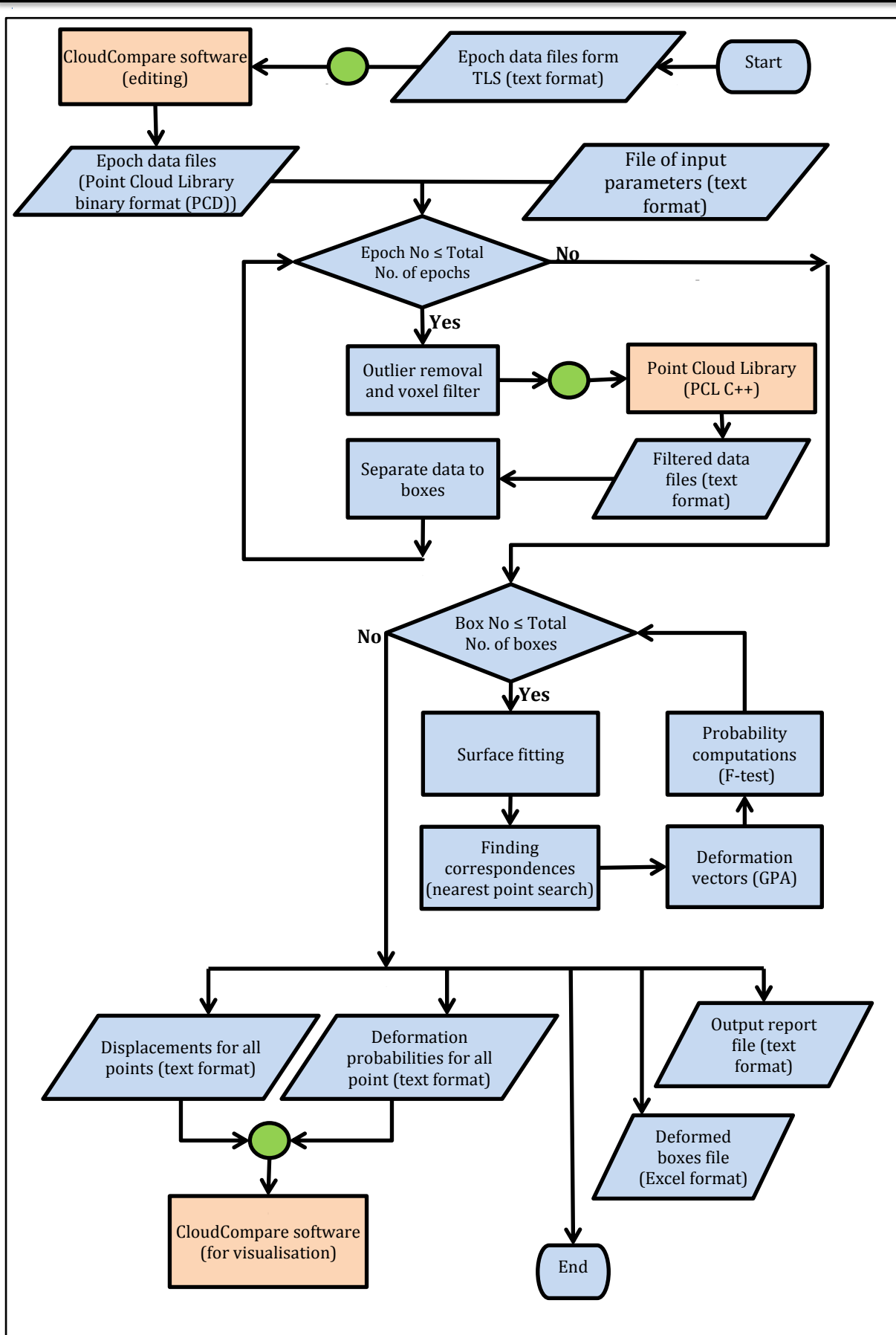


Figure 5-6 Flow chart of the proposed algorithm.

5.8 Chapter Conclusions

From the first part of this chapter, reviewing the Procrustes technique, it can be concluded:

- There are different revisions of it, such as Orthogonal Procrustes Analysis (OPA), Extended Orthogonal Procrustes Analysis (EOPA), Weighted Extended Orthogonal Procrustes Analysis (WEOPA), and Generalized Procrustes analysis (GPA).
- The Procrustes method has been applied in different fields such as Medicine, Psychometry, Statistics, Chemistry, Human Genetics, Geology, and Zoology. Interestingly, it has been shown widely applicable in Geomatics, especially for reference system transformation. However, it has not been used to detect deformations.
- The most important drawback of the Procrustes technique is the lack of reliability criterion to detect and localise the outliers, which might be included in measurements. Consequently, the results produced by the Procrustes technique may be wrong in the case of the existence of outliers in the data set.

From the second part of this chapter, introducing the proposed technique, it can be concluded:

- Dimensions of the boxes can play a key role in the proposed method because bigger boxes can estimation deformations better due to a lot number of redundant. However, smaller size boxes can localise deformation more accurately.
- Boxing structure can cope with unrepeatable measurement of TLS and the deformations can be localised. Also, it can offer better accuracy as the deformation vectors are estimated based on all points within the box (a large number of redundant).
- Boxes contain few points might appear based on resolution and box size. Consequently, these boxes may show wrong indication for deformations.
- It is difficult to detect displacement of a single point in boxes due to dealing with data as groups.

CHAPTER Six: **VALIDATION EXPERIMENTS WITH SIMULATED DATA AND SIMULATED DEFORMATIONS**

6.1 Introduction

Ultimately, the proposed method needs to be conducted in different conditions. For this purpose, a plan has been proposed for validation. The principle of this plan is that tests are undertaken with minimum error contribution, and if they succeed, they are followed by more real conditions, involving more realistic error sources. Accordingly, three validation tests have been conducted, as follows:

1- Simulated data with simulated deformation:

To assess the performance of the developed software and to fix some variables, simulated data is used. Thus, only controlled white noise, distributed according to the normal distribution, is included in this data.

2- Real scan data with simulated deformation:

The purpose of this test is checking the validity of the proposed technique in real circumstances. Consequently, a real scan has been carried out, but with minimum errors contribution, e.g. all measurements have been taken from fixed TLS on the same day. This procedure can mitigate effects of the atmospheric and geometric (registration and georeferencing) errors. Also, simulated deformations have been conducted, through moving an object with known displacements in different scans.

3- Real scan data with actual deformation:

Finally, the proposed method needs to be tested in real data with real deformations. Hence, it was applied on data of Bellmanpark Limekiln, Clitheroe, Lancashire (Historic, 2015a) monitoring project.

The objective of this chapter is to examine validation of the proposed method with simulated data and simulated deformations, and to fix the algorithm variables.

6.2 Create Simulated Data

To prepare simulated data, CloudCompare software was used to create a 3D model (Figure 6-1). This model was chosen as a kind of a complicated structure with curved walls, such as dome and minaret.

Furthermore, to reduce run-time, the dimension of this model was limited to few metres (height=2.5 m, width and depth=1.5 m).

The point cloud was created from this model by using mesh technique existed in CloudCompare software (Figure 6-2). In addition, the point cloud was subsampled to different resolutions (2, 3, 5 mm).

After that, "Hidden Point Removal" command was employed to remove points fallen on the other side of the scene, which cannot be seen from specific viewpoint represents TLS position (Figure 6-3).

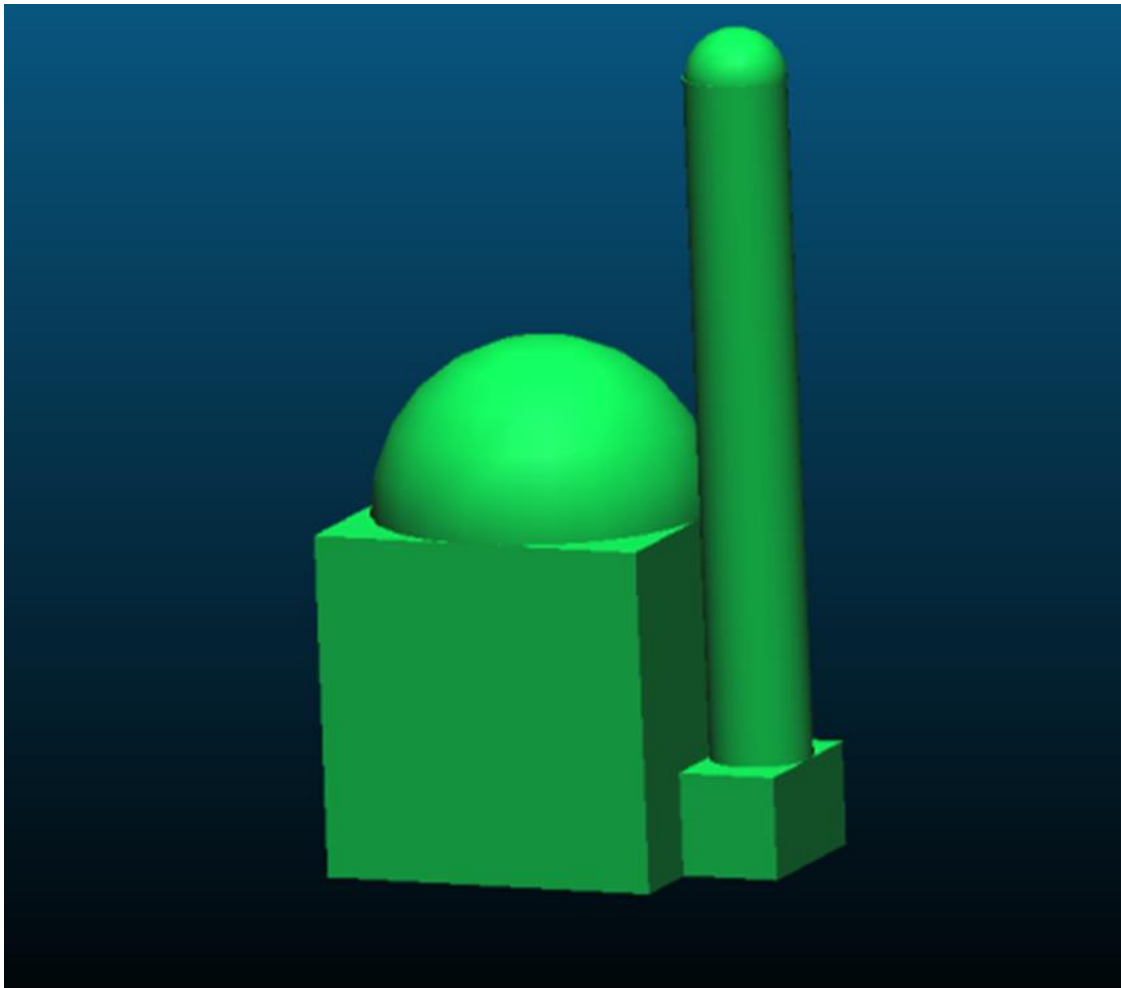


Figure 6-1 3D model created by CloudCompare software.

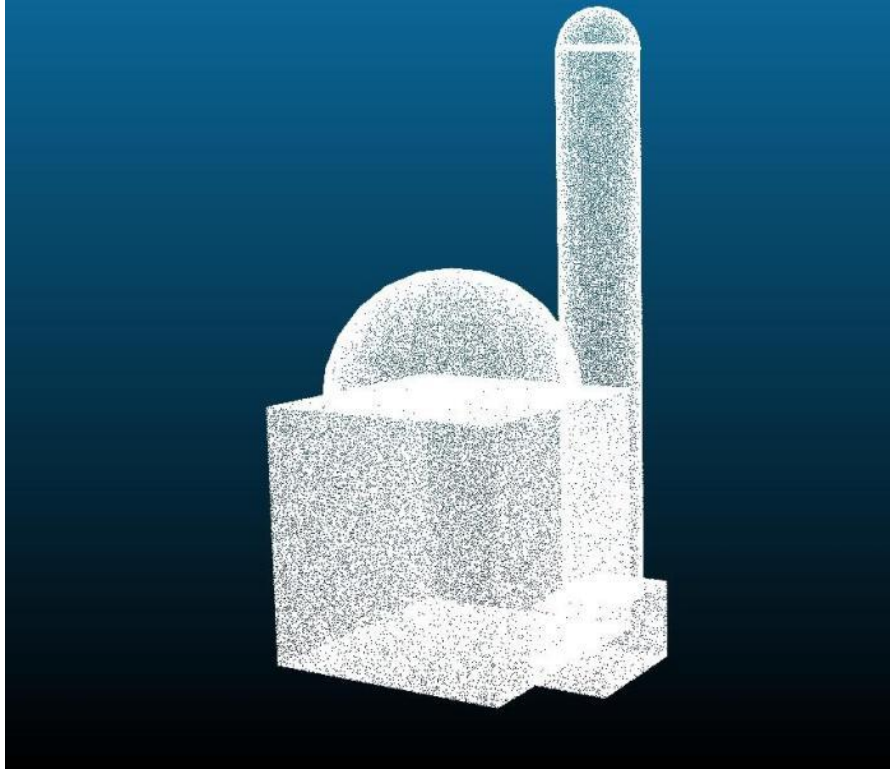


Figure 6-2 The point cloud created from the 3D model.

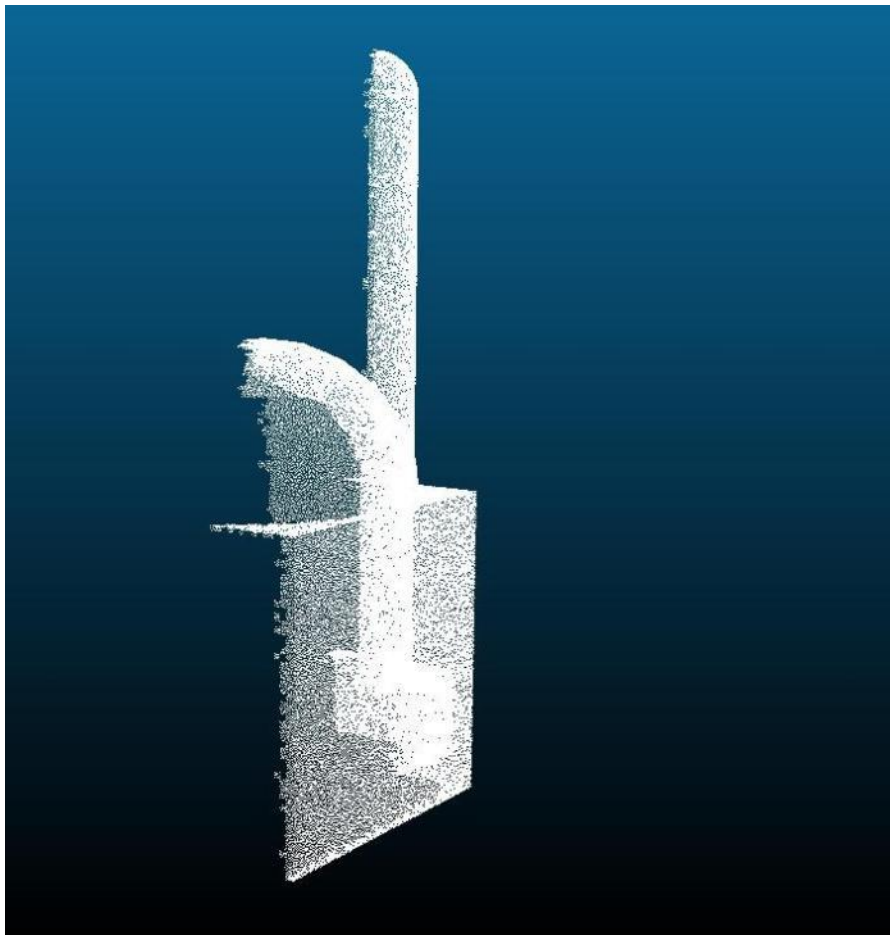


Figure 6-3 Hidden point removal applied on point cloud.

6.3 Adding Noise

To create multiple epochs, normal noise were added to the point clouds. Hence, all epochs are different from each other by noise only. MATLAB software was employed for this purpose. The value of the suggested noise is based on the supposed type of TLS which is employed in the practical test. Therefore, the expected noise for Leica Scanstation P20 (Sec.4.3.1), which is used in the practical test, can be estimated as follows:

- The maximum error in point position $\approx \pm 6$ mm (Leica Geosystems, 2013).
- The error of target acquisition $\approx \pm 2$ mm (Leica Geosystems, 2013) assumed to be the only contribution to registration error.

According to Gaussian theory for error propagation:

$$\text{Expected total error (position)} = \sqrt{6^2 + 2^2} \approx \pm 6.5 \text{ mm}$$

$$\text{Expected total error (single axis)} = \frac{6.5}{\sqrt{3}} \approx \pm 3.75 \text{ mm}$$

Consequently, (± 3.75 mm) normal noise was added to each axis of all points in the point clouds (Figure 6-4).

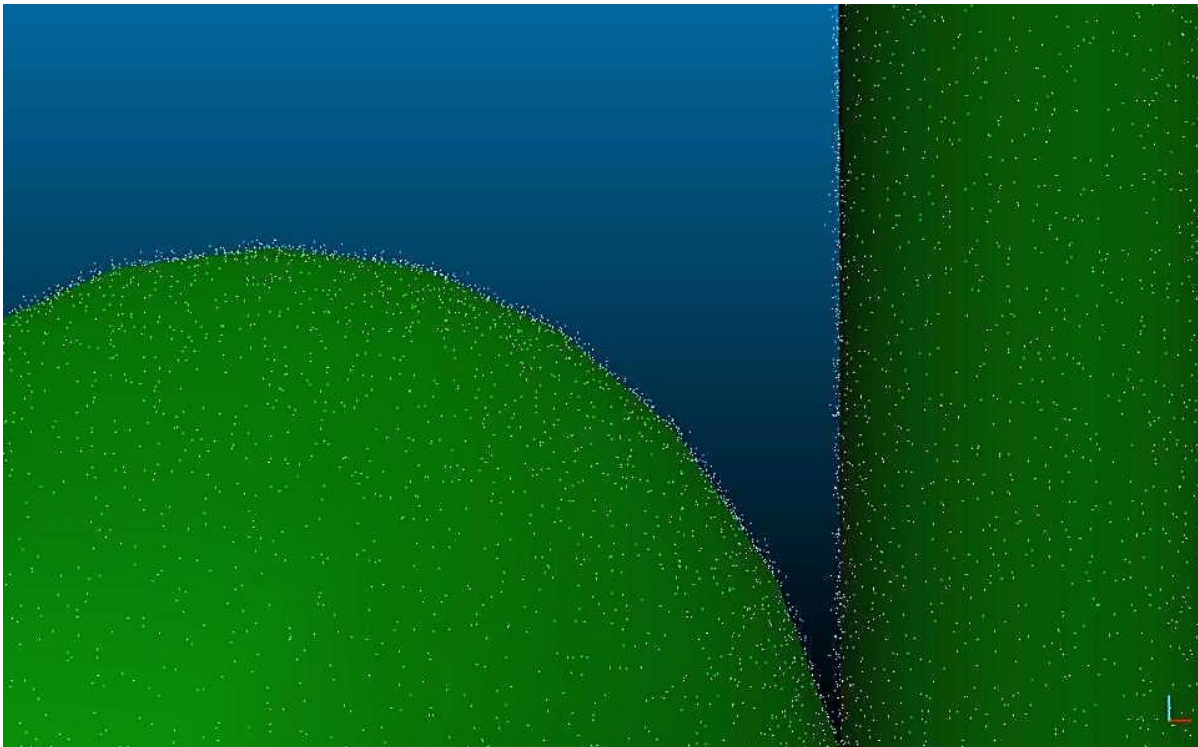


Figure 6-4 The noise in the point clouds.

6.4 Validation for Non-deformed Data

To test validation of the proposed method in case of non-deformations, six epochs were prepared from simulated data. In such a way, each epoch is different from others by noise only. In addition, three different box sizes (Sec.5.6.3) were used, in this case, 27 alternative approaches require to test, i.e. three sample sizes (2, 3, and 5 mm), three surface fitting methods (Sec.5.6.4), and three box sizes (10, 20, and 30 cm).

After applying the proposed technique, all alternatives showed no deformation and the maximum deformation probability is less than 10% (Table 6-1, Table 6-2, and Table 6-3). Hence, it can be considered that it succeeded where no deformations exist.

On the other hand, it can be noticed that some parts are missing in the simulated building after applying the proposed method because the proposed algorithm was designed to filter out boxes have a limited number of points according to following proposed formula:

$$\text{minimum points} = \left(\frac{D}{SZ}\right)^2 \times 10\% \quad (6.1)$$

Where, D is the box dimension, and SZ is the sample size (resolution) of point clouds. The idea of this formula is that it is filtering out box which contains points equal or less than 10% of supposed points in one face. There are three possible solutions to cope with the issue of missing parts, decreasing box dimension, increase sample size, and changing start point of boxing structure.

Table 6-1 The probability of deformation of non-deformed epochs for resolution 2 mm, for different box sizes and different surface fitting techniques.

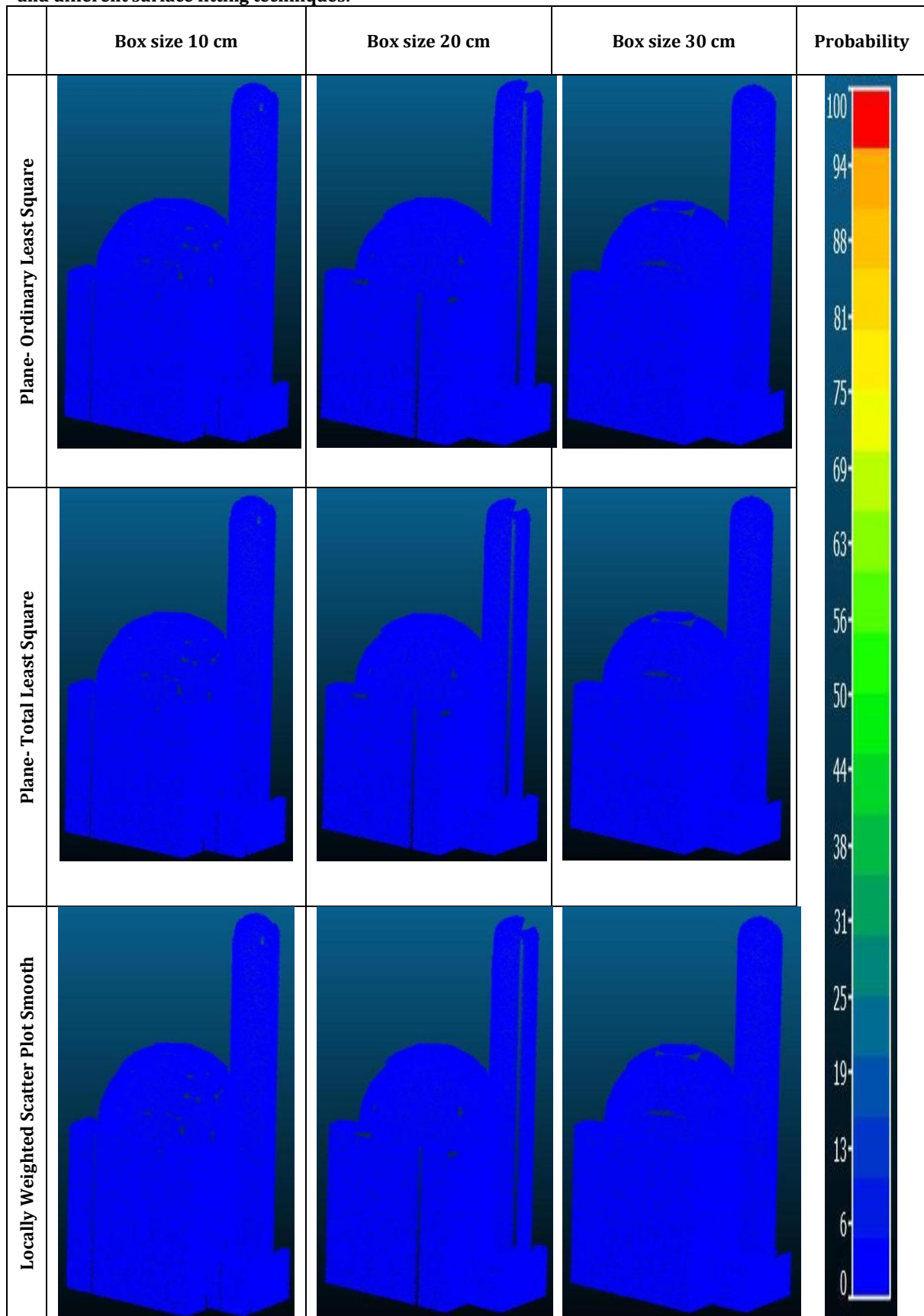


Table 6-2 The probability of deformation of non-deformed epochs for resolution 3 mm, for different box sizes and different surface fitting techniques.

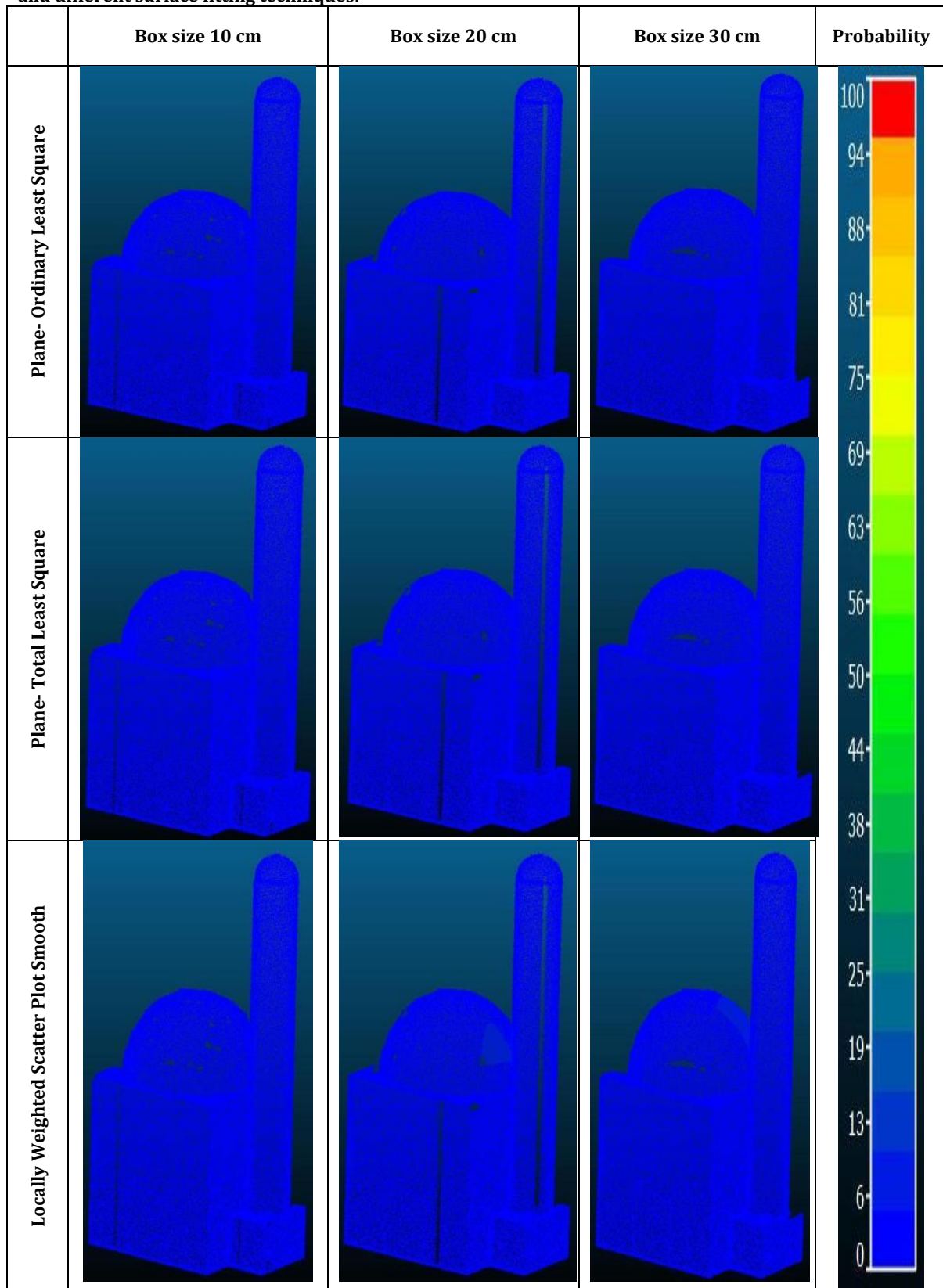
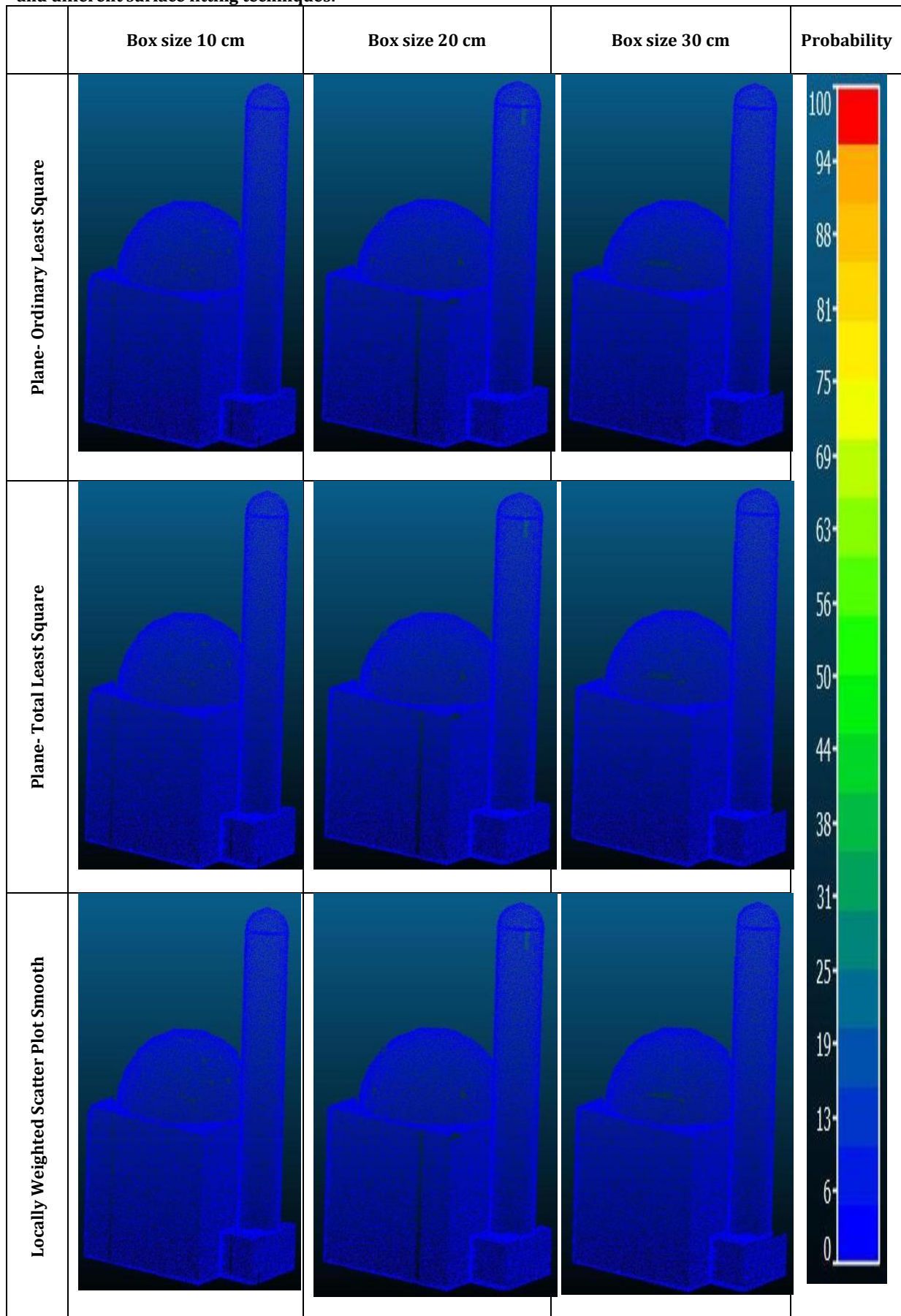


Table 6-3 The probability of deformation of non-deformed epochs for resolution 5 mm, for various box sizes and different surface fitting techniques.



6.5 Validation for Deformed Data

To validate the ability of the proposed technique to detect and localise deformations, simulated deformation is added to the data. Thus, seven epochs were prepared, six non-deformed (same as in section 6.4) and the seventh with simulated deformations. In addition, the same value of noise was added to epoch seven. Also, different amounts and locations of simulated deformations were placed (Figure 6-5 and Table 6-4). Evidently, one of these deformations (A3) was less than the noise, which means, theoretically, it cannot be detected.

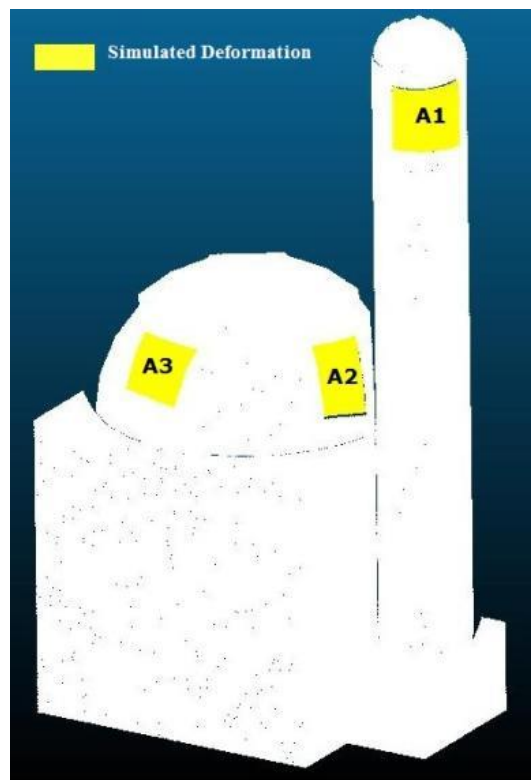


Figure 6-5 Locations of the simulated deformations.

Table 6-4 The simulated deformations for different parts.

Area	Deformation (m)			
	DX	DY	DZ	Displacement
A1	+0.005	-0.006	-0.006	0.0098
A2	-0.009	+0.010	+0.008	0.0156
A3	+0.003	-0.004	+0.003	0.0058

Similarly, according to variables suggested, there are 27 alternative solutions (Table 6-5, Table 6-6, and Table 6-7). In general, box size 10 cm showed more ability to detect deformations than bigger sizes. This might be because bigger size boxes contain more points. Hence, more noise involves in computation.

In addition, although the deformed areas are convex, plane surface interpolation methods detected deformations better than LOWESS method. This is considered optimistic results because the time cost of a plane fitting is much lower than LOWESS method, which will be discussed later.

According to the results, the proposed technique succeeded to detect deformation in some solutions. For instance, the area A1 showed deformation probability more than 95% in two cases when the resolution is 2 mm (Table 6-5), while deformation probability of the area A2 reached more than 95% in four solutions (three in 2 mm resolution, and one in 3 mm resolution).

Interestingly, although the deformation of area A3 is less than noise, it is still recognised in some solutions because its deformation probability is more than surrounding areas, which reached in some solutions to 40%. This results can give an indication for deformations and impose future measurements to examine if there is developing deformations.

Expectedly, 5 mm resolution showed limited ability to detect deformation and in many solutions the maximum deformation probability less than 20%. This outcome might be because with existing noise the number of points in boxes is not enough to perform the proposed technique.

Table 6-5 The probability of deformations of the deformed epochs for 2 mm resolution, different box sizes, and different surface fitting techniques.

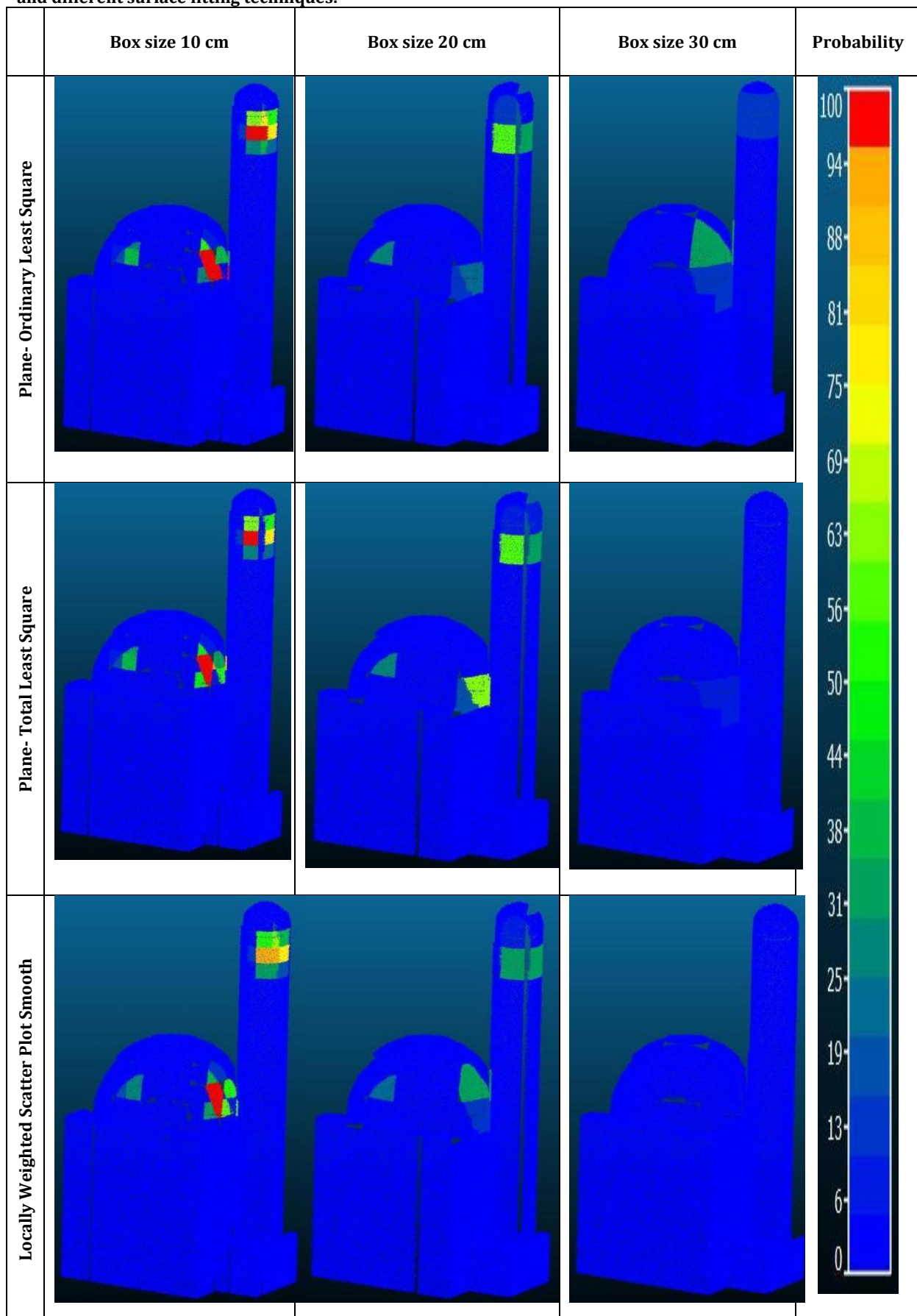


Table 6-6 The probability of deformations of the deformed epochs for 3 mm resolution, various box sizes, and different surface fitting techniques.

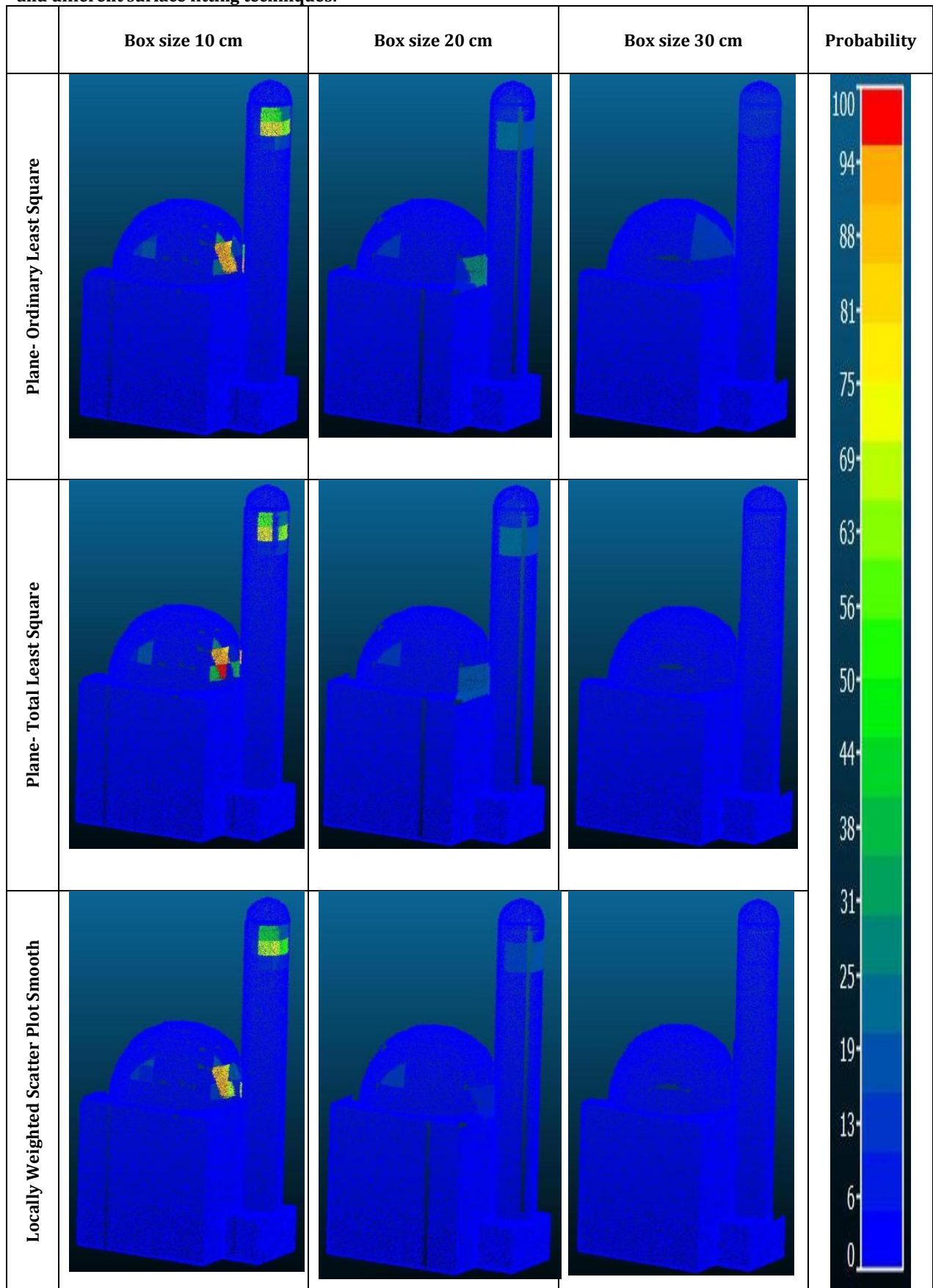
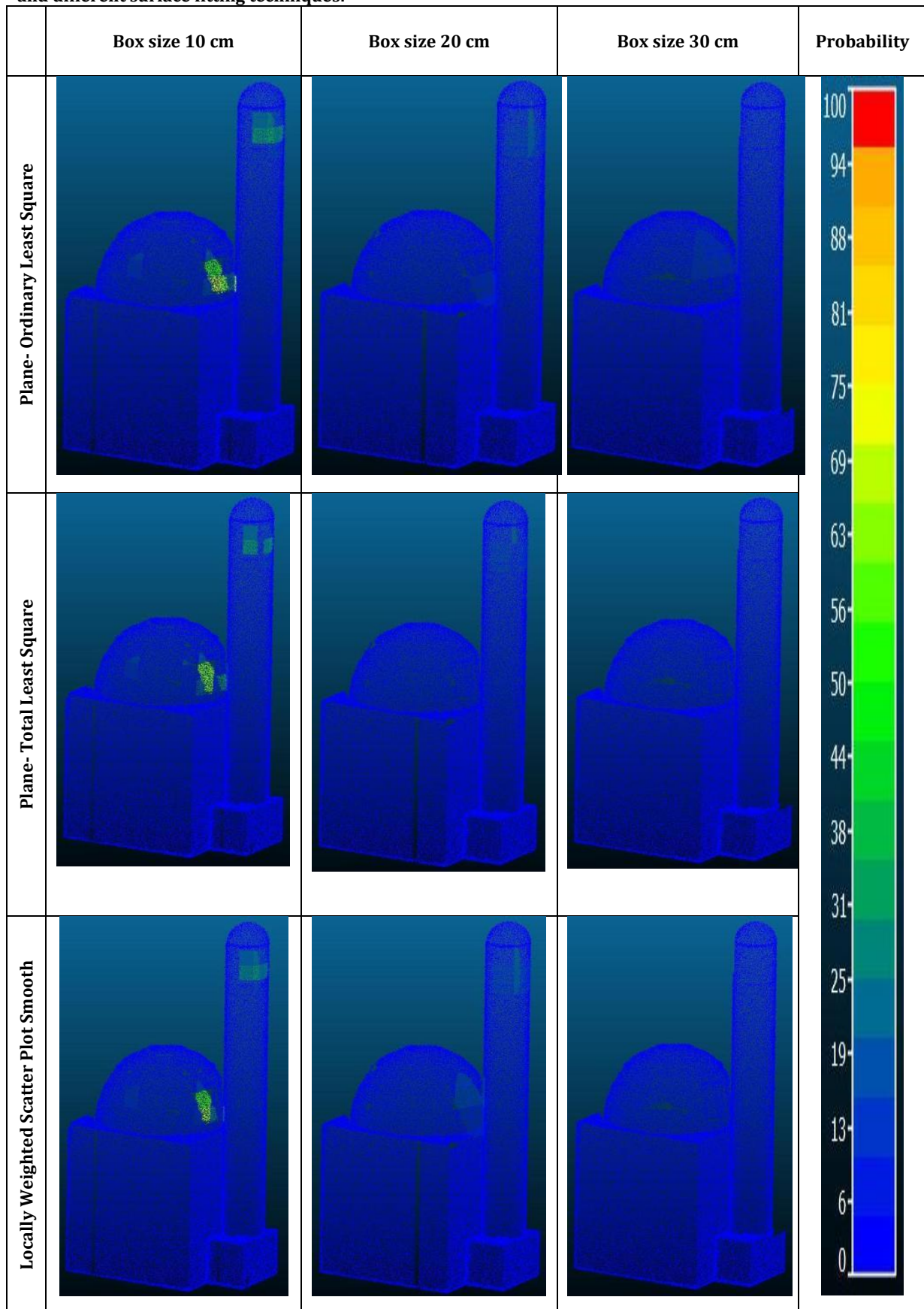


Table 6-7 The probability of deformation of the deformed epochs for 5 mm resolution, different box sizes, and different surface fitting techniques.



6.6 Time Cost

The total execution time for the proposed algorithm can be as short as a minute (box size 10 cm, Plane_TLS, and 5 mm resolution) or as long as eleven hours (box size 30 cm, LOWESS, and 2 mm resolution) which is based on resolution, box size, and surface interpolation model (Table 6-8). Mainly, there are three parts cost most of the execution time in the proposed algorithm, boxing structure, finding corresponding, and surface fitting. It can be seen in Table 6-9, Table 6-10, and Table 6-11 that the percentage of these parts can reach up to 99% from the total execution time.

On the other hand, the time cost of the fitting surface is based on resolution and box size (Figure 6-6, Figure 6-7, and Figure 6-8). Obviously, LOWESS is considered as the most time expensive method compared with Plane-OLS and Plane-TLS.

Table 6-8 Total execution time (second) for the proposed algorithm for different cases.

Resolution (mm)	Interpolation model	Box size (cm)		
		10	20	30
2	Plane_OLS	275.05	490.76	1022.84
	LOWESS	6528.6	18802.1	38891.82
	Plane_TLS	299.91	646.86	1409.07
3	Plane_OLS	195.59	251.1	486.69
	LOWESS	3386.4	8519.69	19072.14
	Plane_TLS	161.36	307.73	678.11
5	Plane_OLS	116.9	99.6	147.58
	LOWESS	1223.2	2444.21	5719.03
	Plane_TLS	69.11	103.56	191.24

Table 6-9 Execution time cost (seconds) for different parts of the proposed algorithm for 2 mm resolution.

Box size (cm)	Surface model	Boxing structure	Finding Corresponding	Surface Interpolation	Σ	%
10	Plane_OLS	68.93	146.01	38.85	253.79	92.3%
	LOWESS	69.08	141.35	6298.64	6509.07	99.7%
	Plane_TLS	73.04	160.71	45.13	278.88	93.0%
20	Plane_OLS	96.37	362.91	12.37	471.65	96.1%
	LOWESS	93.23	354.06	18336.83	18784.12	99.9%
	Plane_TLS	105.65	369.5	153.34	628.49	97.2%
30	Plane_OLS	158.79	839.7	5.15	1003.64	98.1%
	LOWESS	144.76	719.77	38008.83	38873.36	99.9%
	Plane_TLS	152.28	805.23	433.34	1390.85	98.7%

Table 6-10 Execution time cost (seconds) for different parts of the proposed algorithm for 3 mm resolution.

Box size (cm)	Surface model	Boxing structure	Finding Corresponding	Surface Interpolation	Σ	%
10	Plane_OLS	46.17	88.35	44.51	179.03	91.5%
	LOWESS	43.48	83.54	3244.19	3371.21	99.6%
	Plane_TLS	43.79	83.26	19.1	146.15	90.6%
20	Plane_OLS	55.64	170.67	12.44	238.75	95.1%
	LOWESS	53.51	163.08	8290.69	8507.28	99.9%
	Plane_TLS	53.3	175.26	66.17	294.73	95.8%
30	Plane_OLS	78.45	390.96	5.21	474.62	97.5%
	LOWESS	75.89	360.86	18622.09	19058.84	99.9%
	Plane_TLS	87.79	392.11	186.36	666.26	98.3%

Table 6-11 Execution time cost (seconds) for different parts of the proposed algorithm for 5 mm resolution.

Box size (cm)	Surface model	Boxing structure	Finding Corresponding	Surface Interpolation	Σ	%
10	Plane_OLS	22.14	34.25	46.4	102.79	87.9%
	LOWESS	19.79	30.51	1156.73	1207.03	98.7%
	Plane_TLS	20.53	31.74	3.91	56.18	81.3%
20	Plane_OLS	23.4	54.1	12.75	90.25	90.6%
	LOWESS	22.32	51.99	2361.42	2435.73	99.7%
	Plane_TLS	22.29	55.35	17.2	94.84	91.6%
30	Plane_OLS	30.44	104.87	5.26	140.57	95.3%
	LOWESS	28.4	111.28	5572.03	5711.71	99.9%
	Plane_TLS	28.74	109.45	45.81	184	96.2%

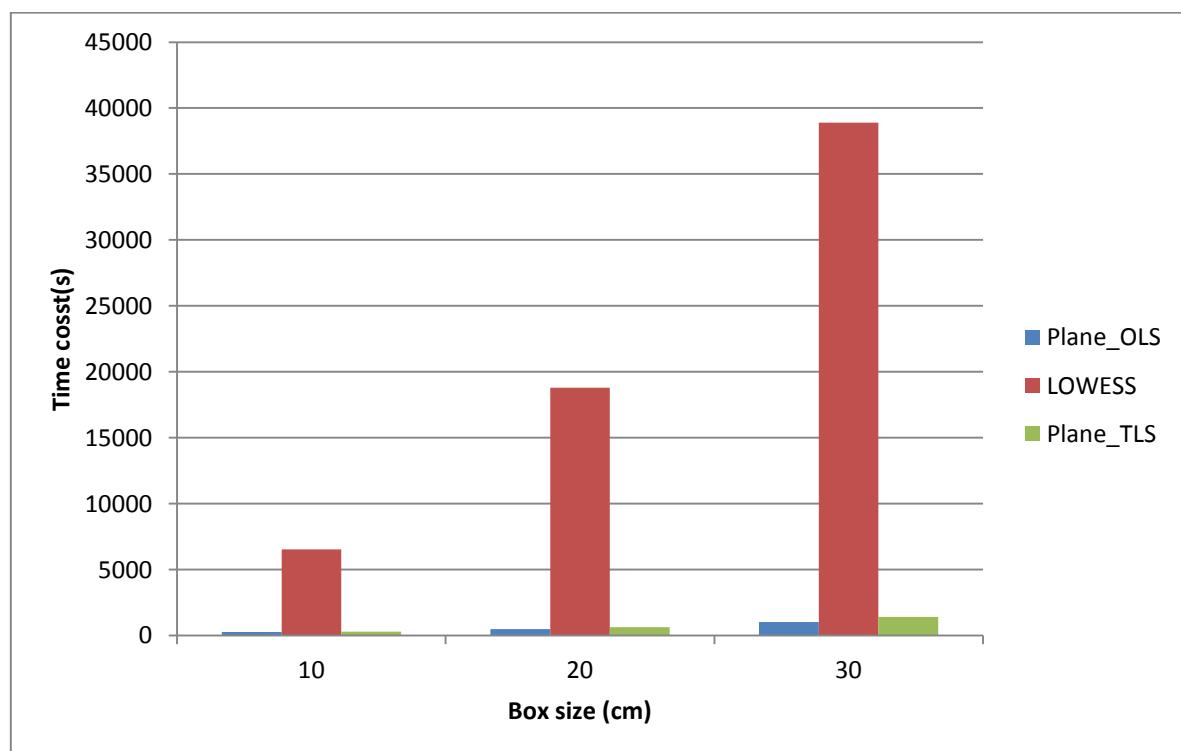


Figure 6-6 Total execution time for different fitting methods, different box sizes, and 2 mm resolution.

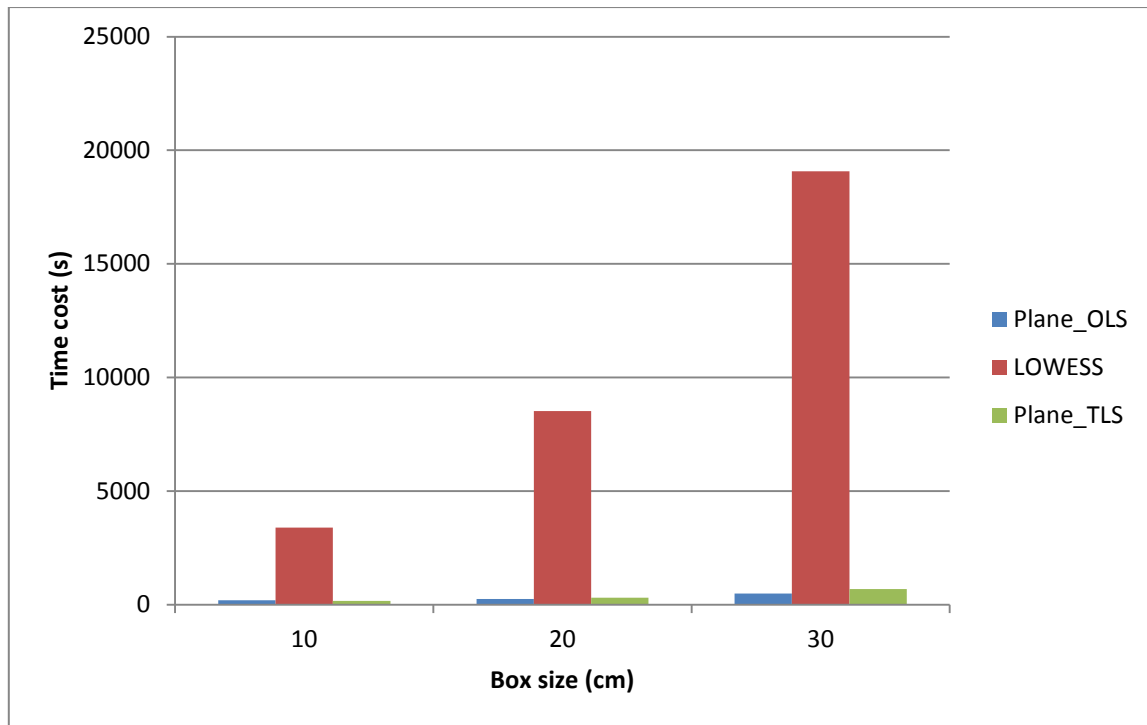


Figure 6-7 Total execution time for various fitting methods, different box sizes, and 3 mm resolution.

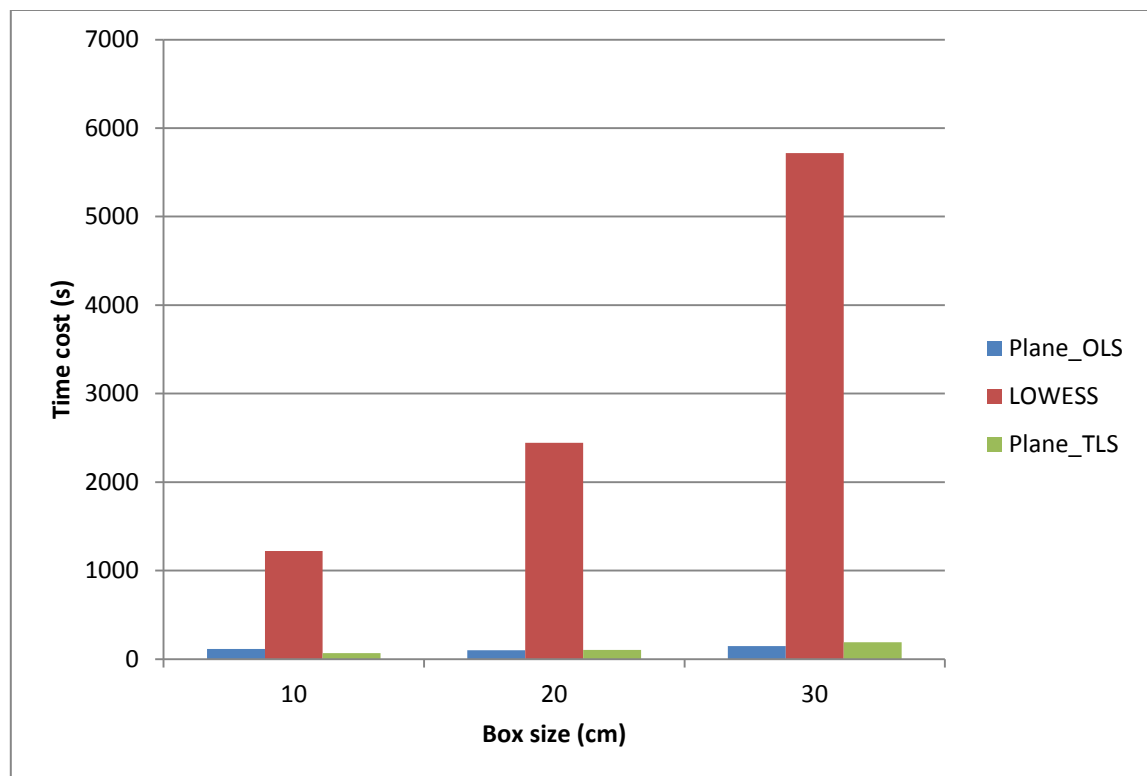


Figure 6-8 Total execution time for various fitting methods, different box sizes, and 5 mm resolution.

6.7 Wisely Downsampling

As has been mentioned and expected, in the high-resolution point cloud, surfaces can be fitted better, consequently, higher ability to detect deformation than low resolution. However, an enormous amount of data, which can be obtained from a higher resolution, is hard to handle and it consumes time to process. In addition, there is a bigger chance to omit some boxes from higher resolution point cloud due to the proposed algorithm.

Accordingly, it has been suggested to reduce resolution wisely. In other words, downsampling the point clouds and at the same time reducing the noise. In this case, the obtained point cloud can inherit advantages of both low and high resolution. Therefore, a few high-quality points are employed to perform the proposed technique.

For this purpose, Voxel filter (Sec.5.6.4) has been suggested to downsample the resolution of the point clouds from 2 mm to 5 mm. The results (Table 6-12) showed the ability of the point clouds to detect deformations as same as 2 mm resolution, although it consumes time as like as 5 mm resolution. Furthermore, it did not omit any box, i.e. no missing parts appear.

However, care should be taken when applying this filter to avoid over-smoothing. In such case, fake deformations might result. For instance, when using Voxel filter to downsample the resolution of the point clouds from 2mm to 10mm (Table 6-13), there are two incorrect solutions obtained, the first showed the probability of deformation more than 95% where box size 10 cm and Plane-Total Least Square (Plane-TLS) surface fitting method, while the second showed about 30% deformation probability where box size 20 cm and Plane_TLS surface fitting method.

Table 6-12 The probability of deformations of the deformed epochs for 5 mm resolution downsampled from 2 mm using voxel filter.

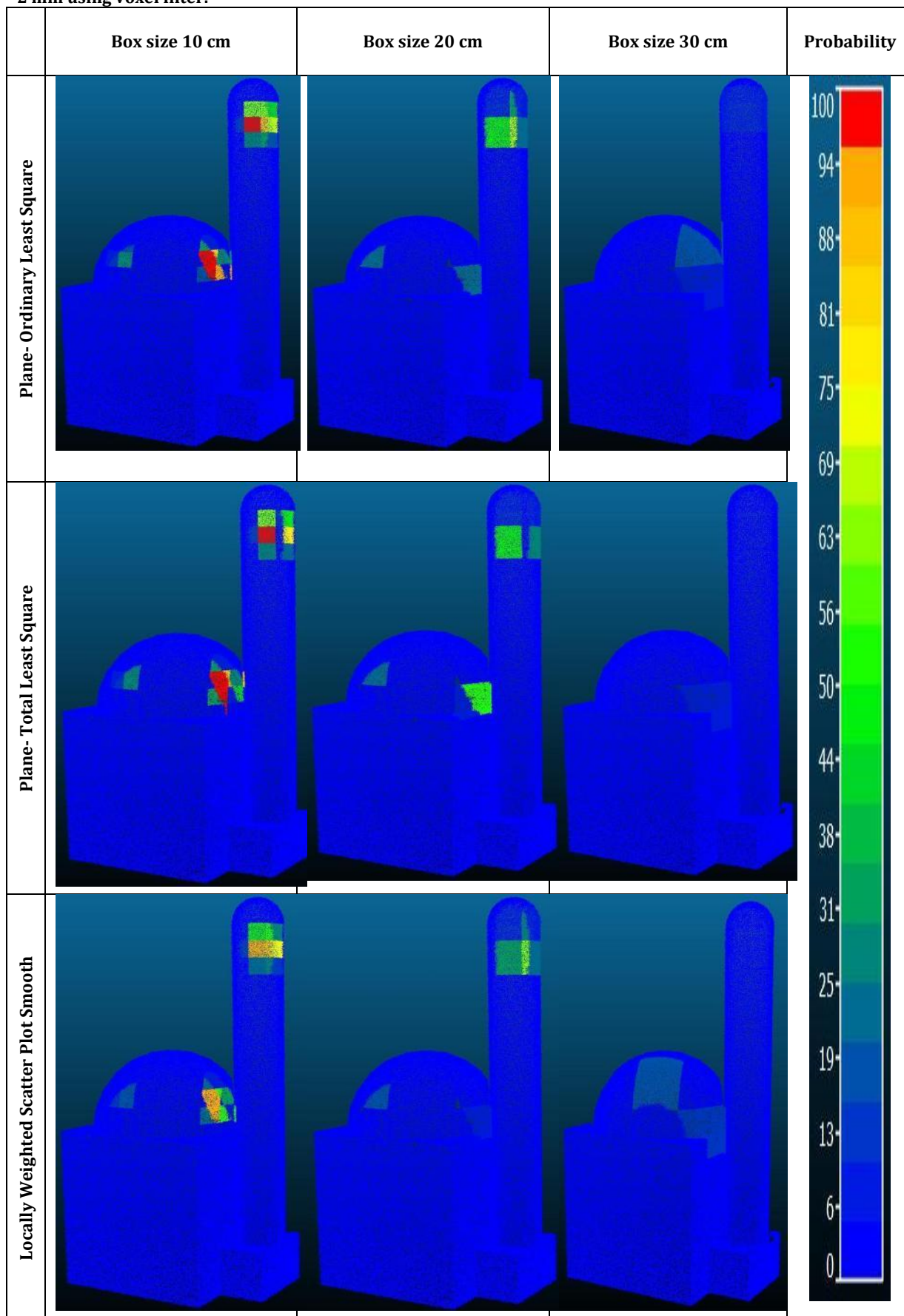
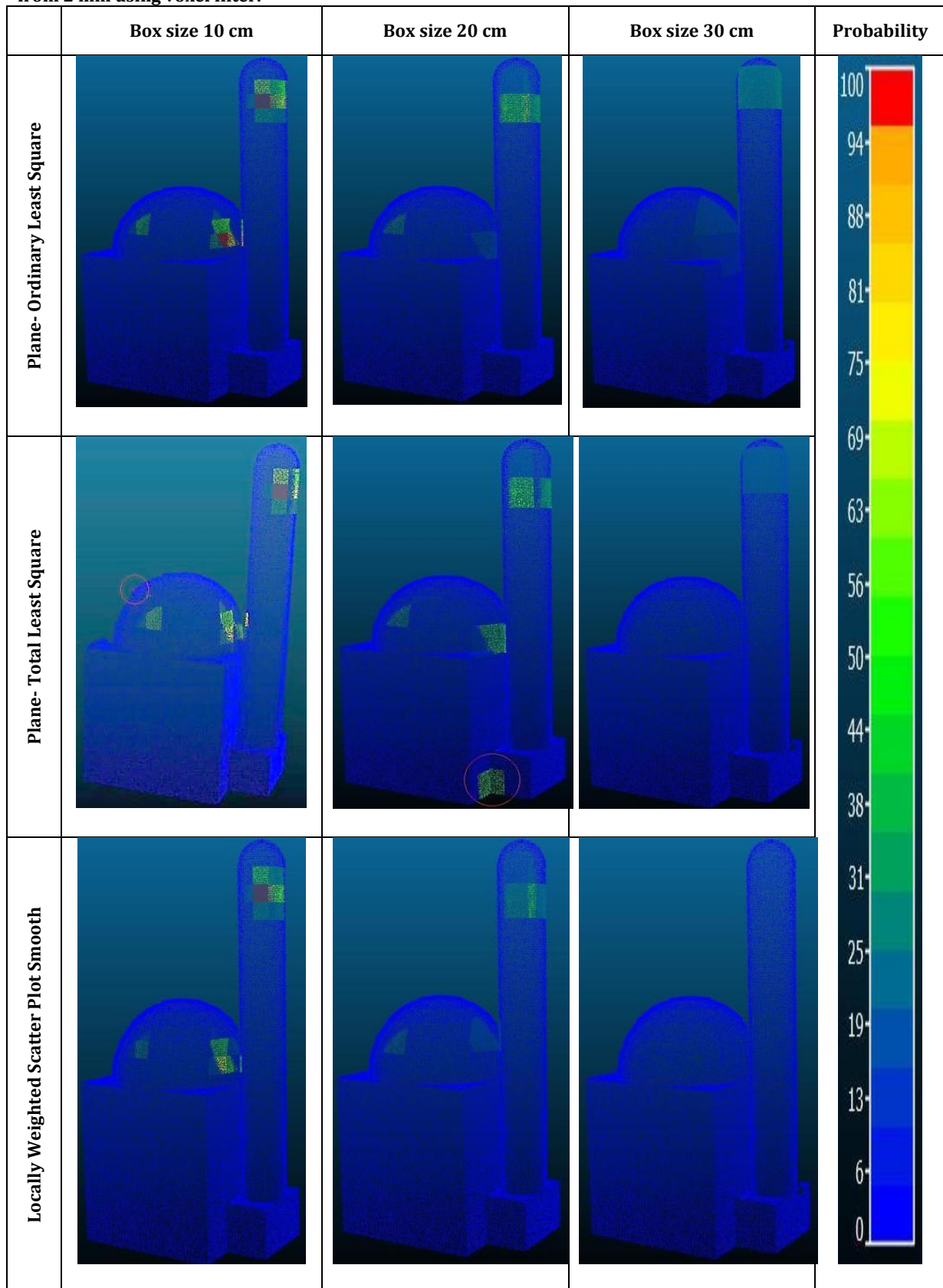


Table 6-13 The probability of deformations of the deformed epochs for the 10 mm resolution downsampled from 2 mm using voxel filter.



6.8 Chapter Conclusions

The objective of this chapter is to examine validation of the proposed method with simulated data and simulated deformations. From these tests, it can be concluded:

- The proposed algorithm succeeded to detect and to localise deformations.
- It showed success when no deformations exist.
- It could observe deformations with a magnitude less than noise which can be considered as promising results.
- Box size 10 cm showed more ability to detect deformations than bigger sizes (30 cm). This might because bigger size boxes contain more points, and therefore more noise involves in computation.
- In the case of 5 mm resolution, it showed limited ability to detect deformation. This might because with existing noise the number of points in boxes is not enough to perform the proposed technique.
- The total execution time is based on resolution, box size, and surface interpolation model.
- LOWESS is considered as the most time expensive method compared with Plane-OLS and Plane-TLS.
- Through applying Voxel filter, it showed the ability to detect deformations as same as 2 mm resolution, although it consumes time as like as 5 mm resolution.
- Plane surface interpolation methods detected deformations better than LOWESS method.
- For LOWESS surface fitting, the best results were obtained with the span equal to (0.25).
- For LOWESS surface fitting, the robust method is the least squares (LAR).
- Voxel size and outlier removal parameter (K and n) are fixed in the real test.

CHAPTER Seven: **VALIDATION EXPERIMENTS WITH REAL DATA AND SIMULATED DEFORMATIONS**

7.1 Introduction

The objective of this chapter is to test validation of the proposed method with real scan data and simulated deformations. For this purpose, two experiments have been conducted. The first test was designed in such a way that the expected errors are at a minimum, hence, scanning different epochs from one station (no registration errors). In addition, the atmospheric errors are at a minimum because all data were collected in a short period (within an hour). Furthermore, to reduce the object-related errors, the scanned area has the same colour of the moving object, which was used for simulated deformations. Finally, the range was about ten metres, which mean the range noise and beam divergence at a minimum.

On the other hand, the second test has the same design, yet the range was about 25 metres, which mean more noise is coming from the range uncertainty and beam divergence. Additionally, different materials have been scanned, which may add object-related errors.

7.2 Real Scan with Close Range

The first real scan was conducted on 10th of March 2015. This test was prepared in such a way that ranges within ten metres long, to reduce errors contribution. The test location was front of the Nottingham Geospatial Building (NGB) (Figure 7-1).



Figure 7-1 The location of the first test which was conducted on 10th of March 2015.

Laser scanner model Leica ScanStation P20 (Sec.4.3.1) was used to collect data. In addition, total station model Leica TS30 was employed to measure simulated deformations.

To create data, some 3D object (Figure 7-2) was pasted on the wall, and it scanned with wall six times, each represented one epoch. After that, the object moved a little and scanned with the wall, which represented epoch seven. Epochs eight and nine were created with the same way after moving the object. The scan resolution was selected as 6.3mm at quality level one (Sec.4.3.1).

On the other hand, the total station was used to determine displacements of the 3D object through measuring coordinates of small targets fixed on it before and after displacements.

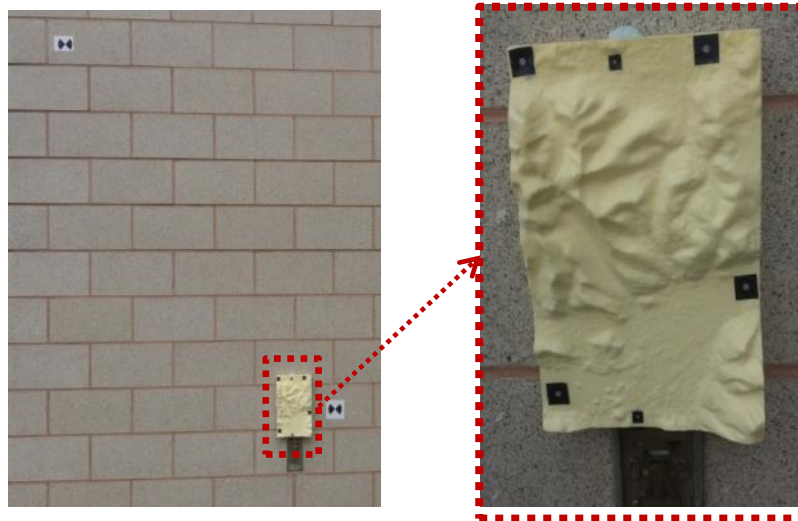


Figure 7-2 The scanned area of the first test with a 3D object which was used simulated deformation.

Ultimately, the whole data consisted from nine epochs, six non-deformed epochs and three with different deformations. Table 7-1 shows the simulated deformations for the pasted object according to the total station measurements.

Table 7-1 The simulated deformations for different epochs.

Epoch No.	DX (mm)	DY (mm)	DZ (mm)	Displacement (mm)
1-6	0.0	0.0	0.0	0.0
7	-1.0	4.5	0.5	4.6
8	-3.0	9.5	0.5	10.0
9	-5.5	16.0	0.5	16.9

7.2.1 Non-deformed Epochs

To test the proposed technique in non-deformed point clouds, the first six epochs was inputted. At first, the voxel filter did not apply; the results are shown in Figure 7-3. Obviously, there is a failure of the proposed method where a lot of non-deformed boxes showed high deformation probabilities (Figure 7-4). The possible reason is that data is contaminated with a lot of noise because the quality level one was used which means less repeating measurements, and therefore more noise (Sec. 4.3.1).

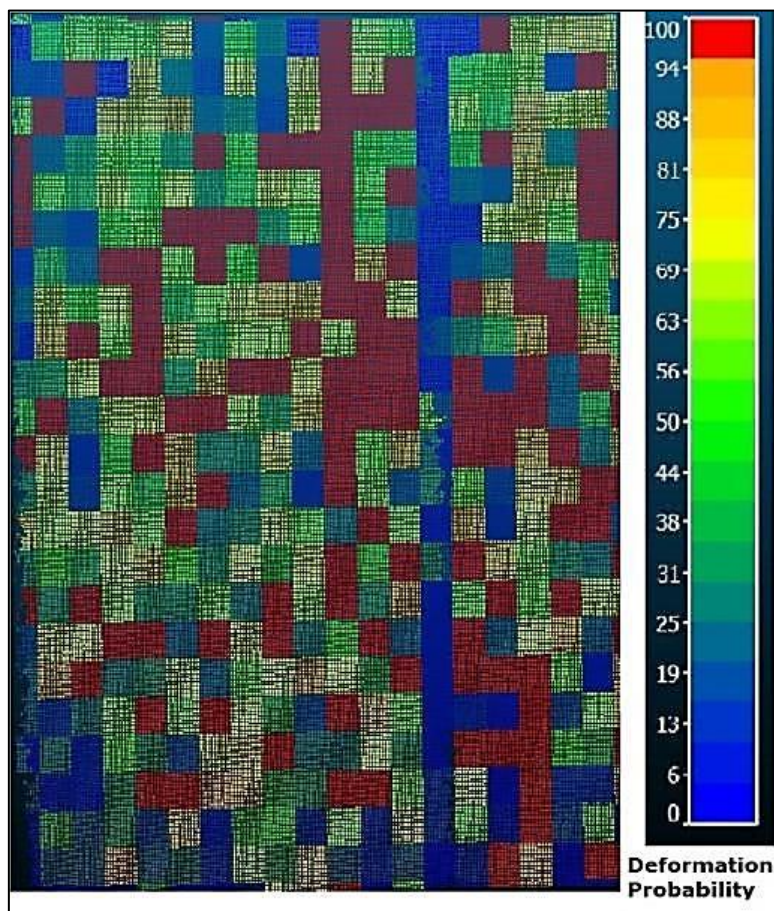


Figure 7-3 The results of the first six epochs without using the voxel filter.

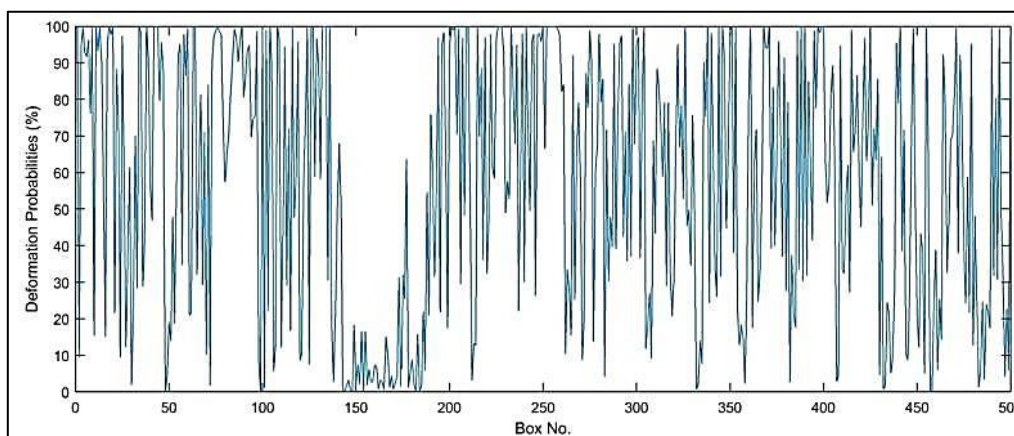


Figure 7-4 The deformation probabilities for epoch six before applying the voxel filter.

To mitigate noise, the voxel filter (Sec. 5.6.4) was applied (Figure 7-5). Evidently, there is an improvement in the results and the maximum deformation probabilities less than 6% (Figure 7-6). Therefore, it can be considered the success of the proposed technique to show no deformations for non-deformed epochs.

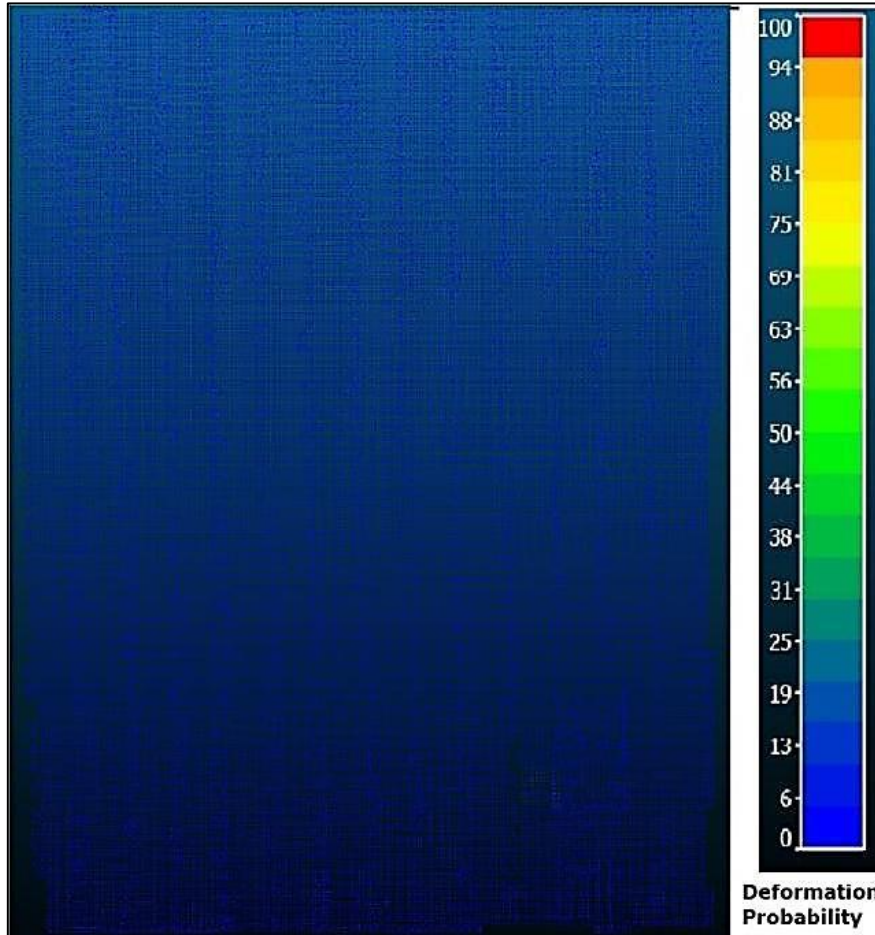


Figure 7-5 The results of the first six epochs after applying the voxel filter.

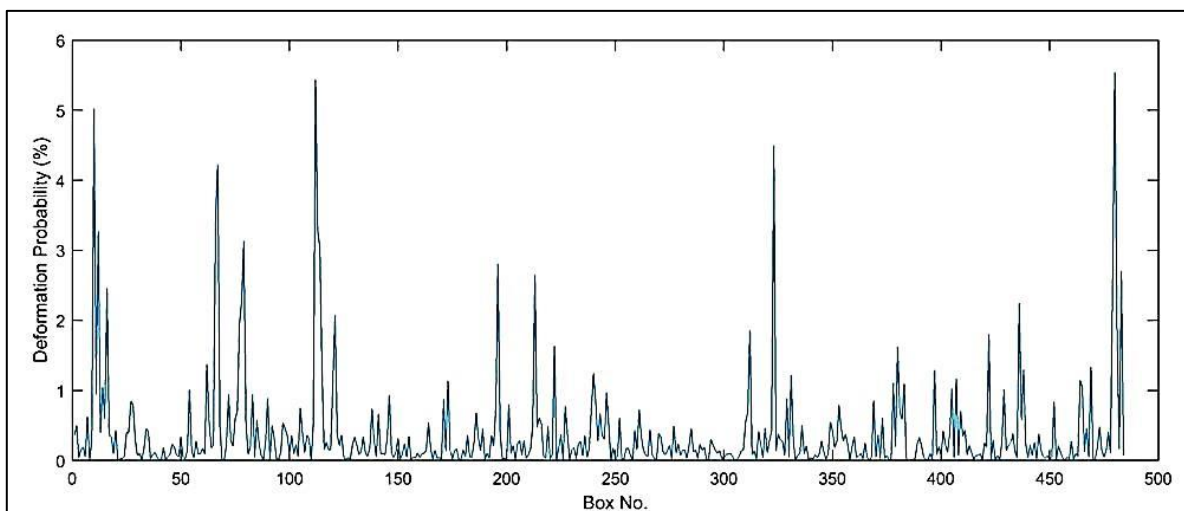


Figure 7-6 The deformation probabilities for epoch six after applying the voxel filter.

7.2.2 Deformed Epochs

As has been mentioned, simulated deformations have been added to some parts of the scanned area through epoch seven to epoch nine. The amount of the deformations was increased gradually (Table 7-1). For all these epochs, the voxel filter was applied before performing the proposed technique.

For the epoch seven, results showed a clear difference compared with the epoch six (Figure 7-7). As can be seen in Figure 7-8, the deformations probabilities increased for the deformed area compared with others, which reached to about 67%. Despite the fact that this probability cannot be considered deformation, it might give an indication.

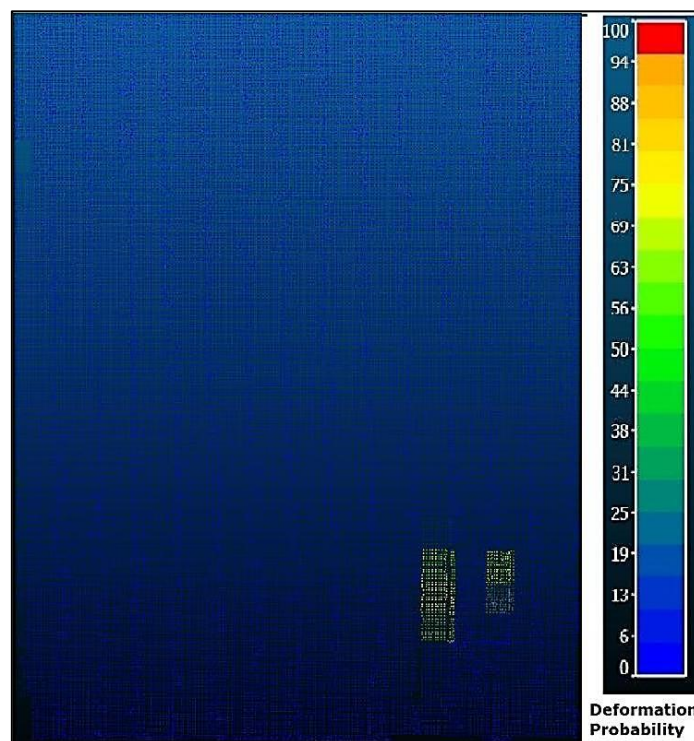


Figure 7-7 The results of epoch seven.

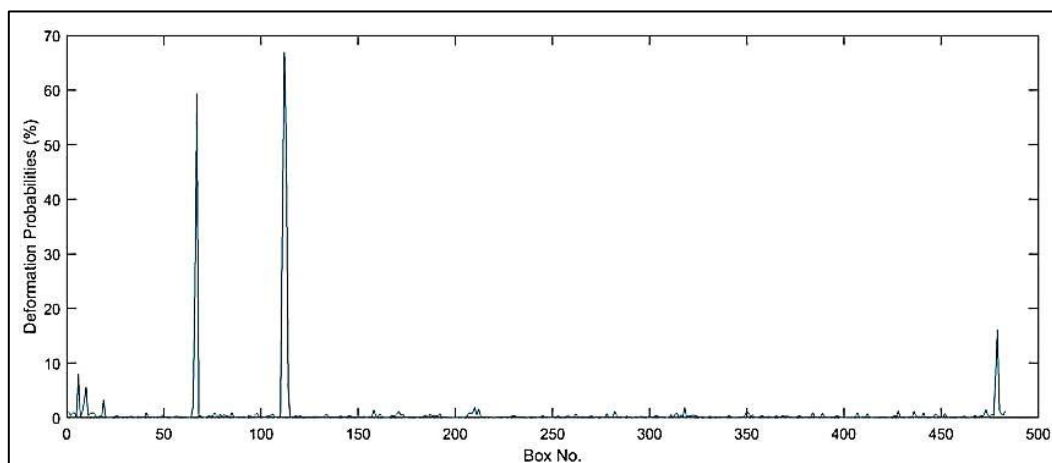


Figure 7-8 The deformation probabilities for epoch seven.

For the epoch eight, the difference became more clarity (Figure 7-9). Hence, the deformation probabilities reached to more than 93% (Figure 7-10). In other words, regarding monitoring, this can set off alarm bells.

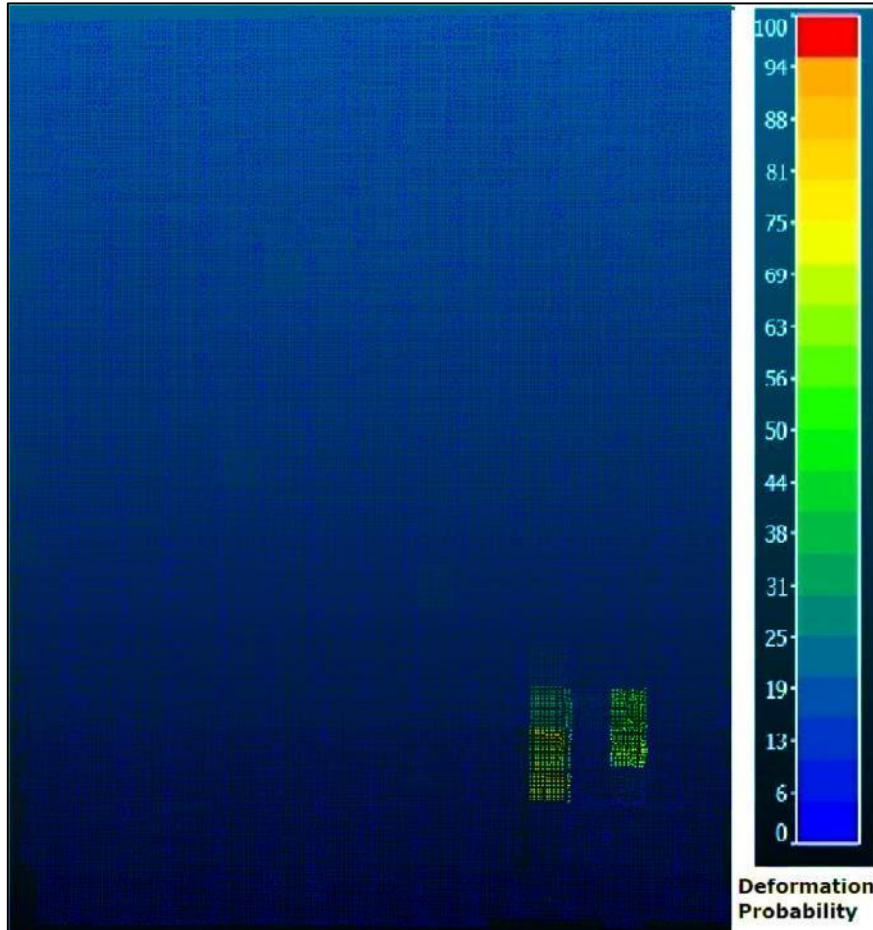


Figure 7-9 The results of epoch eight.

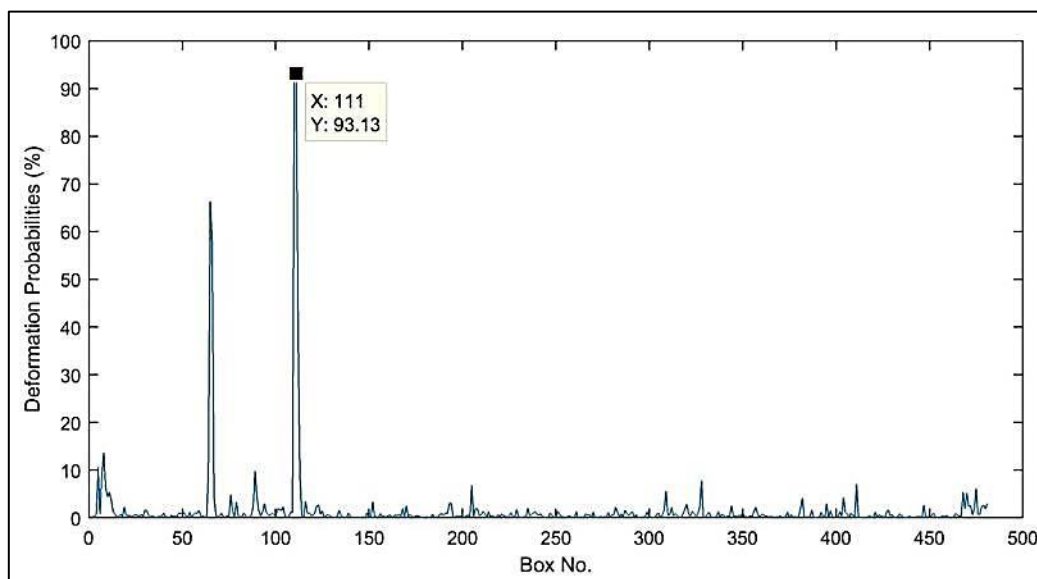


Figure 7-10 The deformation probabilities for epoch eight.

Finally, results of the epoch nine showed a significant difference (Figure 7-11), and the probabilities reached to more than 97% (Figure 7-12). In this case, it can be concluded that there is deformation.

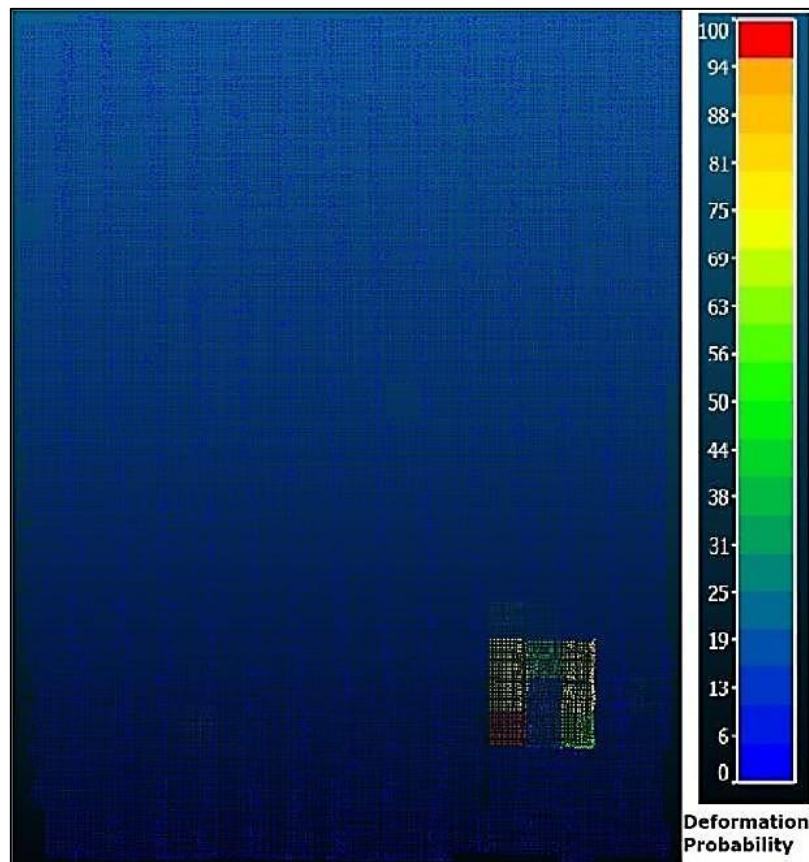


Figure 7-11 The results of epoch nine.

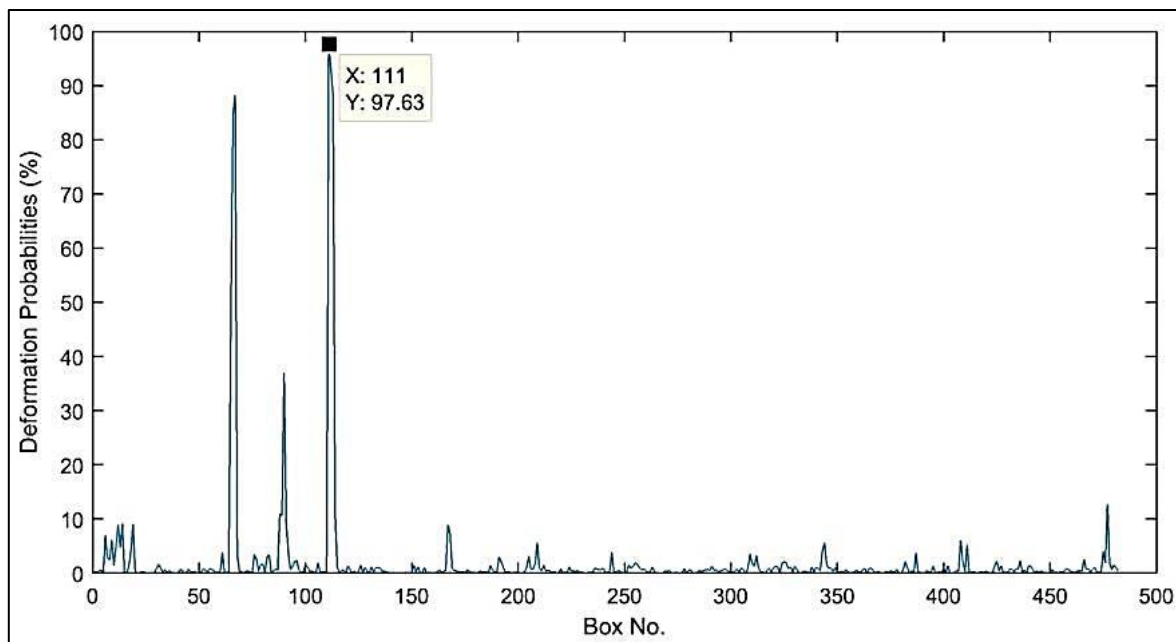


Figure 7-12 The deformation probabilities for epoch nine.

7.2.3 Comparison with Other Methods

To compare the proposed technique with other known methods, the displacement of each point was computed. As an alternative method, CloudCompare software was used to calculate displacements directly from point clouds. For consistency, the voxel filter applied on point clouds inputted for both methods, the proposed and CloudCompare. This process was performed for all deformed and non-deformed epochs, six, seven, eight, and nine.

For non-deformed epochs, the displacements computed by the proposed method are uniform for all parts contrary to that of the CloudCompare (Figure 7-13). In addition, the maximum displacements computed by the proposed method is less than 2mm compared with about 14mm for that calculated by the CloudCompare (Figure 7-14). Consequently, the results of the proposed method can be considered more reliable for non-deformed epochs.

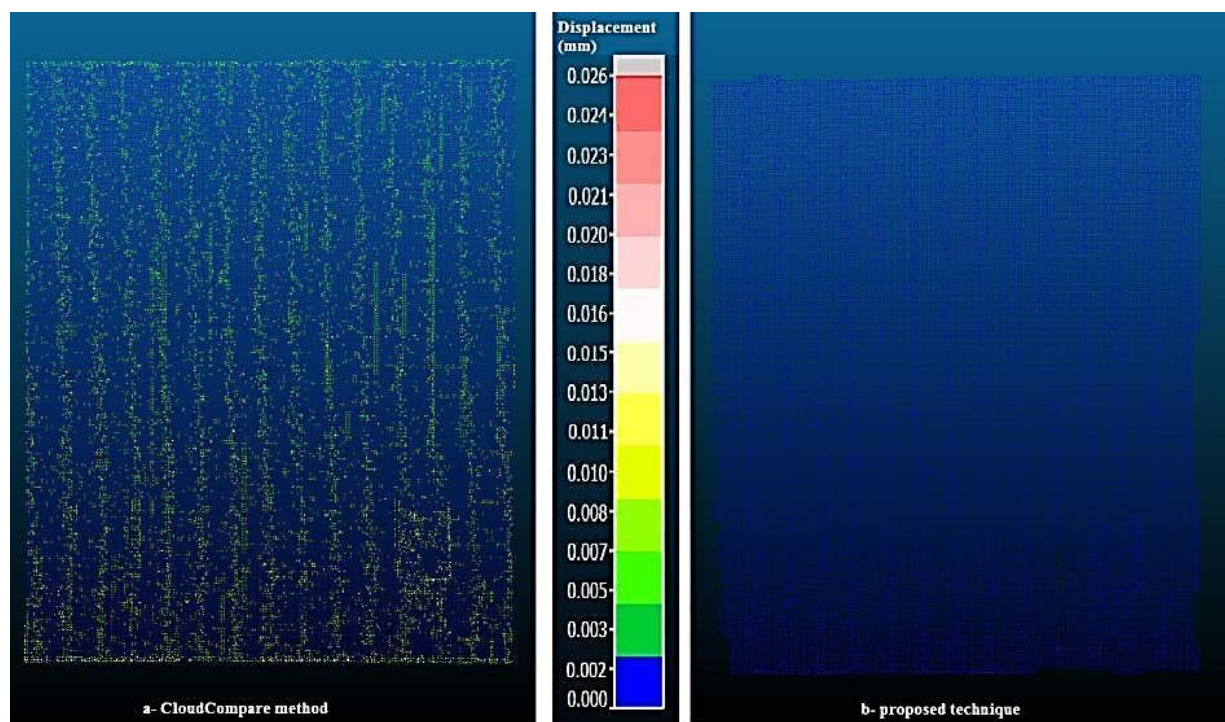


Figure 7-13 The comparison of epoch six displacements computed by CloudCompare and the proposed method.

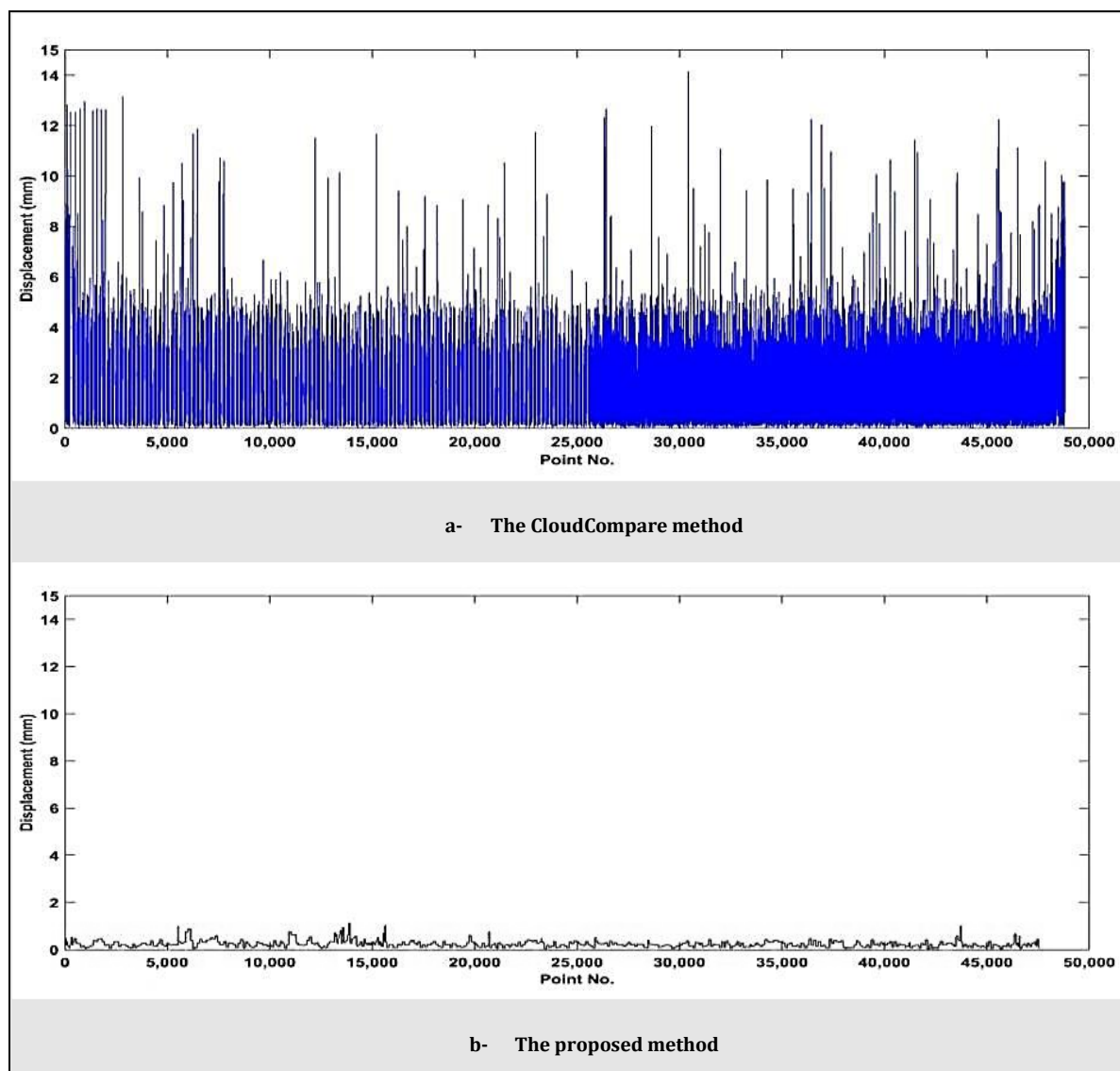


Figure 7-14 The point displacements of epoch six with different methods, CloudCompare and the proposed.

Also, displacements of the deformed epochs computed by the proposed technique are better than that computed by the CloudCompare. For epoch seven, the deformed area can be recognised easily in the proposed technique because its displacements differ significantly from that of other areas (Figure 7-15). In addition, in the proposed method, the displacement value of the deformed area is equal 4mm compared to the actual value (4.6mm), while it reached to 16 mm in the CloudCompare method (Figure 7-16).

Similarly, in epoch eight, the differences of displacements between deformed area and its surrounding are adequate to be recognised in the proposed technique (Figure 7-17). However, the displacement of the deformed area which computed by the proposed method is nearly 8 mm compared to actual deformation

10 mm, while there is a significant difference with that computed by the CloudCompare, which reached to 25 mm (Figure 7-18).

Finally, the results of epoch nine showed the same trends (Figure 7-19, and Figure 7-20), yet the displacements of the deformed area were about 9 mm and 26 mm computed by the proposed and the CloudCompare methods respectively, compare to 16.9 mm actual displacement.

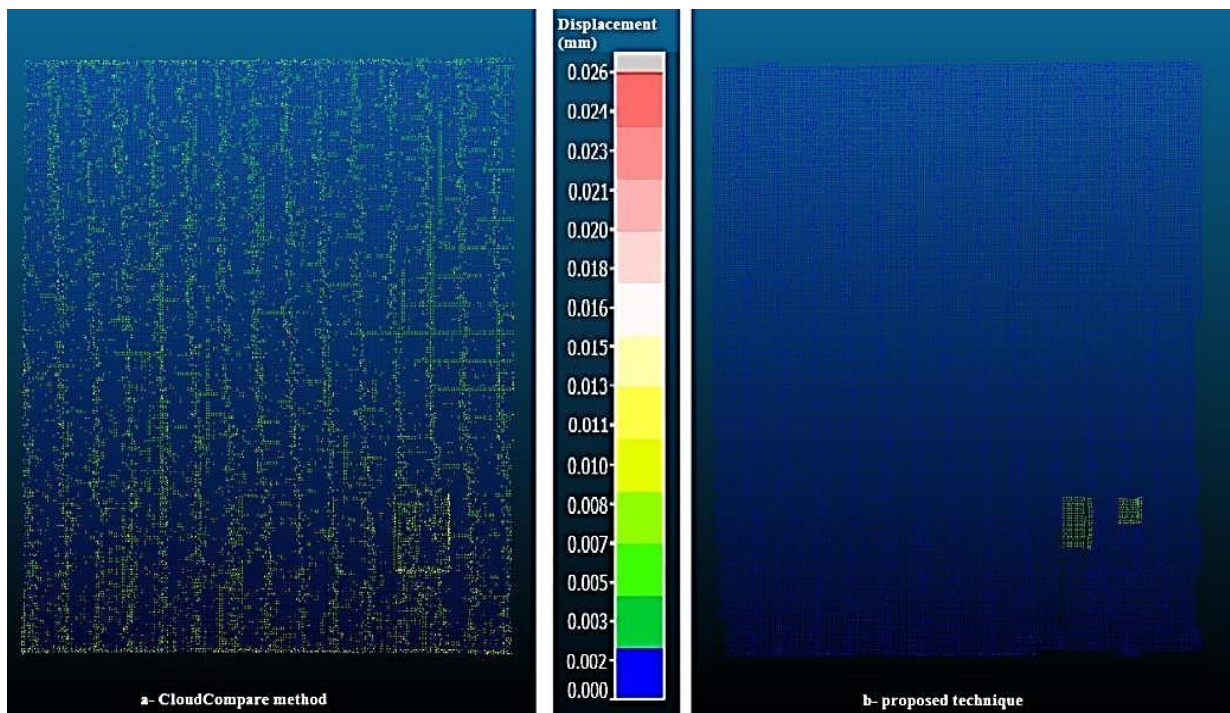


Figure 7-15 The comparison of epoch seven displacements computed by the CloudCompare and the proposed method.

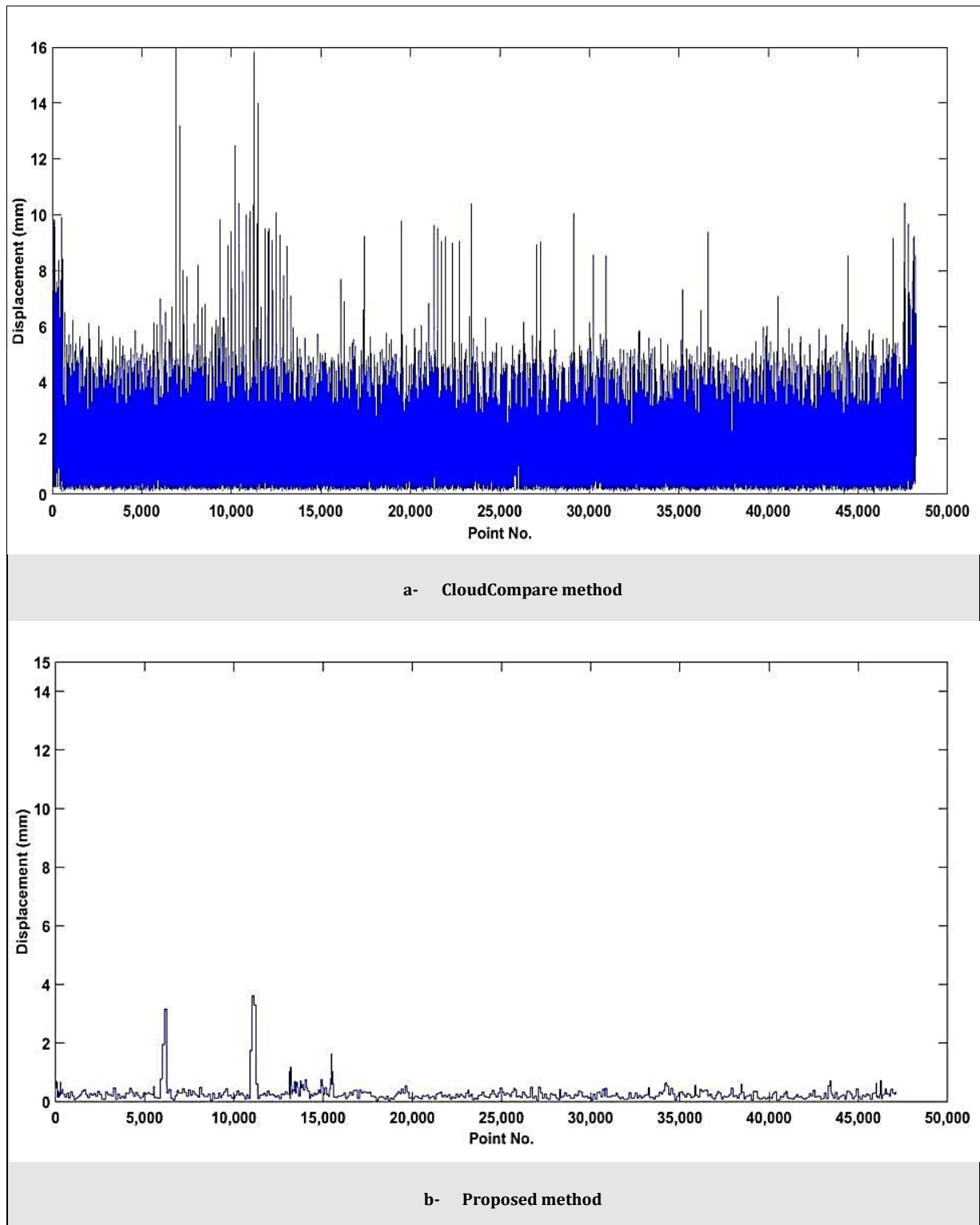


Figure 7-16 The point displacements of epoch seven with different methods, CloudCompare and the proposed.

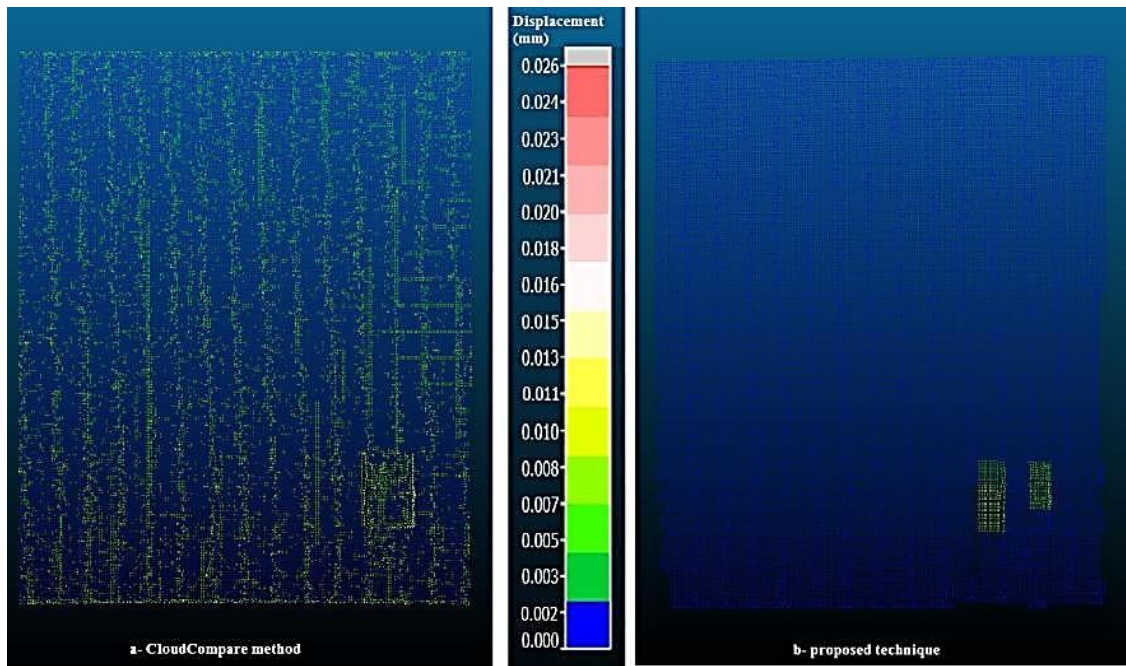


Figure 7-17 The comparison of epoch eight displacements which computed by CloudCompare and the proposed method.

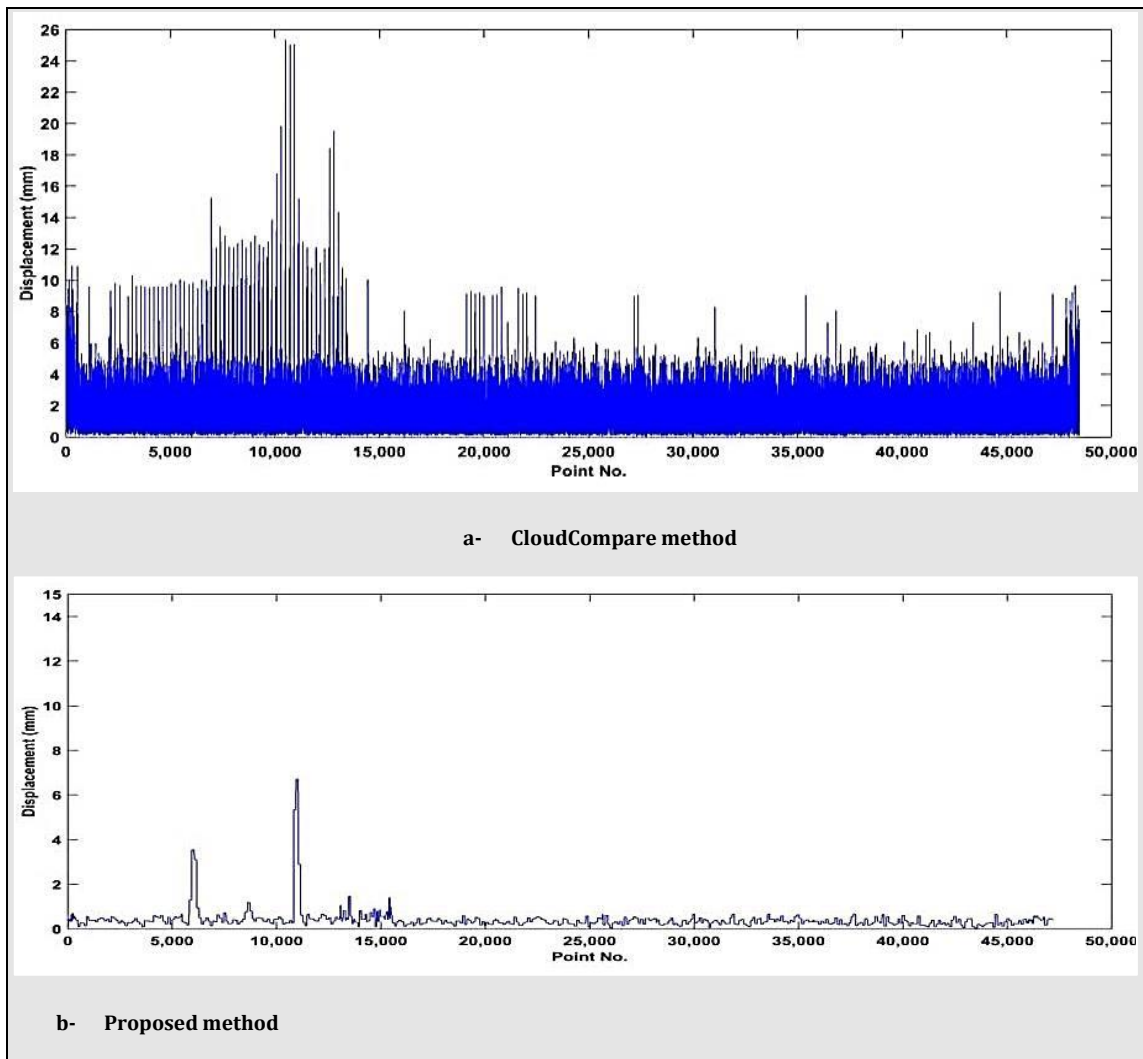


Figure 7-18 The point displacements of epoch eight with different methods, CloudCompare and the proposed.

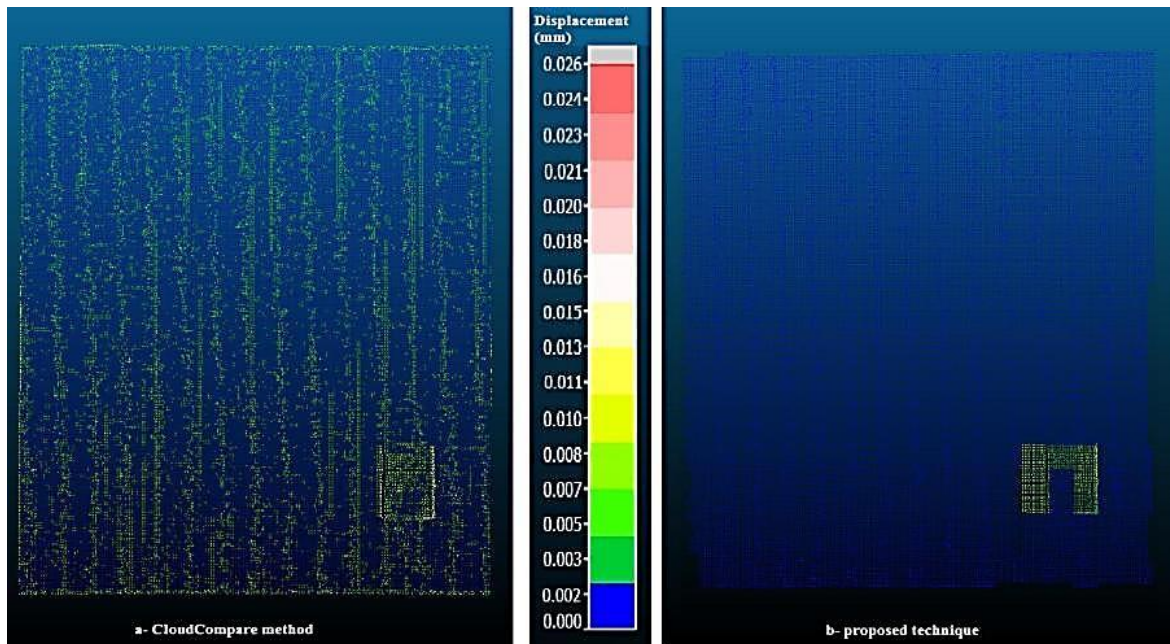


Figure 7-19 The comparison of the epoch nine displacements which computed by CloudCompare and the proposed method.

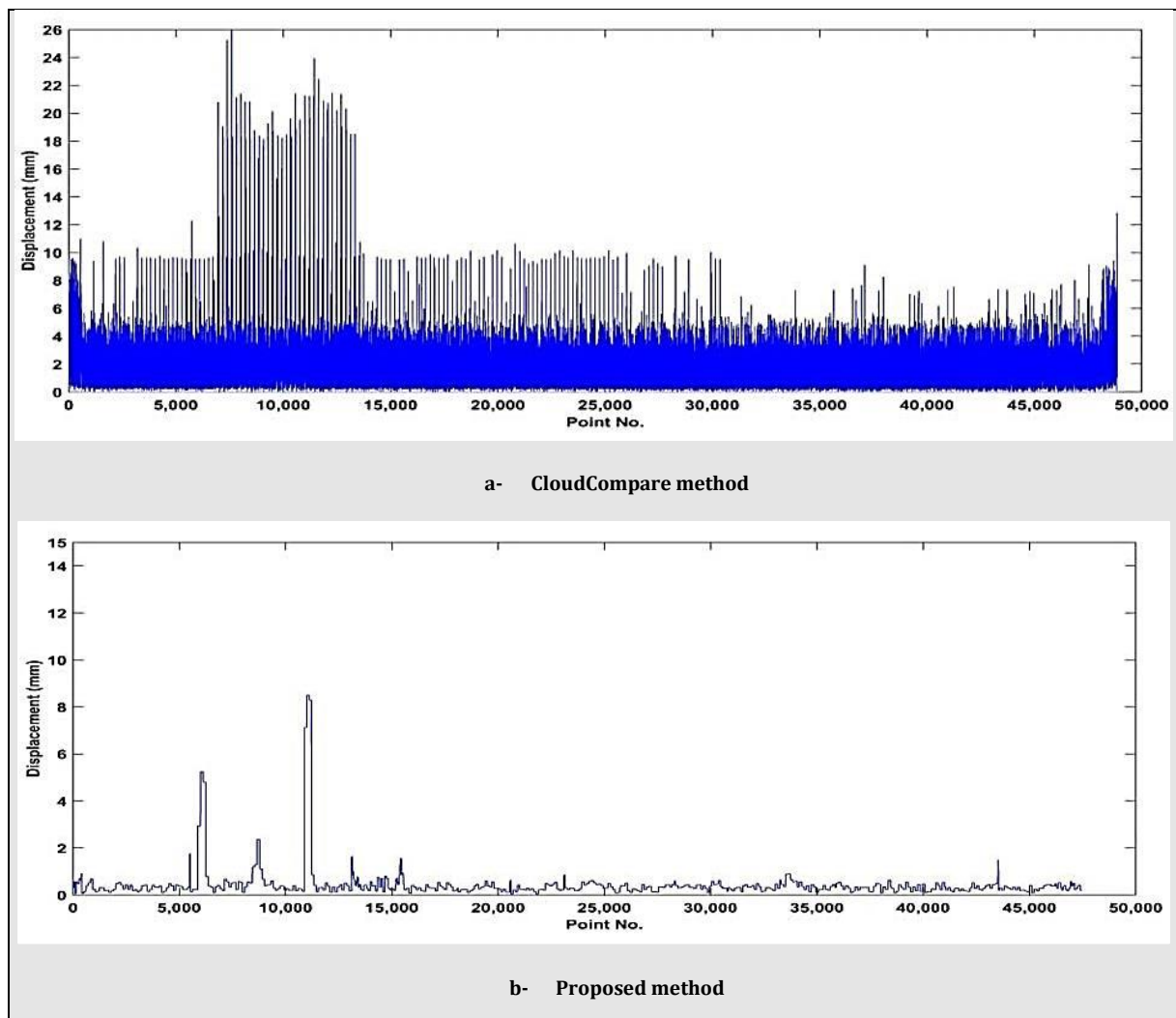


Figure 7-20 The point displacements of the epoch nine with different methods, CloudCompare and the proposed.

7.3 Scanning Complicated Building

In spite the fact that the proposed method is suggested for monitoring historic and heritage buildings where there are unexpected deformations, it has also been tested in modern complicated buildings. The Nottingham Geospatial Building (NGB) was selected for this purpose as it was built from different materials with different textures (Figure 7-21).



Figure 7-21 Different textures and materials of NGB.

The field work was conducted on 19th of March 2015 using scanner Leica Scanstation P20 and total station Leica TS15 (Figure 7-22). According to the scanner position, ranges to the scanned area were between (20 to 25m). In addition, the scanning resolution was set as 3.1 mm with quality level four (Sec. 4.3.1).



Figure 7-22 The location of the second test.

Same as the previous test, a 3D object was pasted on the glass of the NGB (Figure 7-23), and it scanned with building six times, each time representing one epoch. After that, the object moved a little and scanned with the building, which represented epoch seven. Epochs eight, nine, and ten were created with the same way after moving the object. Total station (Leica TS15) was used to determine the displacements of the object through measuring coordinates of small targets fixed on it before and after displacement.

As a result, the whole data contains ten epochs, six non-deformed epochs and four with different deformations. Table 7-2 shows the simulated deformations for the pasted object according to the total station measurements.



Figure 7-23 The 3D object which was used as a simulated deformation.

Table 7-2 The simulated deformations for different epochs.

Epoch No.	DX (mm)	DY (mm)	DZ (mm)
1-6	0.0	0.0	0.0
7	-1.9	-5.0	1.5
8	-5.3	-9.7	7.2
9	-7.6	-16.9	17.2
10	-12.6	-31.5	27.1

7.3.1 Post Processing

Before applying the proposed method, another set of data with less resolution (6 mm) was created from the original data by using the CloudCompare software, employing “Subsample” command which is, unlike the voxel filter, reducing resolution without any smoothing. After that, both the original with 3.1 mm and the new with 6 mm resolution point clouds were processed by the proposed algorithm.

Non-deformed epochs, the first six epochs, showed no significant deformation probabilities in most of the building. However, there were some places with high deformed probabilities (more than 95%) which were located in unstable areas such as cloth fins, in the middle of the building with both 3.1 mm and 6 mm resolutions (Figure 7-24). Consequently, it is not considered failure to the proposed method.

Expectedly, the simulated deformation cannot be recognised in epoch seven where deformation probability is less than 6% (Figure 7-25), due to the fact that the simulated deformation is less than expected noise (Sec.4.3.1). Correspondingly, at the epoch eight, although the deformed area can be distinguished for 3.1 mm resolution, it cannot be seen with 6 mm resolution, where deformation probabilities are 44% and 12% respectively (Figure 7-26).

On the other hand, at epoch nine, the deformation probability for the deformed area reached to 89% for 3.1 mm resolution, while it is still as low as 26% for 6 mm resolution (Figure 7-27). Finally, at epoch ten, the deformed area can be recognised easily for 3.1 mm resolution owing to high deformation probability (99.6%), while 6 mm resolution showed less clarity for the deformed area due to less deformation probability (54%) (Figure 7-28).

To some extent, it might be considered a success for the proposed technique in case of 3.1mm resolution, yet the results of 6 mm resolution cannot be inferred as deformations.

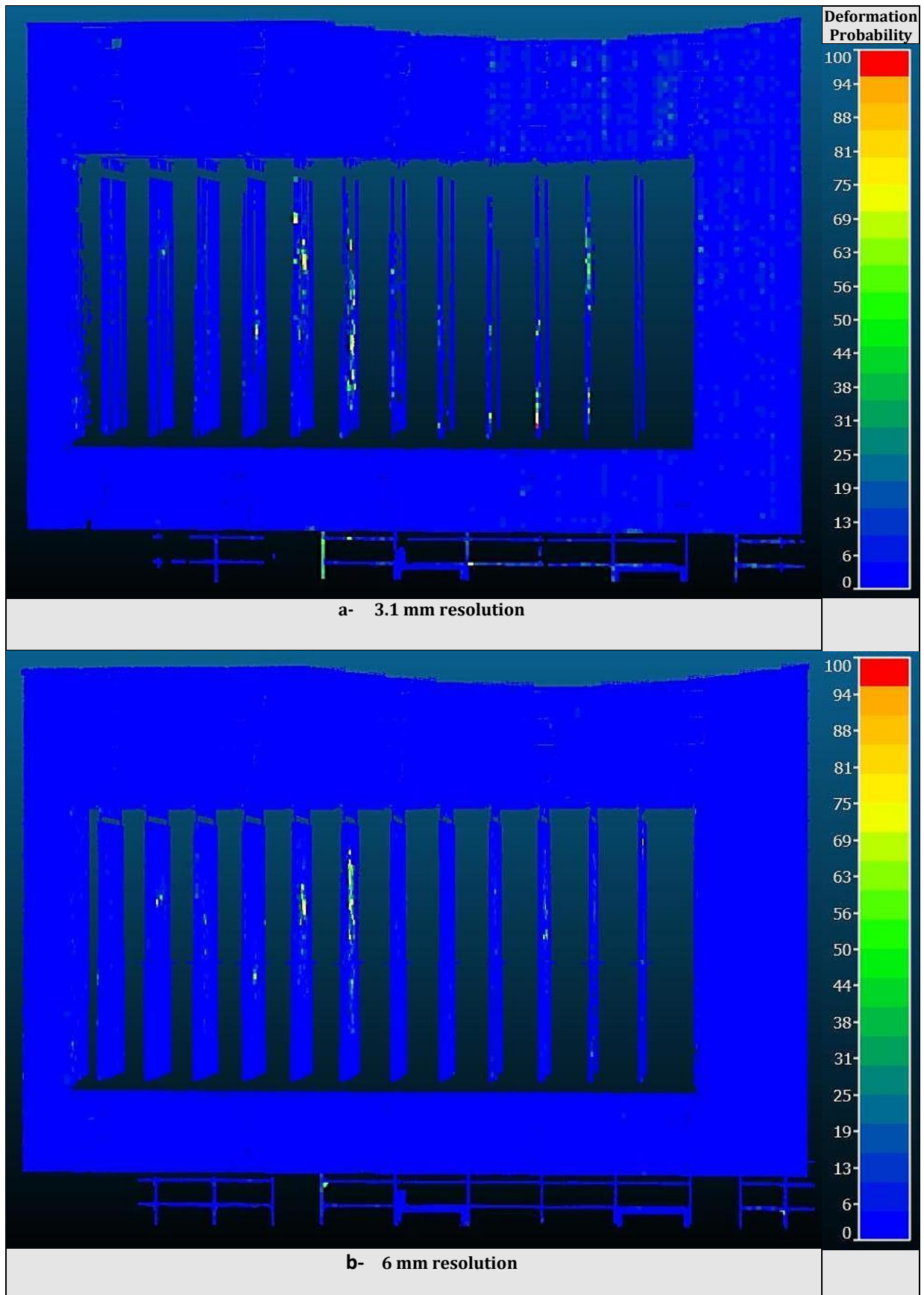


Figure 7-24 The results of epoch six with different resolutions, a- 3.1 mm, and b- 6 mm.

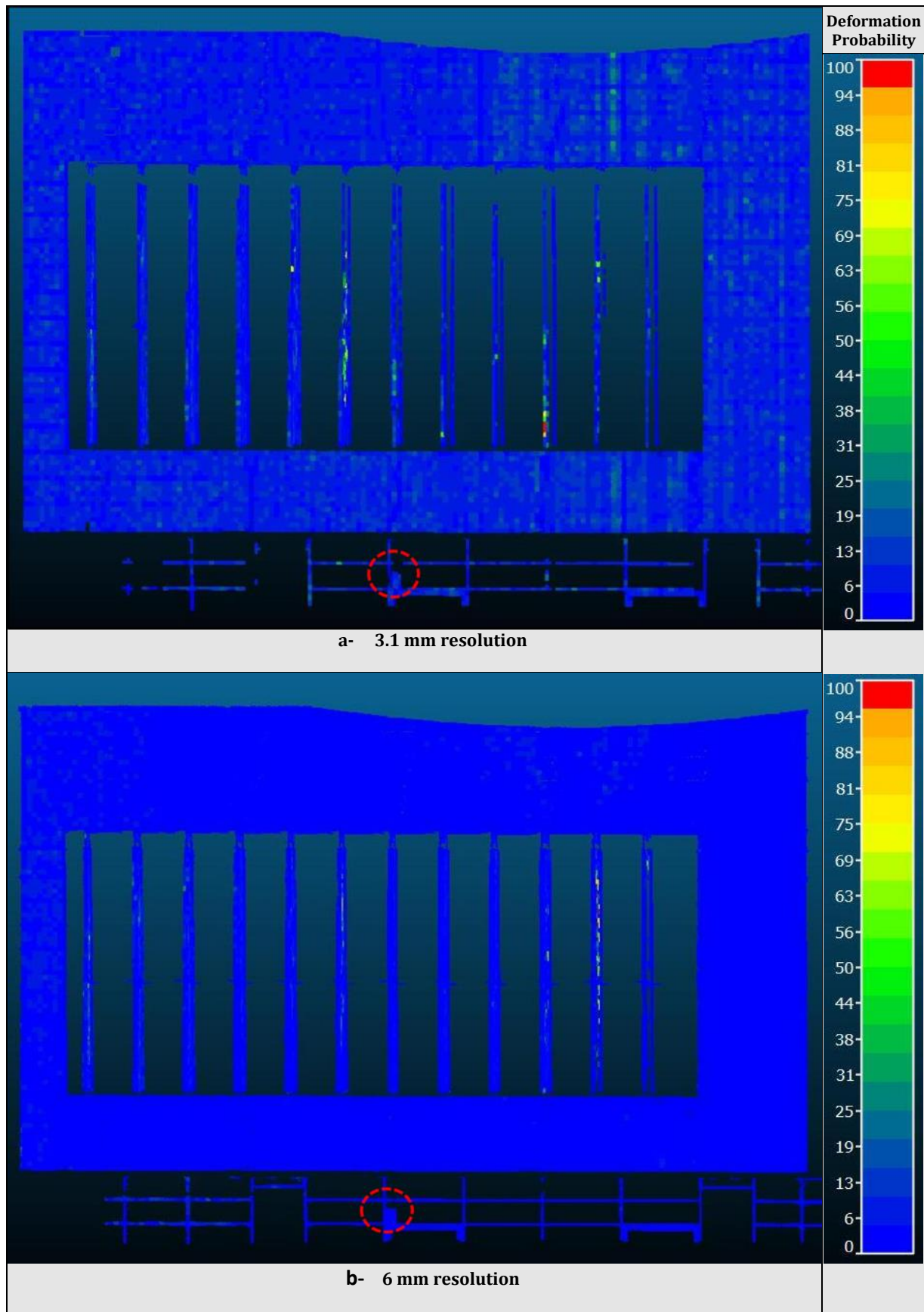


Figure 7-25 The results of epoch seven with different resolutions, a- 3.1 mm, and b- 6 mm.

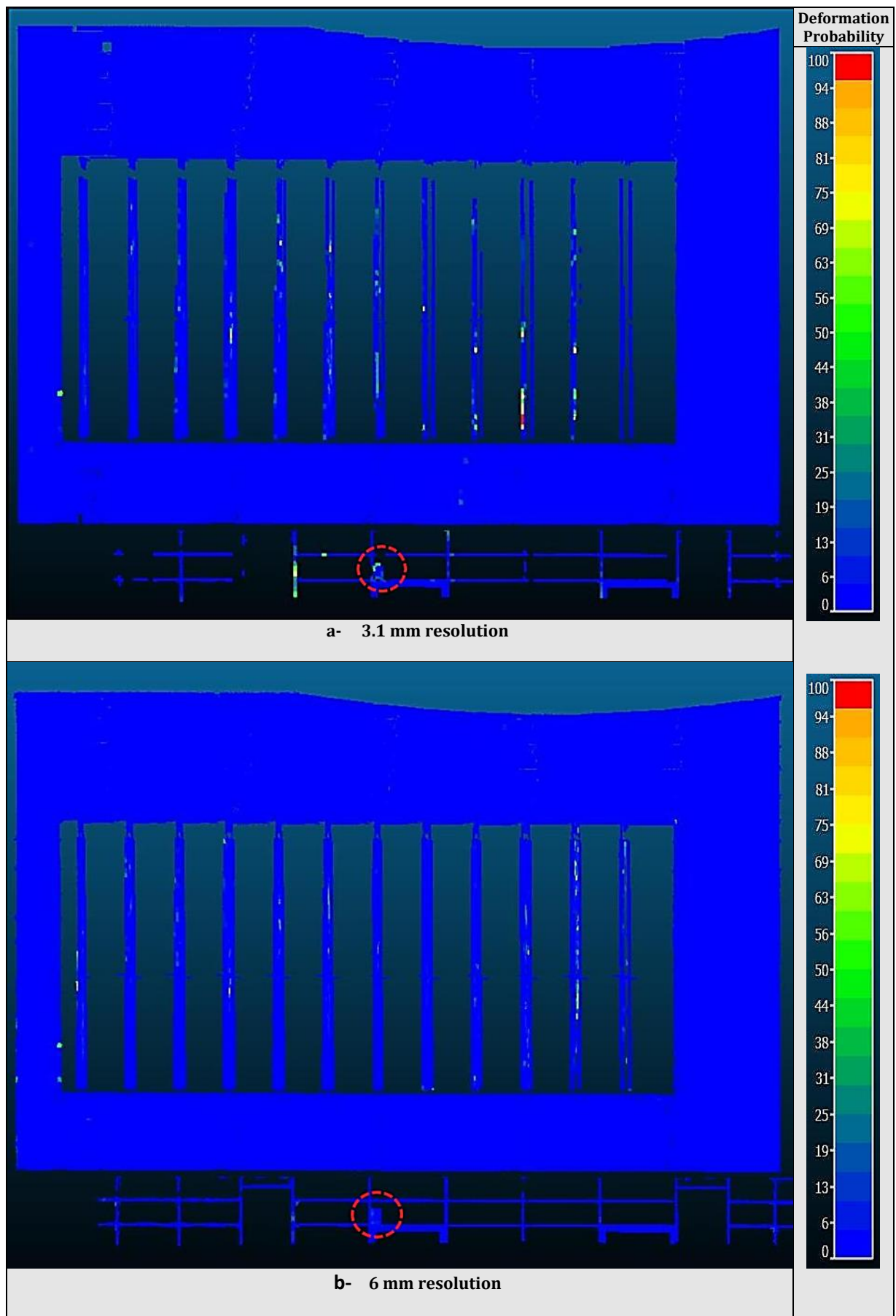


Figure 7-26 The results of epoch eight with different resolutions, a- 3.1 mm, and b- 6 mm.

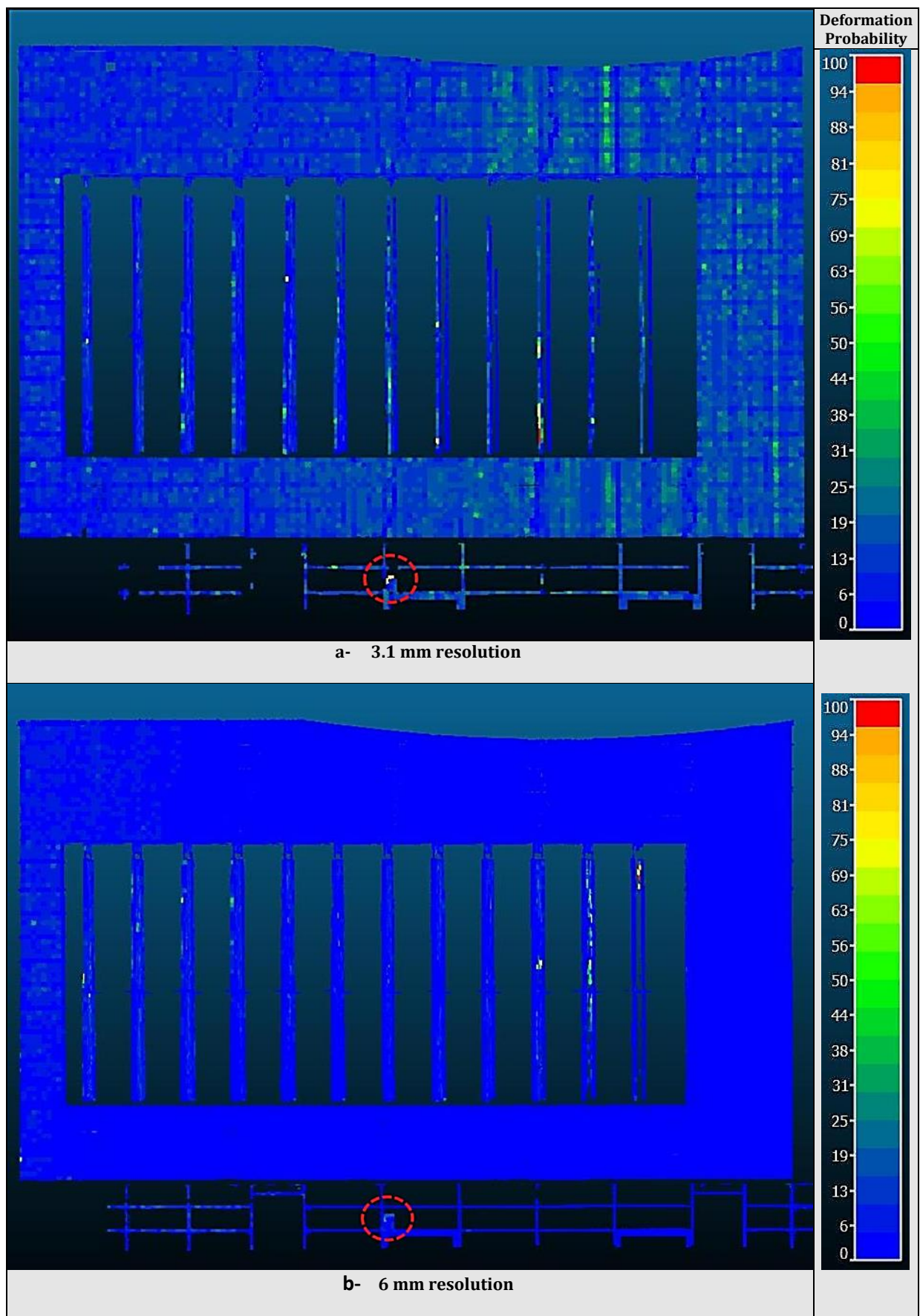


Figure 7-27 The results of epoch nine with different resolutions, a- 3.1 mm, and b- 6 mm.

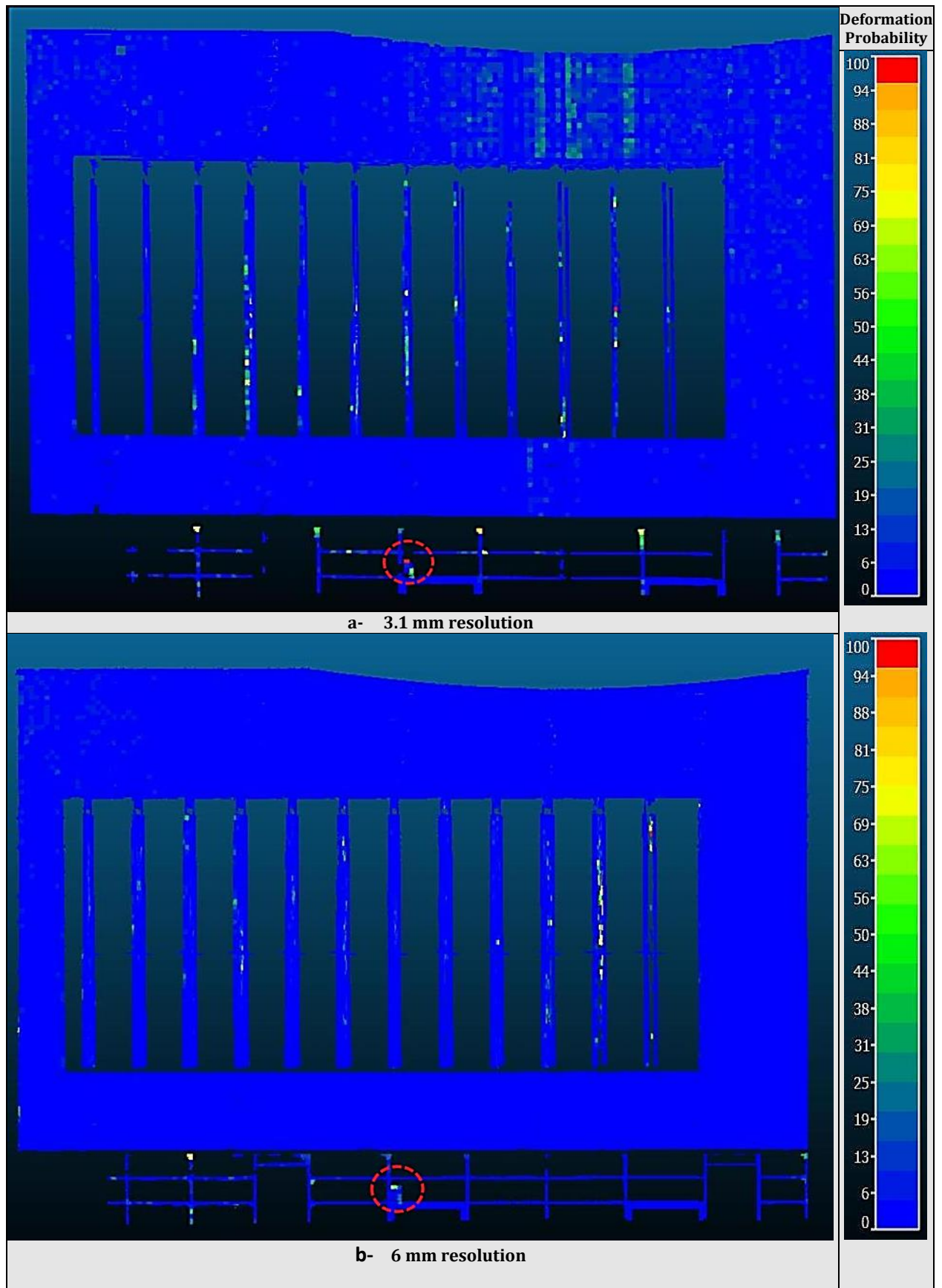


Figure 7-28 The results of epoch ten with different resolutions, a- 3.1 mm, and b- 6 mm.

7.3.2 Improving Results

According to previous tests outputs, it is expected to improve the results through applying downsampling by the voxel filter. Therefore, it was applied on point clouds for all epochs (deformed and non-deformed). Figure 7-29 to Figure 7-33 are the results of the proposed method after applying the voxel filter with 10 mm voxel size. Obviously, there are improvements in the detection ability. For instance, deformation probability of the deformed area of epoch seven increased in this result from 6% to 27% compared to the results of the 3.1 mm resolution. In addition, the results of epoch eight have been improved through increasing deformation probability up to 79%, while it was only 44% in the result of the 3.1 mm resolution. On the other hand, at epoch nine and epoch ten, the probabilities of deformation have not significantly changed, as 83% and 99.8% respectively. Figure 7-34 shows the deformation probabilities of the deformed area in different cases; clearly, after applying the voxel filter the ability of the proposed method to detect deformations increased with lower resolution.

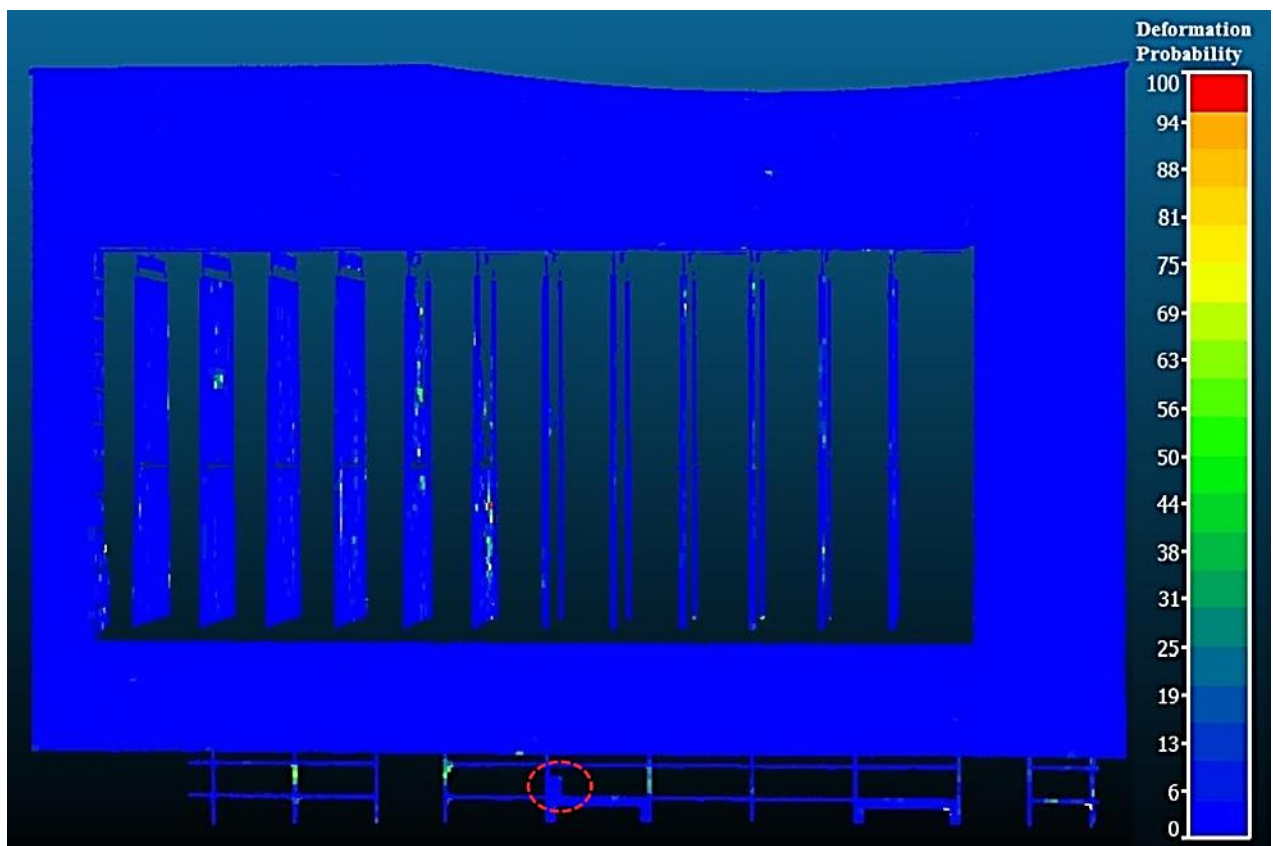


Figure 7-29 The results of epoch six after applying the voxel filter.

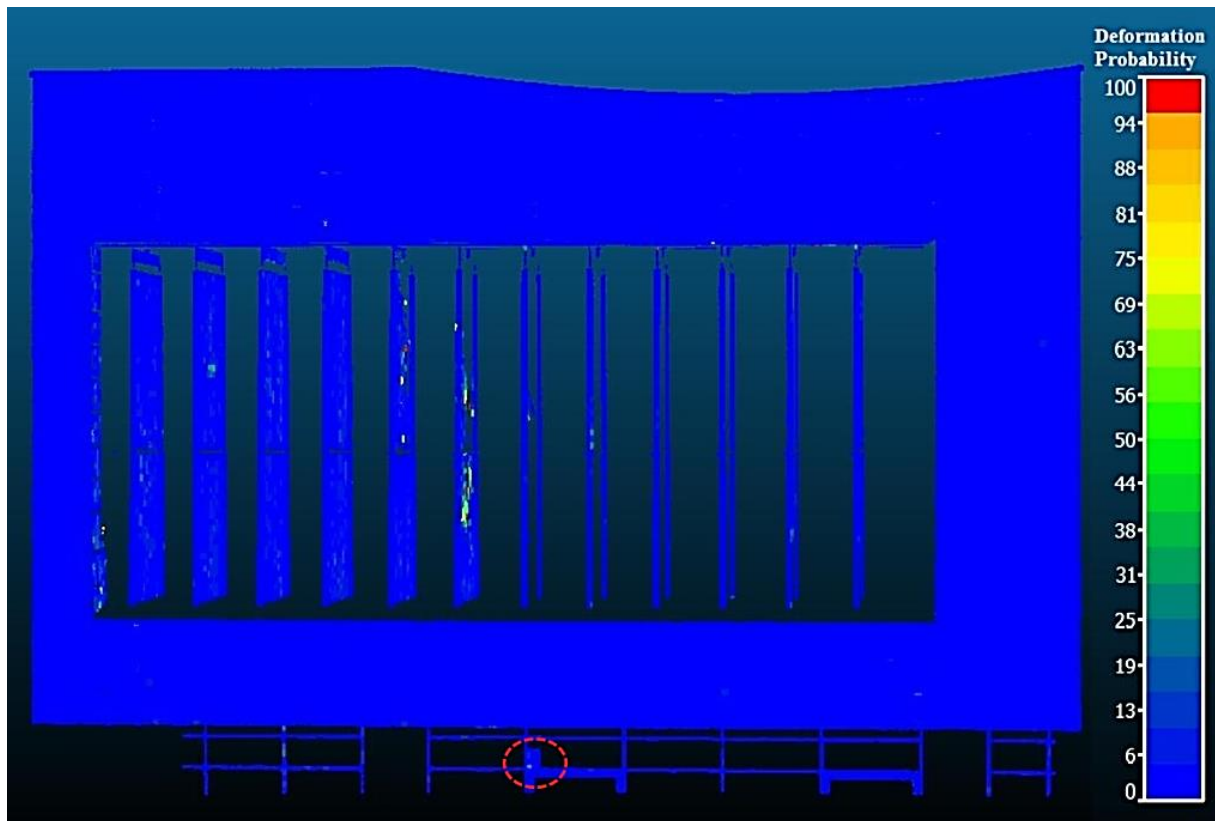


Figure 7-30 The results of epoch seven after applying the voxel filter.

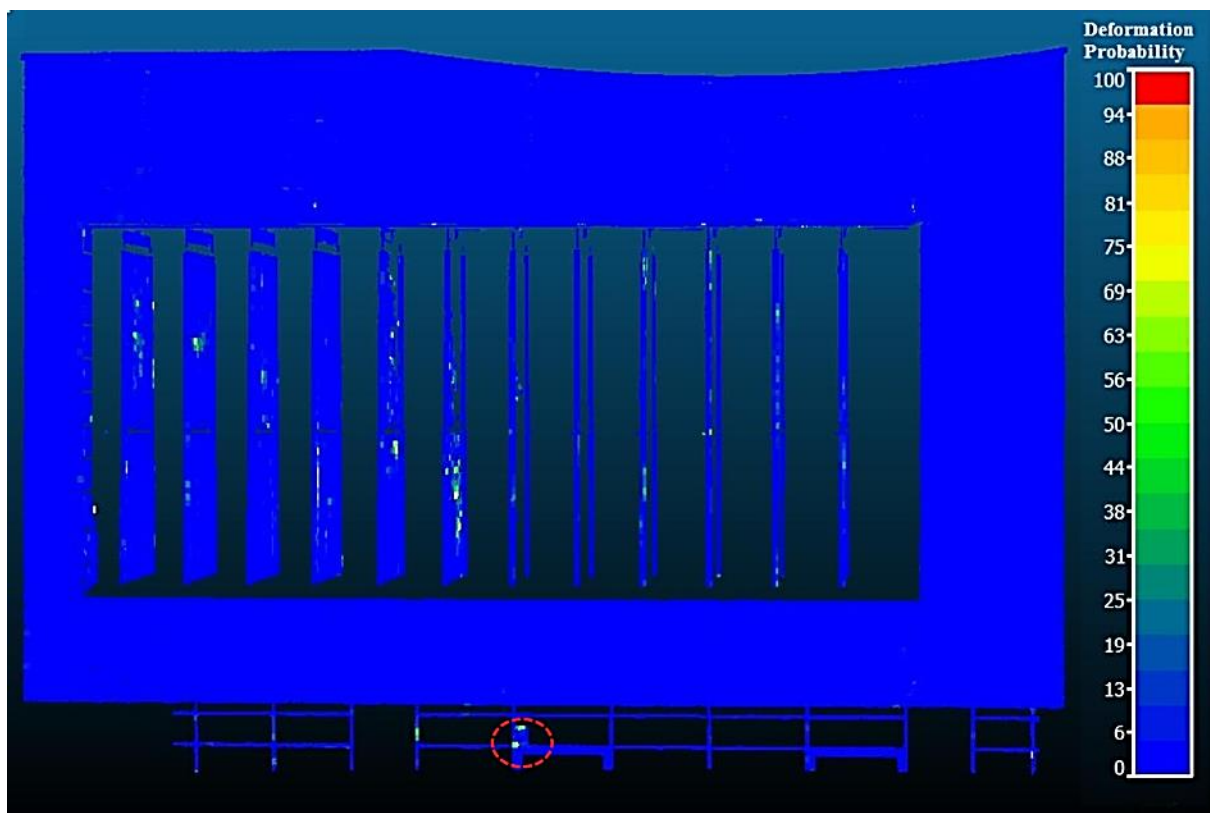


Figure 7-31 The results of epoch eight after applying the voxel filter.

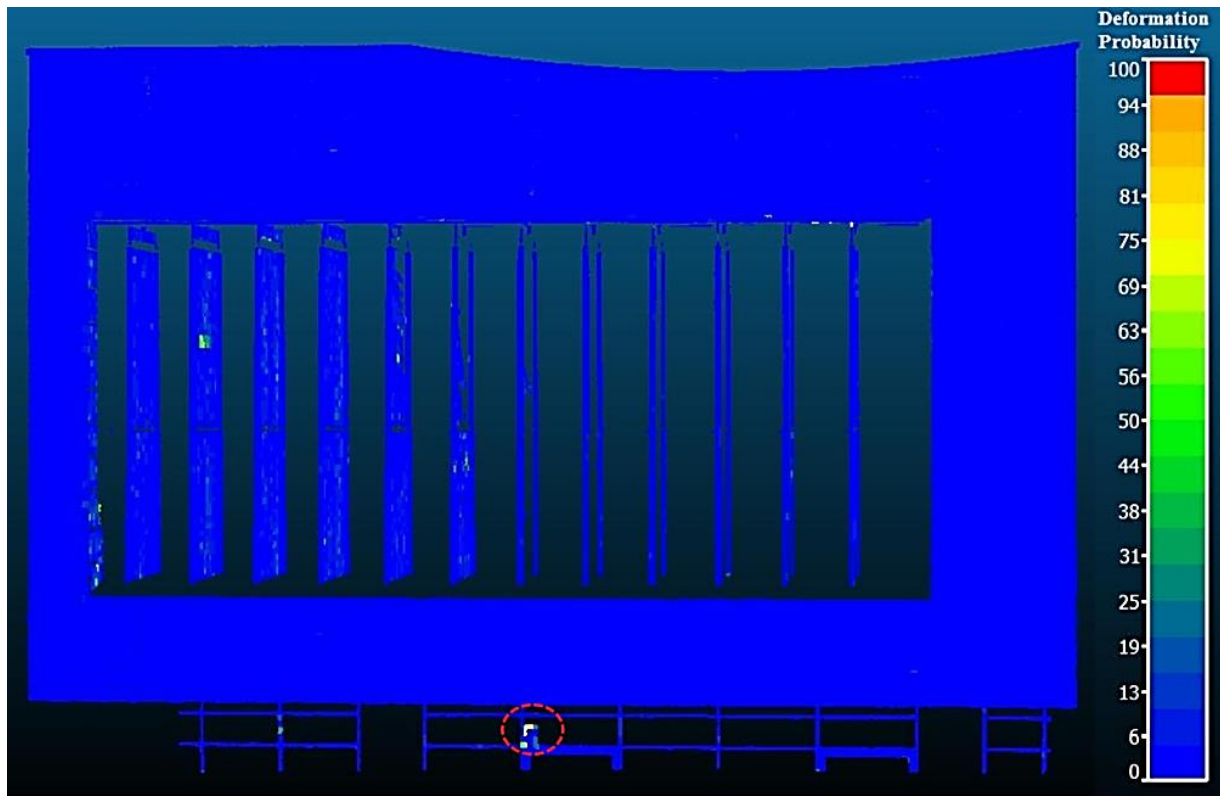


Figure 7-32 The results of epoch nine after applying the voxel filter.

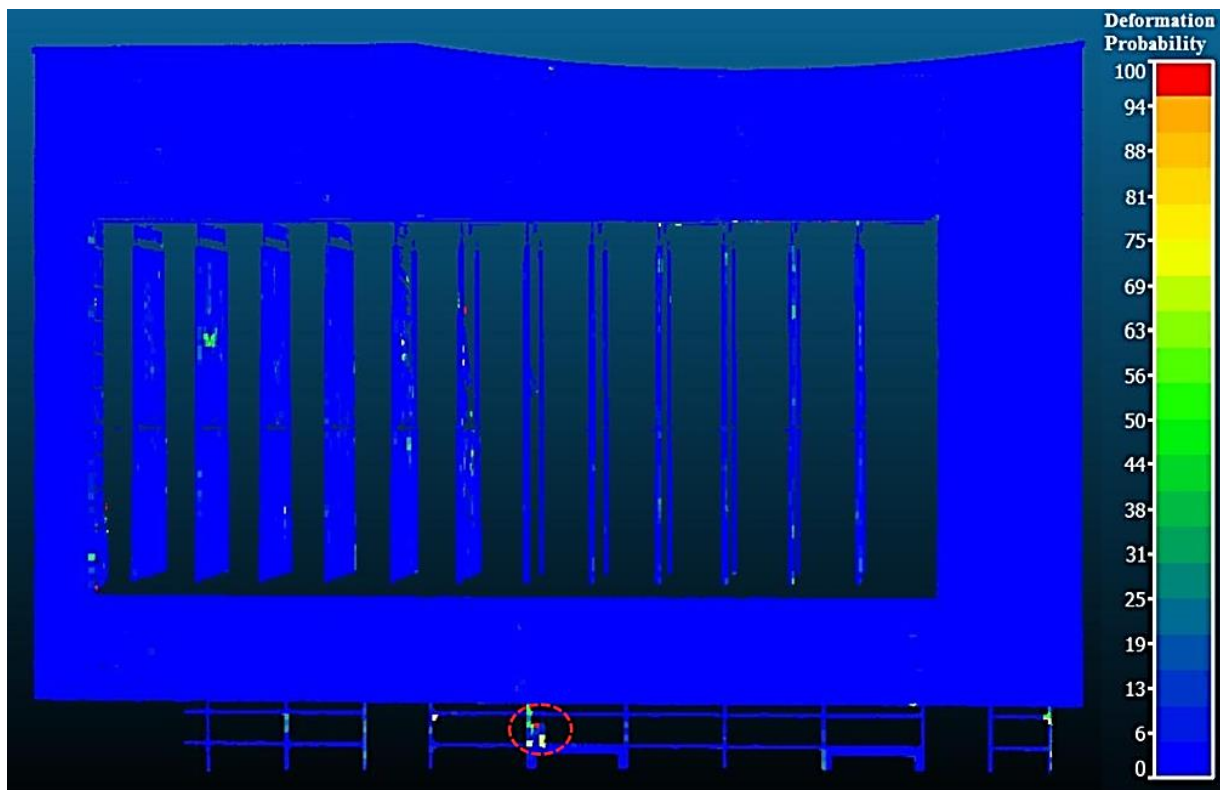


Figure 7-33 The results of epoch ten after applying the voxel filter.

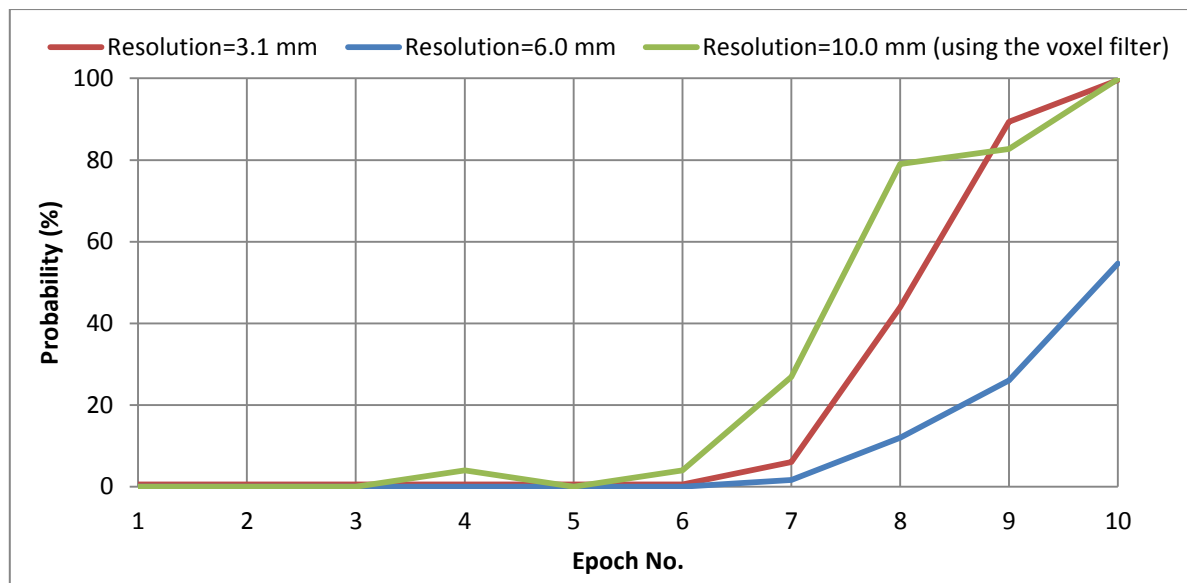


Figure 7-34 The deformation probabilities of the deformed area.

7.4 Chapter Conclusions

In this chapter, the second stage of the validation experiments has been discussed, which is testing the proposed technique in the real scan data with simulated deformations. The indicators of the performance can be summarized as follows:

First test

- In the case of non-deformation, there is a failure of the proposed method where a lot of non-deformed boxes showed high deformation probabilities. The possible reason is that data is contaminated with a lot of noise because the quality level one was used which means less repeating measurements, and therefore more noise.
- After applying voxel filter, the proposed technique succeeded to show no deformations for non-deformed epochs. Also, it succeeded to detect and localise the deformations.
- Potentially, it can give an indication of areas with deformations less than the noise.
- The results of the proposed method can be considered better than that those obtained with CloudCompare software.

Second test

- To some extent, the proposed technique succeeded to detect and localise deformations.
- It is not recommended for monitoring modern and complicated buildings. Yet it has been developed for monitoring historic ruins. Probably, if the proposed method is extended to include intensity, it may work properly with different materials; this is out of the scope of this research.

CHAPTER Eight: **MONITORING OF BELLMANPARK LIMEKILN**

8.1 Introduction

Until this stage of research, the validation of the proposed method has been carried out in both simulated point clouds with simulated deformations and real scan data with simulated deformations. As a final validation test, the proposed method needs to be applied to real data with real deformations. For this purpose, the researcher has contacted English Heritage (Heritage, 2015) for support. Thanks to Historic England (Historic, 2015b), especially Geospatial Imaging(GI)-Remote Sensing Team (RST), we have received data for the Bellmanpark Limekilns, Clitheroe, Lancashire (Historic, 2015a) monitoring project. This is a live project for Historic England and addresses a historic building that currently has some structural issues.

In this chapter, the results and analysis of applying the proposed method to Bellmanpark Limekilns project will be discussed.

8.2 Location and Background

Bellmanpark Limekilns is a part of an archaeological site which is located north-west of Bellman Farm, Clitheroe, Ribble Valley, Lancashire (Figure 8-1). This site was scheduled under the Ancient Monuments and Archaeological Areas on the 3rd of September 2004 (Historic, 2015a). In addition to Bellmanpark Limekilns, it includes 90 m of an associated tramway, embankment and the remains of a bridge (abutment, and buried remains of a trestle) along which lime was transported from Bellmanpark Quarry to the lime kilns (ibid).

The Limekilns was constructed in 1877 adjacent to the railway between Chatburn and Blackburn. It consists of a huge rectangular bank with four kilns built into the slope near the railway. Beneath this bank, there are two partly infilled tunnels through which a railway branch line runs from the adjacent main line. It was built with about 15 m deep, 30 m long and 15 m high and constructed with limestone blocks (ibid) (Figure 8-2).

The structural engineer of Historic England/Heritage At Risk (HAR) for the North West, has advised that cracks in the structure need to be carefully monitored over the foreseeable future (e.g. in six and twelve months) to determine whether the cracks are historical or active, using the full laser scan as baseline data.

Consequently, in June 2015, HAR projects officer for the North West requested support from GI-RST to handle this project.

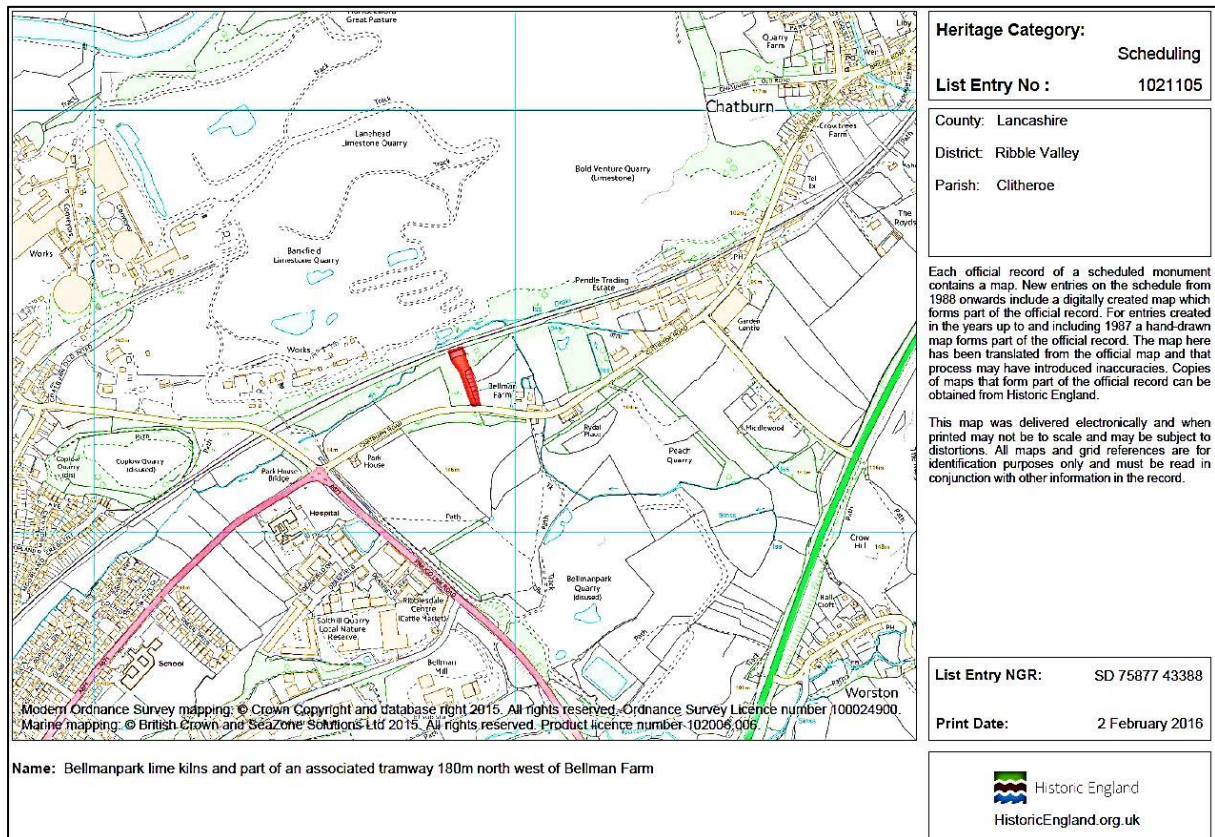


Figure 8-1 Bellmanpark Limekilns location (Historic, 2015a).



Figure 8-2 Bellmanpark Limekilns (source: GI-RST)

8.3 Received Data

The NW HAR team has commissioned a detailed structure report by a contracted structure company, and the latter sub-contracted a full laser scan of the kilns to another company. This scan was acquired on 25-26 of June 2015 and considered as a baseline for monitoring. Unfortunately, there is no metadata available for this scan (e.g. scanner model, resolution, methodology, registration accuracy, etc.). We only know that the data was georeferenced using control stations based on the Ordnance Survey (OS) grid, employing RTK GNSS equipment with a network correction provided by a Virtual Reference Station (VRS).

The second set of data was collected by GI-RST on 8-9 December 2015. A Leica P40 Scanstation was used for scanning while RTK-GNSS based on Smartnet was employed to get two points related to the OS grid system and then traversed off them, using a total station, to survey 25 control points, 17 of them being scanner targets (T1-T17) (Table 8-1). Also, this data consists of 15 scans, and each includes three or more of targets points (Table 8-2).

Table 8-1 Bellmanpark OS control points (source: GI-RST).

Point No.	Easting	Northing	Elevation	Remark
1	375839.494	443404.039	95.746	Not Target points
2	375862.657	443402.990	97.033	
3	375883.199	443415.185	91.332	
4	375876.614	443440.510	93.375	
5	375837.097	443427.683	93.235	
6	375837.294	443428.230	91.629	
7	375858.993	443406.129	97.362	
8	375873.907	443439.687	93.589	
T1	375848.902	443409.889	97.096	Scanner Targets
T2	375863.228	443410.750	96.986	
T3	375858.110	443402.053	95.994	
T4	375874.027	443415.205	94.643	
T5	375880.416	443414.109	92.201	
T6	375878.773	443437.635	92.293	
T7	375871.811	443437.859	91.909	
T8	375874.339	443440.383	93.647	
T9	375869.182	443438.999	92.864	
T10	375868.418	443434.947	94.253	
T11	375855.316	443430.178	94.648	
T12	375854.514	443434.475	93.390	
T13	375839.162	443429.264	92.977	
T14	375836.901	443423.402	94.047	
T15	375831.298	443421.522	91.652	
T16	375833.587	443410.200	95.366	
T17	375841.146	443407.342	96.997	

Table 8-2 Targets of different scans (source: GI-RST data).

Scan	Target points
1	T1-T2-T3
2	T1-T2-T3-T4
3	T2-T3-T4-T5
4	T2-T4-T5-T6
5	T4-T5-T6-T7
6	T5-T7-T8
7	T5-T6-T7-T8
8	T5-T6-T7-T8
9	T9-T10-T11-T12
10	T9-T10-T11-T12
11	T10-T11-T12-T13
12	T11-T12-T13-T14
13	T12-T13-T14-T15
14	T13-T14-T15-T16
15	T14-T15-T16-T17

8.4 Data Issues

As has been mentioned, we have received two sets of data with about a six-month separation period.

Though studying this data, the following problems need to be solved:

- 1- There are only two epochs available, whereas the proposed method based on GPA needs more than two epochs (chapter five). To address this problem, the researcher has duplicated the first epoch and to keep consistency doubled the weight of the second epoch. Hence, the processed data consist of three epochs: the first and the second represent the data collected in June 2015 with unity weight, and the third is data collected in December 2015 with double weight.
- 2- There is no information about the resolution and the scanner model for the first epoch. Theoretically, this does not affect results of the proposed method because it unifies resolutions for all epochs in one step and mitigates data noise in another step (chapter five).
- 3- No report is available for the registration and georeferencing accuracy for the first epoch. Fortunately, it is georeferenced to the OS grid; hence, it has an absolute coordinate system. A logical analysis has been suggested to solve this issue. Accordingly, the proposed method is applied twice; firstly on the original data assuming that both sets are accurately georeferenced to the same coordinate system, and secondly after registering both sets using ICP (Sec 3.3.3.1). Then, we can compare the results and continue with a more logical solution.

- 4- Typically, all scans should be registered to a single coordinates system using tie points; and then georeferenced to a ground coordinates system using control points. This procedure cannot be carried out for the December 2015 epoch because there are only two constraints between scan 5 and 6, and no constraints between scan 8 and 9 (Table 8-2). Fortunately, a total station was used to distribute control points to ensure good accuracy. In addition, all scans have three or more control points. Therefore, it has been suggested to georeferencing all scans directly to OS system using points (T1-T17). The registration report reveals optimistic results with only 0.001m Mean Absolute Error (MAE) (Appendix B).

8.5 Results

For the purpose of the analysis, the structure's sides have been named according to faced directions e.g. SE for side faces South East, SW for side faces South West, etc. (Figure 8-3). In addition, to reduce required memory and accelerate processing, the coordinates system has been shifted ($\Delta X = -375800.00$, $\Delta Y = -443400.00$, $\Delta Z = 0.0$). Furthermore, CloudCompare software is considered as an alternative solution to determine deformations because it is suggested to be used by GI-RST to implement the project.



Figure 8-3 Bellmanpark Limekilns side names.

8.5.1 Unregistered Epochs

As has been mentioned, the proposed method has been applied firstly to the original data before performing any registration between data sets (Appendix C). Figure 8-4 illustrates the deformations probabilities for the Limekilns faces. It can be seen that all faces show high probabilities of deformation. Consequently, with only a six-month period between two epochs, this may give an indication that there is a shift between two coordinates system due to insufficient accuracy for georeferencing.

Similarly, the absolute distances between the two clouds, which were computed by CloudCompare software (Figure 8-5), show significant figures for all Limekilns faces. For instance, the distances for the face NW are more than 0.015m and in some parts reach to 0.035m, although there are no clear structural problems. Furthermore, the opposite face (SE) shows significant distances value (more than 0.035m) in some parts.

Furthermore, benefiting from the outcome of the proposed method, the deformation direction has been computed for each face. As aforementioned, the proposed method computes a deformation vector for each box which was used to compute the deformations result for each face by summation vectors in each face (Appendix C and Table 8-3). Figure 8-6 reveals the representation of the unit vectors for deformations result for each face before ICP-registration. Evidently, three of these vectors are pointing in the same direction. In addition, vectors of opposite faces (SE and NW) are almost identical. This means, the shift between two data sets comes from georeferencing or the whole structure deformation (rigid body movement). The latter reason is less possibility due to the huge size of the structure and the short observation period (six months). Therefore, the likely reason is the georeferencing shift between epochs.

Consequently, ICP registration has been used to register epochs. For this purpose, CloudCompare software has been employed to perform such registration. The registration results (Figure 8-7) reveal a shift of about 2-4 centimetres which is nearly as same as the precision of the RTK-GNSS. However, the RMS can be considered high (0.043 m), and this is probably due to the occurrence of deformations.

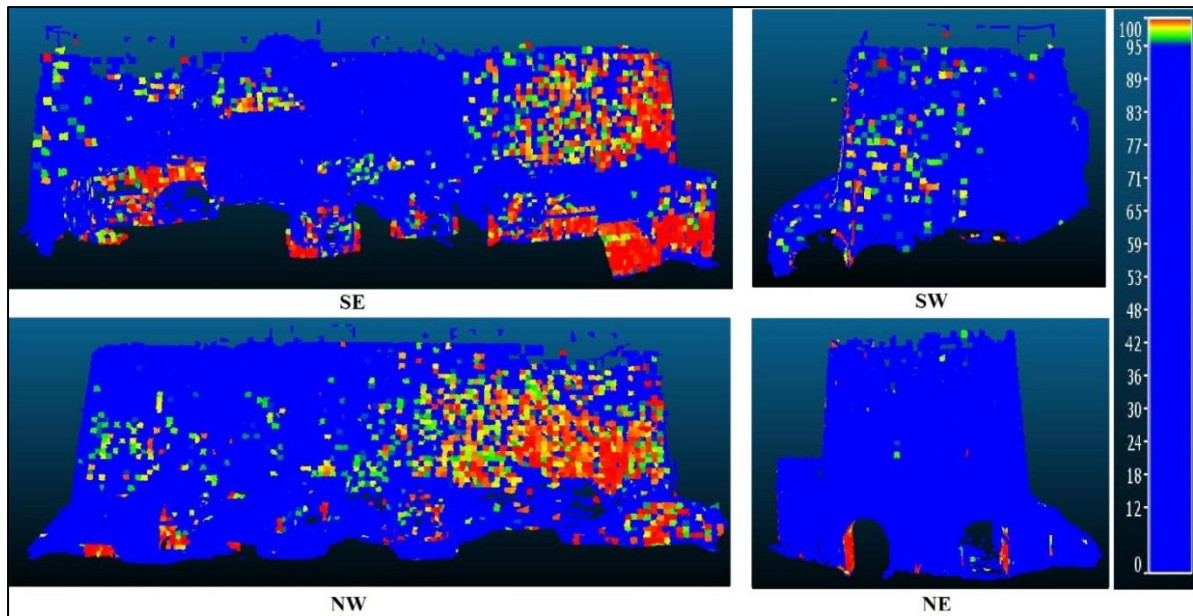


Figure 8-4 Deformation probabilities (%) for Limekilns faces before ICP-registration.

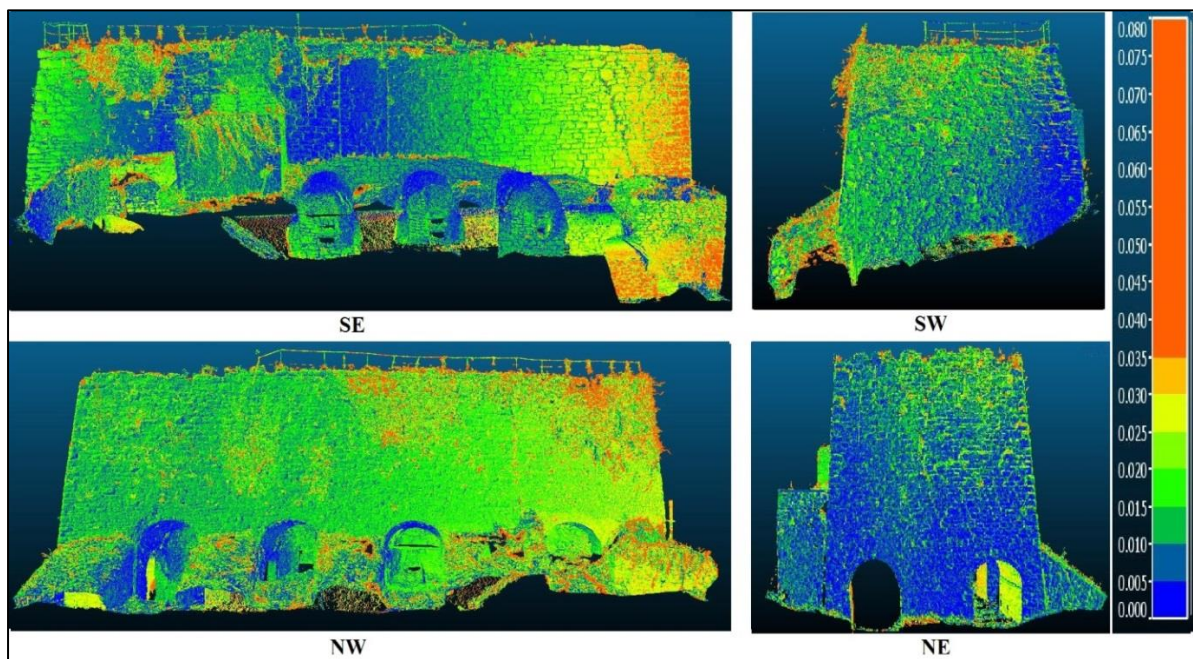


Figure 8-5 Absolute distances (m) by CloudCompare software for Limekilns before ICP-registration.

Table 8-3 Deformation unit vectors before ICP-registration.

Face	Unit Vector		
	V_x (m)	V_y (m)	V_z (m)
SE	-0.193	0.981	-0.014
SW	0.952	0.289	-0.101
NW	-0.199	0.979	0.035
NE	-0.619	0.776	0.121

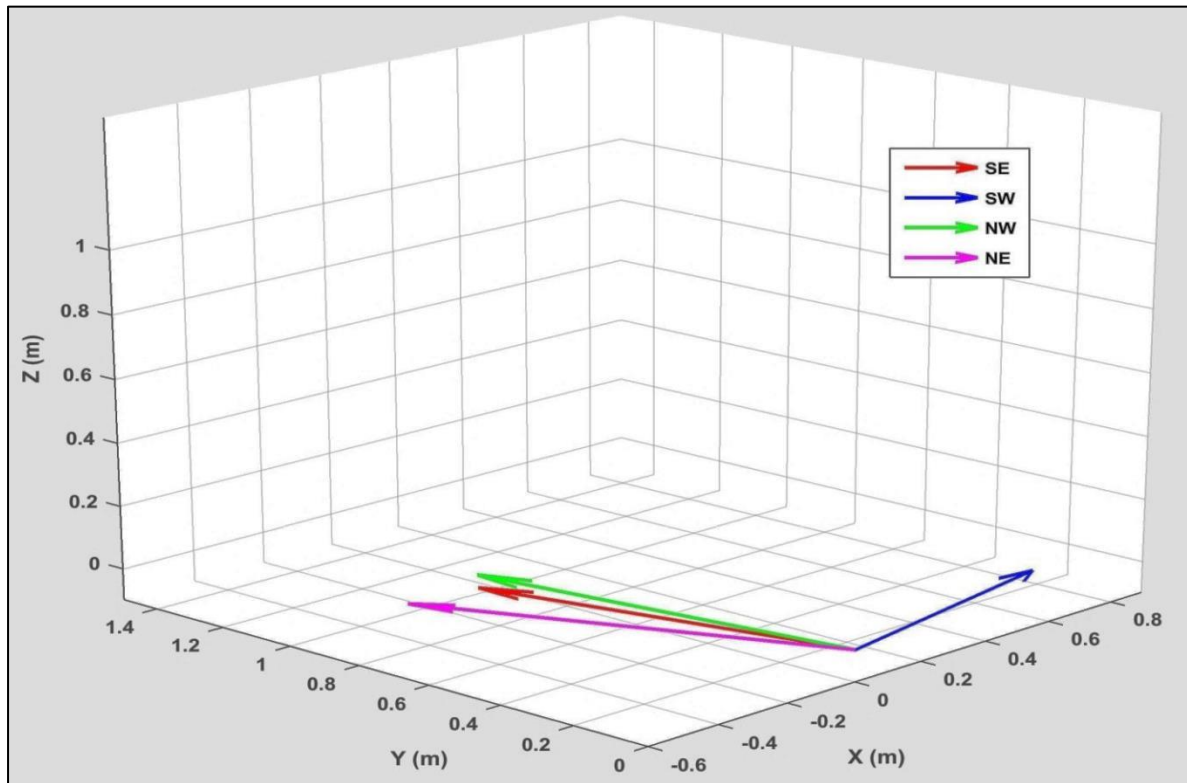


Figure 8-6 Deformation unit vectors for structure faces before ICP-registration.

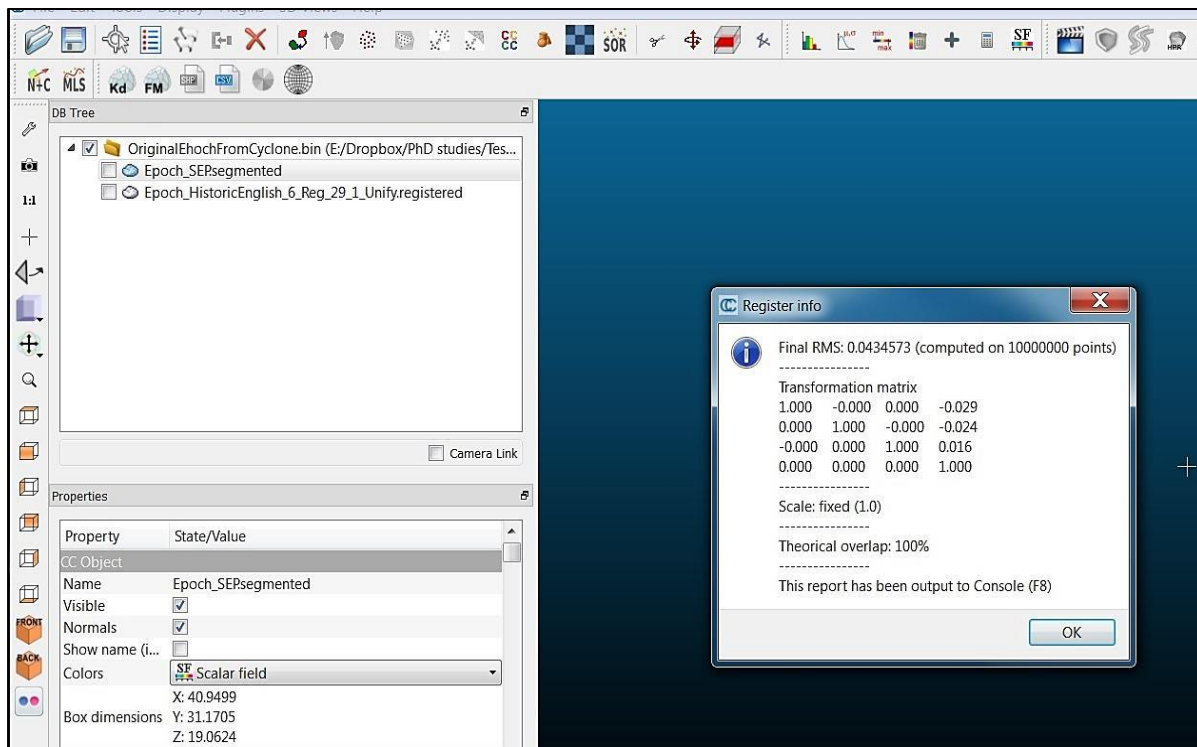


Figure 8-7 Snapshot for results of ICP registration.

8.5.2 After ICP Registration

As has been suggested, the ICP-registered epochs have been used in the second implementation of the proposed method. Generally, there is an improvement in the number of deformed areas, i.e. the number of the deformed boxes was 2386 before ICP-registration decreased to only 1047 after performing it (Figure 8-8, Appendices C and D). Furthermore, the faces deformations vectors (Figure 8-9 and Table 8-4) are pointing to different directions which can be results of deformations rather than a shift.

Consequently, further analysis has been advised for deformed areas based on locations in the structure. For this purpose, all the deformed areas, or supposed to be, were studied according to the actual location on each face.

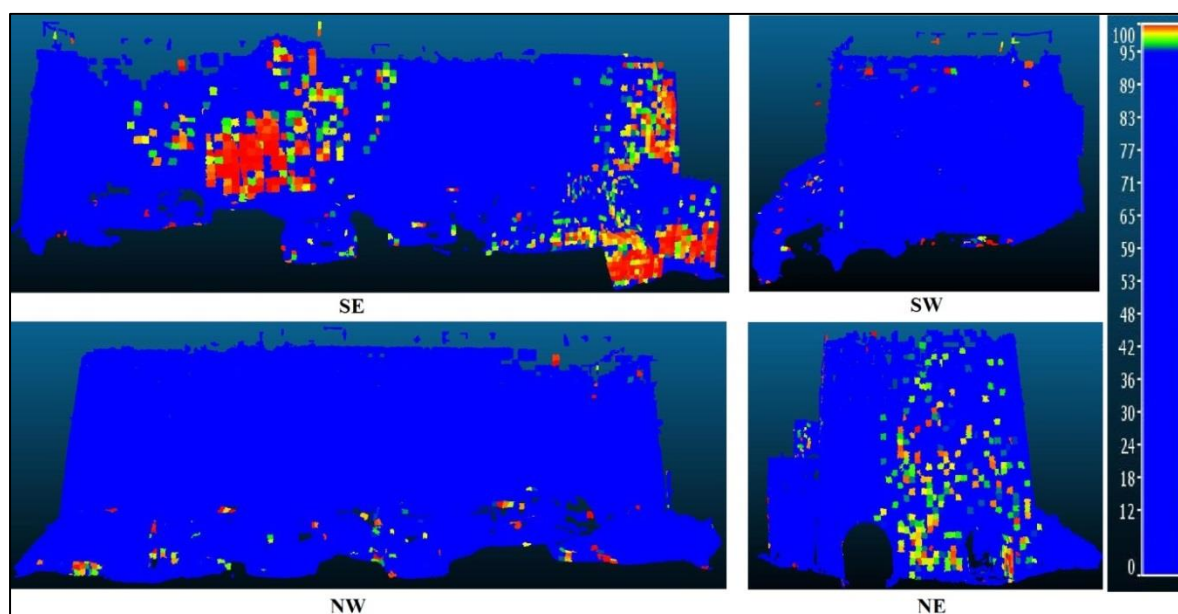


Figure 8-8 Deformation probabilities (%) for all faces after ICP-registration.

Table 8-4 Deformation unit vectors after ICP-registration.

Face	Unit Vector		
	V_x (m)	V_y (m)	V_z (m)
SE	0.484	0.873	0.056
SW	0.931	0.366	0.003
NW	0.126	-0.990	0.060
NE	-0.989	-0.149	-0.020

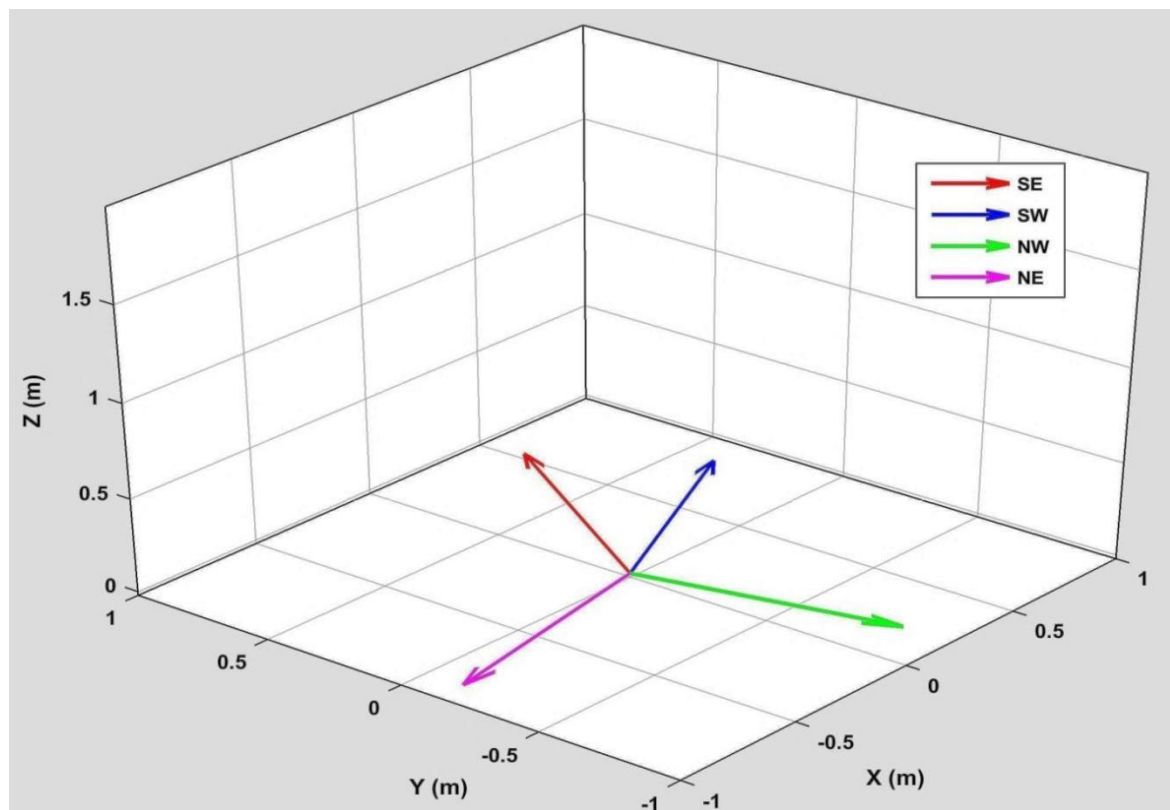


Figure 8-9 Deformation unit vectors after ICP-registration.

Evidently, there is a large area on the SE face with high deformations probabilities of more than 95% (Figure 8-8 and Figure 8-10). Mainly, it can be seen in the two parts: the first one locates at the right edge of the structure (yellow dashed border in Figure 8-10), and the second one locates nearly in the middle of that face (red dashed border in Figure 8-10). From the close view to the pictures, it can be seen an obvious crack in the first part, which is across from the upper-left to the down-right of that part (Figure 8-10). Probably, it is active one which occurred in that place. In addition, there are missing bricks and parts in the second area. Possibly, the materials appear in the Figure 8-11 are the fallen from the structure. Consequently, it is might the reason for detecting deformations in this area.

Similarly, the displacements, which were computed by the proposed and CloudCompare methods, give the same indications (Figure 8-12). However, the proposed method is localising deformations much better than CloudCompare where deformations diffused over a wide area. Furthermore, the maximum of the displacements was detected in the proposed method (0.020m) are more logical than that in CloudCompare (0.035m) (Figure 8-12), owing to only a six-month period.

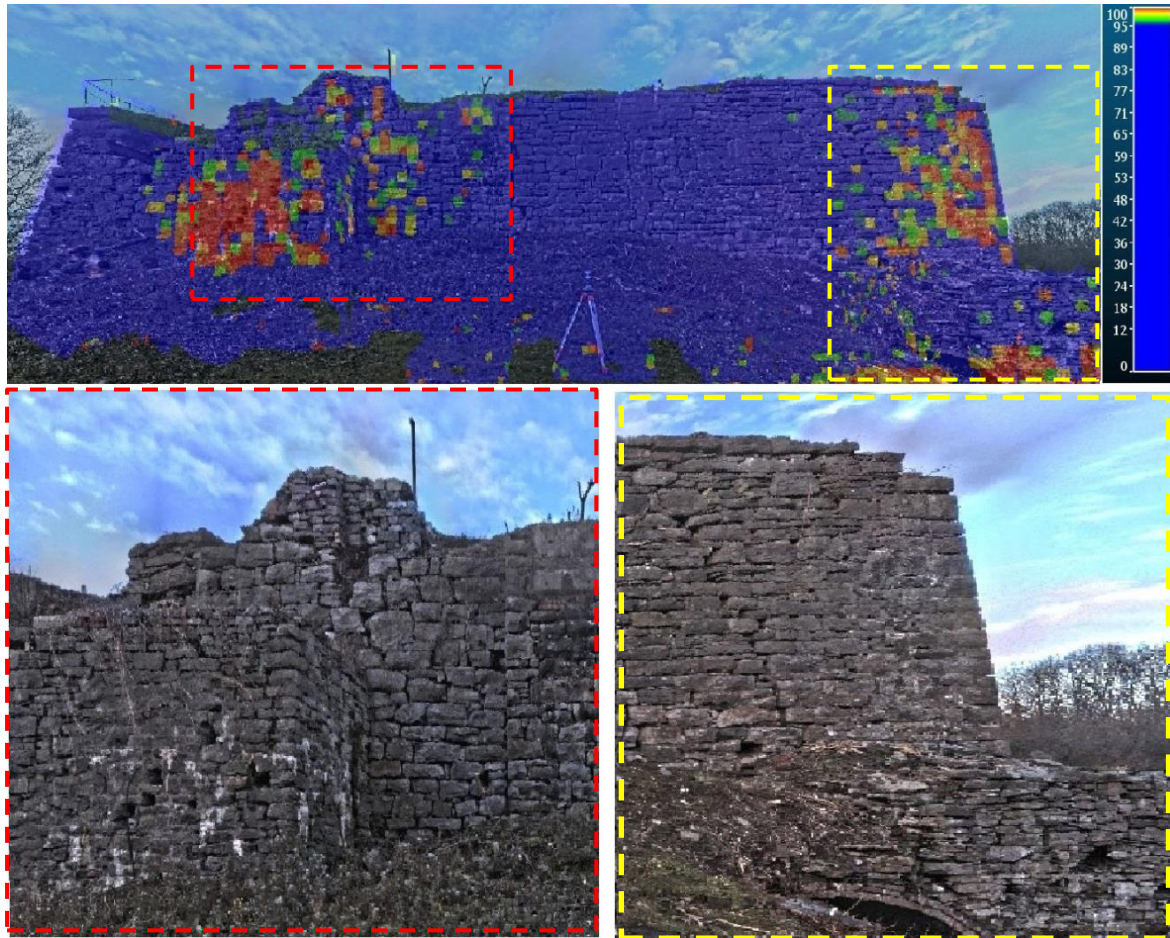


Figure 8-10 Deformation probabilities (%) for the SE face after ICP-registration.



Figure 8-11 Some fallen parts in the SE face.

It can be concluded, according to the proposed method and using CloudCompare, there are deformations in the SE face and needs keeping an eye on it. Consequently, more analysis is undertaken for it though our research.

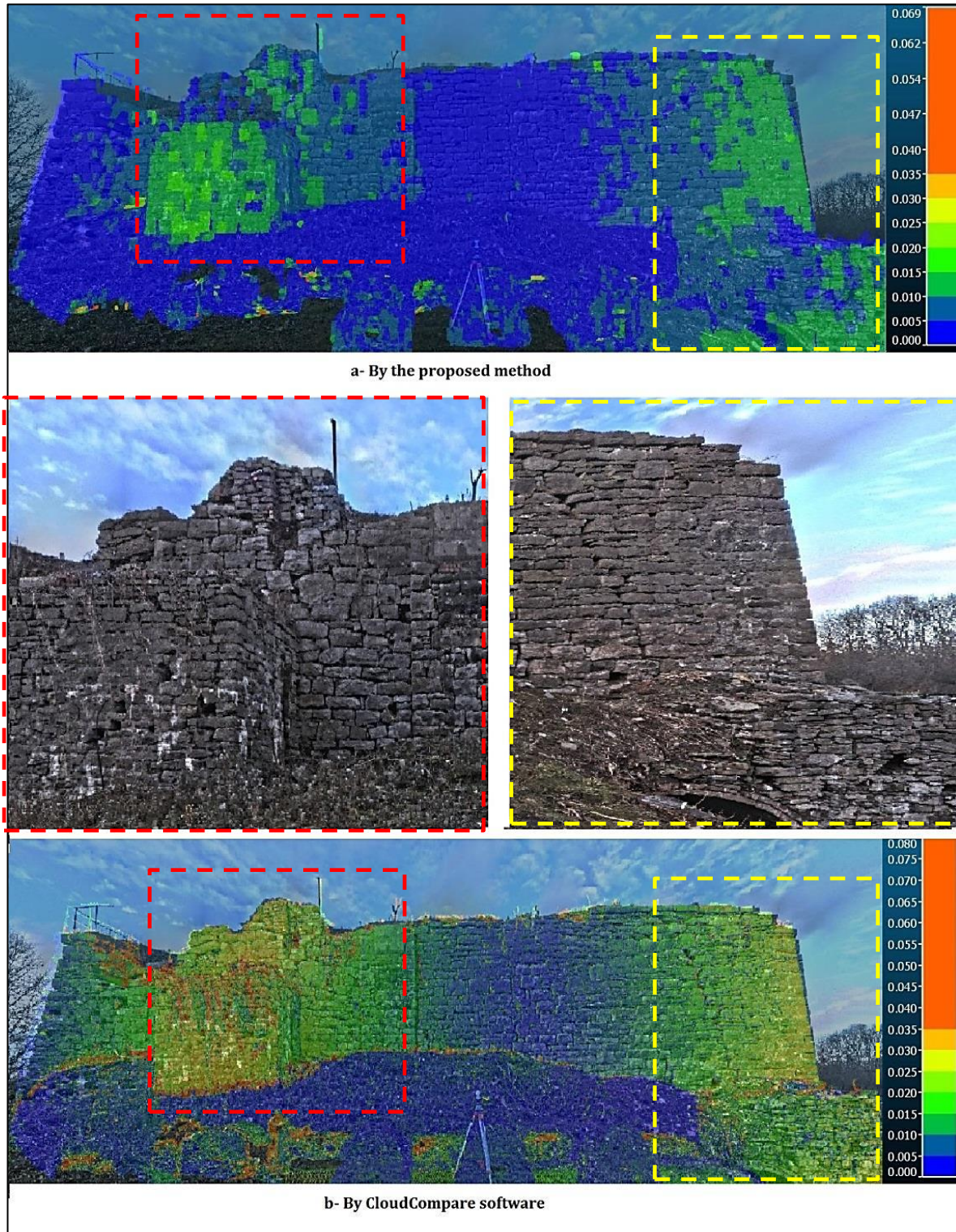


Figure 8-12 Displacements (m) for the SE face after ICP-registration.

On the other hand, the proposed method shows no deformations in the SW face according to the deformation probabilities and the small areas, which have high probabilities for deformations, locate where grass grew (Figure 8-13). Similarly, the displacements occurred in the same place for both methods, the proposed one and CloudCompare (Figure 8-14). Nevertheless, the proposed method reveals less effect by grown grass because it computes displacements based on all points in a specific box, while CloudCompare computes displacements for each point.

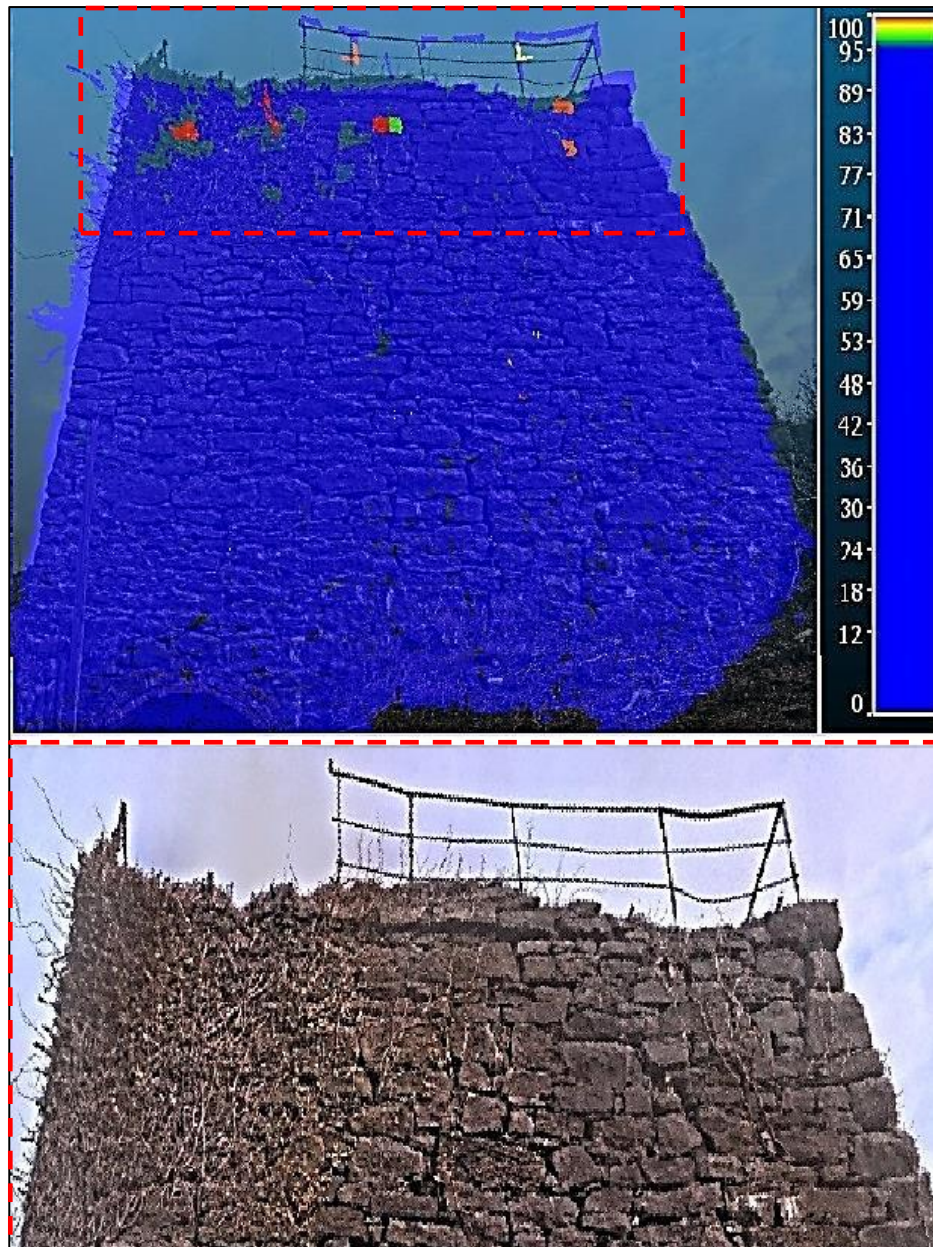


Figure 8-13 Deformation probabilities (%) for the SW face after ICP-registration.

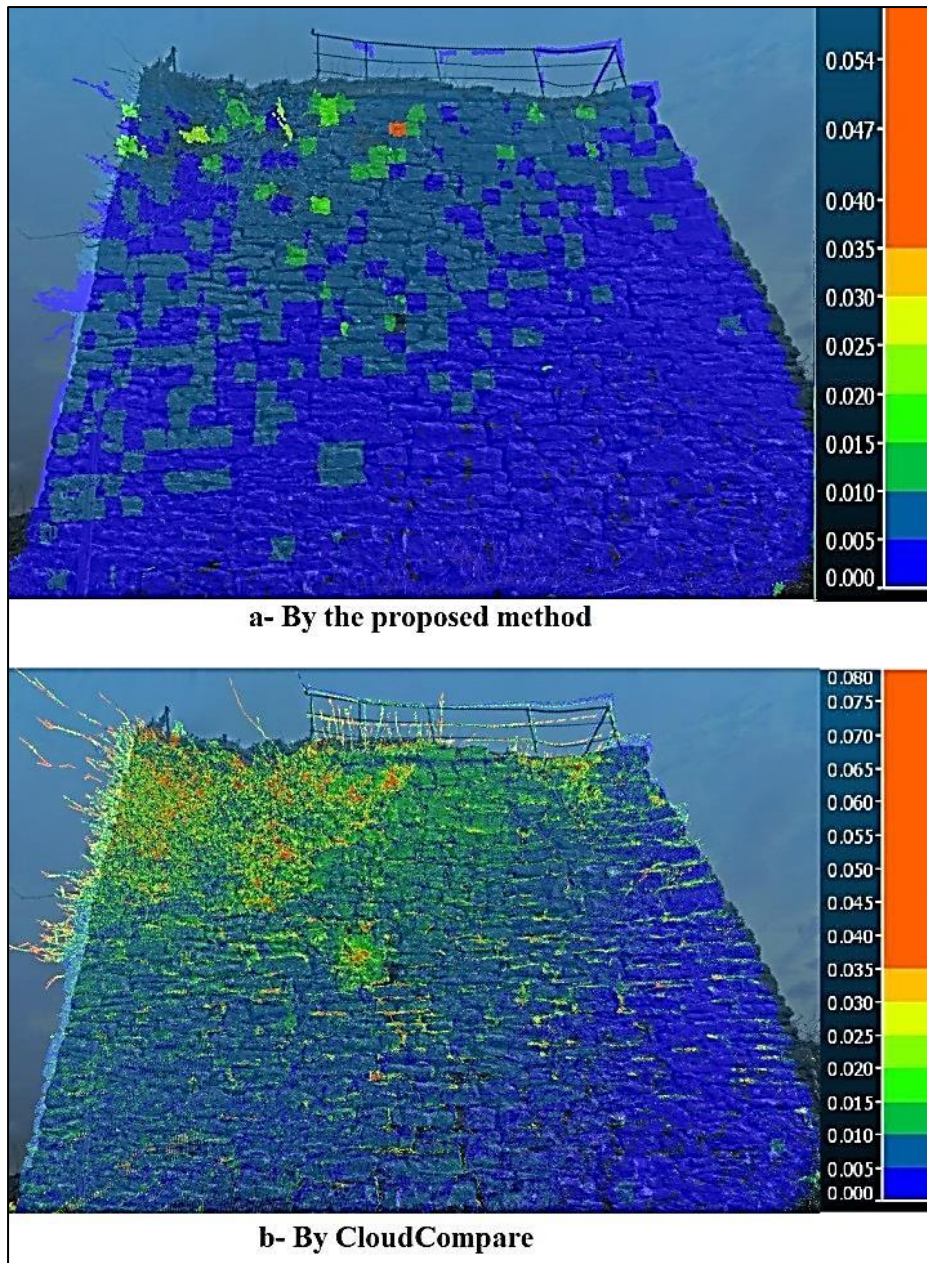


Figure 8-14 Displacements (m) for the SW face after ICP-registration.

The same situation occurred in the NW face where no deformations have been detected by the proposed method according to the deformations probabilities (Figure 8-15). In addition, the displacement computations manifest how the proposed method is less affected by grass than CloudCompare, but this time clearer due to the extended grass areas (Figure 8-16).

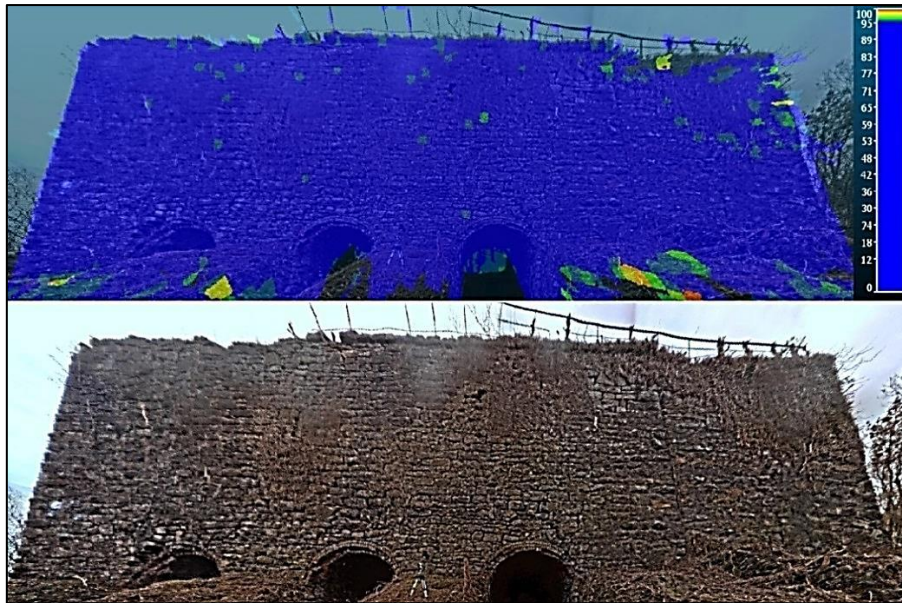


Figure 8-15 Deformation probabilities (%) for the NW face after ICP-registration.

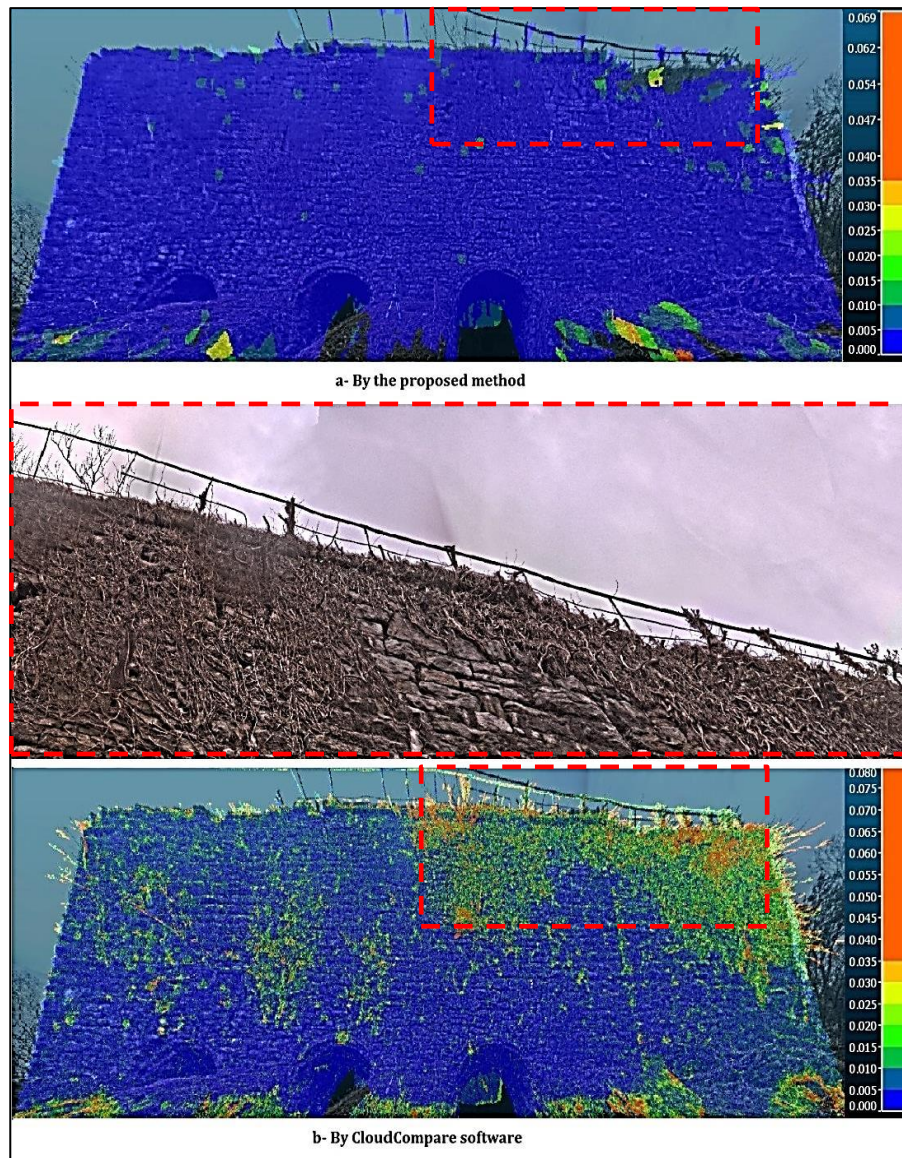


Figure 8-16 Displacements (m) for NW face after ICP-registration.

Regarding the NE face, although no obstructions are existing, the proposed method detects deformations according to the deformations probabilities (Figure 8-17). From the close view to the pictures, it can be seen cracks in the middle of this face (Figure 8-17). Furthermore, the proposed method shows optimistic results regarding the displacements where the deformed areas are tracing the cracks (Figure 8-18). Otherwise, although the CloudCompare results show deformations, they spread over a wide area and there are no clear locations for the deformations (Figure 8-18). Consequently, it can be concluded that the cracks on this face are active which might cause such deformations. Hence, further analysis is undertaken through our research for this face.



Figure 8-17 Deformation probabilities (%) for the NE face after ICP-registration.

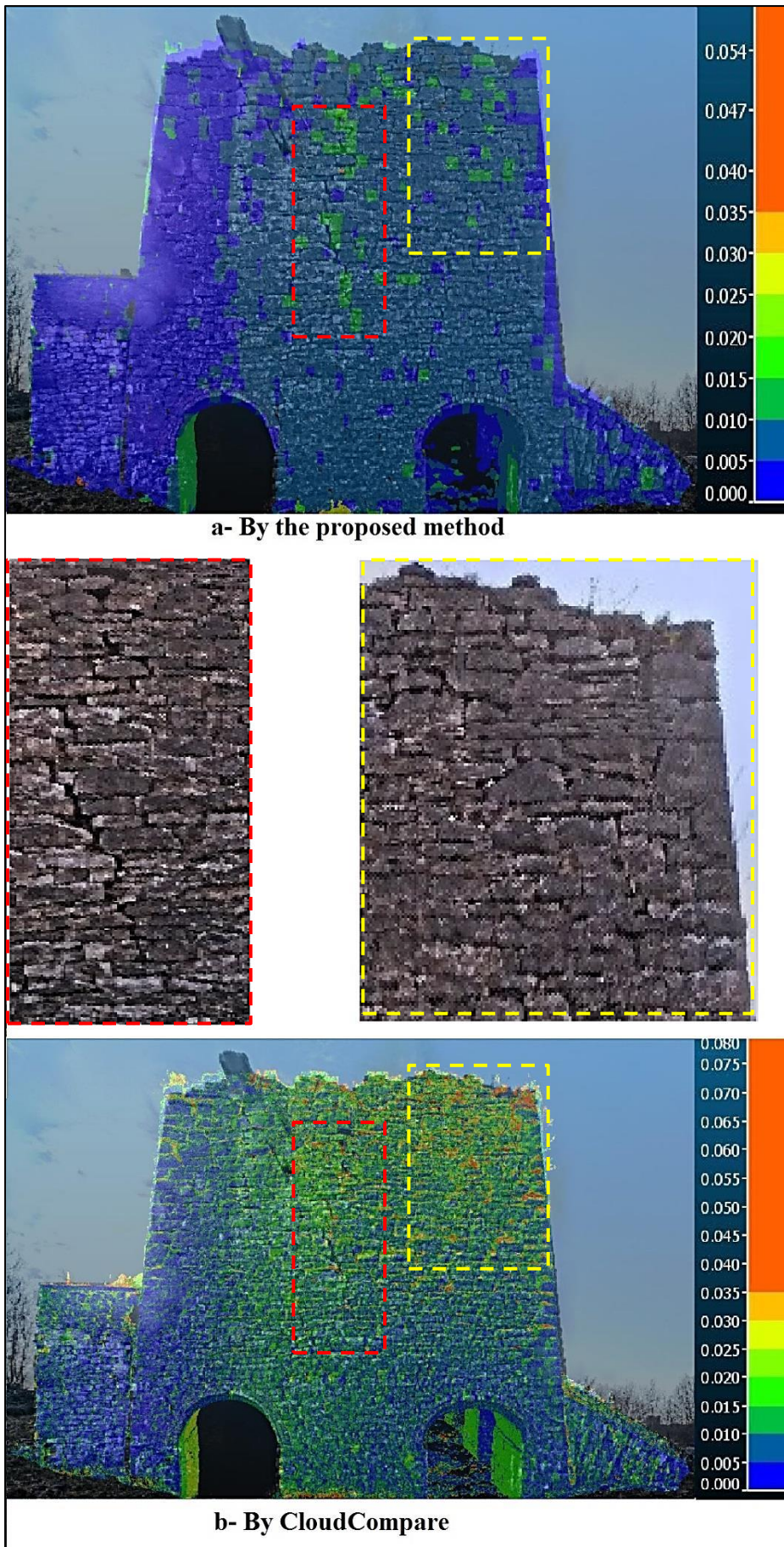


Figure 8-18 Displacements (m) for the NE face after ICP-registration.

8.5.3 Deformation Results

As has been concluded, two faces (SE and NE) could suffer from deformations. Therefore, further analysis for deformations directions is needed. To study deformations directions with relevance to the structure, the point clouds has been rotated (8.1) in such that X-axis is in parallel to faces SE and NW (Figure 8-19), and then the proposed method has been applied again (Appendix E).

$$R(\text{Rotation matrix}) = \begin{bmatrix} 0.955130637 & -0.296184868 & 0 \\ 0.296184868 & 0.955130637 & 0 \\ 0 & 0 & 1 \end{bmatrix}, \quad \Delta(\text{shift}) \begin{bmatrix} -375800.00 \\ -443376.00 \\ 0 \end{bmatrix} \quad (8.1)$$

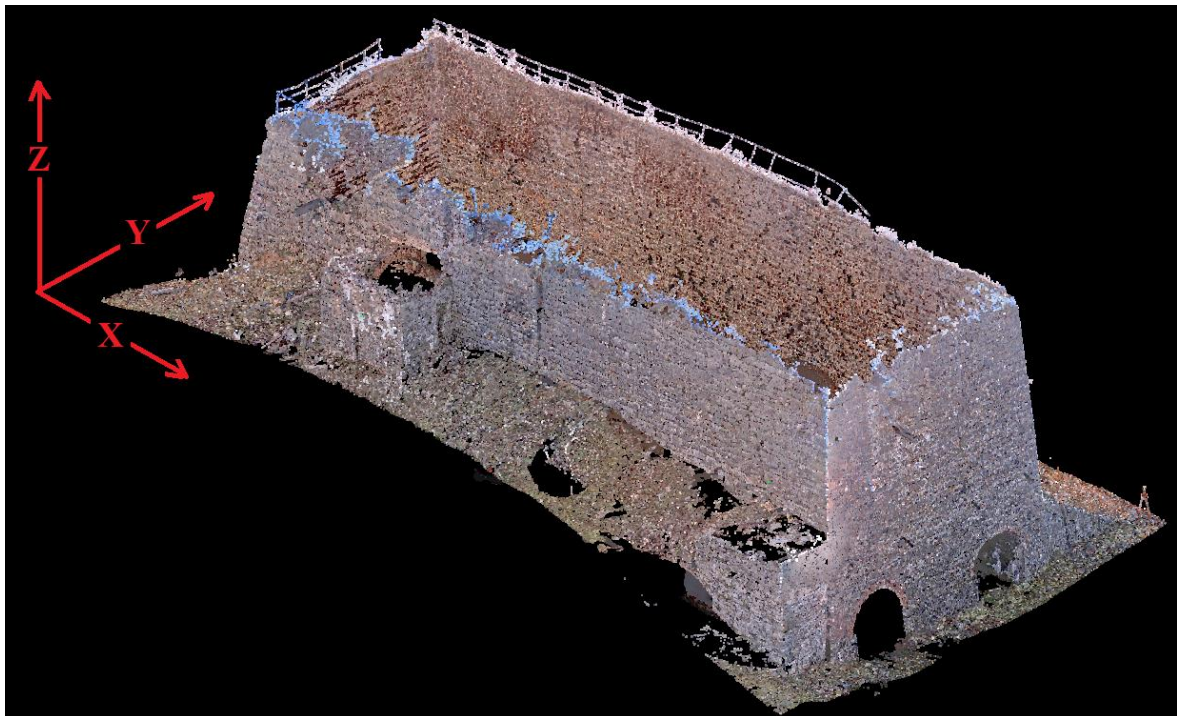


Figure 8-19 Rotated point clouds for Bellmanpark Limekilns.

Furthermore, by examining pictures and point clouds of these faces, three obvious cracks were found, one in the face SE and two in the face NE (Figure 8-20). Therefore, it is important to discover whether these cracks are historical or active.

Using the outcomes of the proposed method, the deformations results have been computed for each joint deformed area. Accordingly, three deformation vectors were computed (Table 8-5), DV1 and DV2 in the face SE; and DV3 in the face NE. These vectors can be represented in point clouds at actual locations because they relate to the same coordinates system. As can be seen in Figure 8-21 and Figure 8-22, the DV1 vector points outward, this probably the reason of the fallen parts (Figure 8-11). The border of the

affected area by this vector is not obvious in the structure, although results of the proposed method revealed it (Figure 8-10 and Figure 8-12).

On the other hand, the DV2 and DV3 point inward this possibly because the structure walls slant inward. In addition, they are pointing to the downhill, in other words, a more logical direction. Regarding affected areas, according to the locations of these vectors, DV2 could be affected in the area extended between cracks on the SE face and the first crack in the face NE (yellow area in Figure 8-23), while DV3 might be affected in that one extended between the two cracks in the face NE (red area in Figure 8-23). It can, therefore, be concluded; the cracks in both faces SE and NE are active and need more attentions.

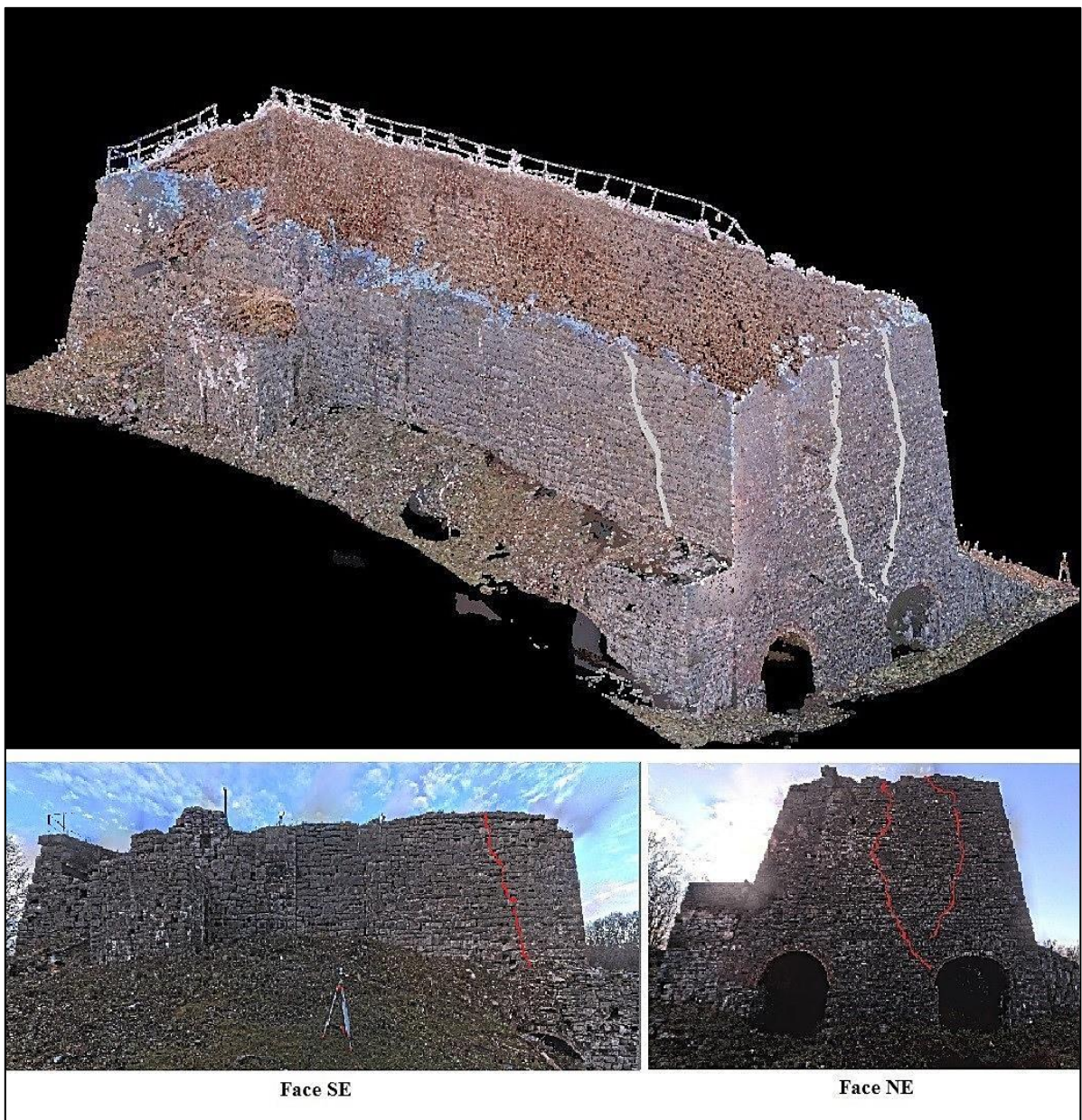


Figure 8-20 Cracks locations in faces SE and NE.

Table 8-5 Deformation results unit vectors (re-rotated to the original coordinates system).

Vector	Location (OS grid)			Unit Vector			Angle Computation	
	E (m)	N (m)	Elv. (m)	V _x (m)	V _y (m)	V _z (m)	Zenith angle (°)	Plane angle (°)
DV1	375860.213	443380.365	100.193	0.032	-0.999	0.020	88.8	88.1
DV2	375878.562	443375.538	98.854	0.002	1.000	-0.019	91.1	89.9
DV3	375883.166	443382.060	96.236	-0.999	0.018	-0.034	92.0	89.0

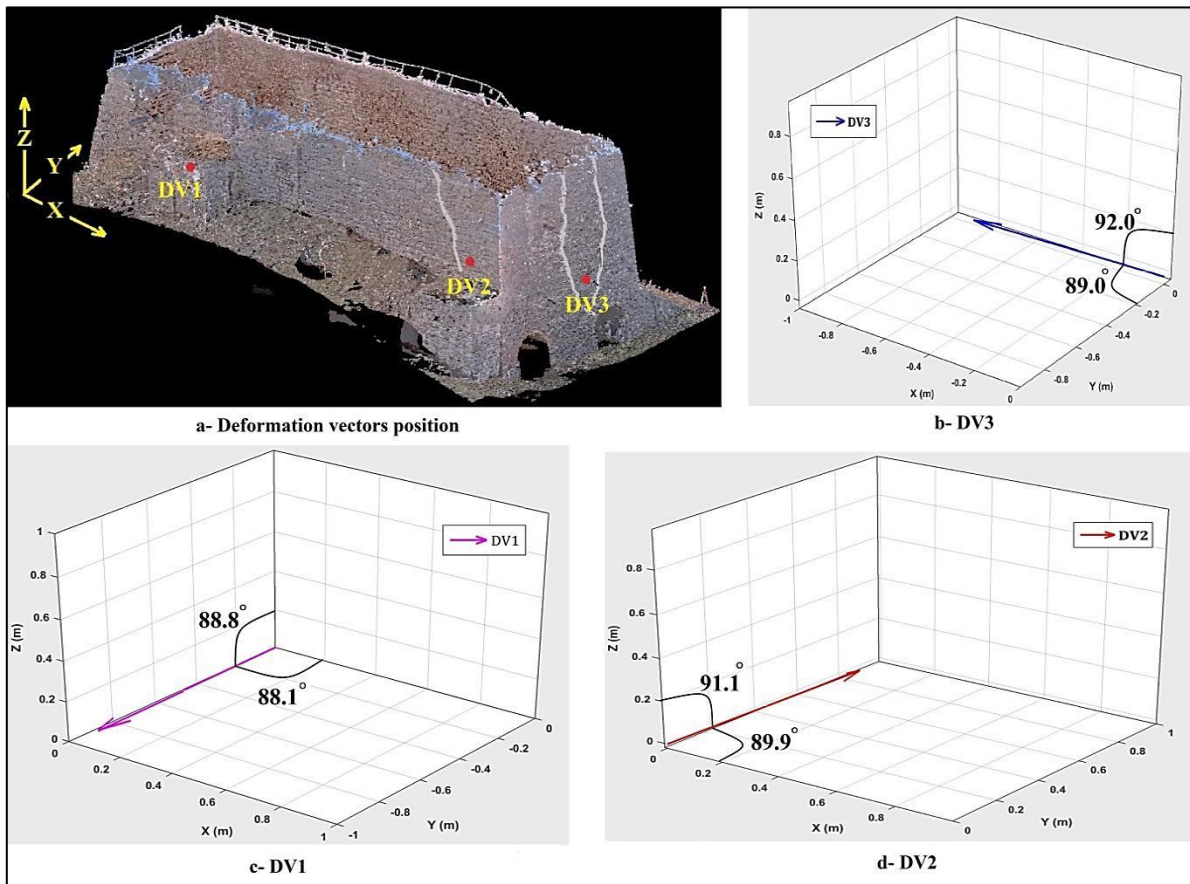


Figure 8-21 Actual locations and directions for deformation vectors.

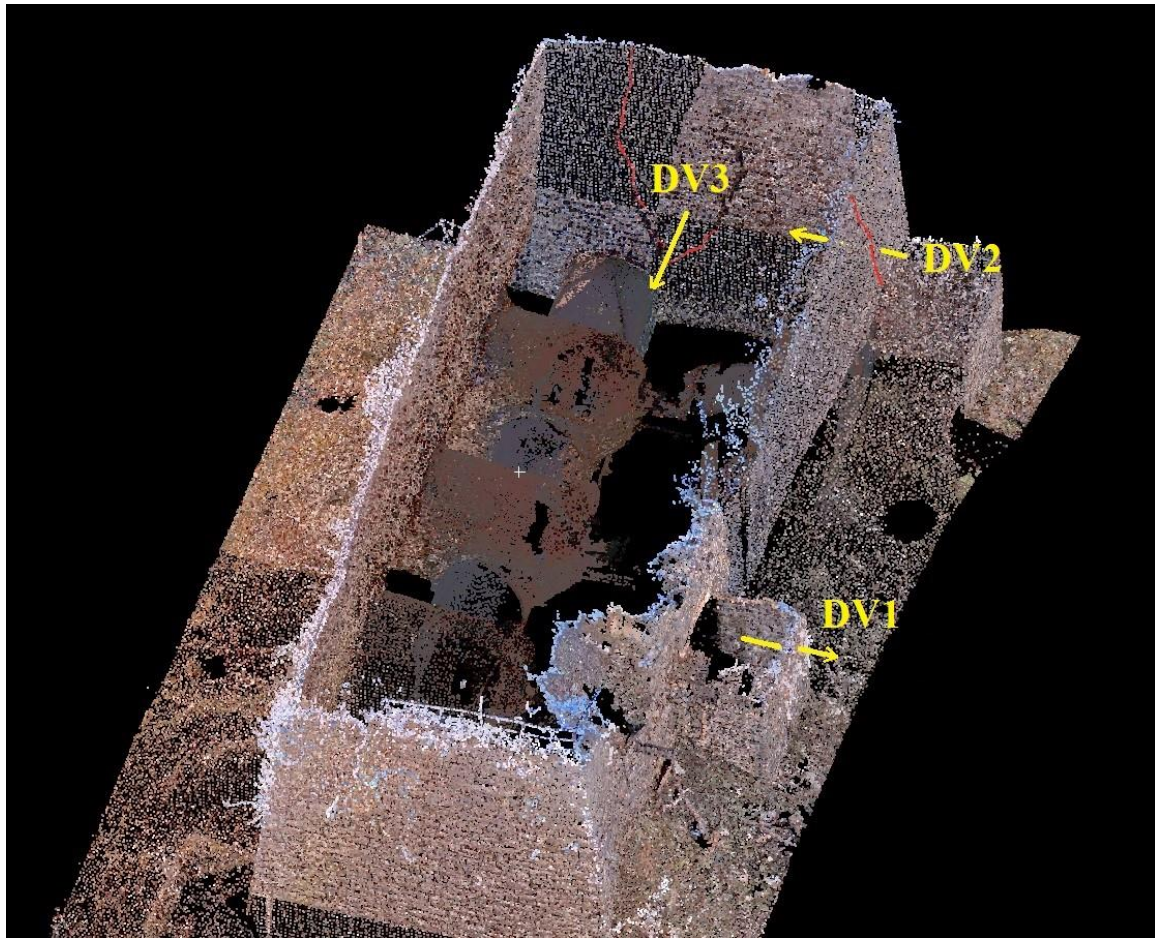


Figure 8-22 Structure point clouds with deformations vectors representation.

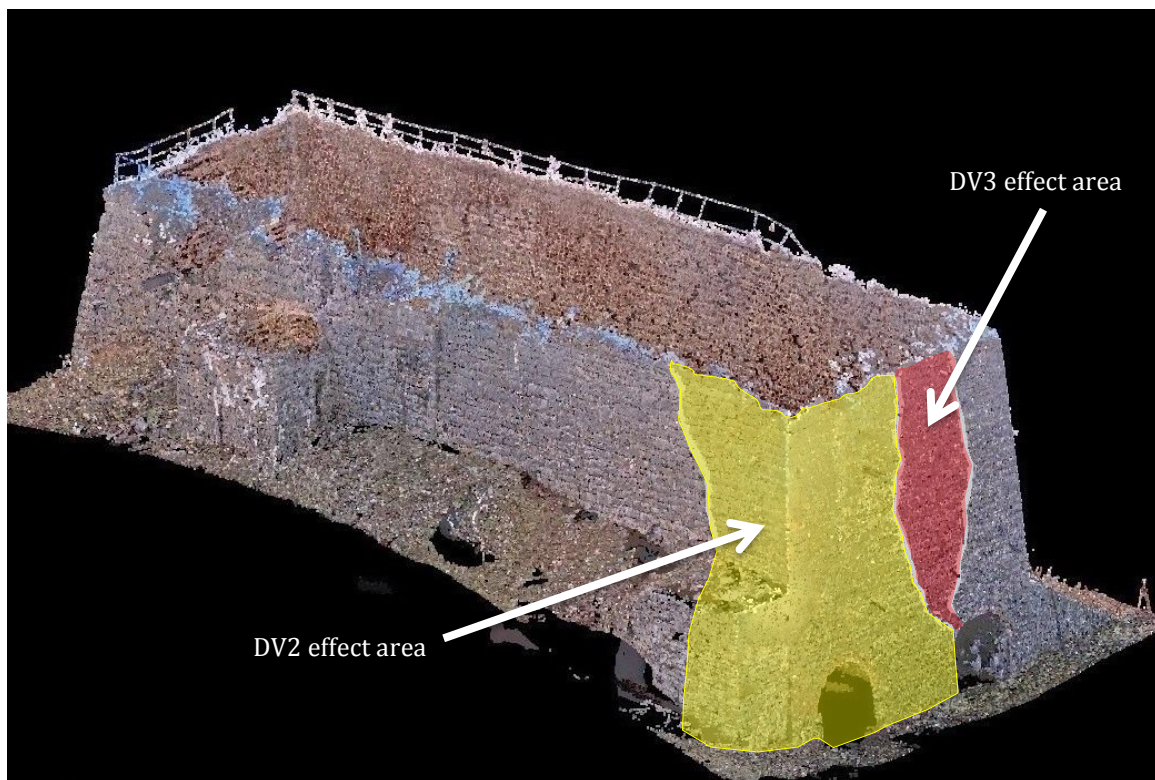


Figure 8-23 Effect areas of DV2 and DV3 deformations vectors.

8.6 Chapter Conclusions

In this chapter the Bellmanpark Limekiln, Clitheroe, Lancashire monitoring project data has been analysed. The following conclusions can be extracted from this analysis:

- The results of ICP-registered data are better than the original data before registration. This is probably due to a georeferencing shift between two epochs. Therefore, the registered epochs are adopted to detect and locate deformations.
- The proposed method revealed deformations in the faces SE and NE while the other faces (SW and NW) have no deformations.
- Three deformed areas were found, two in the face SE and one in the face NE. From the outcomes, the deformation results and actual locations have been computed for these areas.
- The vectors of results showed outward deformation for DV1 and inward for DV2 and DV3.
- There is no clear border for affected area for DV1, but there are cracks determined the deformed areas in case of DV2 and DV3. Therefore, these cracks can be considered as active and need more attention.
- Although CloudCompare software results coincide with the proposed method in detected deformations, it cannot well locate these deformations because it is diffused over a wide area. In addition, it cannot determine actual directions of the deformations as like as the proposed method.

CHAPTER Nine: **CONCLUSIONS AND FUTURE PROSPECTS**

9.1 Conclusions

The aim of this research is to develop a new monitoring approach for unpredicted deformations. The heritage and historic buildings are targeted in this research, where each part of the structure could be subject to deformations. The proposed approach utilises TLS measurements and Generalised Procrustes Analysis (GPA) technique. To achieve the aim of this research, the following objectives have been fulfilled with related conclusions:

1) Investigate TLS based deformations monitoring techniques:

- Commonly, five techniques can be employed to detect deformations from TLS data: using targets; direct cloud to cloud comparison; interpolation models; surfaces matching; and some project specific solutions.
- The advantage of target-based methods is the ability to computing 3D deformation and its considerable high accuracy. However, the single point precision of targets is much higher when conventional surveying is implemented. In addition, it is expensive (in time and cost) compared to conventional methods. Finally, it needs pre-knowledge of the location of the deformed area.
- The advantage of cloud-to-cloud comparison is that it is an easy and quick method, yet it has limited accuracy due to noise.
- Although the interpolation models method can detect deformations with magnitudes less than the nominal single point precision, it detects one dimension deformation.
- The advantage of the surfaces matching method is that it can detect 3D deformations, and it is sensitive to small deformations with magnitudes below the noise of the single TLS points. However, it uses a non-linear functional model, hence it needs approximate values, and therefore convergence might not happen in the case of large deformations. Furthermore, it is rigid transformation, and shift cannot be detected.
- The specific solutions can be considered as accurate methods, yet they apply only to particular cases.

2) Explore registration and georeferencing techniques:

- Because TLS monitoring is a comparative procedure, it rarely needs georeferencing if there is no integration with other sensors. Therefore, it just requires that data for all epochs to be related to

one coordinate system; in other words, only registration is required. However, for large structure monitoring, georeferencing can be used; hence, a control network needs to be established.

- Regarding buildings monitoring, targets-based registration can work perfectly after fixing tie points in stable areas that are part of the concerned building or on surrounding objects. Care should be taken to assess these points each period to be sure that they have not moved over all epochs. This method is adopted in this research.

3) Investigate TLS error sources:

- There are four sources for TLS: instrumental; object-related; environmental; and methodological. Instrumental errors may come from beam divergence, mixed edge, range uncertainty, angular uncertainty, and axes errors. Also, the reflectance and transparency of the object surface play a key role for the source of the object-related error which can introduce speckle noise, detector saturation, and penetrative beam (for semi-transparent coating objects). Regarding environmental errors, there are four sources: temperature (for the instrument and objects), atmosphere, interfering radiation, and dynamic objects. Finally, there are three sources for methodological errors: resolution, registration, and incidence angle.
- Several suggestions to deal with these errors have been introduced in Table 4-10, page 87.

4) Investigate Procrustes Analysis techniques:

- There are different revisions for Procrustes Analysis, such as Orthogonal Procrustes Analysis (OPA), Extended Orthogonal Procrustes Analysis (EOPA), Weighted Extended Orthogonal Procrustes Analysis (WEOPA), and Generalized Procrustes analysis (GPA).
- The Procrustes analysis can be applied in different fields such as medicine, psychometry, statistics, etc. Interestingly, it has been shown to be widely applicable in Geomatics, especially for the reference system transformation. However, it has not been used yet to detect deformation.
- The most important drawback of the Procrustes technique is the lack of a reliability criterion to detect and localise the outliers, which might be present in the measurements. Consequently, the results produced by the Procrustes technique may be wrong in the case of the existence of outliers in the data set.

5) Propose new monitoring approach:

- The proposed method has six main steps:
 - Registration: transforming all epochs to a common reference system.

- Outlier removal: remove outliers by statistical approaches.
 - Voxel approach: separating data into boxes.
 - Noise mitigation: reduce noise by voxel filter and surface fitting.
 - Determination of deformation vectors: computing translation vector for each box based on GPA.
 - Localisation of deformation: Using F-test to compute the probability of the deformations for each box.
- A MATLAB script has been written to execute the proposed technique. In addition, CloudCompare software and PCL library are employed to perform some steps.

6) Undertake validation experiments:

- Four validation tests have been conducted: simulated data with simulated deformation; real scan data with simulated deformations at close range (10 m); real scan data with simulated deformations at mid-range (25 m); and real scan data with actual deformations.
- For simulated data with a simulated deformation test, the proposed algorithm succeeded in detecting and localising deformations. In addition, it was successful when no deformations exist. Furthermore, promising results were obtained when it could observe deformations with a magnitude less than noise, however, the probability was only 40%. Regarding variables, for LOWESS fitting, the best results were obtained with a span equal to (0.25) and the robust method is least squares (LAR).
- For real scan data with simulated deformation at close range (10 m), the results showed the success of the proposed method to reveal no deformations for the non-deformed epochs. Furthermore, it succeeded in detecting and localising the deformations. Potentially, it can give indications for areas with deformations less than the noise level. Moreover, the results of the proposed method can be considered better than that of the CloudCompare software.
- For real scan data with simulated deformation at mid-range (25 m), to some extent, the proposed technique succeeded in detecting and localising deformations. However, it is not suggested for monitoring modern and complicated buildings, but it has been developed for monitoring historic ruins.
- For real scan data with real deformations, the proposed method was applied on the Bellmanpark Limekiln, Clitheroe, Lancashire monitoring project. The outcome of the proposed method revealed

deformations in the faces South East (SE) and North East (NE) of the building. From examining these faces, three deformed areas were found, two in the face SE and one in the face NE, which might cause some cracks appear in these faces. Alternatively, the CloudCompare software has been employed to detect deformation. Although results coincide with the proposed method for detected deformations, it cannot locate these deformations very well because it is diffused over a wide area. In addition, it cannot determine the actual directions of the deformations unlike the proposed method as a result of this research.

9.2 Novelty

A new approach for structure monitoring has been developed in this research based on TLS data and GPA.

The proposed approach may surpass the existing methods with different perspectives, as follows:

- 1) Through creating dense point cloud, the proposed method has the ability to detect and localise changes with unpredicted locations which may happen in heritage and historic buildings.
- 2) It is considered as a non-invasive method which can conduct monitoring remotely (without any contact). This is vital for monitoring of historic and heritage buildings.
- 3) It can provide 3D visualisation of changes. This can help non-engineering clients to understand the conditions of their building. Also, it helps to present and discuss monitoring results with non-experts.
- 4) Through using a voxel approach with estimating the probability of deformations, the proposed method has a good ability to localise changes.
- 5) It can provide more reliable outcomes because they result from multiple epochs.
- 6) Through noise mitigation, the proposed method can detect deformation below the noise level.
- 7) Through a voxel approach, the proposed method has a better solution for obtaining displacements.
- 8) Because it deals with data as matrices, the proposed method has the flexibility to add radiometric data (intensity) to detect deformations. Also, it can be used with point clouds created by digital photogrammetry after modifying the part of errors mitigation.

9.3 Shortcomings and Limitations

Despite the advantages of using TLS in monitoring undoubtedly it has some shortcomings, as follows:

- 1- Although significant improvements have been witnessed using this technique, it is still under development and research. Therefore, clients rarely trust this approach as the sole method and often requiring another known “trusted” technique for checking.
- 2- It is a high cost approach compared with other techniques. For instance, the price of Leica Scanstation P40 (Sec.4.3.2) is more than £100,000, or about tenfold of that of the total station.
- 3- The huge amount of data and the difficulty in handling and processing it. For example, the file size of raw data of one epoch of Bellmanpark Limekilns monitoring project is about 14 Gigabytes.
- 4- Objects shape and reflection play a key role in the distance measurements, which can be regarded an open problem.
- 5- There are different error sources with many variables (e.g. mixed edge, resolution, incidence angle, beam divergence, detector saturation, etc.).

On the other hand, validation tests revealed some limitations in the proposed method which can be identified as follows:

- 1- Due to employing only geometric characteristics of point clouds, the proposed method revealed a failure in complicated buildings which are constructed from different materials (the second test of validation experiments with real scan data and simulated deformations).
- 2- The accuracy of the proposed method is unlikely to surpass that of the total station.
- 3- The proposed method cannot detect displacements of a magnitude equal to or more than the box size.
- 4- Due to filtering boxes with few points, in the case of low resolution, some parts may be removed from the final results (in a similar way to what happened in validation experiments with simulated data and simulated deformations).

9.4 Future Prospects

There are three main suggestions for future work based on the findings of this research and these are detailed below:

1- Adding intensity for the proposed method:

Due to dealing with information as a matrix, the proposed method has the flexibility to add radiometric data (intensity) to detect deformations. In this case, it just needs to add a new column for any further information, i.e. the equation (5.1) will become:

$$A_1 = \begin{bmatrix} X_{11} & Y_{11} & Z_{11} & I_{11} \\ X_{21} & Y_{21} & Z_{21} & I_{21} \\ \dots & \dots & \dots & \dots \\ X_{p1} & Y_{p1} & Z_{p1} & I_{p1} \end{bmatrix}, A_2 = \begin{bmatrix} X_{12} & Y_{12} & Z_{12} & I_{12} \\ X_{22} & Y_{22} & Z_{22} & I_{22} \\ \dots & \dots & \dots & \dots \\ X_{p2} & Y_{p2} & Z_{p2} & I_{p2} \end{bmatrix} \dots A_m = \begin{bmatrix} X_{1m} & Y_{1m} & Z_{1m} & I_{1m} \\ X_{2m} & Y_{2m} & Z_{2m} & I_{2m} \\ \dots & \dots & \dots & \dots \\ X_{pm} & Y_{pm} & Z_{pm} & I_{pm} \end{bmatrix} \quad (9.1)$$

Where I_i : intensity.

However, due to its vulnerability, using intensity to detect deformations needs more research. For example research could focus on measuring intensities for different materials with various instruments (different signals). This could then be used to develop a formula to give constant intensity, regardless of the instrument used or incidence angle.

2- Using point clouds created by digital photogrammetry:

The proposed method can be revised in such a way to work with point clouds created by image-based technique. Accordingly, the errors mitigation and removing outliers' parts need to be reviewed, hence, a new procedure to deal with these needs to be developed. Potentially this could be produced by investigating DP error sources.

3- Integration of TLS and digital photogrammetry point clouds:

As mentioned before, TLS and Digital Photogrammetry technologies are two complementary techniques, hence, the proposed technique can be considered to be a combination of them. Consequently, the research prospects, in this case, will be to investigate which preferred data is to be used in which part of the proposed method. In addition, it may require studying suitable relative weights for different measurements.

REFERENCES

- ABDULLAHI, I. & YELWA, N. 2016. Structural Deformation Monitoring Surveys of New Administrative Building of Federal School of Surveying, Oyo–Nigeria. *International Journal of Science and Technology*, 6.
- ABELLÁN, A., JABOYEDOFF, M., OPPIKOFER, T. & VILAPLANA, J. 2009. Detection of millimetric deformation using a terrestrial laser scanner: experiment and application to a rockfall event. *Natural Hazards & Earth System Sciences*, 9.
- AIGER, D., MITRA, N. J. & COHEN-OR, D. 4-points congruent sets for robust pairwise surface registration. *ACM Transactions on Graphics (TOG)*, 2008. ACM, 85.
- AKCA, D. 2007. *Least Squares 3D Surface Matching*. PhD, SWISS FEDERAL INSTITUTE OF TECHNOLOGY ZURICH.
- AKCA, D., GRÜN, A., AKCA, D., AKCA, D., GRÜN, A., GEODESIST, G. & GRÜN, A. 2005. Fast correspondence search for 3D surface matching. *Laser scanning 2005*. Enschede, the Netherlands: ETH, Eidgenössische Technische Hochschule Zürich, Institute of Geodesy and Photogrammetry.
- AL-DURGHAM, K., HABIB, A. & MAZAHARI, M. SOLUTION FREQUENCY-BASED PROCEDURE FOR AUTOMATED REGISTRATION OF TERRESTRIAL LASER SCANS USING LINEAR FEATURES. ASPRS Annual Conference, 23-28 March 2014 Louisville, Kentucky.
- ALBA, M., FREGONESE, L., PRANDI, F., SCAIONI, M. & VALGOI, P. 2006. Structural monitoring of a large dam by terrestrial laser scanning. *International Archives of Photogrammetry, Remote Sensing and Spatial Information Sciences*, 36, 6.
- ALBA, M. & SCAIONI, M. 2007. Comparison of techniques for terrestrial laser scanning data georeferencing applied to 3-d modelling of cultural heritage. *The International Archives of the Photogrammetry, Remote Sensing and Spatial Information Sciences*, 35, 8.
- ANDREWS, D., BEDFORD, J. & BRYAN, P. 2015. *Metric Survey Specifications for Cultural Heritage*, Swindon/United Kingdom, Historic England.
- ANWARY, A. R. 2012. *Statistical Shape Analysis for the Human Back*. Mphil, University of Wolverhampton.
- APARICIO, S., MARTÍNEZ-GARRIDO, M. I., RANZ, J., FORT, R. & IZQUIERDO, M. Á. G. 2016. Routing Topologies of Wireless Sensor Networks for Health Monitoring of a Cultural Heritage Site. *Sensors*, 16, 1732.
- ARMESTO, J., ROCA-PARDIÑAS, J., LORENZO, H. & ARIAS, P. 2010. Modelling masonry arches shape using terrestrial laser scanning data and nonparametric methods. *Engineering Structures*, 32, 607-615.
- ARYAL, A., BROOKS, B. A., REID, M. E., BAWDEN, G. W. & PAWLAK, G. R. 2012. Displacement fields from point cloud data: Application of particle imaging velocimetry to landslide geodesy. *Journal of Geophysical Research: Earth Surface (2003–2012)*, 117.
- ASSALI, P., GRUSSENMEYER, P., VILLEMIN, T., POLLET, N. & VIGUIER, F. 2014. Surveying and modeling of rock discontinuities by terrestrial laser scanning and photogrammetry: Semi-automatic approaches for linear outcrop inspection. *Journal of Structural Geology*, 66, 102-114.
- AWANGE, J., BAE, K. & CLAESSENS, S. 2008. Procrustean solution of the 9-parameter transformation problem. *Earth Planets and Space (EPS)*, 60, 529.
- AWANGE, J. L. 2003. Partial Procrustes solution of the threedimensional orientation problem from GPS/LPS observations. In *Geodesy-The Challenge of the 3rd Millennium*. Springer Berlin Heidelberg.
- AWANGE, J. L. & GRAFAREND, E. W. 2005. *Solving algebraic computational problems in geodesy and geoinformatics*, Springer.

- BARBARELLA, M. & FIANI, M. 2013. Monitoring of large landslides by Terrestrial Laser Scanning techniques: field data collection and processing. *European Journal of Remote Sensing*, 46, 126-151.
- BARNHART, T. B. & CROSBY, B. T. 2013. Comparing two methods of surface change detection on an evolving thermokarst using high-temporal-frequency terrestrial laser scanning, Selawik River, Alaska. *Remote Sensing*, 5, 2813-2837.
- BEINAT, A. & CROSILLA, F. A direct method for the simultaneous and optimal multidimensional models registration. Remote Sensing and Data Fusion over Urban Areas, IEEE/ISPRS Joint Workshop 2001, 2001. IEEE, 283-287.
- BEINAT, A. & CROSILLA, F. 2002. A generalized factored stochastic model for the optimal global registration of LIDAR range images. *International Archives of Photogrammetry, Remote Sensing and Spatial Information Sciences*, 34, 36-39.
- BELTON, D. & LICHTI, D. D. 2006. Classification and segmentation of terrestrial laser scanner point clouds using local variance information. *IAPRS, XXXVI*, 5.
- BENNANI DOSSE, M., KIERS, H. A. L. & TEN BERGE, J. M. F. 2011. Anisotropic generalized Procrustes analysis. *Computational Statistics & Data Analysis*, 55, 1961-1968.
- BERALDIN, J.-A., PICARD, M., EL-HAKIM, S., GODIN, G., BORGEAT, L., BLAIS, F., PAQUET, E., RIOUX, M., VALZANO, V. & BANDIERA, A. Virtual reconstruction of heritage sites: opportunities and challenges created by 3D technologies. Proc. Int. Workshop on Rec., Modelling and Vis. of Cultural Heritage, 2005 Ascona, Switzerland. Taylor and Francis, 141-156.
- BESL, P. J. & MCKAY, N. D. Method for registration of 3-D shapes. Robotics-DL tentative, 1992. International Society for Optics and Photonics, 586-606.
- BETTI, B., CAZZANIGA, N. E. & TORNATORE, V. 2011. Deformation Assessment Considering an A Priori Functional Model in a Bayesian Framework. *Journal of Surveying Engineering-Asce*, 137, 113-119.
- BILELLO, C., GRECO, E., GRECO, M., MADONIA, N., PIRROTTA, A. & SORCE, A. 2016. A numerical model for pre-monitoring design of historical colonnade courtyards: the case study of Chiaramonte Palace in Palermo. *The Open Construction and Building Technology Journal*, 10.
- BITELLI, G., DUBBINI, M. & ZANUTTA, A. 2004. Terrestrial laser scanning and digital photogrammetry techniques to monitor landslide bodies. *International Archives of Photogrammetry, Remote Sensing and Spatial Information Sciences*, 35, 246-251.
- BOEHLER, W., BORDAS VICENT, M. & MARBS, A. 2003. Investigating laser scanner accuracy. *The International Archives of Photogrammetry, Remote Sensing and Spatial Information Sciences*, 34, 696-701.
- BÖHLER, W. & MARBS, A. 3D scanning and photogrammetry for heritage recording: a comparison. Proceedings of the 12th International Conference on Geoinformatics, 2004. Citeseer, 291-298.
- BURLAND, J. B., BROMS, B. B. & DE MELLO, V. F. 1978. Behaviour of foundations and structures. Building Research Establishment Garston.
- CALLISTER, W. D. & RETHWISCH, D. G. 2007. *Materials Science and Engineering An Introduction*, New York-USA, John Wiley & Sons.
- CARR, J. C., BEATSON, R. K., CHERRIE, J. B., MITCHELL, T. J., FRIGHT, W. R., MCCALLUM, B. C. & EVANS, T. R. Reconstruction and representation of 3D objects with radial basis functions. Proceedings of the 28th annual conference on Computer graphics and interactive techniques, 2001 Los Angeles, CA, USA. ACM, 67-76.
- CARR, J. C., FRIGHT, W. R. & BEATSON, R. K. 1997. Surface interpolation with radial basis functions for medical imaging. *Ieee Transactions on Medical Imaging*, 16, 96-107.

- CASE, F., BEINAT, A., CROSILLA, F. & ALBA, I. M. 2014. Virtual trial assembly of a complex steel structure by Generalized Procrustes Analysis techniques. *Automation in Construction*, 37, 155-165.
- CASTAGNETTI, C., BERTACCHINI, E. & CAPRA, A. 2016. Monitoring leaning towers by geodetic approaches: effects of subsidence and earthquake to the Ghirlandina Tower. *Structural Control and Health Monitoring*, 23, 580-593.
- CERIOTTI, M., MOTTOLA, L., PICCO, G. P., MURPHY, A. L., GUNA, S., CORRA, M., POZZI, M., ZONTA, D. & ZANON, P. Monitoring heritage buildings with wireless sensor networks: The Torre Aquila deployment. Proceedings of the 2009 International Conference on Information Processing in Sensor Networks, 2009. IEEE Computer Society, 277-288.
- CHEN, Y. & MEDIONI, G. Object modeling by registration of multiple range images. Robotics and Automation, 1991. Proceedings., 1991 IEEE International Conference on, 1991. IEEE, 2724-2729.
- CHO, S., JANG, S. A., JO, H., MECHITOV, K., RICE, J. A., JUNG, H.-J., YUN, C.-B., SPENCER JR, B. F., NAGAYAMA, T. & SEO, J. Structural health monitoring system of a cable-stayed bridge using a dense array of scalable smart sensor network. SPIE Smart Structures and Materials+ Nondestructive Evaluation and Health Monitoring, 2010. International Society for Optics and Photonics, 764707-764707-12.
- CORSINI, A., CASTAGNETTI, C., BERTACCHINI, E., RIVOLA, R., RONCHETTI, F. & CAPRA, A. 2013. Integrating airborne and multi-temporal long-range terrestrial laser scanning with total station measurements for mapping and monitoring a compound slow moving rock slide. *Earth Surface Processes and Landforms*, 38, 1330-1338.
- CROSILLA, F. 1983a. A criterion matrix for the second order design of control networks. *Bulletin géodésique*, 57, 226-239.
- CROSILLA, F. 2003. Procrustes analysis and geodetic sciences. In *Geodesy-The Challenge of the 3rd Millennium*. Springer Berlin Heidelberg.
- CROSILLA, F. & BEINAT, A. 2002. Use of generalised Procrustes analysis for the photogrammetric block adjustment by independent models. *ISPRS Journal of Photogrammetry and Remote Sensing*, 56, 195-209.
- CROSILLA, F. T. 1983b. Procrustean transformation as a tool for the construction of a criterion Matrix for control networks. *Manuscripta Geodetica*, 8, 343-370.
- DAL PIAZ, V., GUARNIER, A., PIRTTI, F. & VETTORE, A. 2007. Stability control of an historical structure with TLS survey. *ISPRS Archives*. ETH Zurich, Switzerland: ISPRS
- DE ASÍS LÓPEZ, F., ORDÓÑEZ, C., ROCA-PARDIÑAS, J. & GARCÍA-CORTÉS, S. 2014. Point cloud comparison under uncertainty. Application to beam bridge measurement with terrestrial laser scanning. *Measurement*, 51, 259-264.
- DE STEFANO, A. Structural identification and health monitoring on the historical architectural heritage. Key Engineering Materials, 2007. Trans Tech Publ, 37-54.
- DE STEFANO, A., MATTA, E. & CLEMENTE, P. 2016. Structural health monitoring of historical heritage in Italy: some relevant experiences. *Journal of Civil Structural Health Monitoring*, 6, 83-106.
- DOS SANTOS, D. R., DAL POZ, A. P. & KHOSHELHAM, K. 2013. Indirect Georeferencing of Terrestrial Laser Scanning Data using Control Lines. *The Photogrammetric Record*, 28, 276-292.
- DRUML, T., DOBRETSBERGER, M. & BREM, G. 2015. The use of novel phenotyping methods for validation of equine conformation scoring results. *animal*, 9, 928-937.
- DUVNJAK, I., DAMJANOVIĆ, D. & KROLO, J. Structural health monitoring of cultural heritage structures: Applications on Peristyle of Diocletians Palace in Split. 8th European Workshop On Structural Health Monitoring (EWSHM 2016), 2016.

- ELYAMANI, A., CASELLES, O., ROCA, P. & CLAPES, J. 2016. Dynamic investigation of a large historical cathedral. *Structural Control and Health Monitoring*.
- FASSI, F., FREGONESE, L., ACKERMANN, S. & DE TROIA, V. 2013. Comparison between laser scanning and automated 3D modeling techniques to reconstruct complex and extensive cultural heritage areas. *Proceedings of the International Archives of the Photogrammetry, Remote Sensing and Spatial Information Sciences, Trento, Italy, 2526*, 40-5.
- FUSIELLO, A. & CROSILLA, F. 2015. Solving bundle block adjustment by generalized anisotropic Procrustes analysis. *ISPRS Journal of Photogrammetry and Remote Sensing*, 102, 209-221.
- GARRO, V., CROSILLA, F. & FUSIELLO, A. Solving the PnP Problem with Anisotropic Orthogonal Procrustes Analysis. 3DIMPVT, 2012. 262-269.
- GATTULLI, V., LEPIDI, M. & POTENZA, F. 2016. Dynamic testing and health monitoring of historic and modern civil structures in Italy. *Structural Monitoring and Maintenance*, 3, 71-90.
- GENTILE, C. 2009. Application of microwave remote sensing to dynamic testing of stay-cables. *Remote Sensing*, 2, 36-51.
- GENTILE, C., GUIDOBALDI, M. & SAISI, A. 2016. One-year dynamic monitoring of a historic tower: damage detection under changing environment. *Meccanica*, 51, 2873-2889.
- GEOSYSTEMS, L. 2015. *RE: Quality Level of ScanStation P20*. Type to BONENBERG, L.
- GIRARDEAU-MONTAUT, D., BOUGACHA, S., BEY, A. & MARC, R. 2006. *CloudCompare* [Online]. Available: <http://www.cloudcompare.org/> [Accessed 25/9/2014].
- GIRARDEAU-MONTAUT, D., ROUX, M., MARC, R. & THIBAUT, G. 2005. Change detection on points cloud data acquired with a ground laser scanner. *International Archives of Photogrammetry, Remote Sensing and Spatial Information Sciences*, 36, W19.
- GONZALEZ-AGUILERA, D., GOMEZ-LAHOZ, J. & SANCHEZ, J. 2008. A new approach for structural monitoring of large dams with a three-dimensional laser scanner. *Sensors*, 8, 5866-5883.
- GONZÁLEZ-AGUILERA, D., MUÑOZ-NIETO, A., GÓMEZ-LAHOZ, J., HERRERO-PASCUAL, J. & GUTIERREZ-ALONSO, G. 2009. 3D digital surveying and modelling of cave geometry: Application to paleolithic rock art. *Sensors*, 9, 1108-1127.
- GOODALL, C. 1991. Procrustes methods in the statistical analysis of shape. *Journal of the Royal Statistical Society. Series B (Methodological)*, 285-339.
- GORDON, S. & LICHTI, D. 2004. Terrestrial laser scanners with a narrow field of view: the effect on 3D resection solutions. *Survey Review*, 37, 448-468.
- GORDON, S., LICHTI, D., FRANKE, J. & STEWART, M. Measurement of structural deformation using terrestrial laser scanners. 1st FIG International Symposium on Engineering Surveys for Construction Works and Structural Engineering, Nottingham, United Kingdom, 2004a.
- GORDON, S., LICHTI, D. & STEWART, M. Application of a high-resolution, ground-based laser scanner for deformation measurements. Proceedings of 10th International FIG Symposium on Deformation Measurements, 2001 Orange, California, USA. 19-22.
- GORDON, S., LICHTI, D., STEWART, M. & FRANKE, J. 2004b. Modelling point clouds for precise structural deformation measurement. *International Archives of Photogrammetry and Remote Sensing*, 35, B5.
- GORDON, S. J. & LICHTI, D. D. 2007. Modeling terrestrial laser scanner data for precise structural deformation measurement. *Journal of Surveying Engineering*, 133, 72-80.

- GOWER, J. C. 1975. Generalized procrustes analysis. *Psychometrika*, 40, 33-51.
- GRUEN, A. & AKCA, D. 2005. Least squares 3D surface and curve matching. *ISPRS Journal of Photogrammetry and Remote Sensing*, 59, 151-174.
- GRUEN, A. W. & AKCA, M. D. 2003. Generalized procrustes analysis and its applications in photogrammetry. *Institute of Geodesy and Photogrammetry*. ETH-Hoenggerberg, Zuerich: SWISS FEDERAL INSTITUTE OF TECHNOLOGY.
- GRÜNDIG, L., NEUREITHER, M. & BAHNDORF, J. 1985. Detection and localization of geometrical movements. *Journal of surveying engineering*, 111, 118-132.
- GUARNIERI, A., PIROTTI, F., PONTIN, M. & VETTORE, A. 2005. Combined 3D surveying techniques for structural analysis applications. *International archives of photogrammetry, remote sensing and spatial information sciences*, 36, 6.
- GUIDI, G., REMONDINO, F., RUSSO, M., MENNA, F. & RIZZI, A. 3D Modeling of Large and Complex Site Using Multi-sensor Integration and Multi-resolution Data. VAST, 2008. 85-92.
- HABIB, A. F. & ALRUZOUQ, R. I. 2004. Line-based modified iterated Hough transform for automatic registration of multi-source imagery. *The Photogrammetric Record*, 19, 5-21.
- HARMS, T., BANKS, B., SARVESTANI, S. S. & BASTIANINI, F. Design and testing of a low-power wireless sensor network for structural health monitoring of bridges. SPIE Smart Structures and Materials+ Nondestructive Evaluation and Health Monitoring, 2009a. International Society for Optics and Photonics, 72920U-72920U-8.
- HARMS, T., BASTIANINI, F. & SEDIGH, S. Recent enhancements to the SmartBrick structural health monitoring platform. Intelligent Transportation Systems, 2009. ITSC'09. 12th International IEEE Conference on, 2009b. IEEE, 1-6.
- HARMS, T., SEDIGH, S. & BASTIANINI, F. 2010. Structural health monitoring of bridges using wireless sensor networks. *Instrumentation & Measurement Magazine, IEEE*, 13, 14-18.
- HEJBUDZKA, K. & DUMALSKI, A. 2011. Investigating the accuracy of spatial coordinates of modeled HDS target center depending on the range from terrestrial laser scanner measurements. *Reports on Geodesy*, 1/90, 157-164.
- HERITAGE, E. 2011. 3D laser scanning for heritage. *Advice and guidance to users on laser scanning in archaeology and architecture*. . October 2011 ed. Swindon/United Kingdom: English Heritage.
- HERITAGE, E. 2015. *English Heritage About Us* [Online]. Available: <http://www.english-heritage.org.uk/about-us/> [Accessed 27/7/2015 2015].
- HILL, C. D. & SIPPEL, K. D. 2002. Modern deformation monitoring: A multi sensor approach. *FIG XXII Internatinal Congress*. Washington DC, USA.
- HISTORIC, E. 2015a. *Bellmanpark lime kilns and part of an associated tramway 180m north west of Bellman Farm* [Online]. Available: <https://historicengland.org.uk/listing/the-list/list-entry/1021105> [Accessed 9/12/2015 2015].
- HISTORIC, E. 2015b. *Historic England* [Online]. Available: <http://www.historicengland.org.uk/> [Accessed 22/9/2015 2015].
- HODGE, R., BRASINGTON, J. & RICHARDS, K. 2009. In situ characterization of grain-scale fluvial morphology using Terrestrial Laser Scanning. *Earth Surface Processes and Landforms*, 34, 954-968.
- HODGE, R. A. 2010. Using simulated Terrestrial Laser Scanning to analyse errors in high-resolution scan data of irregular surfaces. *ISPRS Journal of Photogrammetry and Remote Sensing*, 65, 227-240.

- HOLST, C. & KUHLMANN, H. 2016. Challenges and Present Fields of Action at Laser Scanner Based Deformation Analyses. *Journal of Applied Geodesy*, 10, 17-25.
- IKEDA, R., OBEROI, S., WILEY, D. F., WOODHOUSE, C., TALLMAN, M., TUN, W. W., MCNEILL, C., MILLER, A. J. & HATCHER, D. 2016. Novel 3-dimensional analysis to evaluate temporomandibular joint space and shape. *American Journal of Orthodontics and Dentofacial Orthopedics*, 149, 416-428.
- INGENSAND, H. Metrological aspects in terrestrial laser-scanning technology. Proceedings of the 3rd IAG/12th FIG symposium, Baden, Austria, 2006.
- ISLAM, S. 2015. *Least Squares Plane* [Online]. Available: <http://www.sbg.bio.ic.ac.uk/~islam/plane.html> [Accessed 17/2/2015 2015].
- JAVERNICK, L., BRASINGTON, J. & CARUSO, B. 2014. Modeling the topography of shallow braided rivers using Structure-from-Motion photogrammetry. *Geomorphology*, 213, 166-182.
- KAASALAINEN, S., JAAKKOLA, A., KAASALAINEN, M., KROOKS, A. & KUKKO, A. 2011. Analysis of incidence angle and distance effects on terrestrial laser scanner intensity: search for correction methods. *Remote Sensing*, 3, 2207-2221.
- KALKAN, Y., ALKAN, R. M. & BILGI, S. 2010. Deformation Monitoring Studies at Atatürk Dam. *FIG Congress: Facing the Challenges – Building the Capacity*. Sydney, Australia.
- KILPELÄ, A. 2004. *Pulsed time-of-flight laser range finder techniques for fast, high precision measurement applications*. PhD, University of Oulu.
- KIM, J.-T., SIM, S.-H., CHO, S., YUN, C.-B. & MIN, J. 2016. Recent R&D activities on structural health monitoring in Korea.
- KIM, M.-K., SOHN, H. & CHANG, C.-C. 2014. Localization and Quantification of Concrete Spalling Defects Using Terrestrial Laser Scanning. *Journal of Computing in Civil Engineering*, 29.
- KOLECKA, N. 2011. Photo-based 3D scanning vs. laser scanning—Competitive data acquisition methods for digital terrain modelling of steep mountain slopes. *International Archives of the Photogrammetry, Remote Sensing and Spatial Information Sciences*, 38, 4.
- LAEFER, D. F., FITZGERALD, M., MALONEY, E. M., COYNE, D., LENNON, D. & MORRISH, S. W. 2009. Lateral Image Degradation in Terrestrial Laser Scanning. *Structural Engineering International*, 19, 184-189.
- LAGUE, D., BRODU, N. & LEROUX, J. 2013. Accurate 3D comparison of complex topography with terrestrial laser scanner: Application to the Rangitikei canyon (N-Z). *ISPRS Journal of Photogrammetry and Remote Sensing*, 82, 10-26.
- LASER TECHNOLOGIES, C. 2016. *Laser Theory & Laser Safety* [Online]. Alameda, Canda: Convergent Laser Technologies. Available: <http://www.convergentlaser.com/laser-safety> [Accessed 1st Nov. 2016].
- LE, T. S., CHANG, C.-P., NGUYEN, X. T. & YHOKHA, A. 2016. TerraSAR-X Data for High-Precision Land Subsidence Monitoring: A Case Study in the Historical Centre of Hanoi, Vietnam. *Remote Sensing*, 8, 338.
- LEICA GEOSYSTEMS, A. 2013. *Leica ScanStation P20* [Online]. Available: http://www.leica-geosystems.co.uk/downloads123/hds/hds/ScanStation_P20/brochures-datasheet/Leica_ScanStation_P20_DAT_en.pdf [Accessed 4/3/2015 2015].
- LEICA GEOSYSTEMS, A. 2016a. *Leica ScanStation P30/P40* [Online]. Available: http://www.leica-geosystems.co.uk/en/Leica-ScanStation-P40-P30_106396.htm [Accessed 3/3/2016 2016].
- LEICA GEOSYSTEMS, A. 2016b. *Targets* [Online]. Available: http://hds.leica-geosystems.com/en/Targets_19143.htm [Accessed March 2016].

- LERMA, J. L., NAVARRO, S., CABRELLES, M. & VILLAVERDE, V. 2010. Terrestrial laser scanning and close range photogrammetry for 3D archaeological documentation: the Upper Palaeolithic Cave of Parpalló as a case study. *Journal of Archaeological Science*, 37, 499-507.
- LIANG, Y.-B., ZHAN, Q.-M., CHE, E.-Z., CHEN, M.-W. & ZHANG, D.-L. 2014. Automatic Registration of Terrestrial Laser Scanning Data Using Precisely Located Artificial Planar Targets. *Geoscience and Remote Sensing Letters, IEEE*, 11, 69-73.
- LICHTI, D., GORDON, S., STEWART, M., FRANKE, J. & TSAKIRI, M. Comparison of digital photogrammetry and laser scanning. Proc. International Society for Photogrammetry and Remote Sensing, 2002. 39-44.
- LICHTI, D. & GORDON, S. J. Error Propagation in Directly Georeferenced Terrestrial Laser Scanner Point Clouds for Cultural Heritage Recording. FIG Working Week May 22–27 2004 Athens, Greece.
- LICHTI, D. D. 2007. Error modelling, calibration and analysis of an AM–CW terrestrial laser scanner system. *ISPRS Journal of Photogrammetry and Remote Sensing*, 61, 307-324.
- LICHTI, D. D., GORDON, S. J. & TIPDECHO, T. 2005. Error models and propagation in directly georeferenced terrestrial laser scanner networks. *Journal of surveying engineering*, 131, 135-142.
- LICHTI, D. D. & JAMTSHO, S. 2006. Angular resolution of terrestrial laser scanners. *The Photogrammetric Record*, 21, 141-160.
- LINDENBERGH, R. & PFEIFER, N. A Statistical Deformation Analysis of Two Epochs of Terrestrial Laser Scanner Data of a Lock. Optical 3D Measurement Techniques VII, 3-5 October 2005 2005 Vienna. 61-70.
- LINDENBERGH, R., PFEIFER, N. & RABBANI, T. 2005. Accuracy Analysis of the Leica HDS3000 and Feasibility of Tunnel Deformation Monitoring. *Laser scanning 2005*. Enschede, the Netherlands.
- LORENZO, J. M., PURRIÑOS, L. & CARBALLO, J. 2016. A Survey on the Effect of Livestock Production System and Finishing Diet on Sensory Characteristics of Foal Meat Using Generalized Procrustes Analysis. *The Scientific World Journal*, 2016, 6.
- LORENZONI, F., CASARIN, F., CALDON, M., ISLAMI, K. & MODENA, C. 2016. Uncertainty quantification in structural health monitoring: Applications on cultural heritage buildings. *Mechanical Systems and Signal Processing*, 66, 268-281.
- MA, W. & KRUTH, J.-P. 1998. NURBS curve and surface fitting for reverse engineering. *The International Journal of Advanced Manufacturing Technology*, 14, 918-927.
- MAAR, H. & ZOGG, H.-M. 2014. *WFD – Wave Form Digitizer Technology* [Online]. Heerbrugg, Switzerland: Leica Geosystems AG. Available: http://w3.leica-geosystems.com/downloads123/zz/tps/nova_ms50/white-tech-paper/Leica_Nova_MS50_WFD-Wave_Form_Digitizer_Technology_TPA_en.pdf [Accessed 1/4/2016].
- MARGOTTINI, C., GIGLI, G., RUTHER, H. & SPIZZICHINO, D. 2016. Advances in geotechnical investigations and monitoring in rupestrian settlements inscribed in the UNESCO's World Heritage List. *Procedia Earth and Planetary Science*, 16, 35-51.
- MARTÍNEZ-GARRIDO, M. & FORT, R. 2016. Experimental assessment of a wireless communications platform for the built and natural heritage. *Measurement*, 82, 188-201.
- MASCIOTTA, M.-G., RAMOS, L. F., LOURENÇO, P. B. & MATOS, J. A. Development of Key Performance Indicators for the Structural Assessment of Heritage Buildings. 8th European Workshop on Structural Health Monitoring (EWSHM 2016), 2016. 1-12.
- MATHWORKS. 2015. *Filtering and Smoothing Data* [Online]. Available: http://uk.mathworks.com/help/curvefit/smoothing-data.html#bq_6ys3-3 [Accessed 26/2/2015 2015].

- MAURICIO, A., PALAZZO, A., CASELATO, V. & BOLINI, H. 2016. Generalized Procrustes Analysis and External Preference Map Used to Consumer Drivers of Diet Gluten Free Product. *Food and Nutrition Sciences*, 7, 711.
- MEAIKE, J., GUPTA, A., PAGANO, A., CURCIO, D. F., SOM, P. & LAITMAN, J. T. 2016. Using CT Scans to Assess Early Postnatal Development of the Bony Eustachian Tube and Hyolaryngeal Apparatus: A Test of Reliability. *The FASEB Journal*, 30, 780.6-780.6.
- MENG, X. 2002. *Real-time Deformation Monitoring of Bridges using GPS/Accelerometers*. PhD, University of Nottingham.
- MESAS-CARRASCOSA, F. J., VERDÚ SANTANO, D., MEROÑO DE LARRIVA, J. E., ORTÍZ CORDERO, R., HIDALGO FERNÁNDEZ, R. E. & GARCÍA-FERRER, A. 2016. Monitoring Heritage Buildings with Open Source Hardware Sensors: A Case Study of the Mosque-Cathedral of Córdoba. *Sensors*, 16, 1620.
- MILL, T. & ELLMANN, A. Terrestrial Laser Scanning Technology for Deformation Monitoring of a Large Suspension Roof Structure. INGENEO 2014-International Conference on Engineering Surveying, 3-4 April, 2014 2014 Prague, Czech Republic.
- MONSERRAT, O. & CROSETTO, M. 2008. Deformation measurement using terrestrial laser scanning data and least squares 3D surface matching. *ISPRS Journal of Photogrammetry and Remote Sensing*, 63, 142-154.
- MOORE, J. F. A. 1992. *Monitoring Building Structures*, London and Glasgow, Blackie and Son Ltd.
- NADAL-ROMERO, E., REVUELTO, J., ERREA, P. & LÓPEZ-MORENO, J. 2015. The application of terrestrial laser scanner and SfM photogrammetry in measuring erosion and deposition processes in two opposite slopes in a humid badlands area (central Spanish Pyrenees). *SOIL, Volume 1, Issue 2, 2015, pp. 561-573*, 1, 561-573.
- OLSEN, M. J., KUESTER, F., CHANG, B. J. & HUTCHINSON, T. C. 2010. Terrestrial laser scanning-based structural damage assessment. *Journal of Computing in Civil Engineering*, 24, 264-272.
- OUÉDRAOGO, M. M., DEGRÉ, A., DEBOUCHE, C. & LISEIN, J. 2014. The evaluation of unmanned aerial system-based photogrammetry and terrestrial laser scanning to generate DEMs of agricultural watersheds. *Geomorphology*, 214, 339-355.
- PALÁNCZ, B., ZALETNYIK, P., AWANGE, J. & HECK, B. 2010. Extension of the ABC-Procrustes algorithm for 3D affine coordinate transformation. *Earth Planets and Space*, 62, 857.
- PARK, H. S., LEE, H. M., ADELI, H. & LEE, I. 2007. A New Approach for Health Monitoring of Structures: Terrestrial Laser Scanning. *Computer-Aided Civil and Infrastructure Engineering*, 22, 19-30.
- PARK, I. K., YUN, I. D. & LEE, S. U. Constructing NURBS Surface Model from Scattered and Unorganized Range Data. 3-D Digital Imaging and Modeling, 4-8 October 1999 Ottawa-Canada. 312-321.
- PEJIĆ, M. 2013. Design and optimisation of laser scanning for tunnels geometry inspection. *Tunnelling and Underground Space Technology*, 37, 199-206.
- PESCI, A., CASULA, G. & BOSCHI, E. 2011a. Laser scanning the Garisenda and Asinelli towers in Bologna (Italy): Detailed deformation patterns of two ancient leaning buildings. *Journal of Cultural Heritage*, 12, 117-127.
- PESCI, A., LODDO, F. & CONFORTI, D. 2007. The first terrestrial laser scanner application over Vesuvius: High resolution model of a volcano crater. *International Journal of Remote Sensing*, 28, 203-219.
- PESCI, A., TEZA, G. & BONALI, E. 2011b. Terrestrial laser scanner resolution: Numerical simulations and experiments on spatial sampling optimization. *Remote Sensing*, 3, 167-184.

- PESCI, A., TEZA, G., BONALI, E., CASULA, G. & BOSCHI, E. 2013. A laser scanning-based method for fast estimation of seismic-induced building deformations. *Isprs Journal of Photogrammetry and Remote Sensing*, 79, 185-198.
- PINIOTIS, G., GIKAS, V., MPIMIS, T. & PERAKIS, H. 2016. Deck and Cable Dynamic Testing of a Single-span Bridge Using Radar Interferometry and Videometry Measurements. *Journal of Applied Geodesy*, 10, 87-94.
- PRATESI, F., NOLESINI, T., BIANCHINI, S., LEVA, D., LOMBARDI, L., FANTI, R. & CASAGLI, N. 2015. Early warning GBInSAR-based method for monitoring Volterra (Tuscany, Italy) city walls. *IEEE Journal of Selected Topics in Applied Earth Observations and Remote Sensing*, 8, 1753-1762.
- RESHETYUK, Y. 2009. *Self-calibration and direct georeferencing in terrestrial laser scanning*. PhD, Royal Institute of Technology (KTH).
- RETAMOZO, S., ARCE, D., AGUILAR, R., ZVIETCOVICH, F., QUINTANA, M. & CASTA, B. A comparison of digital modelling techniques analyzing a section of Qhapaq?? an. 2015 Digital Heritage, 2015. IEEE, 147-150.
- ROBERTS, G. & BADDLEY, M. 2007. Deformation Monitoring Trials Using a Leica HDS3000.pdf. *Strategic Integration of Surveying Services FIG Working Week 2007*. Hong Kong SAR, China.
- ROCA-PARDIÑAS, J., LORENZO, H., ARIAS, P. & ARMESTO, J. 2008. From laser point clouds to surfaces: Statistical nonparametric methods for three-dimensional reconstruction. *Computer-Aided Design*, 40, 646-652.
- RUSINKIEWICZ, S. & LEVOY, M. Efficient variants of the ICP algorithm. 3-D Digital Imaging and Modeling, 2001. Proceedings. Third International Conference on, 2001. IEEE, 145-152.
- RUSU, R. B. 2011. *Point Cloud Library* [Online]. Available: <http://pointclouds.org/documentation/tutorials/#filtering-tutorial> [Accessed 12/4/2015 2015].
- SAISI, A., GENTILE, C. & RUCCOLO, A. 2016a. Pre-diagnostic prompt investigation and static monitoring of a historic bell-tower. *Construction and Building Materials*.
- SAISI, A., GUIDOBALDI, M. & GENTILE, C. 2016b. On Site Investigation and Health Monitoring of a Historic Tower in Mantua, Italy. *Applied Sciences*, 6, 173.
- SCHÄFER, T., WEBER, T., KYRINOVIČ, P. & ZÁMEČNIKOVÁ, M. Deformation measurement using terrestrial laser scanning at the hydropower station of Gabčíkovo. Proceedings of INGENEO 2004 and FIG Regional Central and Eastern European Conference on Engineering Surveying/Kopačik, A.(ed.), 2004.
- SCHNEIDER, D. Terrestrial laser scanning for area based deformation analysis of towers and water dams. Proc. of 3rd IAG/12th FIG Symp., Baden, Austria, May, 2006. 22-24.
- SCHÖNEMANN, P. H. 1966. A generalized solution of the orthogonal Procrustes problem. *Psychometrika*, 31, 1-10.
- SCHÖNEMANN, P. H. & CARROLL, R. M. 1970. Fitting one matrix to another under choice of a central dilation and a rigid motion. *Psychometrika*, 35, 245-255.
- SOUDARISSANANE, S., LINDENBERGH, R. & GORTE, B. Reducing the error in terrestrial laser scanning by optimizing the measurement set-up. XXI ISPRS Congress, Commission I-VIII, 3-11 July 2008, Beijing, China, 2008. International Society for Photogrammetry and Remote Sensing.
- SOUDARISSANANE, S., LINDENBERGH, R., MENENTI, M. & TEUNISSEN, P. Incidence angle influence on the quality of terrestrial laser scanning points. ISPRS Workshop Laserscanning, 1-2 September 2009 Paris, France.

- SODARISSANANE, S., LINDENBERGH, R., MENENTI, M. & TEUNISSEN, P. 2011. Scanning geometry: Influencing factor on the quality of terrestrial laser scanning points. *ISPRS Journal of Photogrammetry and Remote Sensing*, 66, 389-399.
- STAIGER, R. The geometrical quality of terrestrial laser scanner (TLS). Proceedings of FIG Working Week, 16-21 April 2005 Cairo, Egypt.
- TANG, P., CHEN, F., ZHU, X. & ZHOU, W. 2016. Monitoring Cultural Heritage Sites with Advanced Multi-Temporal InSAR Technique: The Case Study of the Summer Palace. *Remote Sensing*, 8, 432.
- TAPETE, D., CASAGLI, N., LUZI, G., FANTI, R., GIGLI, G. & LEVA, D. 2013. Integrating radar and laser-based remote sensing techniques for monitoring structural deformation of archaeological monuments. *Journal of Archaeological Science*, 40, 176-189.
- TEN BERGE, J. M. 1977. Orthogonal Procrustes rotation for two or more matrices. *Psychometrika*, 42, 267-276.
- TEZA, G., GALGARO, A., ZALTRON, N. & GENEVOIS, R. 2007. Terrestrial laser scanner to detect landslide displacement fields: a new approach. *International Journal of Remote Sensing*, 28, 3425-3446.
- TEZA, G., PESCI, A. & NINFO, A. 2016. Morphological Analysis for Architectural Applications: Comparison between Laser Scanning and Structure-from-Motion Photogrammetry. *Journal of Surveying Engineering*, 04016004.
- THEILER, P., WEGNER, J. & SCHINDLER, K. 2013. Markerless point cloud registration with keypoint-based 4-points congruent sets. *ISPRS Annals of Photogrammetry, Remote Sensing and Spatial Information Sciences*, 2, 283-288.
- THEILER, P., WEGNER, J. & SCHINDLER, K. 2014. FAST REGISTRATION OF LASER SCANS WITH 4-POINTS CONGRUENT SETS—WHAT WORKS AND WHAT DOESN'T. *ISPRS Annals of the Photogrammetry, Remote Sensing and Spatial Information Sciences*, 2.
- TOLDO, R., BEINAT, A. & CROSILLA, F. Global registration of multiple point clouds embedding the Generalized Procrustes Analysis into an ICP framework. 3DPVT 2010 Conference, 2010.
- TOMIC, O., BERGET, I. & NÆS, T. 2015. A comparison of generalised procrustes analysis and multiple factor analysis for projective mapping data. *Food Quality and Preference*, 43, 34-46.
- TSAKIRI, M., LICHTI, D. & PFEIFER, N. Terrestrial laser scanning for deformation monitoring. 12th on deformation measurements and 3rd IAG symposium on geodesy for geotechnical and structure engineering, 2006 Baden, Austria.
- UBERTINI, F., COMANDUCCI, G. & CAVALAGLI, N. 2016. Vibration-based structural health monitoring of a historic bell-tower using output-only measurements and multivariate statistical analysis. *Structural Health Monitoring*, 1475921716643948.
- URREGO, B., ELVIRA, L., VERSTRYNGE, E., VAN BALEN, K., WUYTS, V. & DECLERCQ, P.-Y. Settlement-induced damage monitoring of a historical building located in a coal mining area using PS-InSAR. 6th Workshop on Civil Structural Health Monitoring, 2016. Queen's University.
- USACE 2002. Engineering and Design: STRUCTURAL DEFORMATION SURVEYING. No. 1110-2-1009. Washington, DC: DEPARTMENT OF THE ARMY-US Army Corps of Engineers.
- VALANIS, A. & TSAKIRI, M. Automatic target identification for laser scanners. Proceedings of XXth ISPRS Congress, Istanbul, Turkey, 2004.
- VAN DIJK, N., GAMSTEDT, E. K. & BJURHAGER, I. 2016. Monitoring archaeological wooden structures: Non-contact measurement systems and interpretation as average strain fields. *Journal of Cultural Heritage*, 17, 102-113.

- VAN GENECHTEN, B., QUINTERO, M. S., BRUYNE, M. D., POELMAN, R., HANKAR, M., BARNES, S., CANER, H., BUDEI, L., HEINE, E., REINER, H., GARCÍA, J. L. L. & TARONGER, J. M. B. 2008. Theory and practice on Terrestrial Laser Scanning: Training material based on practical applications. Valencia, Spain: Universidad Politecnica de Valencia Editorial.
- VAN GOSLIGA, R., LINDENBERGH, R. & PFEIFER, N. 2006. Deformation analysis of a bored tunnel by means of terrestrial laser scanning. *Image Engineering and Vision Metrology. ISPRS Commission, 36*, 167-172.
- VERMEESCH, P. & GARZANTI, E. 2015. Making geological sense of 'Big Data' in sedimentary provenance analysis. *Chemical Geology*, 409, 20-27.
- VOEGTLE, T., SCHWAB, I. & LANDES, T. 2008. Influences of different materials on the measurements of a Terrestrial Laser Scanner (TLS). *The International Archives of the Photogrammetry, Remote Sensing and Spatial Information Sciences, XXXVII*. Part B5, 1061-1066.
- WALSH, S. B., BORELLO, D. J., GULDUR, B. & HAJJAR, J. F. 2013. Data Processing of Point Clouds for Object Detection for Structural Engineering Applications. *Computer-Aided Civil and Infrastructure Engineering*, 28, 495-508.
- WANG, C., ZHAN, X., LIANG, L., ABECASIS, G. R. & LIN, X. 2015. Improved ancestry estimation for both genotyping and sequencing data using projection procrustes analysis and genotype imputation. *The American Journal of Human Genetics*, 96, 926-937.
- WANG, G., PHILIPS, D., JOYCE, J. & RIVERA, F. 2011. The Integration of TLS and Continuous GPS to Study Landslide Deformation: A Case Study in Puerto Rico. *Journal of Geodetic Science*, 1, 25-34.
- WENTZELL, P. D., HOU, S., SILVA, C. S., WICKS, C. C. & PIMENTEL, M. F. 2015. Procrustes rotation as a diagnostic tool for projection pursuit analysis. *Analytica chimica acta*, 877, 51-63.
- YANG, B. & ZANG, Y. 2014. Automated registration of dense terrestrial laser-scanning point clouds using curves. *ISPRS Journal of Photogrammetry and Remote Sensing*, 95, 109-121.
- YANG, J., LI, H. & JIA, Y. Go-ICP: solving 3D registration efficiently and globally optimally. *Computer Vision (ICCV)*, 2013 IEEE International Conference on, 2013. IEEE, 1457-1464.
- YAO, J., RUGGERI, M. R., TADDEI, P. & SEQUEIRA, V. 2010. Automatic scan registration using 3D linear and planar features. *3D Research*, 1, 1-18.
- YARDIM, Y. & MUSTAFARAJ, E. 2015. Effects of soil settlement and deformed geometry on a historical structure. *Natural Hazards and Earth System Sciences*, 15, 1051-1059.
- ZHOU, B. X., YUE, J. P. & JIA, K. Y. 2011. Automatic Deformation Acquisition using Terrestrial Laser Scanner. *Applied Mechanics and Materials* 90-93, 2811-2817.
- ZOGG, H. M. 2008. *Investigation of High Precision Terrestrial Laser Scanning with Emphasis on the Development of a Robust Close-Range 3D-Laser Scanning System*. PhD, ETH Zurich.

APPENDICES

A. Published Articles (extracted from thesis)

JAAFAR, H., MENG, X. & SOWTER, A. 2017. New Approach for Monitoring Historic and heritage buildings: Using Terrestrial Laser Scanning and Generalised Procrustes Analysis. *Structural Control and Health Monitoring*, Under publishing.

JAAFAR, H., MENG, X. & SOWTER, A. 2017. Terrestrial laser scanner error quantification for the purpose of monitoring. *Survey Review* Under publishing.

JAAFAR, H., MENG, X. & SOWTER, A. 2016. HEALTH MONITORING OF HISTORIC RUINS AND HERITAGE BUILDINGS USING TERRESTRIAL LASER SCANNING AND GENERALISED PROCRUSTES ANALYSIS. *5th International Conference on Heritage and Sustainable Development*. Lisbon / Portugal: Green Lines Institute.

JAAFAR, H., MENG, X. & SOWTER, A. 2015. DETECTION OF STRUCTURE DEFORMATION USING TERRESTRIAL LASER SCANNING AND GENERALISED PROCRUSTES ANALYSIS TECHNIQUE. *International Conference on Advances in Structural and Geotechnical Engineering*. Hurghada, Egypt.

B. Cyclone Registration Report of Bellmanpark Limekilns Scans

Status: VALID Registration Mean Absolute Error: for Enabled Constraints = 0.001 m for Disabled Constraints = 0.000 m

Date: 2016.01.25 12:12:40

Database name : BellmanparkProject_2

ScanWorlds

Bellman_OS_targets.txt (Leveled)

001: SW-001 (Leveled)
 002: SW-002 (Leveled)
 003: SW-003 (Leveled)
 004: SW-004 (Leveled)
 005: SW-005 (Leveled)
 006: SW-006 (Leveled)
 007: SW-007 (Leveled)
 008: SW-008 (Leveled)
 009: SW-009 (Leveled)
 010: SW-010 (Leveled)
 011: SW-011 (Leveled)
 012: SW-012 (Leveled)
 013: SW-013 (Leveled)
 014: SW-014 (Leveled)
 015: SW-015 (Leveled)

Constraints

Constraint ID	ScanWorld	ScanWorld	Type
Status	Weight	Error Vector	Horz Vert
T5	Bellman_OS_targets.txt (Leveled)	003: SW-003 (Leveled)	Coincident: Vertex -
Vertex	On	1.0000 0.002 m (0.002, 0.001, -0.001) m	0.002 m -0.001 m
T5	Bellman_OS_targets.txt (Leveled)	004: SW-004 (Leveled)	Coincident: Vertex -
Vertex	On	1.0000 0.001 m (0.001, 0.001, 0.000) m	0.001 m 0.000 m
T5	Bellman_OS_targets.txt (Leveled)	005: SW-005 (Leveled)	Coincident: Vertex -
Vertex	On	1.0000 0.001 m (0.000, 0.001, 0.000) m	0.001 m 0.000 m
T5	Bellman_OS_targets.txt (Leveled)	006: SW-006 (Leveled)	Coincident: Vertex -
Vertex	On	1.0000 0.001 m (0.001, 0.000, 0.000) m	0.001 m 0.000 m
T5	Bellman_OS_targets.txt (Leveled)	007: SW-007 (Leveled)	Coincident: Vertex -
Vertex	On	1.0000 0.001 m (0.001, 0.001, 0.000) m	0.001 m 0.000 m
T5	Bellman_OS_targets.txt (Leveled)	008: SW-008 (Leveled)	Coincident: Vertex -
Vertex	On	1.0000 0.001 m (0.001, 0.001, 0.000) m	0.001 m 0.000 m
T16	Bellman_OS_targets.txt (Leveled)	014: SW-014 (Leveled)	Coincident: Vertex -
Vertex	On	1.0000 0.001 m (0.000, 0.000, 0.001) m	0.000 m 0.001 m
T16	Bellman_OS_targets.txt (Leveled)	015: SW-015 (Leveled)	Coincident: Vertex -
Vertex	On	1.0000 0.001 m (-0.001, 0.000, 0.001) m	0.001 m 0.001 m
T14	Bellman_OS_targets.txt (Leveled)	012: SW-012 (Leveled)	Coincident: Vertex -
Vertex	On	1.0000 0.002 m (0.000, 0.002, 0.002) m	0.002 m 0.002 m
T14	Bellman_OS_targets.txt (Leveled)	013: SW-013 (Leveled)	Coincident: Vertex -
Vertex	On	1.0000 0.002 m (0.001, 0.001, 0.001) m	0.002 m 0.001 m
T14	Bellman_OS_targets.txt (Leveled)	014: SW-014 (Leveled)	Coincident: Vertex -
Vertex	On	1.0000 0.002 m (0.000, 0.001, 0.001) m	0.001 m 0.001 m
T14	Bellman_OS_targets.txt (Leveled)	015: SW-015 (Leveled)	Coincident: Vertex -
Vertex	On	1.0000 0.001 m (0.000, 0.001, 0.001) m	0.001 m 0.001 m
T8	Bellman_OS_targets.txt (Leveled)	006: SW-006 (Leveled)	Coincident: Vertex -
Vertex	On	1.0000 0.001 m (0.001, 0.000, -0.001) m	0.001 m -0.001 m
T8	Bellman_OS_targets.txt (Leveled)	007: SW-007 (Leveled)	Coincident: Vertex -
Vertex	On	1.0000 0.001 m (0.000, -0.001, 0.000) m	0.001 m 0.000 m
T8	Bellman_OS_targets.txt (Leveled)	008: SW-008 (Leveled)	Coincident: Vertex -
Vertex	On	1.0000 0.001 m (0.000, -0.001, -0.001) m	0.001 m -0.001 m
T3	Bellman_OS_targets.txt (Leveled)	001: SW-001 (Leveled)	Coincident: Vertex -
Vertex	On	1.0000 0.001 m (-0.001, 0.000, 0.000) m	0.001 m 0.000 m
T3	Bellman_OS_targets.txt (Leveled)	002: SW-002 (Leveled)	Coincident: Vertex -
Vertex	On	1.0000 0.001 m (-0.001, 0.000, 0.000) m	0.001 m 0.000 m
T3	Bellman_OS_targets.txt (Leveled)	003: SW-003 (Leveled)	Coincident: Vertex -
Vertex	On	1.0000 0.001 m (-0.001, 0.000, 0.001) m	0.001 m 0.001 m
T10	Bellman_OS_targets.txt (Leveled)	009: SW-009 (Leveled)	Coincident: Vertex -
Vertex	On	1.0000 0.001 m (0.000, 0.001, -0.001) m	0.001 m -0.001 m
T10	Bellman_OS_targets.txt (Leveled)	010: SW-010 (Leveled)	Coincident: Vertex -
Vertex	On	1.0000 0.002 m (0.000, 0.001, -0.001) m	0.001 m -0.001 m
T10	Bellman_OS_targets.txt (Leveled)	011: SW-011 (Leveled)	Coincident: Vertex -
Vertex	On	1.0000 0.002 m (0.001, 0.001, -0.002) m	0.001 m -0.002 m
T1	Bellman_OS_targets.txt (Leveled)	001: SW-001 (Leveled)	Coincident: Vertex -
Vertex	On	1.0000 0.003 m (0.003, 0.000, 0.000) m	0.003 m 0.000 m
T1	Bellman_OS_targets.txt (Leveled)	002: SW-002 (Leveled)	Coincident: Vertex -
Vertex	On	1.0000 0.002 m (0.001, 0.001, 0.000) m	0.002 m 0.000 m
T2	Bellman_OS_targets.txt (Leveled)	001: SW-001 (Leveled)	Coincident: Vertex -
Vertex	On	1.0000 0.001 m (-0.001, 0.000, 0.000) m	0.001 m 0.000 m

APPENDICES

```
T15          014: SW-014 (Leveled)          015: SW-015 (Leveled) Coincident: Vertex -
Vertex On    1.0000 0.001 m ( 0.000, 0.000, 0.000) m 0.001 m 0.000 m
T16          014: SW-014 (Leveled)          015: SW-015 (Leveled) Coincident: Vertex -
Vertex On    1.0000 0.001 m (-0.001, 0.000, 0.000) m 0.001 m 0.000 m
```

ScanWorld Transformations

```
Bellman_OS_targets.txt (Leveled)
translation: (0.000, 0.000, 0.000) m
rotation: (0.0000, 1.0000, 0.0000):0.000 deg
```

```
001: SW-001 (Leveled)
translation: (375848.033, 443400.517, 97.656) m
rotation: (0.0000, 0.0000, 1.0000):168.477 deg
```

```
002: SW-002 (Leveled)
translation: (375864.142, 443405.397, 96.927) m
rotation: (0.0000, 0.0000, 1.0000):143.821 deg
```

```
003: SW-003 (Leveled)
translation: (375871.540, 443410.792, 95.564) m
rotation: (0.0000, 0.0000, 1.0000):171.255 deg
```

```
004: SW-004 (Leveled)
translation: (375882.208, 443417.043, 93.069) m
rotation: (0.0000, 0.0000, 1.0000):125.366 deg
```

```
005: SW-005 (Leveled)
translation: (375882.455, 443426.262, 92.624) m
rotation: (0.0000, 0.0000, 1.0000):129.199 deg
```

```
006: SW-006 (Leveled)
translation: (375881.330, 443433.345, 92.557) m
rotation: (0.0000, 0.0000, 1.0000):150.598 deg
```

```
007: SW-007 (Leveled)
translation: (375876.612, 443440.510, 93.429) m
rotation: (-0.0000, -0.0000, -1.0000):18.931 deg
```

```
008: SW-008 (Leveled)
translation: (375876.612, 443440.510, 93.429) m
rotation: (-0.0000, -0.0000, -1.0000):18.942 deg
```

```
009: SW-009 (Leveled)
translation: (375863.527, 443437.317, 93.213) m
rotation: (-0.0000, -0.0000, -1.0000):122.699 deg
```

```
010: SW-010 (Leveled)
translation: (375857.844, 443435.195, 93.261) m
rotation: (0.0000, 0.0000, 1.0000):65.306 deg
```

```
011: SW-011 (Leveled)
translation: (375851.560, 443433.438, 93.230) m
rotation: (0.0000, 0.0000, 1.0000):8.297 deg
```

```
012: SW-012 (Leveled)
translation: (375843.353, 443430.909, 93.274) m
rotation: (-0.0000, -0.0000, -1.0000):108.694 deg
```

```
013: SW-013 (Leveled)
translation: (375836.379, 443426.725, 93.041) m
rotation: (0.0000, 0.0000, 1.0000):17.362 deg
```

```
014: SW-014 (Leveled)
translation: (375832.191, 443417.290, 93.483) m
rotation: (0.0000, 0.0000, 1.0000):172.393 deg
```

```
015: SW-015 (Leveled)
translation: (375835.122, 443405.713, 96.872) m
rotation: (-0.0000, -0.0000, -1.0000):138.771 deg
```

Unused ControlSpace Objects

```
001: SW-001 (Leveled):
  Vertex : unlabeled
```

```
002: SW-002 (Leveled):
  Vertex : unlabeled
```

APPENDICES

003: SW-003 (Leveled):
Vertex : unlabeled

004: SW-004 (Leveled):
Vertex : unlabeled

005: SW-005 (Leveled):
Vertex : unlabeled

006: SW-006 (Leveled):
Vertex : unlabeled

007: SW-007 (Leveled):
Vertex : unlabeled

008: SW-008 (Leveled):
Vertex : unlabeled

009: SW-009 (Leveled):
Vertex : unlabeled

010: SW-010 (Leveled):
Vertex : unlabeled

011: SW-011 (Leveled):
Vertex : unlabeled

012: SW-012 (Leveled):
Vertex : unlabeled

013: SW-013 (Leveled):
Vertex : unlabeled

014: SW-014 (Leveled):
Vertex : unlabeled

015: SW-015 (Leveled):
Vertex : unlabelled

C. The Output of the Proposed Method Applied on Bellmanprak Project

Before ICP-Registration

Output of GPA software, which created by Hasan Jaafar.
31-Jan-2016 18:15:51

Input file:

Outlier removal, number of points use for mean distance estimation (k)=30 (Put zero if you don't want to apply it)

Outlier removal, standard deviation multiplier threshold=3 (Put zero if you don't want to apply it)

Number of Epochs=3

Voxel Size(m)=0.03

Box Dimension(m)=.30

Sample Size(mm)=30

Surface Interpolation Method (1-Poly 2-LOWESS 3-TLS)=2

Number of None deformed Epochs=3

Epochs' Weights= 1-1-2

Cloud before Outlier removal: 84329932

Cloud after Outlier removal: 82971323

PointCloud before filtering: 82971323 data points (x y z).

PointCloud after filtering: 3555277 data points (x y z).

Cloud before Outlier removal: 84329932

Cloud after Outlier removal: 82971323

PointCloud before filtering: 82971323 data points (x y z).

PointCloud after filtering: 3555277 data points (x y z).

Cloud before Outlier removal: 36423996

Cloud after Outlier removal: 36044042

PointCloud before filtering: 36044042 data points (x y z).

PointCloud after filtering: 2041218 data points (x y z).

Time cost (seconds):

Voxel Filter: 4494.88

Boxing Structure: 289.73

Time cost for Epoch_3 (seconds):

Finding Correspondences: 195.74

Surface Interpolation: 5773.55

GPA and F-test: 180.22

Visualisation (CloudCompare files): 48.04

Total Run Time (seconds): 12003.78

Finished time: 31-Jan-2016 21:35:54

Total number of deformed boxes (more than 95% deformation probability)=2386

D. The Output of the Proposed Method Applied on Bellmanprak Project

After ICP-Registration

Output of GPA software, which created by Hasan Jaafar.
10-Feb-2016 15:19:55

Input file:

Outliers Removal, number of points use for mean distance estimation (k)=30 (Put zero if you don't want to apply it)
Outlier removal, standard deviation multiplier threshold=3 (Put zero if you don't want to apply it)
Number of Epochs=3
Voxel Size(m)=0.03
Box Dimension(m)=.30
Sample Size(mm)=30
Surface Interpolation Method (1-Poly 2-LOWESS 3-TLS)=2
Number of None deformed Epochs=2
Epochs' Weights= 1-1-2

Cloud before Outlier removal: 84329932
Cloud after Outlier removal: 82971323
PointCloud before filtering: 82971323 data points (x y z).
PointCloud after filtering: 3555277 data points (x y z).

Cloud before Outlier removal: 84329932
Cloud after Outlier removal: 82971323
PointCloud before filtering: 82971323 data points (x y z).
PointCloud after filtering: 3555277 data points (x y z).

Cloud before Outlier removal: 36423996
Cloud after Outlier removal: 36044042
PointCloud before filtering: 36044042 data points (x y z).
PointCloud after filtering: 2040882 data points (x y z).

Time cost (seconds):
Voxel Filter: 4331.77
Boxing Structure: 286.12

Time cost for Epoch_3 (seconds):
Finding Correspondences: 191.17
Surface Interpolation: 5806.91
GPA and F-test: 162.52
Visualisation (CloudCompare files): 42.99

Total Run Time (seconds): 11411.08

Finished time: 10-Feb-2016 18:30:07

Total number of deformed boxes (more than 95% deformation probability)=1047

E. The Output of the Proposed Method Applied on Bellmanprak Project

After ICP-Registration and Rotation

Output of GPA software, which created by Hasan Jaafar.
22-Feb-2016 15:00:59

Input file:

Outlier removal, number of points use for mean distance estimation (k)=30 (Put zero if you don't want to apply it)

Outlier removal, standard deviation multiplier threshold=3 (Put zero if you don't want to apply it)

Number of Epochs=3

Voxel Size(m)=0.03

Box Dimension(m)=.30

Sample Size(mm)=30

Surface Interpolation Method (1-Poly 2-LOWESS 3-TLS)=2

Number of None deformed Epochs=2

Epochs' Weights= 1-1-2

Cloud before Outlier removal: 84329932

Cloud after Outlier removal: 82971343

PointCloud before filtering: 82971343 data points (x y z).

PointCloud after filtering: 3495699 data points (x y z).

Cloud before Outlier removal: 84329932

Cloud after Outlier removal: 82971343

PointCloud before filtering: 82971343 data points (x y z).

PointCloud after filtering: 3495699 data points (x y z).

Cloud before Outlier removal: 36423996

Cloud after Outlier removal: 36044035

PointCloud before filtering: 36044035 data points (x y z).

PointCloud after filtering: 1991706 data points (x y z).

Time cost (seconds):

Voxel Filter: 4429.56

Boxing Structure: 268.70

Time cost for Epoch_3 (seconds):

Finding Correspondences: 177.99

Surface Interpolation: 5807.06

GPA and F-test: 151.17

Visualisation (CloudCompare files): 35.81

Total Run Time (seconds): 11286.52

Finished time: 22-Feb-2016 18:09:05